Structure and Electronic Properties of Endohedrally Doped II-VI Hollow Nanoclusters

Doctoral Dissertation

Elisa Jimenez Izal

Director: Jon M. Matxain

Co-director: Jesus M. Ugalde

September 2014

ESKERRIK ASKO!

Eta azkenik eskerrak emateko momentua heldu da... Lehenik eta behin talde osoari eman nahi dizkiot eskerrak, benetan oso urte politak pasa ditudalako eta oso babestuta sentitu naizelako zuen artean. Asko maite zaituztet!

Txoni, mila esker! Urte hauetan zure laguntza behar izan dudan momentu guztietan hor egon zarelako, beti gauzak azaltzeko prest eta alderdi desberdinei buruzko aholkuak ematen. Gauza asko erakutsi dizkidazu pazientzia handiarekin. Eskerrik asko ere agobiatu naizenean zure positibotasunarekin lasaitu nauzulako. Lan hau bion arteko fruitua da eta dakidan ia guztia zuri zor dizut. Benetan oso gustora egon naiz zurekin lanean Txoni! Eta azkenik mila esker ni zaintzeagatik, adibidez tesia hasi nintzenean, Mariok eta zuk gomendatu zenidatenean ez zela egokia katedratikoz betetako autobus batean "welcome to Tijuana" kantatzea...

Jesus, zuri ere gauza asko eskertu nahi dizkizut, hasteko taldean doktoradutza egiteko aukera ematea. Zure konfiantzagatik ere eskerrik asko, eta beti irribarre batekin zabiltzalako, eman dizkidazun animo guztiengatik, eta zure positibotasuna kutsatzeagatik. Bidaiatzeko eta pertsona eta toki desberdinak ezagutzeko eman didazun aukera benetan eskertzen dizut! Taldean hain giro ona egotea ere zuregatik da, errespetuan oinarritutako taldea osatu duzulako.

Xabi, eskerrik asko bihotz-bihotzez! Batez ere urte hauetan zehar izan ditugun elkarrizketengatik eta bizitako momentu xarmangarriengatik! Badakizu beti maiteko zaitudala, behintzat burusoil geratzen ez zaren bitartean :)

Txemita! Zer egingo nukeen zu gabe ordenagailu madarikatuen artean igarotako urte hauetan! Eta a ze pazientzia izan duzun nire pazientzia faltarekin. Baina ez nizuke hori bakarrik eskertu nahi, eman dizkidazun iritzi eta aholkuengatik ere. Gainera, tesian zehar ikasi dudan beste gauza bat, zurekin inoiz ez eztabaidatzea da, azken finean beti arrazoia daukazu!

Mayito! Muchas gracias por toda tu alegria y tu dinamismo! Todavía no entiendo como ya desde la hora del café estás tan lleno de energía... Y como no, gracias por haberme ayudado con los ejercicios de los cursos de doctorado, explicándome todas esas ecuaciones y con ese maravilloso programa que es siesta, y sus maravillosos pseudopotenciales!

John Wayne! Zuri bereziki eskerrak eman nahi nizkizun, bizitako momentu polit guztiengatik. Triestetik Meridara, mundua elkarrekin ezagutu dugu! Eta esan behar dut plazer handia izan dela. Baina ez hori bakarrik, tokatu zaigu doktoradutza aldi berean egitea eta ezingo nukeen lagun hobeago bat izan horrelako esperientzia konpartitzeko.

Elenita, ni hasi nintzenean hemen zinen eta 3 urte Suitzan pasatu ondoren berriz bueltan etorri zinenean kriston ilusioa egin zidan, benetan pertsona inportantea zarelako taldean. Mila esker denbora guzti horretan behar izan dudan guztietan laguntzeagatik!

Fernandito eta Joni! Ezin dut ahaztu zuen laguntza guztia eta batez ere elkarrekin bota ditugun parreak! Mila esker!

Eli, zuri ere eskerrik asko, batez ere post-doc-ari begira eman zenizkidan aholku guztiengatik.

Uriangato, Slawek, Oier, Andreas, Ivan, Noelia, eskerrik asko; David y Matitus Maximus moltes gràcies!

Vorrei ringraziare anche Piero Ugliengo per avermi accolto così bene nel suo gruppo e per tutto quello che mi ha insegnato durante i tre mesi in cui sono stata a Torino. Grazie a Fabio, Max, Enrikito e Marta, per avermi insegnato tante cose, da Crystal all'italiano! Grazie anche a Matteo, Elisa, Alessandro... e sopratutto a Martina e Claire per i bellissimi momenti che abbiamo passato insieme!

También mis más sinceros agradecimientos a Gabriel y su familia y a todo el grupo de Mérida por lo bien que nos trataron en México. Órale! Sigfrido, Claudia, Maryel, Alberto y Said, realmente hicisteis del tiempo que estuvimos con vosotros algo mágico. Nunca olvidaré aquellos dos meses, muchas gracias de corazón!

Amaia eta Edur, eskerrik asko karreran elkar ezagutu ginenetik bizitako guztiarengatik! Elkarrekin parre egin dugu, eta negar ere bai, kadenetak eta kexa eskutitzak egin eta azken finean bizitzan gertatu zaizkigun gauza desberdinak konpartitu. Eskerrik asko benetan behar izan zaituztedanean nire ondoan egoteagatik!

Txikita, nire bizitzako pertsona garrantzitsuenetarikoa zara, ez dakizu zenbat maite zaitudan! Eskerrik asko bihotzez nire ondoan egoteagatik, nire txapa guztiak entzuteko prest eta nire egonkortasun emozionala mantentzen laguntzeagatik. Ziur nahiz beti lagunak izango garela eta bizipen guztiak konpartitzen jarraituko dugula.

Eskerrak eman nahi dizkiet nire kuadrilakoei, paregabeko bizipenengatik eta momentu zailetan ere zuen laguntzagatik, nahiz eta leku desberdinetan bizi garen, beti hurbil sentitzen zaituztedalako. Aupa Irrealkuadri!

Eskerrik asko nire familiari, beti nire ondoan egon direlako, maitasuna eta umorea konbinatuz, eta haien artean familiako hurrengo kimikariari, Nerea. Asko maite zaituztet! Eskerrik asko ere Oskarren familiari, familiako kide bat gehiago sentiarazi nauzuelako, oso babestuta sentitu nahiz zuen artean eta asko maite zaituztet!

Txintxu, mila esker zure babes eta maitasunagatik. Perfekzioa existitzen ez dela esaten dutenek zu ezagutzen ez zaituztelako diote hori. Bizitzak eman didan opari bat zara niretzat, nire maitea, nire laguna. Zure irribarrarekin mundua askoz politago bilakatzen da eta geratzen zaigun bizitza osoa zurekin konpartitzen jarraitu nahi dut. Ikaragarri maite zaitut bihotza!

Eta bereziki eskerrak eman nahi dizkiot amari, dena zuri zor dizut, naizen guztia zuregatik da eta tesi hau zuri dago dedikatuta.

Amari

Contents

Part I

Introduction

Chapter 1

Sarrera Orokorra

1.1 Nanozientzia eta Nanoteknologia

Nanozientzia eta naoteknologia definitzeko modu desberdinak daude. Eskala atomiko eta molekularreko materialen manipulazio eta azterketatik sortzen den zientzia eta teknologia bezala ikus daitezke. Dimentsio bat edo gehiago 100nm baino txikiago dauzkan materialen (nanomaterialak) diseinu, produkzio eta erabileraz arduratzen diren zientzia eta teknologia bezala ere ulertu daitezke. Alor hauek fisika, kimika, medikuntza eta ingenieritzaraino iristen dira, arazo ezberdinei erantzuna emanez, zientzia basikotik aplikazio teknologiko desberdinetara. Material erdieroaleen industriaren miniaturizazio beharra edo bioentitate nanometrikoak eta haien elkarrekintzak beste materialekin dira gaur egun nanozientzia eta nanoteknologia ekiditen saiatzen ari diren arduren adibideak.

Atomoak banan-bana manipulatzearen posibilitatea, lehen aldiz Richard Feynman-ek aipatu zuen 1959. urtean, bere esaldi ospetsuan islatuta “hondoan leku asko dago”. 80ko hamarkadan bi garapen berritzailek momentu horretara arte bakarrik kontzeptuak zirenak errealitate bilakatzea ahalbideratu zuten, nanozientzia eta nanoteknologiaren garapenean izugarrizko inpaktua izanik. Horietako lehenengoa tunel bidezko mikroskopioaren (STM) sorkuntza izan zen [1]. Teknologia honek gainazaletako atomoen banakako identifikazioa ahalbidetu zuen lehenengo aldiz. Gainera, STM-ren zenbait arazo, erabilgarritasun mugatua material eroaleekin adibidez, ondorengo indar atomikoko mikroskopioaren [2] kreazioarekin konpondu ziren. Bigarren gertaera klusterren zientziaren jaiotza izan zen, metal alkalinoen izu-

garri egonkorrak ziren estekiometrien detekzioarekin [3] eta C_{60} buckminsterfulerenoaren aurkikuntzarekin [4] .

Nanoteknologoek nanoeskalan materialak fabrikatzeko edo gailuak manipulatzeko bi hurbilketa garatu dituzte: behetik-gora (bottom-up) eta goitik-behera (top-down). Behetik-gorako hurbilketa nanomaterialak atomoka edo molekulaka eraikitzean datza. Bere sorburua kimika molekularra da, atomoak edo molekulak abiatze puntua izanik, eta bere helburua nanomaterialen diseinua eta tamaina handitzean propietateen transformazio ez-lineala aztertzea da. Goitik-beherako metodoa, aldiz, solido baten elkarren segidako mozketan datza, nanopartikulak lortu arte. Egoera solidoko fisikatik dator eta tamaina txikitzearen ondorioak aztertzen ditu. Bi hurbilketek nanopartikula-erregimenean konbergitu egiten dute. Nanomaterialek solido eta konposatu atomiko edo molekularren arteko zubia eratzen dute [5, 6].

Inportantea da azpimarratzea materia nanoeskalan antolatzen denean, bere portaera eta propietateak guztiz desberdinak izan daitezkeela solidoarekin konparatuz. Propietateak tamainarekiko menpekotasuna erakusten dute eta diskontinuoki aldatu egiten dira. Azkenik, tamaina batetik aurrera, propietateak gutxi aldatzen dira, solidoaren mugara heldu arte. Bi faktore dira fenomeno honen arduradun nanoeskalan. Alde batetik, elektroien uhin-luzera material osoaren ordenakoa denean, efektu kuantikoek sistemaren portaeran eta propietateetan eragin handia dute. Ondorioz, elektroiak espazioko eremu txikian konfinatuta daude, nanopartikularen ezaugarri optoelektronikoak aldatuz. Beste alde batetik, beraien gainazal/bolumen erlazioak eragin handia dauka. Atomo gehienak gainazalean daudenez, lotura asegabeen zenbakia txikitzeko, berrantolatu egiten dira, ustekabeko egiturak osatuz. Beraz, nanoeskalan lan egiteak zientzialariei nanomaterialen propietateak aztertu eta erabiltzeko aukera eskaintzen die. Izan ere ikusi izan da nanopartikulen erregimenean konposatu isolatzaileak eroale bilakatu daitezkeela [7], kolorea aldatu dezaketela [8], erreaktibitatea handitu [9], eta abar, aplikazio mota desberdinetarako balio daitezkeenak. Aurrean aipatutako gailu elektronikoen miniaturizazioaz eta aplikazio biologikoaz gain, bai diagnostikorako eta gaixotasunen kontrako lehiarako, nanopartikulen gainazal hedatuari esker katalisirako edo sentsore bezalako aplikazioetarako material egokiak izan daitezke. Bestalde, nanomaterialek eskaintzen duten abantaila harrigarriena, beraien aldagarritasuna da: propietateak tamaina eta konposizioaren arabera aldatzen direnez, printzipioz, borondatez al-

datu daitezke.

Aurreko bi hamarkadetan, material hauen propietate fisikokimikoen ulermenak aurrerapauso handia suposatu du nahitako egitura zehatzen kontrol tekniken garapenean. Ondorioz, konposizio atomiko zehatza duten nanopartikulak sintetizatu daitezke gaur, bai gas fasean eta baita disoluzioan ere. Teknika esperimentalak erabili ezin daitezkeenean, aldiz, teoria konputazionala funtsezko tresna bihurtu da, iragarpena oinarri bezala, esperimentuak gidatuz. Metodo eta gaitasun konputazionalen hobekuntzak material berrien inguruko iragarpenak egiteko eta beraien ulermena hobetzeko aukera eskaintzen du, froga-eta-errorea saihestuz. Zentzu honetan, aipatu beharra da nahiz eta C_{60} buckminsterfulerenoaren detekzio esperimentala 80ko hamarkadan egin, 1970. urtean teorikoki aurreikusi izan zela [10].

Esperimentu eta kalkulu teorikoen arteko erlazioa ezinbestekoa da nanoteknologia garatu ahal izateko eta, Marks-ek esan bezala "partikula txikien egitura ezin da esperimentuez baliatuz soilik ulertu, aldi berean modelizazio teorikoa edo beste motatakoa erabiltzea beharrezkoa da" [11].

1.2 Nanoklusterrak

Nanomaterialen artean, nanoklusterrak nanoestrukturarik txikienak kontsideratu daitezke. Nahiz eta nanoklusterren definizio adosturik ez dagoen, nanometroetako tamaina duten atomo edo molekulen multzo bezala ikus daitezke, $\sim$10 to 10^4 inguruko partikulaz osatuta. Neutralak edo kargatuak izan daitezke. Indar desberdinen bidez egon daitezke lotuta: kontrako kargak dituzten ioien arteko erakarpena, (NaCl nanokulsterrak adb.), van der Waals atrakzioa (He eta Ar klusterren artean bezala), lotura kobalentea (Si klusterrak), edo lotura metalikoa (Al edo Cu klusterretan bezala). Klusterrak estudiatzeko motibazio desberdinak daude [12]. Solido eta konposatu atomiko edo molekularraren arteko zubia direnez, interes zientifikoa daukate. Ondorioz, propietate kimiko eta fisikoen eboluzioa tamainarekin aztertzeko aukera paregabea eskaintzen dute. Gainera, kristalen nukleazioa eta hazkuntza ulertzeko oso erabilgarriak izan daitezke. Azkenik, klusterren estudioa, beraien propietate eta paregabeko naturarekin batera, alor erakargarria da benetan. Tesi hau azkeneko alorrean kokatu egiten da.

Klusterren edertasun dotorea "kluster magikoak"-etan azaltzen da.

Izan ere, klusterren egonkortasuna hazkuntza eta deskonposizioari dagokionez, ez da monotonikoki aldatzen tamainarekin, baizik eta zenbait tamainek egonkortasun nabaria erakusten dute, hau da, kluster magikoak. Horregatik nanoklusterrei buruz esan egiten da "atomo batek desberdintasuna egiten duela". Kluster magikoen egonkortasun handia osagai elektroniko eta geometrikoa daukate. Orokorrean efektu elektronikoek tamaina txikietan menperatzen dute eta trinkotasun geometrikoa tamaina handiagoetan [13]. Teoria eta esperimentuen arteko sinergia ezinbestekoa izan da klusterren alorrean. Izan ere, esperimentuen bitartez zuzenean klusterren geometriak aurkitzea zaila da, eta teoriak ezinbesteko papera betetzen du materia forma honen egitura atomikoa zehazteko [5]. Kluster magikoen artean, ezagunenetako bat C_{60} fulerenoa da, 1985. urtean aurkituta R. F. Curl, R. E. Smalley eta H. W. Kroto-ren eskutik [4]. 1812 isomero posibleen artean, kaxa huts esferikoko itxura daukan egitura da egonkorrena, 12 pentagonoz eta 20 hexagonoz osatutakoa, non atomo guztiak egiturako gainazalean kokatuta dauden, ikusi Fig. 1.1. Era honetan, karbono bakoitza beste hiru karbono atomoetara dago lotuta, sp^2 orbital hibridoen bidez. Fulerenoak karakterizatzen duen kurbadura Gaussiar positiboaren arduradunak pentagonoak dira. Pentagonoak eta hexagonoak, pentagono bakoitza bost hexagonoz inguratuta egon daitezela kokatuta daude, Pentagono Isolatuaren Araua (IPR ingelesez) betez [14]. Kluster honen egonkortasun nabaria faktore elektroniko eta geometrikoetan dauka jatorria. Izan ere, geruza elektroniko itxia eta I_h simetria dauka.

Figure 1.1: C_{60} buckminsterfulerenoa 1985. urtean aurkituta Kroto *et al.*-en eskutik.

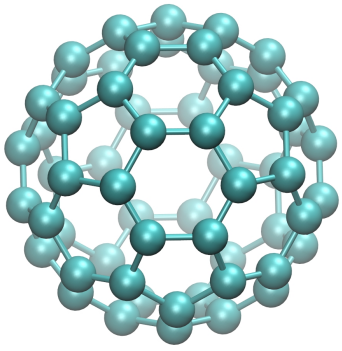

C_{60} klusterraz gain, beste fulereno egonkorrak sintetizatu izan dira esperimentalki, hala nola C_{84}, C_{80}, C_{76}, C_{70} eta C_{20}, orain arte sintetizatutako karbonozko nanoklusterik txikiena. Tamaina edozein delakoa ere, pentagonoak eta hexagonoak (eta heptagonoak aldizka) hondar motiboak dira kaxa motatako egitura hauetan. Unitate hauen sorrera tentsio geometrikoaren minimizazioarekin dago lotuta. Karbonozko fulerenoak poliedro itxien Eulerren teorema jarraitzen dutela ikusi izan da: aldeen (F), erpinen (V) eta ertzen (E) kopurua hurrengo erlazioa bete behar dute V+F-E = 2. Pentagonoz eta hexagonoz bakarrik osaturiko karbonozko klusterren kasuan, pentagonoen kopurua beti n_{penta}= 12 da eta hexagonoen kopurua n_{hexa}> 1 da. Aipatu behar dugu beranduago beste karbono alotropoak sintetizatu izan dira, karbonozko nanohodiak [15] eta grafenoa bezalakoak [16].

Karbonozko fulerenoen aurkikuntzaren ondoren, ahalegin nabarmenak egin izan dira beste materialez egindako nanoklusterrak sintetizatzeko eta karakterizatzeko. Silizioa eta karbonoa taula periodikoaren talde berdinean daudenez, Si klusterrak ikertu egin ziren lehenbizi. Nano-gailuetan aplikatzeko posibilitatea ere izan zen ikerkuntza honetarako interesa. Hala ere, fulereno motako egiturak osatzeko silizioak zailtasunak dauzkala ikusi zen. Arrazoia da karbonoak, sp^2 hibridazioaz baliatuz, kaxa motako egiturak π loturen bidez egiten dituen bitartean, silizioak joera sendoa daukala sp^3 loturak egiteko, zeinek hiru dimentsioko diamante bezalako egiturak eratzen dituen. Beraz, silizio atomoekin kaxak eta hodiak osatzea zaila da. Siliziozko klusterrak egonkortzeko bi mekanismo garatu dira. Lehenengoa dopaketa endoedrikoa da eta 1.4 subatalan azalduko da. Bigarrena, siliziozko fulerenoen gainazaleko lotura asegabeak hidrogeno atomoekin asetzea da [17, 18]. Lortutako egiturek simetria (karbonozko klusterrak bezala) eta HOMO-LUMO gap handiak erakusten dituzte. Bi mekanismoen konbinazioak ere emaitza onak emango dituztela aurreikusten da [19].

Beste kluster elementalen inguruan ikerketa zabala egin da, batez ere kluster metalikoen inguruan, hala nola metal alkalinoak [3, 20, 21], aluminioa [22, 23, 24], burdina [25], zilarra [26], urrea [27, 28, 29, 30, 31], etab. Sakonduko ez dugun arren, aipatu nahiko genuke nanokluster metalikoen estudioak Jellium modeloaren [32] garapena ekarri zuela, esperimentalki detektaturiko oso egonkorrak diren estekiometriak azaltzeko. Modu honetan, kluster magikoak geruza elektronikoen betetzearekin erlazionatu ziren.

Boro nitruroa karbonoarekiko isoelektronikoa denez, ikertutako sistema binarioetako lehena izan zen nanoeskalan, fulereno bezalako egiturak osatuko zituztenentz aztertzeko. Bestalde, BN eta C antzeko lotura kimikoa azaltzen duten arren, BN-k erreaktibitate txikiagoa dauka, egokia izanik karbonoa erabili ezin den zenbait aplikazioetarako. BN-ren batera, beste III-V elementuetako klusterrak ere sakonki aztertuak izan dira. Guztiak band-gap handiko erdieroaleak dira, apropos izanik tratamendu mediko, informazio biltegi, eta beste aplikazio optoelektronikoetarako. Gainera, nanoeskalaraino tamaina txikitzeak eskaintzen dituen aukerak izugarriak dira.

Figure 1.2: $(BN)_{12}$ nanoklusterraren egoera fundamentala. B atomoak laranjan eta N atomoak urdinez irudikatuta daude.

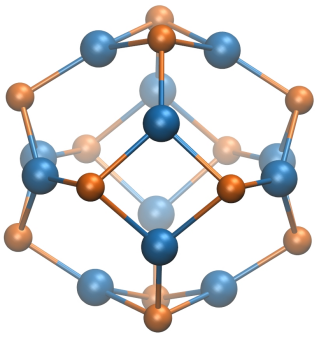

Kluster elementalen eta AB kluster estekiometriko binarioen arteko desberdintasun bat da lotura homonuklearrak (A-A, B-B) energetikoki oso desegonkorrak direla lotura heteronuklearrekin (A-B) konparatuta, nahiz eta zenbait nanokluster egonkor izan daitezkeen atomo elektroemaileen arteko lotura homonuklearrak izanik [33, 34]. Ondorioz, nanokluster binarioak laukiz eta hexagonoz osatuta daude (eta oktogonoz aldizka). Pentagono Isolatuaren Arauaren antzera, sistema hauetarako Tetragono Isolatuaren Araua proposatu da [35, 36]. C_{60}-ren analogoa $(BN)_{30}$ izango litzateke, baina ezegonkorra da. Pentagonoek elkarren segidako B-N loturak izateko posibilitatea deusezten dute, zeren eta B-B eta N-N lotura homonuklearrak izatera bortxatuko lituzkete pentagono bakoitzean. Ikerketek, ordea, boro nitrurozko nanoklusterrak aurkitu dituzte [37, 38]. Adibidez, kaxa motako $(BN)_{12}$, $(BN)_{16}$, $(BN)_{28}$ eta $(BN)_{36}$ kluster magikoak, egonkortasun nabaria on-

doko tamainetako klusterrekin konparatuta eta HOMO-LUMO gap handiak dituztelarik [36, 39, 34, 40, 41]. Aipagarria da n=12 simetria handiko kluster magiko txikiena dela, Tetragono Isolatuaren Araua asetuz [42, 43, 39]. Halaber, BN fulerenoen topologiak, beste III-V nanokluster binarioetarako energetikoki aldekoak direla aurkitu dira, hau da, $(AlN)_n$ [44], $(GaP)_n$ [45], $(AlP)_n$ [46], eta $(GaN)_n$ [47]. Hala ere, BN fulereneoak beraien III-V homologoak baino egonkorragoak dira [48], tamainaren araberako bang-gap-aren aldakortasun handiagoa erakusten duten bitartean [49].

1.3 II-VI Nanoklusterrak

II-VI nanomaterialak sakonki ikertuak izan dira azken bi hamarkadetan. Konfinamendu kuantiko eta beraien gainazal morfologia bereziei esker, II-VI nanokonposatu erdieroaleak maiz erabiltzen dira, adibidez fotokatalizatzaile bezala [50]. Beraien propietate optoelektroniko ikusgarriak direla eta, sentsore [51], eguzki zelula fotoboltaiko [52] eta gailu optoelektroniko [53] bezalako aplikazioetarako erabilgarriak direla ikusi da. Halaber, II-VI nanomaterial erdieroaleen erabilera ikerketa biologikoetan nabarmenki handitu da, azaltzen dituzten propietate optikoengatik eta biofuntzionalizazioan izandako azken aurrerakuntzengatik [54]. Lan esperimental eta teoriko askok arreta jarri dute II-VI kluster estekiometriko eta ez-estekiometrikoetan.

II-VI kluster ultra-txikiak laser ablazioaren bidez sintetizatu izan dira, C_{60}-ren aurkikuntzan erabilitako metodo berdina. Kontutan hartu behar da kluster ioien konposizioen distribuzioak sintetizazio metodoaren menpekotasuna daukala [55]. Teknika hau erabiliz eta ondoren ioi positiboak "time-of-flight" (TOF) deituriko masa espektrometroaren bidez analizatuz, Burnin *et al.*-ek $(ZnS)^+$-rentzat 3, 6 eta 13 monomero unitatez konposatutako klusterrak ultraegonkorrak direla aurkitu zuten, baina $(ZnO)^+$-rentzat kluster magikorik ez zuten aurkitu [56, 57]. Sanville *et al.*-ren arabera [58], $(ZnSe)_n^+$, $(CdS)_n^+$, eta $(CdSe)_n^+$ klusterrentzat, n=16-raino izanik, n= 6 eta 13 klusterrak magikoak dira. Kukreja *et al.*-ek antzeko saioak burutu zituzten ZnO eta ZnSerekin. ZnO-ri dagokionez, ez zuten kluster magikorik aurkitu. ZnSerentzat zenbait piko nabari bildu zituzten, $(ZnSe)_6^+$, $(ZnSe)_{13}^+$, $(ZnSe)_{19}^+$, $(ZnSe)_{23}^+$, eta $(ZnSe)_{33}^+$-ri zegozkienak [59]. Ondorengo lanek, aldiz, zink oxido kluster katioikoentzat, n= 34, 60, eta 78 kluster magikoak identifikatu zituzten [60, 61]. Emaitza hauek zink peroxidoa prekur-

sore bezala erabilita lortu zituzten, ohiko ZnO erabili ordez. Kluster magiko hauen egoera fundamentaleko egiturak kaxa modukoak direla proposatu zen.

Kimika koloidala ere nanoklusterrak sortzeko aplikatu izan da. Alor honetan nanokluster magikoak partikula ultra-txikietatik tamaina distribuzio estuak (eta adsortzio piko estuak) eta hazkuntzari dagokionez egonkortasun handia azaltzen dituztelako desberdintzen dira. Honek hazkuntza kuantizatua bide ematen du, non nanoklusterrek tamaina diskretu batetik bestera igaro egiten duten [62, 63]. Parametro desberdinak optimizatu daitezke nanokluster magiko hauek eskuratu ahal izateko, tamainaren kontrola lortuz: produkzio metodologia, tenperatura, prekursorea, surfaktante mota eta kontzentrazioa, ligandoak, eta abar [64, 65, 66]. CdSe nanoklusterrak ur disoluzioan sintetizatu ziren, non $(CdSe)_{33}$ and $(CdSe)_{34}$ kluster magikoak identifikatu ziren [67]. Hala ere, laser ablazioa erabiliz, zein metodo bortitzagoa den, autoreek beste bi piko gehiago lortu zituzten, n= 13, 19, 33, eta 34-ei dagozkienak. Autoreen arabera, gertaera honek 13 eta 19, 33 eta 34-en fragmentazioaren ondorioz sortzen direla adierazten du. Halaber, Kasuya *et al.*-ek $(CdSe)^+$-rentzat n= 13, 33, and 34 kluster magikoak aurkitu zituzten, disolbatzaile organikoan sortu eta TOF masa espektrometroarekin identifikatu zituztelarik [68, 69]. Beste II-VI konposatuentzat, ZnS, CdS eta ZnSe bezalakoentzat adibidez, kluster magiko berdinak identifikatu ziren [68, 69, 70, 71]. Gainera, $(CdSe)^+_{33}$ eta $(CdSe)^+_{34}$ bereziki egonkorrak direla ikusi zuten, nahiz eta hazkuntza faboratzen duten baldintzetan egon. Autoreek kluster hauen egoera fundamentalentzat $[(CdSe)_5@(CdSe)_{28}]^+$ eta $[(CdSe)_6@(CdSe)_{28}]^+$ nukleo-kaxa egiturak proposatu zituzten. Molekula surfaktanteei dagokienez, nanoklusterrei tinko lotuta ez zeudela ikusi zen, baizik eta modu errazan askatu zitezkeela. Ildo honetan, duela gutxi Wang *et al.* $(CdSe)_{13}$ isolatzeko gai izan ziren, orain arte isolatutako CdSe nanokluster txikiena [72]. Ondorengo lan teoriko batek $Se@Cd_{13}Se_{12}$ (Fig. 1.3) isomero egonkorrena dela aurreikusi zuen, ligandoak izan edo ez, eta bai gas fasean eta disoluzioan ere [73]. $(CdS)_{13}$ kasurako beste lan teorikoek egitura berdina proposatu dute [68, 74, 75]. $(ZnSe)_{13}$ eta $(ZnS)_{13}$ kasuetarako, aldiz, nukleo-kaxa isomero hau minimo lokala dela iradoki izan da [76, 58]. Koordinazio laukoitzarekin egiturak osatzeko, kadmioaren joera zink-arena baino handiagoa delako proposatu da.

Figure 1.3: $(CdSe)_{13}$ nanoklusterraren aurreikusitako egoera fundamentala. Cd atomoak urdinez eta Se laranjaz irudikatuta daude.

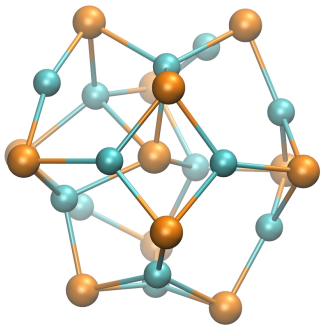

Lan esperimentalekin batera, ahalegin teoriko handia egin da II-VI nanoklusterrak modelizatzeko. Izan ere, atomo gutxi batzuetaz osatutako klusterren karakterizazio esperimentala lan zaila da eta teknika konputazionalak beraien egitura eta propietateak zehazteko ezinbesteko tresna bilakatu dira.

Nanoklusterren formari dagokionez, orokorrean ondo bereiztutako zenbait erregimen daude, tamainaren funtzio direnak. Erregimen desberdinen arteko trantsizioa konposizioarekin menpekotasuna dauka, eta kasu batzuetan ze tamaina zehatzetan gertatzen den trantsizio horri buruz oraindik eztabaida dago [55]. Kluster txikienek, atomo gutxi batzuetaz osatutakoak, koordinazio bikoitza eta eraztun moduko egiturak dauzkate. Kadmio eta zink oxidoentzat eraztun egitura hauek minimo globalak direla aurreikusten da n= 7 arte, nanokluster handiagoak esferoide hutsak diren bitartean [77, 78, 79, 80]. CdX eta ZnX, X= S, Se eta Te izanik, aldiz, kluster tamaina txikiagoetan (eraztun egiturak n $\leq$5-entzat) jasaten dute trantsizio hau, ikus Fig. 1.4 [57, 81, 82, 83]. Eraztunetik esferoidetarako trantsizioa bi kontrako joeretatik dator. Lehenengo X-Zn(Cd)-X loturen joera linearitaterako eraztunen alde egiten du. Bigarren, koordinazio handiagoak lortzeko joerak esferoideak faboratzen ditu. Egia esan, wurtzita eta zink-blenda solidoen egituretan atomoek koordinazio laukoitza daukate. Estudio konputazionalek jakinarazi dute, koordinazio handiagoak, loturen arteko angeluen tentsioa handia dakarrenean, lehenengoak nagusitzen dela. Matxain *et al.*-ek proposatu dute, zink eta kadmio oxidoen eta kalkogenoen arteko desberdintasunaren jatorria, oxigenoaren d orbitalak energian altuago egotea eta, beraz, S, Se eta Te-ren trebetasuna koordi-

nazio handiagoa lortzeko handiagoa izatea dela [83].

Figure 1.4: Ezkerretik eskuinera $(ZnS)_4$, $(ZnS)_6$, eta $(ZnS)_{12}$ nanoklusterren egoera fundamentalak. Zn atomoak grisez eta S atomoak horiz irudikatuta daude.

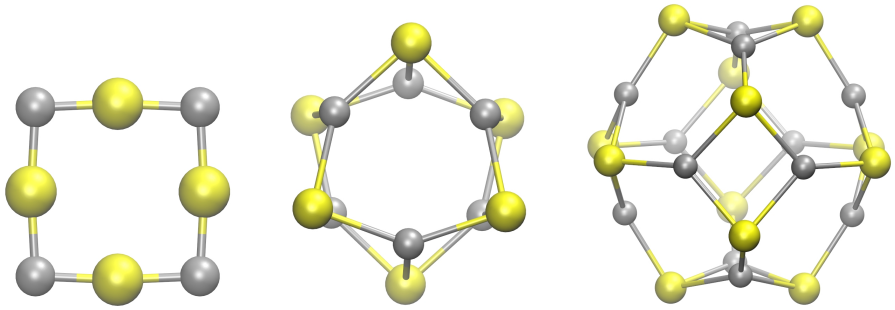

Tamaina-erdiko kaxa moduko klusterren egoera III-V klusterren antzekoa da: tetragono isolatuaren araua jarraitzen dute eta lotura heteronuklearrak dira homonuklearrak baino energetikoki egokiagoak dira. Bestetik, kluster egonkorrenek ez dute oktogonorik izaten eta tetragono eta oktogonoen kopuruaren handitzeak sistema desegonkortu egiten du [84]. Beraz, III-V nanoklusterren motibo estruktural berdinak azaltzen dira, n= 12 simetria altuko kluster magiko txikiena izanik. Izan ere, $(AB)_{12}$ kaxak T_h simetria erakusten du eta ikaragarri egonkorra dela iragarri da. $(AB)_{16}$ klusterra ere, T_d simetria daukana, arras egonkortzat hartzen da. Hau egonkortasun eta simetriaren arteko seinale da. Konturatu II-VI materialen gas faseko esperimentuetan, 13 monomero unitate dauzkaten klusterrak direla detektatzen direnak baina hauek katioiak dira eta kargak egonkortasun erlatiboan eragina izan dezake. Teoria eta esperimentuen arteko konparaketa egiteko, kluster neutral, anioiko eta katioikoek egitura atomiko eta elektroniko desberdinak izan ditzaketela ere kontuan hartu behar da.

Kluster esferoidalek edo kaxa modukoek poliedro itxietarako Eulerren teorema betetzen dute, beraz lauki, hexagono, eta oktogono kopurua hurrengo moduan kalkulatu daiteke:

$$N_{6-ring} = n - 4 - 2N_{8-ring} \tag{1.1}$$

$$N_{4-ring} = 6 + N_{8-ring} \tag{1.2}$$

II-VI nanokluster handiagoek tipula edo burbuila motako egitura hartzen dute, hau da, kaxa moduko kluster bat beste handiago baten barruan edukita. $(ZnS)_{50}$, $(ZnS)_{60}$, $(ZnS)_{70}$, eta $(ZnS)_{80}$ klusterrak dira honen adibide, zeintzuk $(ZnS)_6@(ZnS)_{44}$, $(ZnS)_{12}@(ZnS)_{48}$, $(ZnS)_{12}@(ZnS)_{58}$, eta $(ZnS)_{17}@(ZnS)_{63}$ bezala ikus daitezkeen hurrenez hurren [85, 86]. Nahiz eta atomo batzuk koordinazio laukoitza izan, gehienak koordinazio hirukoitza daukate egitura hauetan.

Gero, tamaina batetik aurrera (2.5 nm gutxi gora behera), klusterrak kristalinoak dira, BCT zeolitaren egitura berdina dutenak [87, 88, 89]. Konposatu hauetan barruko partea kristalinoa da, gainazalean halako desordena maila dagoen bitartean, atomoen koordinazioa laukoitza izanik. BCT-ren egonkortasun nabarmena dagokien solido egiturekin konparatuta (wurtzita eta zink-blenda), distortsioak moldatzeko trebetasun handiagoa azaltzen duelako da, lotura asegabeen kopurua eta momentu dipolarra txikitzen dituen bitartean [84]. Azkenik, zenbait nanometroko diametroa duten II-VI materialek solidoen egitura daukate, hau da, wurtzita edo zink-blenda [90, 91, 92, 93].

Figure 1.5: $(ZnS)_{60}$-ren egoera fundamentala, non $(ZnS)_{48}$ kaxak $(ZnS)_{12}$ inguratzen duen. Zn atomoak grisez eta S atomoak horiz irudikatuta daude.

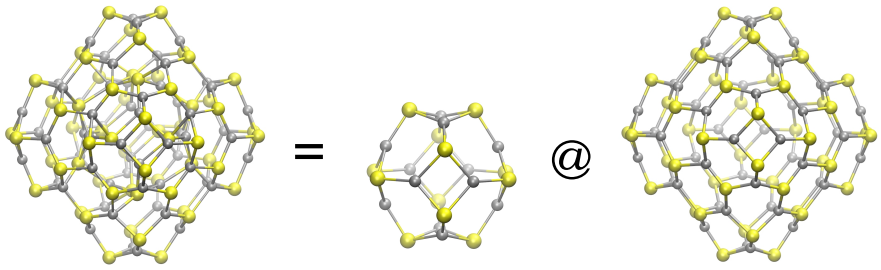

Nanomaterial hauen adsortzio espektroskopiaren bidez monitorizatutako edo karakterizatutako esperimentuek solidoekiko “blue-shift”

erakusten dute, nanoeskalan gertatzen den konfinamendu kuantikoaren ondorioz [94, 95, 96, 68, 97]. Lan konputazionalek tamainarekin batera gertatzen den band-gap-aren txikitzea konfirmatu dute, tamaina txikienetan portaera oszilakorra izanik, eta azkenik solido mugara iritsiz tamaina handitzen den heinean. Nanokluster txikienei dagokienez, Matxain *et al.*-ek kitzikapen elektronikoen energiak klusterraren geometriarekin lotuta daudela erakutsi zuen [98, 99]. Beraien ikerketek eraztun egiturek kaxa egiturek baina kitzikapen energia handiagoak azaltzen dituztela erakutsi zuten. Konposizioa edozein izanda ere, kitzikapen txikienak kalkogenoaren p orbital ez-lotzailetik (HOMO) metalaren s orbitalera (LUMO) gertatzen dira. Orbital hauek molekularen planoarekiko perpendikularrak dira eraztunen kasuan eta 3D esferoideen kasuan gainazalarekiko normalak. Nabaria da Hamad *et al.*-en lana, non $(ZnS)_n$ nanokluster esferoideen (n= 10-47) HOMO-LUMO gap-ak kalkulatu zituzten, 4.4 - 4.8 eV-eko balioak lortuz, solidoen egitura duten kluster berdinen HOMO-LUMO gap-ak 3.65 - 3.95 eV balioak dituzten bitartean [85].

1.4 Dopaketa Endoedrikoa

Nanoteknologiak zientzia ikusteko modua aldatu du, propietate berriak dituzten materialak sortzeko aukera emanez, nanokonposatuen natura paregabea dela eta. Nanomaterialen konposizioa eta egituraren kontrolak, aplikazio zehatzetarako propietate elektroniko kimiko, fisiko eta biologikoak egokitzea eta optimizatzea ahalbidetzen du. Gainera, beraien solido analogoen antzera, nanoklusterrak dopatu daitezke, hau da, ezpurutasunak apropos sartu. Kaxa moduko egitura hutsetan, C_{60} bezalakoetan, hiru modu nagusi daude dopaketa egiteko, Fig. 1.6-ran erakusten direnak. Lehenengoa ordezkapenezko dopaketa da, non atomo bat edo gehiago beste elementuetako atomoekin ordezkatzen diren, arrunki B edo N atomoekin. Bigarrena dopaketa exoedrikoa da, atomo edo molekula arrotzak kaxaren kanpoaldean kokatzen direnean. Azkenik dopaketa endoedrikoa daukagu, atomoak edo molekulak kaxaren barrualdean harrapatzen direnean. Azkeneko aukera honek besteekin konparatuta abantaila handia dakar ensanblatuari begira, zeren eta klusterren ensanblatuan oinarritutako materialetan dopatzaileak posizio zehatza izango du kaxaren barrualdean, dopatzaileen arteko distantziaren kontrola lortuz.

Figure 1.6: Ezkerretik eskuinera dopaketa egiteko hiru modu desberdinak: C_{60} fulerenoa nitrogenoarekin ordezkapeneko, exoedriko eta endoedriko dopaketa. C atomoak urdinez eta N laranjaz irudikatuta daude.

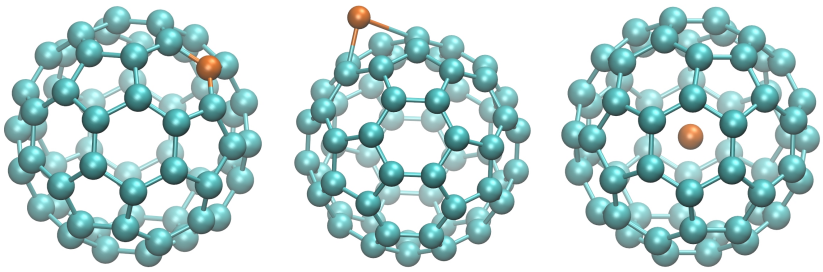

Fulerenoen ikerkuntzaren lehengo momentuetatik, fulerenoek beraien barrualdean atomoak eduki ditzaketela ikusi zen, egitura mantenduz. Sintetizatutako lehenengo fulereno endoedrikoa La@C_{60} izan zen [100]. Harrezkero, karbonozko nanokluster endoedriko ugari sintetizatu izan dira. Kaxaren kabidadearen tamainaren arabera, fulerenoak molekula txikiak edukitzeko ere gai dira. Adibidez, C_{60} nanoklusterra ur molekula bat edukitzeko gai dela aurreikusi izan da, C_{180} hamazazpi ur molekula edukitzeko gai izan daitekeen bitartean [101, 102]. Ravinder *et al.*-ek ziklopentadienilo anioiaren ((η^5-cp)$_2$Fe) enkapsulazioa karbonozko kluster desberdinetan estudiatu zuten, hurrengoa ondorioztatuz: C_{60}-ren kasuan ez da energetikoki bideragarria efektu esterikoengatik, baina C_{80} eta C_{180} klusterrek posible dute (η^5-cp)$_2$Fe anioia edukitzea [103]. Dopaketa endoedrikoaren bidez fulerenoen propietateak aldatu egiten dira. Adibidez, metalen enkapsulazioak karbonozko nanoklusterren elektroafinitatea handitu egiten du. Beraz, endoedrikoki dopatutako karbonozko fulerenoak etorkizun handiko materialak dira, beraien propietate optoelektronikoak aldatu daitezkeelako bakarrik atomo dopatzailea aldatuz, eta kanpoko karbonozko egitura aldatu gabe [104].

Gainera, ezegonkor izango liratekeen klusterrak egonkortzeko dopaketa endoedrikoa mekanismo egokia dela ikusi da, hala nola IPR betetzen ez duten karbonozko fulerenoak, dopatzailearen karga transferentziaren bidez [105, 106, 107, 108]. Siliziozko klusterrak egonkortzeko ere oso tresna eraginkorra izan daiteke. Zehazki, trantsizio metalak dopatzaile egokienak direla proposatu da, beraien d orbitalen ezaugarriei esker [109, 110, 111]. Hala ere, beste atomo dopatzaile des-

berdinak ere siliziozko klusterrak egonkortzeko gai direla proposatu da [112, 113]. Atomo bakarren enkapsulazioa fulereno txikienentzat mugatzen da, 20 atomo inguruko kaxentzat. Antzera, klusterren enkapsulazioa beste handiagoen barrualdean siliziozko fulerenoak egonkortzen dituela ikusi izan da. Horrela, Si_i klusterrak, i = 27-39 izanik, Si_j klusterrak, non j = 2-5, siliziozko kaxaren barruan erantsiz osatu egin dira [114]. Aipagarria da karbonozko fulerenoak [115, 116] eta aluminiozko klusterrak [117] siliziozko kaxen barruan ere estudiatu izan direla. Azken lanak Si_{60} $Al_{12}X$ klusterrak (X = Si, Ge, Sn, Pb) barruan sartuz egonkortu daitekeela erakusten du, nahiz eta aluminiozko klusterra deskonposatu egiten den eta siliziozko kaxa nahiko distortsionatu.

Nanokluster metalikoen dopaketa endoedrikoa esperimentalki eta teorikoki ikertu egin da, hala nola urrezko nanoklusterrak [118, 119, 120], estainuzkoak [121, 122], berunezkoak [123, 124], aluminiozkoak [125], beriliozkoak [126], germaniozkoak [127, 128], itriozkoak [109], ... Nahi diren propietateak lortzeko, atomo arrotzen txertatzea kontuan hartu beharreko parametroa da kasu guztietan.

III-V eta II-VI material erdieroaleen dopaketa endoedrikoei buruzko ikerketak urriak dira. $(BN)_i$ [129], $(GaAs)_i$ [130], $(ZnS)_i$ [131, 132] eta $(ZnO)_i$ [133] klusterrak trantsizio metal batekin edo gehiagorekin dopatzerakoan, metalek propietate magnetikoak eman diezaiekete klusterrei, eta aldi berean band-gap kontrolatzeko erabili daitezke. Modu berean, ikerketa teorikoek $(ZnS)_i$ nanoklusterren (i= 4-16) barruan metal alkalinoak sartzeak metaletik kaxara elektroi baten transferentziarako bidea ematen duela antzeman dute, halogeno bat enkapsulatzean, elektroi bat kaxatik dopatzailera transferitzen den bitartean [134]. Bestalde, halogenoen enkapsulazioak, halogeno beren baino elektroafinitate handiagoko klusterrak ematen ditu. Kluster hauek, beraz, superhalogenoak kontsideratzen dira, $Al@Al_{12}$ kasua bezala [22, 135]. Orokorrean, II-VI nanokluster endoedrikoen ikerketak, beraien egonkortasuna hiru parametroen bitartez arrazionalizatu daitekeela erakutsi du: i) nanokluster eta atomo dopatzailearen tamainaren arteko konbinazio egokia; ii) klusterraren forma, esferikoenak atomoak enkapsulatzeko gaitasun handiagoa dute; iii) atomo dopatzailearen karga, negatiboki kargatutakoak termodinamikoki egonkorragoak direla ikusi izan da.

1.5 Ensanblatua

Nanozientzia eta nanoteknologia oraindik "haurtzaroan" daudela aipatu behar dugu. Nanoklusterren aurkikuntza eta ikerkuntzaren ondoren, kontsideratu beharreko hurrengo pausoetako bat beraien ensanblatua solidoak sortzeko da. Nanoklusterren garrantzia monomero bezala ezin da gutxietsi, diseinu arrazionala erabiliz fase solido berriak eratzeko aukera ematen baitu. Nanoklusterrak, solidoen propietate desberdinak dituztelako dira bereizgarri. Eta propietateak tamaina eta konposizioarekin aldatzen direnez, printzipioz propietateak beharrei edo nahiei egokitu daitezke. Ondorioz, klusterren ensanblatua hiru dimentsiotan fase solido berriak lortzeko aukera zabaltzen du, zeinen propietateak solido tradizionalen desberdinak izango diren. Polimorfo desberdinak aurkitzearen garrantzia bestelako propietate lortzean datza (enpaketamenduzkoak, termodinamikoak, espektroskopikoak, egonkortasunezkoak eta mekanikoak), bestelako aplikazioetan erabili ahal izateko. Polimorfismoaren ohiko adibidea karbono alotropoak dira, grafitoa faserik egonkorrena (Fig. 1.7 a), eta diamantea, metaegonkorra dena (Fig. 1.7 b). Konposizio kimiko berdina izan arren, beraien propietateak guztiz desberdinak dira eta, beraz, aplikazio diferentetarako erabilgarriak dira.

C_{60} buckminsterfulerenoaren detekzio esperimentala aurkikuntza guztiz berritzailea izan zen. Modu berean, koaleszentziaren bitartez lorturiko lehenengo solidoetako bat fulerita izan zen, C_{60} fulerenoetaz osatuta (Fig. 1.7 c). Solido berri honetan, C_{60} nanoklusterrak van der Waals elkarrekintzen bidez ahulki lotuta daude, FCC egitura kristalinoa osatuz. Baina polimorfo honek daukan alderik garrantzitsuena fulereno bakoitzaren egitura eta propietate molekularrak mantendu egiten direla da. Hortaz, ensanblatuaren ondoren klusterrek beraien identitatea mantendu egiten dute. Gogortasun mekaniko bikainaz gain, diamantearenaren parekoa dena, diamantea (band-gap handiko erdieroalea) eta grafitoa (semimetala) ez bezala, erdieroale intrintsekoa da, aplikazio praktikoetarako posibilitate handiak erakutsiz. Gainera, aipatu behar dugu karbonozko fulerenoen dopaketa exoedrikoa beraien ensanblatuan eragin handia izan duela, metal alkalinoen dopaketa posizio interstizialetan orain arte ikertuena izanik [136, 137, 138, 139]. Fulerita kristalen sintesiak klusterren ensanblatua solidoak osatzeko aukera errealista dela frogatu du, propietate berriak izango dituzten solidoak lortuz.

Figure 1.7: Karbono alotropo desberdinak.

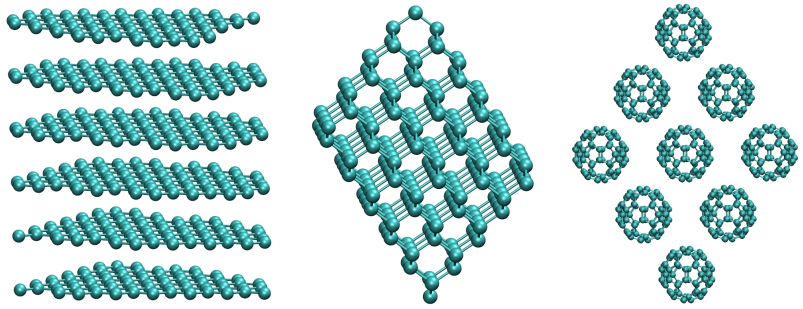

a) Grafito b) Diamante c) Fulerita

Hala eta guztiz ere, horrelako materialak eraikitzea erronka berriak planteatzen ditu, monomero superatomikoen sorkuntza eta karakterizazioarekin erlazionatuta, ensanblatua zuzentzen dituzten arauak ulertzearekin batera. Orokorrean, klusterren ensanblatuaren bidez lortutako solidoak metaegonkorrak izango dira, energia potentzial gainazaleko minimo sakonean kokatuta eta energia langa batez babestuta [140]. Aurretik aipatutako fuleritaren kasua da hau, karbonozko alotropo metaegonkorra dena. Puntu honetan simulazio teorikoa iragarpen tresna garrantzitsua da, energetikoki bideragarriak diren egiturak identifikatzeko. "Ohiko" solidoetan, hau da atomoen ensanblatuaren bidez eraikitutakoak, ondo definitutako lotura dago. Metalikoa, kobalentea edo van der Waals motakoa izan daiteke. Klusterren ensanblatuaren bidez sortutako solidoetan aldiz, bi lotura mota desberdin egon daitezke: klusterra osatzen duten atomoen arteko lotura eta klusterren artekoa [141].

Nanoklusterren bereizgarria den gainazal/bolumen proportzio handiak, solido nanoporotsuak emango ditu ensanblatzerakoan. Solido baten gainazal azalera nanoporotsua den heinean handitu egiten da. Ondorioz propietate katalitiko, adsorbatzaile eta absorbatzaileak hobetzen dira, materiala eguzki zelula fotoboltaiko [142], biosensore [143, 144], iragazki molekular [145, 146, 147] edo katalisi hetereogeneo [148, 149] bezalako aplikazioetarako erabilgarria bilakatuz. Honetaz gain, solido nanoporotsuak energetikoki eraginkorrak diren materialak eta bereizketa prozesu eta erreakzio katalitikoak ekologikoki kudeatzeko materialak eraikitzeko oso erakargarriak dira [150]. Gain-

era, industrian SO_2 or NO_x emisioa eliminatzeko, energia gordetzeko eta bereizketa teknologietarako oso material erabilgarriak dira [151]. Solido nanoporotsu berriak sintetizatzeko posibilitatea, klusterrak monomero bezala erabiliz, haundituz doa, azken aurrerapen esperimentalei esker, zeintzuk konposizio eta tamaina zehatzak dituzten klusterren produkzioa ahalbidetzen duten [152]. Hala ere, ensanblatua arrakastatsua izan dadin, propietate interesgarriak dituzten klusterrak, eta batez ere egitura eta identitatea mantenduko dituzten klusterrak identifikatzea inportantea da. Honek esan nahi du klusterrak egonkortasun intrintseko handia izan beharko dutela, koaleszentziaren kontrako erresistentzia handia izan dezaten. Kluster metalikoak, adibidez, orbital molekular deslokalizatuak dauzkatenez, kluster desberdinen orbitalen arteko gainezarpena gertatu daiteke, nahi ez dugun koaleszentzia gertatuz. Bestetik, klusterren arteko orientazio erlatibo optimoa oso lagungarria izan daiteke ensanblatua arrakastatsua izan dadin [153].

Dagoeneko sintetizatutako fuleritez gain, beste klusterren ensanblatuaren bidezko solidoak sintetizatu izan dira eta teorikoki iradoki ere bai, hala nola beste karbonozko fulerenoak [154, 155, 156, 157], endoedrikoki dopatutako siliziozko klusterrak [158, 159, 160], edo nanokluster metaliko desberdinak [161, 162, 163, 164] erabiliz osatutakoak.

III-V nanoklusterren ensanblatuaren bidez solidoak eraikitzeko posibilitatea ere landu egin da. Nahiz eta orain arte solido gehienak hipotetikoak izan, boro nitrurozko E-fasea, lehengo aldiz 1965. urtean sintetizatutakoa [165], $(BN)_{12}$ klusterrez osatutako solido bezala ikus daiteke. Fase berri honi E-fase izena jarri zioten sintesian erabilitako metodoarengatik (leherketa edo explosion ingelesez). Denbora luzea igaro zen bere egitura molekularra eta kristalinoa aurkitu zuten arte. Lehenengo diamantearen egitura proposatu zen, XRD-ko pikoen antzekotasuna zela eta. Hala ere Pokropivny-ek [166], datu teoriko eta esperimentalak konparatuz, E-fase hau $(BN)_{12}$ klusterren polimerizazioz osatutako egitura zela ondorioztatu zuen, non klusterrak aurpegi hexagonalen bitartez elkarri lotuta dauden. E-BN-k sare kubikoa dauka, $(BN)_{12}$ molekulak diamante moduko sarean paketatuta daudelarik (ikus Fig. 1.8), eta faujasita zeolitarekin daukan antzekotasuna dela eta FAU-$(BN)_{12}$ izena ere ematen zaio. Nanoklusterrez osatutako zenbait solido egonkor dagoeneko existitzeak, azken urtetako proposamen teorikoen bideragarritasuna babesten du.

Figure 1.8: E-BN edo FAU-$(BN)_{12}$ fasea. B atomoak laranjaz eta N urdinez irudikatuta daude.

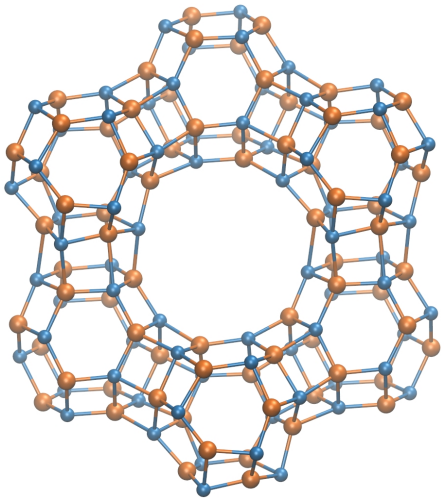

III-V klusterren ensanblatuari buruzko lan teorikoen artean, Yong *et al.*-ek [167] $(InAs)_{12}$-ren ensanblatua aztertu zuten, elkarrekintza posible guztiak kontutan hartuta. $(InAs)_{12}$-$(InAs)_{12}$ elkarrekintzen energiak kalkulatuz, hexagono-hexagono interakzioa energetikoki egokiena zela ikusi zuten, FAU-$(InAs)_{12}$ zeolita moduko solidoa osatuz. Fase berri hau dagokion zinkblenda egitura baino ezegonkorragoa izan arren, dagoeneko sintetizatu den rock-salt InAs fasea baino egonkorragoa dela iragarri zuten. Gainera aurreikusitako fase honen band-gap zinkblendarena baino handiago da. Bestalde, $(MN)_{12}$ (M = Al, Ga) nanoklusterrei buruzko ikerketa teoriko batek solido nanoporotsu kubiko eta ronboedrikoen berri eman zuen, non klusterrak laukien edo hexagonoen bitartez lotzen diren. Bi faseak band-gap zabaleko erdieroaleak direla proposatu zen, ronboedrikoa egonkorrena izanik [167].

Azken urteetan zenbait lan teorikok II-VI nanoklusterren ensanblatuan jarri dute arreta. Adibidez, Carrasco *et al.*-ek dentsitate baxuko solidoak iragarri zituzten $(MO)_{12}$ (M = Mg, Zn) nanoklusterren ensanblatuan oinarrituta [168]. Egitura hauek LTA, FAU eta SOD zeoliten itxura daukate, silikatoen topologiei dagokien notazioa jarraituz [169]. Aipagarria da polimorfo berrien egonkortasuna lehian daudela MO fase ezagunekin. Gainera, SOD-ZnO H atomoak garraiatzeko gaitasuna izango luke, energia langa txikiekin [170]. Ondorengo lan batean,

ZnO fase berri bat iragarri zen, sare ronboedrikoa daukana, non $(ZnO)_{12}$ klusterrak hexagonoetatik lotzen diren [171]. Bestetik, ab-initio kalkuluak erabiliz Wang *et al.*-ek sodalita bezalako egitura baten berri eman zuten, $(ZnO)_{12}$-en koaleszentziaren bidez lortutakoa [172]. Azkenik, $(Cd_nS_n)_m$ kluster kondentsatuak (n= 1-4, m= 1-9) ere modelatu egin ziren, eta $(Cd_3S_3)_m$ bereziki egonkorrak zirela kalkulatu zuten [173].

1.6 Lan Honen Helburua

Gaur egun kimika konputazionala kimikako adar garrantzitsua da, bi helburu nagusi dituena. Lehenengo, emaitza esperimentalen ulermena hobetzea da. Bigarren, ikerketa konputazionalak orain arte guztiz ezezagunak diren sistema kimikoen bideragarritasuna iragartzeko erabil daitezke. Tesi hau azkeneko helburuan kokatzen da. Tesi honetan, zehazki, DFT kalkuluak erabili dira sintetizatu ez diren endoedrikoki dopatutako II-VI klusterretan oinarritutako sistema kimiko desberdinen egonkortasuna aurreikusteko eta propietateak aztertzeko. Xedea hau izanik, minimo lokalen optimizazioaz gain, dinamika molekularreko simulazioak erabili dira karakterizatutako minimoen egonkortasun termikoa baieztatzeko. Gure emaitzek sistema hauen natura kimikoa ulertzeko eta bideragarriak diren egiturak detektatzeko balio dute. Gainera, esperimentalistak konposatu hauek sintetizatzeko bultzatu ditzakete.

Tesi honen lehenengo partean, $(CdS)_{9,12,15,16}$ nanoklusterren dopaketa endoedrikoa kontsideratu da. Alde batetik metal lur-alkalino eta kalkogenoekin dopatu ditugu. Beste aldetik, kluster hauek metal alkalino eta halogenoekin dopatu ditugu. Azkeneko hauetan, dopaketaren ondorioz klusterrek jasaten duten deformazioa arbuiagarria dela ikusi dugu eta alkalinoekin dopatutako klusterren ionizazio potentziala eta halogenoekin dopatutakoen elektroafinitatea antzekoak direla ikusi dugu. $(CdS)_{12}$ eta $(CdS)_{16}$ esferikoenak direla kontutan harturik, beraien ensanblatua kontsideratu dugu. Kluster huts eta dopatuen ensanblatuaren ikerketak solido hipotetiko hauetan dopaketaren eragina aztertzeko aukera eman digu.

Tesi honen bigarren partean, $(ZnS)_{12,16}$ nanoklusterren dopaketa endoedrikoa lehenengo eta bigarren lerroko trantsizio metalekin aztertu dugu. Propietate elektroniko eta magnetikoak estudiatu ditugu, konposatu hauen egonkortasunarekin batera. Azkenik, propietate ferromagnetiko eta antiferromagnetikoak dituzten dimeroak osatzeko posi-

bilitatea aztertu dugu.

Chapter 2

General Introduction

2.1 Nanoscience and Nanotechnology

There are different ways of approaching nanoscience and nanotechnology. They may be seen as the science and technology arising from the study and manipulation of matter at the atomic and molecular scale. They also can be understood as the science and technology of designing, producing, and using structures and devices having one or more dimensions no larger than 100 nm (nanomaterials). These fields extend through physics, chemistry, medicine and engineering, and cover a huge number of important issues, ranging from basic science to a variety of technological applications. The demand of miniaturization from the semiconductor industry as well as the opportunity to study bioentities of nanometer size and their interactions with other materials are examples of current concerns that nanoscience and nanotechnology are trying to address nowadays.

The first mention of the possibility of direct manipulation of individual atoms came by the hand of Richard Feynman in 1959, captured on his famous sentence "There is plenty of room at the bottom". In the '80s the emergence of two ground-breaking developments allowed what had been previously just concepts to materialize, creating an extraordinary impact on the further advance of both nanoscience and nanotechnology. The first one was the invention of the scanning tunneling microscope [1]. This technology afforded the identification of individual atoms on surfaces for the first time. Moreover, some of its limitations, like its usefulness to only conductive materials, were resolved with the subsequent creation of the Atomic Force Microscope

[2]. The second development was the birth of clusters science with the detection of extremely stable stoichiometries for clusters of alkali metals [3] and the discovery of the C_{60} buckminsterfullerene [4].

Nanotechnologists have developed two approaches for fabricating materials or manipulating devices at nanoscale: bottom-up and top-down. The bottom-up approach is the construction of nanomaterials atom by atom or molecule by molecule. It derives from the molecular chemistry, using atoms or molecules as starting point, and its aim is to design nanomaterials and to analyze the non-linear transformation of properties as the size increases. The top-down method, conversely, refers to successive cutting of a bulk material until getting nanoparticles. It comes from the solid state physics and it studies the effects of the reduction of the size. Both approaches converge in the nanoparticle regime. Indeed, nanomaterials constitute a bridge between bulk materials and atomic and molecular compounds [5, 6].

It is important to note that, when matter is organized at the nanoscale, its behavior and properties can be dramatically different from those in the bulk. The properties become size-dependent and they change discontinuously with the size. Then, beyond a certain size, properties will change smoothly, eventually reaching the bulk limit. Two main factors are responsible for such a phenomenon in the nanometer scale. On the one hand, when the wavelength of the electrons are in the order of the size of the material in which lie, the quantum effects rule the behavior and properties of the system. As a result electrons are confined in a small region of space, modifying the optoelectronic properties of the nanoparticle. On the other hand, their high surface-to-volume ratio plays an important role. As most of the atoms of a nanoparticle are at the surface of the structure, they rearrange in order to minimize the number of dangling bonds and the surface energy, giving rise to unexpected structures. Thus, working at nanoscale enables scientist to study and use the unique properties that nanostructured materials present. In fact, it has been observed that in the nanoparticle regime insulator compounds might become conductor [7], change the color [8], increase the reactivity [9], and so on, opening the possibility for a wide range of new applications. Apart from the previously mentioned miniaturization of electronic devices and the biological applications to diagnosis and fight diseases, the expanded surface makes the nanoparticles ideal for catalysis or sensor applications. Furthermore, the most amazing advantage of nanomate-

rials is that, since their properties vary with the size and composition, in principle they can be tailored at will.

Advances in the degree of understanding of the physicochemical properties of these materials has had an enormous impact in the development of accurate deliberate structure control techniques over the past two decades. Thus, nanoparticles with precisely defined atomic compositions can now be produced in large amounts both in gas phase and in solution. Where experimental techniques are not yet at hand, however, computational theory has become an essential tool as a predictive basis for guiding experiment. The improvement of computational methods and capabilities allow the prediction and the better understanding of new materials, avoiding, in some cases, the high cost of experimental random trial and error search. In this vein it is notable that, in spite that the experimental detection of the C_{60} buckminsterfullerene was made in the eighties, its existence was theoretically predicted in 1970 [10]. The interplay between experiments and theoretical calculations is fundamental in the field of nanotechnology and, as Marks claimed, "small particle structures cannot be understood purely from experimental data, and it is necessary to simultaneously use theoretical or other modeling" [11].

2.2 Nanoclusters

Among nanomaterials, nanoclusters may be considered as the smallest nanostructures. Although there is not a general agreement about the definition of nanoclusters, they can be thought of as aggregates of atoms or molecules of nanometric size, containing a number of constituent particles, ranging from $\sim$10 to 10^4. They may be neutral or charged. They may be held together by very different kinds of forces: strong attraction between oppositely charged ions (e.g. in NaCl clusters), van der Waals attraction (as in He and Ar clusters), covalent chemical bond (Si clusters) or metallic bond (as in Al or Cu clusters). Motivations for studying clusters are diverse [12]. They are of scientific interest as they are an intermediate state of matter between bulk materials and atomic and molecular compounds. Therefore they afford a unique chance to analyze the evolution of chemical and physical properties with the size. In addition, they can be very useful for understanding the nucleation and growth process of crystals. Finally, the study of clusters themselves, along with their properties and the com-

prehension of their incomparable nature is a fascinating area. This thesis will be demarcated in the latter.

The exquisite beauty of clusters manifests in the so called "magic clusters". Indeed, cluster stability with respect to growth and decay does not change monotonically with the size, but there are certain sizes with enhanced stability, i. e. magic clusters. This is why it is said that in nanoclusters, "one atom makes the difference". The high stability of magic clusters has an electronic and a geometric component. In general the electronic effects dominate at small sizes and the geometric compactness at larger sizes [13]. Synergy between theory and experiment has been critical in the development of the field of clusters. In fact, the geometry of clusters is difficult to directly probe with available experimental techniques, and theory plays an indispensable role in elucidating the atomic structure of nanoparticles [5]. One of the best known magic cluster is the C_{60} fullerene, discovered in 1985 by R. F. Curl, R. E. Smalley and H. W. Kroto [4], who were awarded the 1996 Nobel Prize in Chemistry for this discovery. Among the 1812 possible isomers, the lowest-lying structure is a spherical hollow cage-like structure built by 12 pentagons and 20 hexagons, where all atoms are located at the surface of the structure, see Fig. 2.1. In this way, each carbon atom is bonded to three other carbon atoms by sp^2 hybrid orbitals. Pentagons are responsible of introducing the positive Gaussian curvature that characterizes fullerenes. The five and six-membered rings are disposed so that every pentagon is surrounded by five hexagons, satisfying the so called Isolated Pentagon Rule (IPR) [14]. The high stability of this cluster arises from the combination of electronic and geometric factors. Indeed, it has a closed-shell electronic structure and it belongs to the highest possible symmetry point group, I_h.

Besides C_{60}, other highly stable carbon fullerenes have been experimentally produced such as C_{84}, C_{80}, C_{76}, C_{70} and C_{20}, which is the smallest carbon nanocluster synthesized hitherto. Irrespective of the size of the cluster, pentagons and hexagons (and heptagons occasionally) are recurrent motifs in these cage-like structures. The formation of these units is related with the minimization of the geometrical strain. It has been noticed that carbon fullerenes follow the Euler's theorem of closed polyhedron: the relation between the numbers of

Figure 2.1: C_{60} buckminsterfullerene discovered in 1985 by Kroto *et al.*.

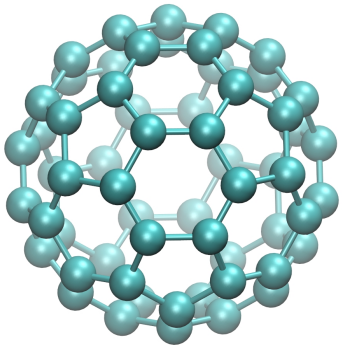

faces (F), vertices (V), and edges (E) must fulfill the relation V+F-E = 2. For carbon fullerenes with only pentagonal and hexagonal faces, the number of pentagonal rings is always n_{penta}= 12 and the number of hexagonal rings is n_{hexa}> 1. Later on, other carbon allotropes like carbon nanotubes [15] or graphene [16] have been also synthesized.

After the discovery of carbon fullerenes a significant effort has been devoted to the synthesis and characterization of nanoclusters made of other materials. Since silicon and carbon are members of the same group in the periodic table, first, Si clusters were investigated. The interest in these compounds was also the possible applicability in nanodevices due to the semiconductor properties of bulk silicon. However, it was found that for silicon it is difficult to form fullerene-like structures. The reason is that while carbon, with sp^2 hybridization, is able to form cage-like structures through π bonds, the silicon strongly prefers sp^3 bonds which favors a three-dimensional diamond-like structure. Accordingly, it is difficult to form cages or tubes purely with silicon atoms. Two main mechanisms have been developed to stabilize silicon nanoclusters. The first one is the endohedral doping and it will be addressed in Subsection 2.4. The second one is to cap the dangling bonds on the surface of silicon fullerenes with hydrogen atoms [17, 18]. The resulting structures display high symmetries (as the corresponding carbon fullerenes do) and well opened HOMO-LUMO gaps. The combination of both mechanism is predicted to give good results too [19].

A lot of research has been done on other elemental nanoclusters, primarily on metallic clusters such as those made of alkali metals [3, 20, 21], aluminum [22, 23, 24], iron [25], silver [26], gold [27, 28,

29, 30, 31], etc. Although we are not going to go into detail, we would like to point out that the study of metallic nanoclusters led to the Jellium model [32] to explain the experimentally observed extremely stable stoichiometries. In this way these magic clusters were associated with the filling of the electronic shells.

Because boron nitride is isoelectronic to carbon, it was one of the first binary system studied at the nanoscale, to elucidate if it might form fullerene-like structures. Moreover, although BN displays similar chemical bonding comparing to C, it shows lower reactivity, making it amenable for certain applications were carbon clusters can not be used. Along with BN, nanoclusters made of other III-V elements have been extensively studied. All of them are wide band gap semiconductors, so they are suitable for applications in medical treatments, information storage and other optoelectronic devices. Furthermore, the opportunities offered by reducing the size of these materials up to the nanoscale are immense.

Figure 2.2: The ground state of $(BN)_{12}$ nanocluster. B atoms are depicted in orange and N in blue.

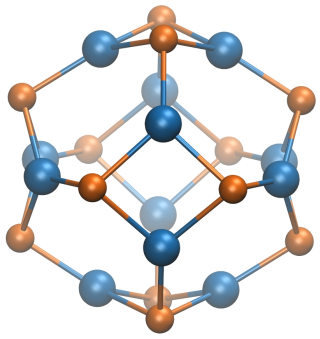

One of the main differences between elemental nanoclusters such as those of carbon, and stoichiometric binary AB nanoclusters is that the homonuclear bonds (A-A, B-B) are energetically highly unfavorable compared to the heteronuclear bonds (A-B) that stabilize these compounds, albeit certain nanoclusters can be stable with homonuclear bonds between electron-donor atoms [33, 34]. As a result, binary nanostructures are made of squares and hexagons (and octagons occasionally). Similar to the isolated pentagon rule, the isolated tetragon

rule is proposed for these systems [35, 36]. The analogous of C_{60} would be $(BN)_{30}$, but it is unstable. Its fivefold rings rule out the possibility of a fully alternating B-N sequence of atoms and would force homonuclear B-B or N-N bond in each pentagon. Nevertheless, studies revealed that fullerene-like structures are found for boron nitride nanoclusters [37, 38]. For example, cage-like $(BN)_{12}$, $(BN)_{16}$, $(BN)_{28}$, $(BN)_{36}$ have been found to be magic clusters, as they showed an enhanced stability and large HOMO-LUMO gaps comparing with their next sizes [36, 39, 34, 40, 41]. It is worth noting that n=12 is regarded as the smallest possible high-symmetry magic cluster, satisfying the isolated tetragonal rule [42, 43, 39]. Likewise, BN-fullerene topologies are found to be energetically preferred for other III-V binary clusters, namely, $(AlN)_n$ [44], $(GaP)_n$ [45], $(AlP)_n$ [46], and $(GaN)_n$ [47]. However, BN fullerenes are more stable than their III-V counterparts [48], as well as they display the greatest amount of variability of band gap as a function of the size [49].

2.3 II-VI Nanoclusters

II-VI nanomaterials have been extensively studied in the last decades. Due to the combined effect of the quantum confinement and their particular surface morphologies, semiconductor II-VI nanocompounds are recurrently utilized, for instance, as photocatalysts [50]. Owing to their outstanding optoelectronic properties, they have found application as sensors [51], photovoltaic solar cells [52] and optoelectronic devices [53]. Likewise, the use of II-VI semiconductor nanomaterials in biological investigations has increased notably due to their unique optical properties and to recent advances in biofunctionalization [54]. Many experimental and theoretical works have concentrated on the study of stoichiometric and non-stoichiometric II-VI nanoclusters.

Ultrasmall II-VI clusters have been produced by laser ablation, the same technique used in the discovery of C_{60}. It has to be taken into account that the distribution of the cluster ion compositions depends upon the generation method of cluster ions [55]. Using this technique, and then analyzing the positive ions by time-of-flight (TOF) mass spectrometer, Burnin *et al.* found that for $(ZnS)^+$, clusters composed of 3, 6 and 13 monomer units were ultrastable, while for $(ZnO)^+$ no magic cluster was identified [56, 57]. According to the experiments by Sanville *et al.*, [58] for $(ZnSe)_n^+$, $(CdS)_n^+$, and $(CdSe)_n^+$ up to n=16, n= 6 and

13 were found to be magic clusters. Kukreja *et al.* carried out a similar study, with ZnO and ZnSe. Regarding ZnO they neither found any magic number. For ZnSe some prominent peaks were observed in the mass spectrum, which corresponded to $(ZnSe)_6^+$, $(ZnSe)_{13}^+$, $(ZnSe)_{19}^+$, $(ZnSe)_{23}^+$, and $(ZnSe)_{33}^+$ [59]. Later works, however, found magic clusters for zinc oxide cationic nanoclusters at n= 34, 60, and 78 [60, 61]. They achieved this result by using zinc peroxide as precursor in the laser ablation, instead of the usual ZnO powder. For these magic clusters, cage-like structures were proposed to be the lowest-lying isomers.

Colloidal chemistry has also been applied to produce nanoclusters. In this area, magic size nanoclusters are distinguished from ultrasmall nanoparticles because they exhibit an extremely narrow size distribution (and narrow absorption peaks) and high stability with respect to the growth. This leads to quantized growth, where nanoclusters jump from one discrete size to another larger discrete size [62, 63]. A variety of parameters can be optimized in order to gain access to these magic nanoclusters with control over the size: production methodology, temperature, precursor, type and concentration of surfactant, ligands, etc. [64, 65, 66]. CdSe nanoclusters were synthesized in aqueous solution and cys-capped $(CdSe)_{33}$ and $(CdSe)_{34}$ were identified as magic [67]. However, using laser ablation, which is more violent, instead of this slow synthetic rout, the authors obtained two more peaks corresponding to n= 13, 19, 33, and 34. According to authors, this fact indicates that 13 and 19 are produced by fragmentation of 33 and 34. Likewise, Kasuya *et al.* found magic numbers for $(CdSe)^+$ at n= 13, 33, and 34 formed in organic solvent and then dried for the time-of-flight (TOF) mass spectrometer [68, 69]. For other II-VI species such as ZnS, CdS and ZnSe the same magic clusters were identified [68, 69, 70, 71]. Moreover, they observed that $(CdSe)_{33}^+$ and $(CdSe)_{34}^+$ are particularly stable, being highly resistant against ripening even under conditions that favor the growth of larger particles. Authors proposed the ground state of these structures to be core-cage $[(CdSe)_5@(CdSe)_{28}]^+$ and $[(CdSe)_6@(CdSe)_{28}]^+$ respectively. Regarding the surfactant molecules, it was shown that they were not firmly attached to the clusters but they were easily removed. In this vein, Wang *et al.* recently were able to isolate alkylamine-capped $(CdSe)_{13}$, the smallest magic-size CdSe nanocluster isolated hitherto [72]. Subsequent computational work predicted the core-cage-like $Se@Cd_{13}Se_{12}$ (Fig. 2.3) to be the most stable isomer, regardless of being bare or

ligand-capped, in gas phase or in solution [73]. For the case of $(CdS)_{13}$ other works predicted the same ground state [68, 74, 75]. For $(ZnSe)_{13}$ and $(ZnS)_{13}$, however, it is suggested that this core-shell structure is only a local minimum [76, 58]. This is proposed to be because Cd has a higher tendency than Zn to stabilize four-coordinated structures.

Figure 2.3: The predicted ground state of $(CdSe)_{13}$ nanocluster. Cd atoms are depicted in cyan and Se in orange.

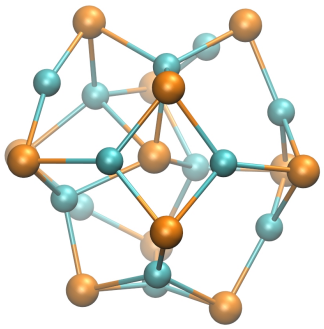

Along with the experimental work, a notable theoretical effort has been devoted to the modeling of bare II-VI nanoclusters. Indeed, the experimental characterization of clusters with only small number of atoms is a difficult task, and computational techniques have become an essential tool for determining their structure and properties.

Regarding the shape of nanoclusters, in general there are several well-separated regimes as a function of size. The transition between regimes is composition dependent and in certain cases there is still some controversy about the exact size at which it happens [55]. The smallest clusters, made of very few atoms, have two-fold coordination and planar ring structures. Ring-like structures are predicted to be the global minima for cadmium and zinc oxide nanoclusters as large as n= 7, whereas larger nanoclusters are hollow spheroids [77, 78, 79, 80]. CdX and ZnX, with X= S, Se, and Te, however, undergo this transition at smaller cluster size (ring-like for n $\leq$5), see Fig. 2.4 [57, 81, 82, 83]. The ring-to-cage (2D-to-3D) structural transition arises from a balance between two opposite tendencies. First the tendency to linearity of X-Zn(Cd)-X bonds favors rings. Second, the tendency to achieve higher coordination favor the spheroids. Indeed, in the bulk-like wurtzite

and zincblende solids, atoms are four-coordinated. Computational studies reveal that the former prevails when the higher coordination carry too much strain for the bond angles. Matxain *et al.* proposed the difference between zinc and cadmium oxides and chalcogens to be due to the fact that oxygen d orbitals lie higher in energy and therefore the ability of S, Se, and Te to achieve higher coordination is larger [83].

Figure 2.4: From left to right the ground state geometries of $(ZnS)_4$, $(ZnS)_6$, and $(ZnS)_{12}$ nanoclusters. Zn atoms are depicted in gray and S atoms in yellow.

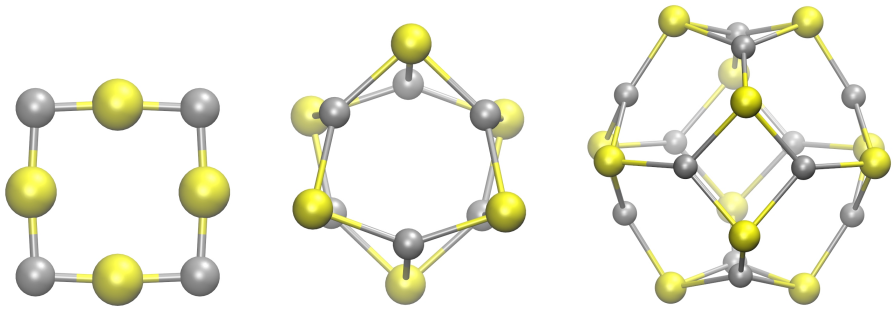

For cage-like clusters found in medium-sized range, a similar picture as for III-V clusters is found: isolated tetragonal rule is followed and the heteronuclear bonds are energetically favored over the homonuclear ones. In addition, the most stable clusters do not have any octagons and an increase in either the number of tetragons or octagons tends to destabilize the system [84]. Thus, same structural motifs are observed as in III-V nanoclusters, n=12 being regarded as the smallest possible high-symmetry magic cluster. In fact, $(AB)_{12}$ cages display T_h symmetry and are predicted to be extremely stable. $(AB)_{16}$ cluster which has T_d symmetry has been predicted to be highly stable too. This points forward to a relationship between the stability and symmetry. Notice that in the gas phase experiments, clusters with 13 monomer units are detected for II-VI materials but they are cations and this might influence their relative stability and therefore their relative abundance. For a comparison of theory and experiments one needs to take into account that neutral, positively and negatively charged clusters may have different atomic and electronic structures.

The spheroidal or cage-like clusters also obey the Euler's theorem for closed polyhedra, so the number of rings can be predicted by:

$$N_{6-ring} = n - 4 - 2N_{8-ring} \tag{2.1}$$

$$N_{4-ring} = 6 + N_{8-ring} \tag{2.2}$$

Larger II-VI nanoclusters are predicted to adopt the onion-like or bubble-like structure, namely, a cage-like cluster enclosed inside a bigger one. This is the case of $(ZnS)_{50}$, $(ZnS)_{60}$, $(ZnS)_{70}$, and $(ZnS)_{80}$, which can be viewed as $(ZnS)_6$@$(ZnS)_{44}$, $(ZnS)_{12}$@$(ZnS)_{48}$, $(ZnS)_{12}$@$(ZnS)_{58}$, and $(ZnS)_{17}$@$(ZnS)_{63}$ respectively [85, 86]. In this structures, although the atoms connecting the two cages are four-coordinated, most of them are still three-coordinated.

Then, beyond a certain size (ca. 2.5 nm), it has been found that clusters' structure is analogous to the BCT zeolite [87, 88, 89]. In such compounds, the inside is crystalline whereas there is some degree of disorder at the surface, with four-coordinated atoms. It is suggested that the bigger stability of BCT over bulk-like (wurtzite or zincblende) structures is due to their bigger ability to accommodate distortions reducing the number of dangling bonds and the dipole moments [84]. Finally, II-VI materials with diameters of few nanometers are found to have bulk-like (wurtzite or zincblende) structures [90, 91, 92, 93].

Figure 2.5: The lowest-lying isomer of $(ZnS)_{60}$, in which $(ZnS)_{48}$ shell encloses a $(ZnS)_{12}$ core. Zn atoms are depicted in gray and S atoms in yellow.

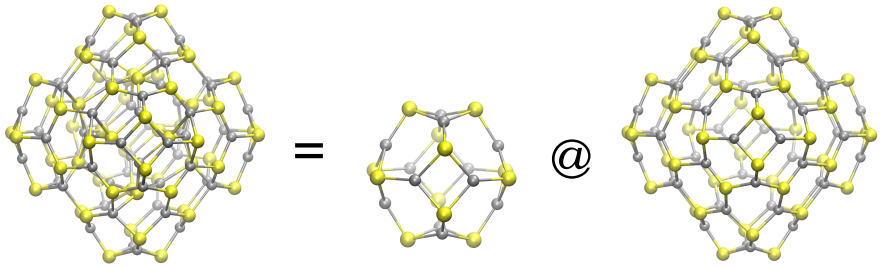

Experiments that are monitored or characterized through absorption spectroscopy have observed a blue-shift with respect to the bulk, as expected, due to the quantum confinement effect at the nanoscale [94, 95, 96, 68, 97]. Computational works have confirmed the increase in the band-gaps upon the reduction of the size with an oscillatory behavior of band-gaps at smallest sizes, finally reaching the bulk limit as the size increases. Regarding the smallest nanoclusters, Matxain *et al.* showed that the electronic excitation energies strongly depend on the geometry of the cluster [98, 99]. Their studies revealed ring-like structures to have larger excitation energies than cage-like clusters. Interestingly, and irrespective of the composition, the lowest excitations occur from a non-bonding p orbital of the chalcogen (HOMO) to the s orbital of the metal (LUMO). These orbitals are perpendicular to the molecular plane in the case of the rings and normal to the spheroid surface for 3D clusters. It is worth mentioning the work by Hamad *et al.*, who calculated the HOMO-LUMO gaps of $(ZnS)_n$ nanoclusters (n= 10-47) with spheroidal shape to lie within the range of 4.4 - 4.8 eV, while the HOMO-LUMO gaps of the same clusters with bulk-like structure were in the range of 3.65 - 3.95 eV [85].

2.4 Endohedral Doping

Nanotechnology has changed the view of science because it offers the possibility of creating materials with novel properties, due to the unique nature of nanoscaled compounds. Control of the composition and structure of nanomaterials allows the tuning and optimization of the electronic, chemical, physical and biological properties for particular applications. Moreover, as their bulk counterparts, nanoclusters can be doped to tailor the properties, which means to intentionally introduce impurities. In hollow cage structures, like C_{60}, there are mainly three types of doping strategies, shown in Fig. 2.6. The first one is the substitutional doping, consisting on the replacement of one or more atoms by other element atoms, usually B or N. Another type of doping is the exohedral doping, where foreign atoms or molecules are placed outside the cage. Finally, the endohedral doping, where atoms or molecules are trapped inside the nanocluster. The latter presents a clear advantage over other doping strategies facing toward the assembly, since in the cluster-assembled materials the dopant atoms would occupy a well-fixed center of the nanocluster, providing in this way a

better dopant-dopant distance control to experimentalists.

Figure 2.6: From left to right three different ways of doping: substitutional, exohedral and endohedral doping of C_{60} fullerene with nitrogen. C atoms are depicted in blue and N in orange.

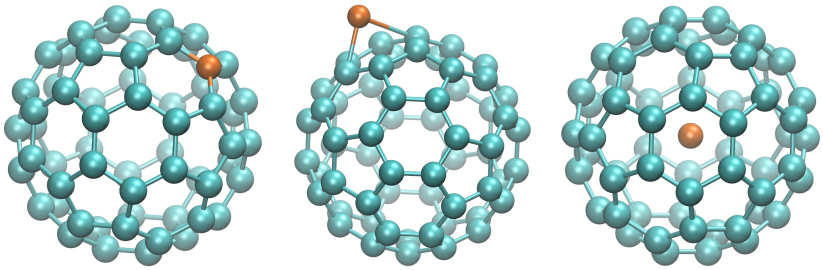

From the early stages of fullerene research it was shown that fullerenes were in general able to host atoms in their interior, while maintaining the structure. The first synthesized endohedral fullerene was La@C_{60} [100]. Since then, a wide range of endohedral carbon nanoclusters have been synthesized. Carbon fullerenes are able to trap small molecules too, depending on the cavity size. For instance, it was predicted that C_{60} nanoclusters exothermically encapsulates one water molecule, while C_{180} might be able to trap up to seventeen water molecules [101, 102]. Ravinder *et al.* studied the encapsulation of a cyclopentadienyl anion, (η^5-cp)$_2$Fe, in different carbon clusters and they concluded that it is not energetically feasible to happen in the case of C_{60} due to the steric effects, but it is possible that C_{80} and C_{180} can trap the (η^5-cp)$_2$Fe anion [103]. Trough the endohedral doping the properties of fullerenes are modified upon encapsulation. For instance, the introduction of metal atoms into carbon cages leads to an increase of their electron affinities comparing to that of the corresponding bare clusters. Thus, endohedral carbon fullerenes are promising materials as their optoelectronic properties can be tuned just by changing the dopant atom, without changing the structural features of the outer carbon shell [104].

Additionally, the endohedral doping has been found to be a valuable mechanism to stabilize clusters that otherwise would not be stable, such as non-IPR carbon fullerenes by a charge transfer from the enclosed species [105, 106, 107, 108]. Likewise, doping has emerged as

an effective tool to stabilize silicon fullerenes. In particular transition-metals are proposed to be the most suitable dopant atoms, due to the d orbitals features [109, 110, 111]. However, other guest atoms have been predicted to be a able to stabilize silicon clusters [112, 113]. The encapsulation of single atoms is restricted to very small fullerenes, of the order of 20 silicon atoms. Similarly, the encapsulation of clusters inside the others has shown to stabilize silicon fullerenes. In this framework, Si_i clusters with i = 27-39 have been constructed embedding Si_j with j = 2-5 inside a cage of silicon atoms [114]. Interestingly, the encapsulation of carbon fullerenes [115, 116] and aluminum clusters [117] in silicon fullerene has been also studied. The latter work showed that Si_{60} could be stabilized by putting $Al_{12}X$ clusters (X = Si, Ge, Sn, Pb) inside, although embedded aluminum clusters were all decomposed, and the outer silicon shell was significantly distorted.

Endohedral doping of metallic nanoclusters has been investigated both experimentally and theoretically, as it is the case of gold [118, 119, 120], tin [121, 122], lead [123, 124], aluminum [125], beryllium [126], germanium [127, 128], yttrium [109], etc. The insertion of a foreign atom into a nanocluster is an interesting parameter to take into account for obtaining the desired properties in all the cases.

Studies of the properties of endohedrally doped III-V and II-VI semiconductor materials are scarce. When doping $(BN)_i$ [129], $(GaAs)_i$ [130], $(ZnS)_i$ [131, 132], $(ZnO)_i$ [133] clusters with one or more transition metals, dopant atoms can confer to them magnetic properties, as well as they can be used to control the energy gap. Likewise, theoretical studies show that the confinement of alkali metals inside $(ZnS)_i$ nanoclusters (i= 4-16) gives rise to one electron transfer from the metal to the cage, whereas encapsulated halogen atoms withdraw an electron from the cage [134]. Furthermore, encapsulation of halogen atoms results in endohedral nanoclusters with enhanced electron affinity relative to the guest halogen atom. These nanoclusters ought, therefore, to be considered as superhalogens in the same vein as the $Al@Al_{12}$ cluster [22, 135]. Overall, the study of endohedrally doped II-VI nanoclusters has shown that, in general, the stability of these complexes can be rationalized in terms of three parameters: i) the appropriate matching between the size of the nanocluster and the size of the trapped atom; ii) the shape of the nanocluster, most spherical ones are more prone to incarcerate atoms than the irregular ones; iii) the charge of the trapped atom, negatively charged guest atoms are found

to be the thermodynamically most stable ones.

2.5 Assembling

We must emphasize that nanoscience and nanotechnology are still in their infancy. After the discovery of nanoclusters and their study, one of the possible next step to consider might be their assembly to form solids. The importance of nanoclusters as building blocks can hardly be underestimated, as it will enable us to create new solid phases by using rational design. Nanoclusters are characterized for having distinct properties from bulk and, since the properties vary with the size and composition, in principle they could be tailored at will. Hence, the 3D assembling of nanoclusters broadens the possibility of finding novel solid phases whose properties differ significantly from the traditional ones. The importance of finding diverse polymorphs arises mainly because of their different properties (packing, thermodynamics, spectroscopy, kinetics like dissolution rate, stability, and mechanical properties) which give rise to various applications. A typical example of polymorphism are the carbon allotropes, graphite, the most stable phase, (Fig. 2.7 a) and diamond, a metastable solid, (Fig. 2.7 b), that despite having the same chemical composition, posses very different properties and therefore have been found suitable for very diverse applications.

The experimental detection of C_{60} buckminsterfullerene was a groundbreaking discovery. Likewise, one of the first solids obtained via cluster coalescence was the fullerite built up of C_{60} fullerenes (Fig. 2.7 c) [174]. In these new solid the C_{60} nanoclusters are weakly bonded by van der Waals interactions in the face-centered cubic motif. But the most important aspect of this new polymorph is that the structure of each fullerene is kept and its molecular properties preserved. Thus, the clusters after assembling them into the solid, do retain their identity. Besides its outstanding mechanical strength, comparable to diamond, it possesses intrinsic semiconductor properties unlike diamond (a wide band gap semiconductor) and graphite (a semimetal), showing great prospects for practical applications. Additionally we must emphasize that the exohedral doping of carbon fullerenes has had a deep impact in their assembly, and the doping with alkali metals in the interstitial sites has been most extensively studied [136, 137, 138, 139]. The synthesis of fullerite crystals confirmed that the assembly of clus-

ters into solids is a realistic possibility and that the properties of the resulting phases will differ from those of the traditional ones.

Figure 2.7: Different carbon allotropes.

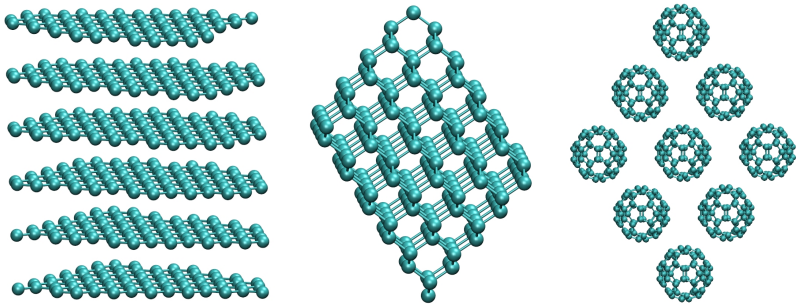

a) Graphite b) Diamond c) Fullerite

Nevertheless, building up such materials displays new challenges, related to making and characterizing a new set of superatomic building blocks along with understanding the rules that govern their assembly. In general, the cluster-assembled solids will be metastable, trapped in a deep minimum of the potential energy surface protected by an energy barrier [140]. This is the case of the above mentioned fullerite crystal, which is a metastable carbon allotrope. At this point, the theoretical simulations constitute an important predictive tool for the identification of energetically feasible structures. For the "traditional" solids, namely atom assembled solids, there is a well defined bonding. It can be metallic, ionic, covalent or van der Waals type. For the cluster-assembled solids, however, there can be two different kind of bonds: the bonding of atoms inside the clusters and the bonding between clusters. As a consequence, while in the usual solids there is just one characteristic length scale, i. e. the lattice constant, the cluster-assembled solids are characterized by two length scales: the intra-cluster and the inter-cluster distances [141].

The characteristic high surface to volume ratio of nanoclusters, will give rise to nanoporous solids. The presence of pores in a material can render itself all sorts of useful properties that non-porous materials would not have. The surface area of a solid increases when it becomes nanoporous and, as a consequence, it improves catalytic,

absorbent, and adsorbent properties, making them suitable for applications such as photovoltaic solar cells [142], biosensors [143, 144], molecular sieves [145, 146, 147], heterogeneous catalysis [148, 149], and so on. Moreover, nanoporous solids are attractive materials for energetically efficient and environmentally friendly catalytic and adsorption separation processes [150]. They are highly useful in industries for removal of SO_2 or NO_x emission as well as for energy storage and environmental separation technologies [151]. The possibility of synthesizing new nanoporous solids with clusters as building blocks is gaining momentum due to the recent experimental advances that allow the production of clusters of a given size and composition [152]. However, for the assembly to be successful, it is important to identify clusters with interesting properties and maintain their structure and identity in the assembly. This means that nanoclusters must have high intrinsic stability to prevent them from the coalescence. Metallic clusters, for example, have largely delocalized molecular orbitals and, consequently, the overlap between orbitals from different clusters may happen, giving rise to the undesired coalescence. Additionally, an optimized relative orientation of the clusters is a favorable condition for a successful assembling [153].

Along with the already synthesized fullerites, other cluster assembled solids have been synthesized and also theoretically suggested, such as those made of other carbon fullerenes [154, 155, 156, 157], endohedrally doped silicon clusters [158, 159, 160], or different metallic nanoclusters [161, 162, 163, 164].

The possibility of building up solids made of III-V nanoclusters has been addressed as well. Although hitherto most of the solids are hypothetical, the boron nitride E-phase, which was synthesized for the first time in 1965 [165], can be viewed as a $(BN)_{12}$-cluster-assembled solid. This new phase was called the E-phase owing to the method (explosion) by which it was synthesized. Its molecular and crystal structures were not resolved for a long time. First of all, it was proposed the E-phase to have a diamond-like crystal structure, due to the similarity in the peaks of the XRD pattern. However, Pokropivny resolved its structure by the comparison of theoretical and experimental data [166] and concluded that the E-phase is formed by the polymerization of $(BN)_{12}$ clusters by hexagonal faces. E-BN has cubic lattice of $(BN)_{12}$ molecules packed in a diamond lattice, see Fig. 2.8, and due to its similarity with faujasite zeolite, it is also named FAU-$(BN)_{12}$. The fact

that there are already some stable solids, where nanoclusters are the building blocks, supports the feasibility of the theoretical proposals that have been done in the recent years.

Figure 2.8: E-BN or FAU-$(BN)_{12}$ phase. B atoms are depicted in orange and N in blue.

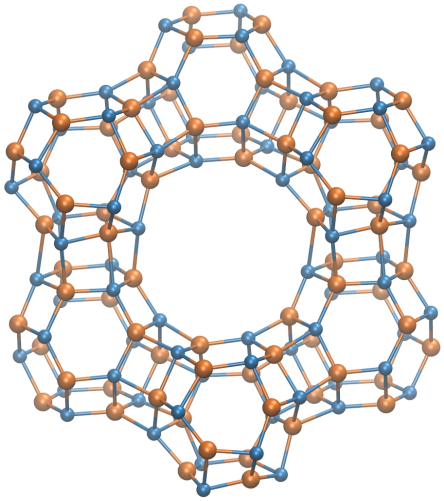

Among theoretical works relating to the assembly of III-V clusters, Yong *et al.* [167] explored different cluster-assembled solids based on $(InAs)_{12}$, taking into account all possible interactions. The viability of the proposed structures was assessed by calculating the energetics of $(InAs)_{12}$-$(InAs)_{12}$ interactions. In this way, it was shown that the hexagon-hexagon interaction was energetically preferred, leading to FAU-$(InAs)_{12}$ zeolite-like solid. Although this new phase is less stable than its corresponding zincblende phase, it is predicted to be thermodynamically more stable than the already synthesized rock-salt InAs phase. Furthermore, the characterized new phase has a larger gap value than that of the zincblende solid. In addition, a theoretical study of the assembly of $(MN)_{12}$ (M = Al, Ga) nanoclusters by either square or hexagonal faces, giving rise to cubic or rhombohedral nanoporous phases was reported. Both phases were found to be wide-gap semiconductors, the rhombohedral one being energetically more favorable [167].

In the last years, several works has focused on the assembly of II-VI nanoclusters. For instance, Carrasco *et al.* predicted new low-density

solid phases via assembling $(MO)_{12}$ clusters (M = Mg, Zn) [168]. These structures resemble that of LTA, FAU and SOD zeolites, following the framework notation of the corresponding silicate topologies [169]. Interestingly, the new polymorphs have energetic stabilities competing with those of known MO phases. Moreover, theoretical analysis showed that SOD-ZnO would be able to transport H atoms with relatively small energy barriers [170]. In a later work, a new three dimensional ZnO phase with a rhombohedral lattice framework was hypothesized, attaching $(ZnO)_{12}$ cages by hexagonal faces [171]. Moreover, Wang *et al.* found by using first principles calculations a metastable solid-phase sodalite structure via coalescence of $(ZnO)_{12}$ cages [172]. Finally, the 1-D condensed clusters $(Cd_nS_n)_m$, where $_n$ = 1–4 and $_m$ = 1–9, were also modeled and it was observed that $(Cd_3S_3)_m$ frameworks are energetically more stable as compared with other-sized condensed clusters [173].

2.6 Aim of This Work

Nowadays computational chemistry is an important brunch of chemistry that has two main goals. First, the better understanding of experimental results. Second, computational studies can be used to predict the feasibility of so far entirely unknown chemical systems and reactions. This thesis is demarcated in the latter. More specifically, in this thesis DFT calculations are used to examine the stability of different chemical systems based on endohedrally doped II-VI nanoclusters, which have not been synthesized yet. With this purpose, in addition to the local minima optimization, we have carried out molecular dynamics calculations to check the thermal stability of the calculated minima. We believe that our results are useful to understand the chemical nature of these systems and for the identification of energetically feasible structures. Moreover, they can encourage experimentalists to synthesize these compounds.

In the first part of this thesis, the endohedral doping of $(CdS)_{9,12,15,16}$ nanoclusters is considered. On the one hand, these clusters are endohedrally doped with alkali metals and halogens. On the other hand, they are doped with earth alkali metals and chalcogens. In the former we observed that the clusters do retain their structural identity upon the doping and the ionization potential of the alkali doped nanoclusters and the electron affinities of halogen doped clusters is similar.

Given the fact that $(CdS)_{12}$ and $(CdS)_{16}$ are the most spherical clusters studied, we considered their assembly. The study of the assembly of both bare and endohedrally doped nanoclusters gives us the chance to determine the effect of the doping in these hypothetical cadmium sulfide phases.

In the second part of this thesis, the endohedral doping of $(ZnS)_{12,16}$ nanoclusters with first and second-row transition metals is addressed. The electronic, magnetic and structural properties are analyzed, along with the stability of these new compounds. Finally, the possibility of building up dimers with ferromagnetic or antiferromagnetic properties is discussed too.

Chapter 3

Methods

The theory of quantum mechanics, developed in the twenties of the last century [175, 176, 177], changed the viewpoint of physicist over the microscopic world. Before it, all attempts that tried to explain the phenomena occurring at this level failed. For instance, the observed atomic spectra, along with the stability of atoms, could not be explained with the physical theories of the XIX.th century. Therefore, a new theory was developed in the first decades of the XX.th century: Quantum Mechanics.

Over the years, the development of quantum chemistry and new approximations, along with the improvement of computational capabilities, has made the quantum chemistry to become a very important tool for chemists. On the one hand, it is used post facto in order to clarify or for the better understanding of experiments. On the other hand, quantum chemistry is a very powerful predictive instrument, helping in the reduction of the high cost of experimental random search (trial and error).

In this thesis we have studied the structure and properties of endohedrally doped II-VI hollow nanoclusters, along with their assembly into into dimers and solids. In this chapter we will make a general revision of the methods that have been used along this thesis. Note that further methods have been occasionally used and they will be discussed in the corresponding chapter.

3.1 Born-Oppenheimer Approximation

In principle, all the information of a molecule may be obtained from its wave-function. In order to know it, we 'only' have to solve the Schrödinger equation (here in its time independent form):

$$\widehat{H}\Psi = E\Psi \tag{3.1}$$

where the Hamiltonian $\widehat{H}$ contains the kinetic energy terms of the electrons and the nuclei, the interactions between the nuclei, the electrons, and the nuclei-electrons.

Eq. (1.1) can be written also as follows:

$$(\hat{T}_N + \hat{V}_{NN} + \hat{T}_e + \hat{V}_{ee} + \hat{V}_{Ne})\Psi_{tot}(\{R_\alpha\},\{r_i\}) = E_{tot}\Psi_{tot}(\{R_\alpha\},\{r_i\}) \tag{3.2}$$

Since nuclei are much heavier than electrons, on the time-scale of electron motion nuclei can be considered as stationary objects, fixed at certain positions in space. Based on this idea, the Born-Oppenheimer approximation [178] decouples nuclear and electronic motions, where the nuclei move into the potential created by the electrons and the nuclei. Thus, a simplified Schrödinger equation which does not treat nuclear motion is solved for electrons only. The so-obtained electronic wave-function and energy depends on the nuclear positions as on the external parameters.

$$\hat{H}_e\Psi_e = E_e\Psi_e \tag{3.3}$$

$$(\hat{T}_e + \hat{V}_{ee} + \hat{V}_{Ne} + V_{NN})\Psi_e(\{r_i\};\{R_\alpha\}) = E_e\{R_\alpha\}\Psi_e(\{r_i\};\{R_\alpha\}) \tag{3.4}$$

In the Born–Oppenheimer picture, the nuclei move on a potential energy surface (PES) which is a solution to the electronic Schrödinger equation. Nuclear motion is treated in a separate Schrödinger equation, which employs the electronic energy obtained as a potential energy function:

$$(\hat{T}_N + E_e)\Psi_N(\{R_\alpha\}) = E_{tot}\Psi_N(\{R_\alpha\}) \tag{3.5}$$

Unfortunately, Eq. (1.4) can only be cast into a closed analytical

form for one electron systems, i.e., the hydrogen atom. Therefore, approximate methods have been developed:

1. Wave-function based methods: variational (configurational interaction, direct expansion of Ψ in some suitable basis) and many-body perturbation theory.
2. Density functional theory (DFT).
3. Quantum Monte-Carlo.
4. Density matrix based methods: variational (DMFT, NOFT, ...) and Contracted Schrödinger Equation.

It is beyond the scope of this section to develop a full description of these methods, so refer the interested reader to the literature devoted to these topics. See for example [179, 180, 181, 182, 183].

Wave-function based methods were the earliest developed ones. Two of these methods have been widely used throughout the years, the Valence Bond (VB) method and the Molecular Orbital (MO) method. The VB method was formulated in 1927 by Heitler and London [184]. The MO method was developed a bit later by Hund [185], Mulliken [186] and others. This theory became the most popular due to its quantitative power, which come from the use of orthogonal orbitals, in opposition to the VB theory which plays with non-orthogonal orbitals.

One of the first developed molecular orbital method was the Hartree-Fock method [187, 188], where the wave-function is an antisymmetrized product of one-electron orbitals. The electrons are treated as moving in a mean field due to the nucleus and the remaining electrons. The main drawback of this method is that correlation of electrons with opposite spins is neglected. There are different ways in which this correlation can be taken into account. One of them are the perturbational methods such as Moller-Plesset [189] theory (denoted as MPn, where n is the order of the perturbation). In these methods the electron correlation is treated as a perturbation of the HF problem. In the Configuration-Interaction (CI) method [190, 191] the wave-function is expressed as a linear combination of configurations to provide a better variational solution to the exact many-electron wave-function. There are other more sophisticated methods such as Coupled Cluster [192, 193, 194], Multi-Reference Configuration Interaction (MR-CI) or Complete-Active-Space (CAS) methods [195, 196], which are very

useful tools to study electronic properties of both ground and excited states.

Quantum Monte Carlo methods have been shown to be very powerful in the calculation of the electronic properties of ground states [197, 198, 199] or excited states [200, 201] of many systems. They have not been used in this work, and we refer the reader to more detailed papers [183, 202].

Density matrix based methods has emerged in recent years [203, 204, 205, 206, 207] as an alternative method to conventional ab-initio approaches and density functional theory (DFT) for considering the electronic correlation. A major advantage of the NOF method is that the kinetic energy and the exchange energy are explicitly defined using the one-particle reduced density matrix (1-RDM) and do not require the construction of a functional. The unknown functional in a 1-RDM theory only needs to incorporate electron correlation.

Mainly all the work presented in this thesis has been carried out within the density-functional framework. In the following subsection these methods are described in more detail.

3.1.1 Density Functional Theory

The Density Functional Theory formalism replaces the N-electron wave-function by a much simpler electron density $\rho(\vec{r})$ which is a function of the three spatial variables. Then, the electronic state, the energy and all the electronic properties of a system can be described in terms of this $\rho(\vec{r})$ [181, 182].

Hohenberg and Kohn [208] proved that the electronic properties of a system with a non-degenerate ground state are uniquely determined by the electron density $\rho(\vec{r})$. Hence, the ground-state energy E_0 is a functional of $\rho(\vec{r})$, and therefore, if we know the ground-state electron density it is possible to calculate all the ground-state electronic properties from ρ once we have been able to set all the appropriate functional dependencies. They also established an energy variational principle for the energy functional, analogous to the variational principle for wave-functions. Thus, knowing the exact form of the $E[\rho]$ functional, we can search for the ground state density (as it is the case for the wave-function). However, since the exact form of the functional is unknown, Kohn and Sham [209] developed an indirect approach to this functional, the Kohn-Sham method, and DFT turned

into a practical tool for rigorous calculations. They showed that the exact ground-state purely electronic energy E_0 of an N-electron molecule with ground-state electron probability density ρ is given by

$$E^{KS} = -\frac{1}{2}\sum_{i=1}^{N} < \psi_i(1)|\nabla_1^2|\psi_i(1) > + \int \upsilon(r)\rho(1)d\vec{r}_1 + \\ + \frac{1}{2}\int\int \frac{\rho(1)\rho(2)}{r_{12}} d\vec{r}_1 d\vec{r}_2 + E_{xc}[\rho] \tag{3.6}$$

where $\upsilon(r) = -\sum_\alpha \frac{Z_\alpha}{r_{1\alpha}}$ is the external potential due to the nuclei, ψ_i are the Kohn-Sham orbitals, and the $E_{xc}[\rho]$ is the exchange-correlation energy.

In the Kohn-Sham procedure, the exact ground state ρ can be found from the Kohn-Sham orbitals according to,

$$\rho = \sum_{i=1}^{N} |\psi_i|^2 \tag{3.7}$$

and the Kohn-Sham orbitals are found by solving the one-electron equations

$$\hat{F}_{KS}(1)\psi_i(1) = \varepsilon_i\psi_i(1) \tag{3.8}$$

being the Kohn-Sham operator $\hat{F}_{KS}$

$$\hat{F}_{KS} = -\frac{1}{2}\nabla_1^2 + \upsilon(1) + \sum_{j=1}^{n} \hat{J}_j(1) + V_{xc}(1) \tag{3.9}$$

where $\hat{J}$ is the Coulomb operator, and V_{xc} is called the exchange-correlation potential. $\hat{F}_{KS}$ is like the Fock operator in HF equations, except that the exchange operators are replaced by V_{xc}, which handles the effects of both the exchange and electron correlation.

These equations are iteratively solved. Starting from a guess density, $\hat{F}_{KS}$ is build and the set of equations, Eq. (1.8), solved. The solution then is transfered to $\hat{F}_{KS}$, in order to build a new $\hat{F}_{KS}$. This process is repeated until convergence is achieved.

The physical significance of the Kohn-Sham orbitals is still under debate. Some authors claim that they do not have any significance other than in allowing the exact ρ to be calculated from Eq. (1.7). Likewise, the Kohn-Sham orbital energies should not be confused with molecular orbital energies. However, others based on the fact that the exact Kohn-Sham orbital energy for the HOMO is just the negative of

ionization potential [210, 211], and due to the fact that the set of Kohn-Sham equations remind us, as in the HF case, the independent particle model, they associate to the Kohn-Sham orbitals a similar physical significance and legitimacy than to the HF canonical orbitals. In recent publications it is shown the results obtained from molecular orbitals obtained from DFT are quite similar to the molecular orbitals from standard MO-LCAO methods, and that one can extract a lot of useful information about molecular systems from analysis of their MOs even if the density functional methods are used [210, 212].

However, there is one more problem: the exchange-correlation functional $E_{xc}[\rho]$ and hence the exchange-correlation potential $v_{xc}[\rho; \overrightarrow{r}]$ is not known except for the case of the uniform electron gas. Fortunately, approximate functionals have been developed. One simple approximation is the so called local density approximation (LDA). The idea is to consider each volume element with local density $\rho(\overrightarrow{r})$ to be a homogeneous electron gas. From this point of view the approximation would be expected to be accurate if the density varies slowly in space. Then, $E_{xc}[(\rho)]$ is given by

$$E_{xc}^{LDA}[(\rho)] = \int \rho(\vec{r})\varepsilon_{xc}(\rho)d\vec{r} \tag{3.10}$$

where $\varepsilon_{xc}(\rho)$ is the exchange plus correlation energy per electron in a homogeneous electron gas with electron density ρ. An accurate expression for $\varepsilon_{xc}(\rho)$ was found by Vosko, Wilk and Nusair [213]. Application of this expression leads to the local density approximation (LDA), or local spin density approximation (LSDA) [214], if one uses different orbitals and densities ρ^{α} and ρ^{β} for electrons with different spins. Of course, in the case of molecules these are only approximations to the true functionals, since ρ is far from being homogeneous. One might hope to improve the approximation by introducing an expansion in terms of gradients of the density. These methods are called generalized gradient approximations (GGA), and are of great importance in the study of molecules, where the electron density can not be considered as homogeneous. Recently, several new GGA functionals have been develop, both, from first principles but also highly parametrized ones using fits to exact data on atoms and small molecules. Most recently, so called meta-GGA functionals were proposed, where besides the local density and its gradient also the laplacian (or the kinetic energy density) enters the equations.

Density functional methods have proved to give excellent results in most chemical systems [215], with results comparable to those given by CPU intensive electron-correlation methods. However they frequently overestimate bond dissociation energies [216]. The hybrids of HF and DFT theories increment the accuracy of the dissociation energy as was validated by Johnson et al. *[217]*. The hybrid [218] Becke 3 combined with the correlation functional Lee-Yang-Parr (B3LYP) [208, 219, 220] has become one of the most popular one, having the following form:

$$(1-a_0)E_x^{LSDA} + a_0E_x^{HF} + a_xE_x^{B88} + a_cE_c^{LYP} + (1-a_c)E_c^{VWN} \qquad (3.11)$$

being the values of the parameters a_0=0.20, a_x=0.72 and a_c=0.81. This functional is known as the Becke's 3 parameter functional, B3LYP.

Since density-functional calculations do not use the exact E_{xc} they are not, strictly speaking, ab-initio calculations. However, they do not use parameters fitted to experimental data, hence they lie closer in spirit to ab-initio calculations than to semiempirical ones. One of the main advantages of these methods is that with a similar computational cost to HF methods, they include some kind of electron correlation, being the major drawback that the correlation effects cannot be sorted out precisely. They are already mixed from the beginning with the uncorrelated solution. Besides, there is not any systematic way to improve the calculations by applying more and more sophistication, so the results must be accepted as they stand. In spite of these facts, DFT have been found to yield good results for ground state properties of various chemical systems, with a quality comparable to MP2 results , or even better in some cases. Due to their relative low computational cost, DFT is the method of choice for large systems, for which the inclusion of electron correlation by MP or CI methods is prohibitive.

3.1.2 Special Features of Solid State Calculations

In spite that a crystals can be considered as "infinite" systems, they exhibit a very important symmetry property, namely, they are translation invariant. This translational symmetry makes the computational modeling of a solid feasible. Indeed, a perfect solid can be seen as a three-dimensional array of atoms, ions, or molecules, a few of which form a spatial pattern that is repeated identically throughout the crystal. This pattern is called the unit cell. In this way, a crystal is de-

scribed as a fundamental unit cell being repeated in three dimensions to form an infinite system. The unit cell in three dimensions is characterized by three translation vectors $\bar{a}_1$, $\bar{a}_2$ and $\bar{a}_3$ with the lattice parameters a, b and c, as norms. Additionally, the extended system can be generated by translation of the unit cell by lattice vector $\bar{t}$:

$$\bar{t} = n_1\bar{a}_1 + n_2\bar{a}_2 + n_3\bar{a}_3 \tag{3.12}$$

Therefore, filling the unit cell with atoms, ions or molecules in a well-defined geometrical arrangement and applying the translation pattern permits the creation of an ideal crystal. Then, the unit cell in the real space can be represented in the reciprocal space by a Fourier transform, by the prescription that the reciprocal lattice basis vectors ($\bar{b}_1$, $\bar{b}_2$ and $\bar{b}_3$) obey the orthonormality condition, $\bar{a}_i\bar{b}_j = 2\pi\delta_{ij}$, so:

$$\bar{b}_1 = 2\pi\frac{\bar{a}_2 \times \bar{a}_3}{L^3}; \qquad \bar{b}_2 = 2\pi\frac{\bar{a}_3 \times \bar{a}_1}{L^3}; \qquad \bar{b}_3 = 2\pi\frac{\bar{a}_1 \times \bar{a}_2}{L^3} \tag{3.13}$$

The equivalent of a unit cell in reciprocal space is called the first Brillouin zone. Just as a point in real space may be described by a vector $\bar{r}$, a "point" in reciprocal space may be described by a vector $\bar{k}$, often called wave-vector. Since the (idealized) system under study is invariant in all three spatial directions, its electronic potential $V(\bar{r})$ will have the periodicity of the lattice, expressed by the lattice vector $\bar{t}$, so the electronic state is identical within each unit cell:

$$V(\bar{r} + \bar{t}) \equiv V(\bar{r}) \tag{3.14}$$

We then will obtain some wave-functions $\phi(\bar{r})$ which are solutions of the Schrödinger equation for V($\bar{r}$) .

Bloch theorem states that the $\phi(\bar{r})$ wave-function value at equivalent positions in different cells are related by a complex phase factor involving the lattice vector $\bar{t}$ and the $\bar{k}$ wave-vector in the reciprocal space:

$$\phi(\bar{r};\bar{k}) = e^{i\bar{k}\cdot\bar{r}}\varphi(\bar{r};\bar{k}) \tag{3.15}$$

With $\bar{k}$ any allowed wave-vector for the electron that is obtained for a constant potential, and $\phi(\bar{r})$ arbitrary functions, but always with the periodicity of the lattice:

$$\varphi(\bar{r}+\bar{t}) = \varphi_k(\bar{r}) \tag{3.16}$$

Any wave-function meeting this requirement is called a Bloch function. Likewise, Bloch's theorem can also be rewritten in a different form:

$$\phi(\bar{r}+\bar{t};\bar{k}) = e^{i\bar{k}\bar{t}}\phi(\bar{r};\bar{k}) \tag{3.17}$$

This means that any function $\phi(\bar{r})$ that is a solution to the Schrödinger equation of the problem, differs only by a phase factor $e^{i\bar{k}\bar{t}}$ between equivalent positions in the lattice. This immediately implies that the probability of finding an electron is the same at any equivalent position in the lattice. In this way, the problem has been transformed from treating an infinite number of atoms (electrons) to only treating those within the unit cell. The price is that the solutions become a function of the reciprocal space wave-vector $\bar{k}$ within the first Brillouin zone. It is important to stand out that the importance of the Brillouin zone stems from the Bloch wave description of functions in a periodic medium, in which it is found that the solutions can be completely characterized by their behavior in a single Brillouin zone. The $\bar{k}$ appears as a parameter in the equation similarly to the nuclear positions in molecular Hartree–Fock theory. The solutions are continuous as a function of $\bar{k}$, and provide a range of energies called a band, with the total energy per unit cell being calculated by integrating over k space.

3.1.3 Quantum Molecular Dynamics

Molecular dynamics (MD) is a form of computer simulation in which atoms and molecules are allowed to interact for a period of time, giving a view of the motion of the particles. One convenient approach to include the electronic structure in molecular dynamic simulations consists of straightforwardly solving the static electronic structure problem in each molecular dynamics step given the set of fixed nuclear positions at that instance of time. This is what we do in the Born-Oppenheimer molecular dynamic simulations. Born-Oppenheimer molecular dynamics follows the adiabatic time evolution of a system, dividing time into series of timesteps. In order to solve the Newton's equations of motion, electrons are treated quantum mechanically (solving the electronic equation by means of density functional theory)

and nuclei classically.

Thus, we solve the static electronic structure problem in each molecular dynamics step given the set of fixed nuclear positions at that instance of time. Hence, the electronic structure part is reduced to solving a time–independent quantum problem, namely by solving the time–independent Schrödinger equation, concurrently to propagating the nuclei via classical molecular dynamics.

The resulting Born-Oppenheimer molecular dynamics method is propagated for the electronic ground state by

$$F = -\frac{dE}{dR_\alpha} = ma = m\frac{d^2R_\alpha}{dt^2} = -\nabla_\alpha \min_{\Psi_0}\{< \Psi_0|H_e|\Psi_0 >\} \tag{3.18}$$

where the minimum of $< H_e >$ has to be reached in each Born-Oppenheimer molecular dynamics step according to Eq. (1.12).

Since we use DFT as outlined before to solve the electronic problem, the total ground-state energy of the interacting system of electrons with classical nuclei fixed at positions $\{R_\alpha\}$ can be obtained as the minimum of Kohn-Sham energy:

$$\min_{\Psi_0}\{< \Psi_0|H_e|\Psi_0 >\} = \min_{\{\varphi_i\}} E^{KS}[\{\varphi_i\}] \tag{3.19}$$

where the Kohn-Sham energy is defined in Eq. (1.6) and $\{\varphi\}_{i=1}^{k}$ being the Kohn-Sham orbitals according to Eq. (1.8).

The molecular dynamics simulations carried out along this thesis are made at constant temperature. In such a way the average temperature of the system is fixed, but it is allowed for a fluctuation of the temperature with a canonical distribution. In the canonical ensemble moles, volume and temperature are conserved. We have used the Nose thermostat implemented in the SIESTA code [221], where the system is in thermal contact with a heath bath, made into an integral part of the system by adding an artificial variable associated with an artificial mass. Finally, the time step employed is an important control parameter for a simulation. The maximum time-step is determined by the rate of the fastest process in the system, i.e. typically an order of magnitude smaller than the fastest process. Molecular vibrations typically occur in the range of 10^{-12}-10^{-15} seconds, so timesteps of the order of fetmtoseconds are required to model such motions with enough accuracy.

3.2 Basis Sets and Pseudopotentials

In both wave-function based methods and density functional theory a set of functions to span the molecular orbitals are needed. These sets of functions are the so called basis sets. The choice of an appropriate basis set is an essential requirement for the success of the calculation. However, we have to balance the precision of the basis set and its size, since increasing the size of the basis set the calculation cost becomes more expensive.

In the characterization of the gas phase structures we have used the Contracted Gaussian Functions (CGF), which are the most used in quantum chemistry calculations. They consist of linear combinations (contractions) of Gaussian functions (primitives),

$$\varphi_{\mu}^{CGF}(|\bar{r} - \bar{R_A}|) = \sum_{p=1}^{L} d_{p\mu} g(\alpha_{p\mu}, |\bar{r} - \bar{R_p}|) \tag{3.20}$$

where the exponent of the primitives $\alpha_{p\mu}$ and the contraction coefficients $d_{p\mu}$ are optimized for the different elements.

Additionally, for the quantum molecular dynamic simulations and the solid state calculations, we have used numerical linear combination of atomic orbitals basis set. These orbitals are zero beyond a certain radius. Within this radius, the atomic basis orbitals are products of a numerical radial function and a spherical harmonic, namely, for atom I located at R_I, where $r_I = r - R_I$,

$$\phi_{Ilmn}(\bar{r}) = R_{Iln}(|\bar{r}_I) Y_{lm}(\bar{r_I}) \tag{3.21}$$

A single parameter, orbital energy shift, $\triangle E_{PAO}$, defines the confinement radii of different orbitals. With this basis set the self-consistent potential is calculated on a grid in real space. The fineness of this grid is determined in terms of an energy cutoff, E_{Cutoff}, in analogy to the energy cutoff when the basis set involves plane waves. Notice that the smaller the $\triangle E_{PAO}$ value and the larger the E_{Cutoff} value, the more accurate the calculation.

It must be pointed out that sometimes all-electron basis sets are used, which means that all electrons are considered in the basis set. However, in some cases, due to the large number of electrons, the computational cost is prohibitive. Core electrons are very localized and deep in energy, so they are chemically inert. In order to reduce

the computational cost, they can be frozen, i. e. ignore the dynamics of the core electrons and replace their effects by an effective potential. Thus, the core electron states may be assumed to be fixed and a pseudopotential may be constructed for each atomic species which takes into account the effects of the nucleus and core electrons. Therefore, the pseudopotentials replace the core electrons, while the valence electrons are treated by regular basis functions. In this way, the chemically active valence electrons are considered to move in the potential caused by the chemically inert core electrons.

3.3 Search of Transition State and Life-time Calculation

A transition state of a chemical reaction is a first order saddle point on the potential energy surface. Like the minima, the first order saddle points are stationary points with all forces zero. However, unlike the minima, one of the second derivatives in the first order saddle point is negative. Thus, the transition state structure associated with the first-order saddle point has one imaginary frequency and the normal mode of vibration associated with this negative frequency emulates the motion of the atoms along the reaction coordinate. Among the different methods available for locating transition states, we have used the Synchronous Transit-Guided Quasi-Newton, STQN, method developed by Peng *et al.* [222, 223]. Contrary to other methods, STQN does not require a guess for the transition structure. Instead, the initial structure of transition state is interpolated from the structures of the reactant and the product.

To asses that the calculated transition states connect indeed the appropriate reactants and products, we have performed Intrinsic reaction coordinate calculations, IRC. The idea of this technique is to start at a transition state and follow the gradients toward reactants in one side and to products in the other side of the reaction coordinates.

The energy of transition state structure is important to determine the energy barrier for the reaction and, thus, the reaction rate. In 1889 the Arrhenius equation [224] was proposed to determine energies for the reaction barrier. However, this equation derives from empirical

Figure 3.1: Schematic representation of a chemical reaction. The ‡ notation refers to the value of interest at the transition state.

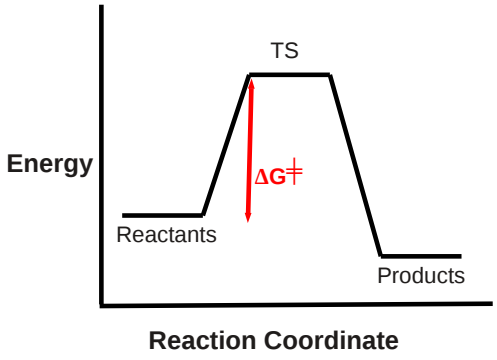

observations and the mechanical basis was not understood. Thus, in 1935 the Transition State Theory and the Eyring equation were developed [225]. Transition state theory explains the reaction rates of elementary chemical reactions. It details a hypothetical transition state that exists between reactants and products during a chemical reaction. This theory is used to explain how chemical reactions take place and led to the Eyring equation:

$$k = \frac{k_B T}{h} e^{-\frac{\triangle G^{\ddagger}}{RT}} \tag{3.22}$$

where $\triangle G^{\ddagger}$ is the Gibbs free energy difference between the TS and reactant, k is the reaction rate constant, T is the absolute temperature, k_B is the Boltzmann constant, h is the Planck's constant, and R is the universal gas constant. The lifetime of the reactants can be then calculated as the inverse of the reaction rate constant. While Arrhenius equation is useful only in gas phase reactions, the Eyring equation can be applied in the study of gas, condensed and mixed phase reactions. However, it is important to emphasize that the Eyring model is an approximation to calculate reaction rate constants and then lifetimes. In addition, these lifetimes are calculated from the reaction rate constants which are very sensitive with respect to the activation energies. Consequently, the data obtained from this equation should be taken qualitatively.

Part II

Endohedrally Doped CdS Nanoclusters

Chapter 4

Structure and Stability of the Endohedrally Doped $(X@Cd_iS_i)^{q=0,\pm1}_{i=4,9,12,15,16}$, X= Na, K, Cl, Br, Nanoclusters

Endohedral $(X@Cd_iS_i)^{q=0,\pm1}$ structures have been characterized by means of the Density Functional Theory, with X being alkali metals such as Na and K or halogens such as Cl and Br, i= 4, 9, 12, 15, 16. These nanoclusters have been chosen due to their high sphericity, which is known to be one of the parameter determining the stability of the endohedral nanoclusters, along with the charge and sizes of the guest atom. In these structures, the atoms are trapped inside previously characterized spheroid hollow structures with positively charged Cd atoms and negatively charged S atoms. Moreover, although the radii of all atoms are similar, Cd atoms are located more inside the structure. For alkali metals, neutral and cationic endohedral compounds have been characterized and, for halogens, neutral and anionic nanoclusters. It is observed that some of these guest atoms are trapped in the center of mass of the cluster, while others are found to be displaced from that center, leading to structures where the guest atom presents a complex dynamical behavior. This fact was confirmed by quantum molecular dynamics calculations, which further confirmed the thermal stability of these endohedral compounds.

4.1 Introduction

Nanostructured materials have fundamental and technological importance for their novel structural, physical and chemical properties, which usually differ markedly with respect to those of their corresponding bulk material. Since these properties vary with the size of the nanoparticle, materials with modified properties can in principle be obtained. Size control, therefore, appears crucial at this point in order to monitor and stabilize the targeted physical property, and much effort has been dedicated towards this goal in the last decade [226].

Concomitantly, on purpose modification of the physical and chemical properties of nanoparticles can be achieved by doping. In this vein, spherical hollow clusters provide the chance for endohedral doping, namely, the dopant is placed in the interior of the cavity of the hollow nanoparticle.

The first endohedrally doped nanoparticles described as such in the literature, were a number endohedral fullerenes [100, 227, 228, 229, 230, 231]. Later, it was found that elements other than carbon may also be used to build hollow structures with sufficient space as to trap guest atoms. As a matter of fact, endohedrally doped nanoclusters of gold [232], tin [121, 122, 233], lead [234, 235, 233] and germanium [236, 237, 238] have been reported recently.

Hollow binary nanoclusters of II-VI semiconductor elements have also been widely studied in the literature, both theoretically and experimentally [85, 81, 78, 82, 77, 83, 57, 58, 68]. However, studies of the properties of endohedral compounds made of these hollow nanoclusters are scarce [131, 239]. Of particular relevance to the present research is the previous characterization of the $(X@Zn_iS_i)^{0,\pm1}_{i=4-16}$ compounds [134], being X alkali metals or halogens. In this work it was observed that alkali metals transferred an electron to the cage, while halogen atoms took an electron from the cage, leading to charged ions inside the cage. Moreover, encapsulation of halogen atoms resulted in endohedral nanoclusters with enhanced electron affinity relative to the guest halogen atom (4.5 eV compared to 3.5 eV). These nanoclusters ought, therefore, to be considered as superhalogens in the same vein as the $Al@Al_{12}$ cluster, for which recent research has confirmed its predicted [22] high electron affinity (EA) of 3.20 eV as well as its ability to ionize spontaneously into $(Al@Al_{12})^-K^+$ in the gas phase [135].

Notice that the Cl and Br endohedral nanoclusters studied in this

work have electron affinities substantially larger than $Al@Al_{12}$. Hence, they are expected to have even a stronger superhalogen character. Furthermore, the electron affinities of the halogen endohedral nanoclusters and the ionization energies of the alkali endohedral nanoclusters of Zn_iS_i are rather similar, rendering them good candidates to form cluster-assembled materials under mild conditions, since large IE/EA differences would yield substantial heat release during assembling that might destroy the assembled material as it is formed. Such solids, based on $X@Zn_{12}S_{12}$ structures, have been recently theoretically characterized [240]. They have fcc crystal lattice structure, and, interestingly, the band-gap is decreased from 3.66 eV found in wurtzite to 2.2 eV in the bare solid, and even further, to 1.8 eV, in the doped solids. These solids may be seen as semiconducting materials, with smaller band-gaps than the solids found in nature, namely, wurtzite and zincblende. Ab-initio quantum dynamics calculations further confirmed the thermal stability of the calculated structures. Moreover, the predicted metastability of the fcc structures was supported by the predicted energy barriers towards collapsing into wurtzite, which were found to be larger than 6 eV.

The potential technological applications of these newly designed materials in a large variety of fields, like solar cells, heterogeneous catalysis, molecular transport, optical sensors and so on, makes the searching of new building blocks for such materials worthwhile. Within this context, the theoretical investigations reported herein could help, or guide, experimentalists towards such goal.

Thus, Cd_iS_i, i=1–16 clusters have been synthesized and characterized by BelBruno et. al. [58]. Consequently, one could think of using these clusters as building blocks to synthesize new stable molecular solids. However, we propose that using endohedrally doped selected Cd_iS_i hollow clusters should represent a wiser choice, because (i) the stability of the cluster structures themselves are not compromised by the endohedral doping and (ii) a larger variety of properties can be tailored by such doping.

Herein, we will describe the physico-chemical properties of $(X@Cd_iS_i)^{0,\pm1}_{i=4,9,12,15,16}$ clusters, with X= Na, K, Cl, Br, based on our density functional theory and quantum molecular simulation calculations. These clusters were chosen due to their hollow spherical shape, which is one main parameter determining their stability.

Our results, along with the earlier mentioned work by BelBruno

et al. and the related experimental work on cadmium chalcogenide stoichiometric hollow clusters by Kasuya *et al.* [68, 241], and by Riehle et. al. [242], suggest that these hypothetical cluster-like compounds could be within experimental reach in the near future.

4.2 Methods

All geometries have been fully optimized using the gradient corrected hybrid B3LYP [243, 218, 219] functional within the Kohn-Sham implementation [209] of density functional theory [208]. Harmonic vibrational frequencies are determined by analytical differentiation of gradients, in order to determine whether the structures found are true minima or not, and to extract zero-point energies and Gibbs free energy contributions.

The relativistic compact effective core potentials and shared-exponent basis set [244] of Stevens *et al.* have been used for Cd and S, as in the study of the isolated clusters [83], and the all-electron 6-311+G(d) basis set was used for the trapped atom. The 4d electrons of Cd were included in the valence. In order to perform the geometry optimizations and harmonic frequency calculations an extra d function was added on Cd and S, due to its importance for the proper description of the high coordination of the atoms in the three-dimensional cluster structures. Note that pure angular momentum functions were used throughout this study.

To further explore the thermal stability of these compounds, we also undertook ab-initio thermal MD simulations at 298K on the calculated local minima structures, controlled by means of the Nose thermostat as implemented in the SIESTA code [221] within DFT approach. Exchange and correlation effects were described using the generalized gradient approximation (GGA), within the revised Perdew-Burke-Ernzerhof (rPBE) functional [245, 246, 247]. Core electrons were replaced by Troullier-Martins norm-conserving pseudopotentials [248] in the Kleinman-Bylander factorized form [249]. In the context of Siesta, the use of pseudopotentials imposes basis orbitals adapted to them. Furthermore, SIESTA employs a localized basis set to represent the Kohn-Sham orbitals for valence electrons. Accordingly, the basis set of atomic orbitals is constructed from numerical solutions of the atomic pseudopotential, and are constrained to be zero beyond a cutoff radius. We used a basis set of double-ζ plus polarization quality (DZP).

A single parameter, orbital energy shift (ΔE_{PAO}), defines the confinement radii of different orbitals. With this basis set, SIESTA calculates the self-consistent potential on a grid in real space. The fineness of this grid is determined in terms of an energy cutoff (E_{Cutoff}) in analogy to the energy cutoff when the basis set involves plane waves. We have first checked the influence of the ΔE_{PAO} and E_{Cutoff} parameters for different endohedral compounds. These values are set to be ΔE_{PAO} =150 meV and E_{Cutoff} = 200 Ry in routine calculations, but in addition to this, we have carried out the quantum dynamics simulations for ΔE_{PAO} =50 meV and E_{Cutoff} = 200 Ry, and ΔE_{PAO} =50 meV and E_{Cutoff} = 300 Ry, to check the influence for both parameters on the obtained results. Notice that the smaller the ΔE_{PAO} value and the larger the E_{Cutoff} value, the more accurate the calculation.

In order to analyze the effect of the orbital energy shift and the mesh cutoff, we have focused on X@$Cd_{12}S_{12}$ endohedral nanoclusters, being X= Na, K, Cl and Br. The effect of changing ΔE_{PAO} and E_{Cutoff} appears to be dramatical for the smallest atom, Na, as can be seen in Figure 4.1. There, the distances of the Na atom with respect to the center of mass of the nanocluster and the total energy along the simulations are depicted, for three different cases mentioned above. One may observe that for $\Delta E_{PAO} = 150$ meV and E_{Cutoff}=200 Ry, the endohedral Na@$Cd_{12}S_{12}$ structure is not altered, the Na atom moves near the center of the nanocluster, and the total energy oscillates around the same value. However, more fine calculations, with $\Delta E_{PAO} = 50$ meV and E_{Cutoff}=200 Ry, show that Na atom moves from the center towards the surface of the nanocluster, which leads to a more stable structure, as can be seen in the total energy picture. This is due to the small size of sodium compared to the cavity available in the nanocluster, which allows to move close to the surface, interacting covalently with it. Further increase in E_{Cutoff} has no influence in the final result, and thus calculations using $\Delta E_{PAO} = 50$ meV and E_{Cutoff}=300 Ry does not produce any change in the dynamics. For larger trapped atoms, namely K, Cl and Br, we have observed that changing ΔE_{PAO} and E_{Cutoff} does not alter the final result (see supplementary material). We therefore conclude that endohedral Na@Cd_iS_i compounds need a higher degree of fineness in the calculations. Therefore, ab-initio Quantum Dynamics calculations have been carried out with $\Delta E_{PAO} = 50$ meV and$E_{Cutoff} = 200$ Ry for X= Na, and $\Delta E_{PAO} = 150$ meV and$E_{Cutoff} = 200$ Ry for the rest, to save

computational resources. All these simulations were carried out for 6 ps with a chosen time step of 1 fs.

Figure 4.1: The total energy (eV) of the endohedral Na@$Cd_{12}S_{12}$ compound and the distance of the Na atom from the center of mass of the $Cd_{12}S_{12}$ nanocluster (Å) as a function of the simulation time (fs) for three different choices of the ΔE_{PAO} and E_{Cutoff} parameters. Top panels: $\Delta E_{PAO} = 150$ meV and $E_{Cutoff} = 200$ Ry. Middle panels: $\Delta E_{PAO} = 50$ meV and $E_{Cutoff} = 200$ Ry. Bottom panels: $\Delta E_{PAO} = 50$meV and $E_{Cutoff} = 300$ Ry.

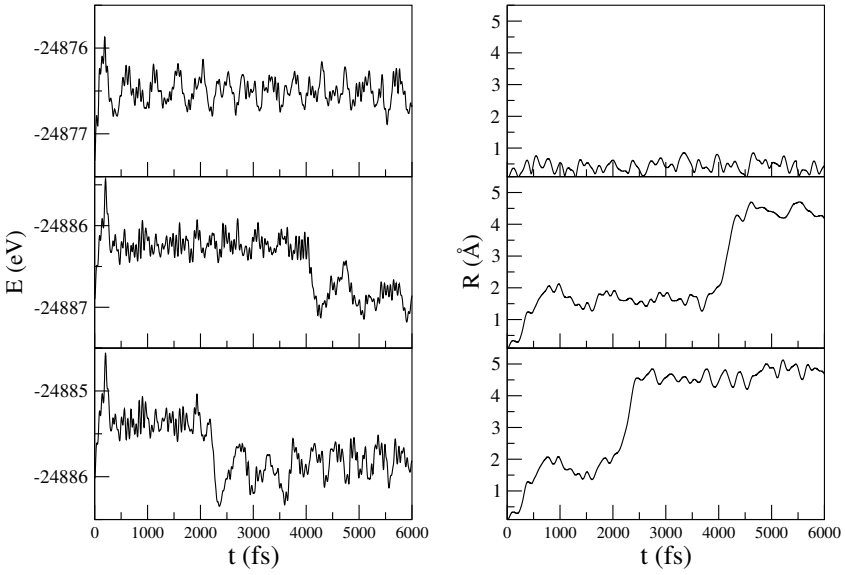

4.3 Results

First, the effect of the charge on the geometry of the bare nanoclusters will be analyzed in subsection 4.3.1. We anticipate that the most salient geometrical feature of the charged nanoclusters is that the size of the cavity, as compared to their neutral counterparts, changes noticeably. In this subsection the ionization energies and the electron affinities of the bare nanoclusters are also discussed. Then, we will focus on the endohedral compounds, in subsection 4.3.2. Both, neutral and cationic nanoclusters has been found to be able to encapsulate alkali metals. Halogen atoms, on the other hand, can be encapsulated by the neutral and anionic nanoclusters.

Table 4.1: Average Radii of the Sphere Defined by the Cd Atoms, r_{Cd}, the Standard Deviation (σ), the Cavity inside the Clusters, r_{cavity}, in Å, and the Ionization Potentials (IE) and Electron Affinities (EA) in eV.

				r_{cavity}		
i	IE	EA	r_{Cd} (σ)	q=0	q=1	q=-1
4	7.85	2.35	1.95 (0.00)	0.98	0.98	1.04
9	7.80	2.45	3.12 (0.18)	2.15	2.17	2.20
12	7.90	2.50	3.62 (0.00)	2.65	2.68	2.71
15	7.69	2.67	4.11 (0.37)	3.14	3.14	3.17
16	7.68	2.71	4.24 (0.09)	3.27	3.29	3.30

First the structures of charged and neutral endohedral nanoclusters will be characterized and their properties analyzed. Then, ab-initio molecular dynamics simulations will be carried out in order to assess the thermal stability of these compounds.

4.3.1 Bare Nanoclusters and Atoms

The structures of the cationic and anionic bare nanoclusters were characterized first. Starting from the neutral nanoclusters, an electron was either, removed (for the cations) or added (for the anions), followed by geometry optimizations and frequency calculations to obtain and characterize the optimized structures of the nanocluster ions. For the structures, the adiabatic ionization energies (IE) and electron affinities (EA) were calculated. The structures of the cationic and anionic nanoclusters followed the well-known square-hexagon rule as do their neutral counterparts.

In Table 4.1, the average radii of the sphere defined by the Cd atoms, r_{Cd}, their standard deviation, and the cavity of the cluster, r_{cavity}, are given along with Ionization Energies (IE) and Electron Affinities (EA) for the neutral clusters. The radius of the cavity inside the spheroidal nanoclusters is defined by the Cd atoms (see Ref. [134]) and is given by $r_{cavity} = r_{Cd} - r^{ionic}_{Cd^{+2}}$, with $r^{ionic}_{Cd^{+2}} = 0.97$ Å. r_{cavity} is given for all the neutral, cationic and anionic nanoclusters. Notice that, compared with the neutral structures, cationic r_{cavity} values are slightly affected while anionic ones are significantly increased. Recall that Cd atoms, which are located inner in the structure, have positive partial charges of $\sim$1e, while S atoms have negative partial charge of $\sim$-1e.

Comparing r_{cavity} for the neutral and ionic nanoclusters, we can conclude that r_{cavity} in general keeps constant in cationic clusters but it increases from neutral to anionic structures. The maximum increase is 0.06 Å.

However, the sphericity of the nanoclusters is not the same. A way of measuring the sphericity of these clusters is the standard deviation (σ) of the distances between the Cd atoms and the center of the nanoclusters. The smaller the σ, the more spherical the nanocluster is. It must be pointed out that the structures of the cationic and anionic nanoclusters retain the sphericity of their neutral counterparts. It may be seen that Cd_iS_i nanoclusters with i = 4, 12, 16 have $\sigma \simeq 0$ and are almost fully spherical. The i = 9 nanocluster has only a small sphericity deviation ($\sigma = 0.15$). Hence, all these nanoclusters are highly spherical. However, the case of $Cd_{15}S_{15}$ is particular which, with a $\sigma = 0.37$, is far from sphericity. Nevertheless, this structure is highly symmetric. It resembles a rugby ball, which is symmetric but the distances to the center of the ball are not the same. The significance of this particular structure will be clarified later.

The ionization energies of these clusters oscillate around 7.8 eV and the electron affinities around 2.5 eV. These values are indicative of the high stability of the neutral bare nanoclusters.

4.3.2 Endohedral Nanoclusters

We have considered all possible $(X@Cd_iS_i)^q$ endohedral compounds, with i= 4, 9, 12, 15, 16; q= 0, 1, -1 and X= Na, K, Cl, Br. As seen in Section 4.2, ab-initio quantum molecular dynamics calculations show that sodium atoms moves toward the surface in $Cd_{12}S_{12}$. This is indicative of the low thermal stability of these compounds. For other sodium-doped nanocluster similar behavior has been observed, and, consequently, we focus the discussion on the thermally stable $K@Cd_iS_i$, $Cl@Cd_iS_i$ and $Br@Cd_iS_i$ nanoclusters. Information about the thermally unstable $Na@Cd_iS_i$ local minima is available in the appendix (see 10).

The thermodynamic stability of the minima will be assessed by the free energy of encapsulation (ΔG_{enc}) defined by the following reaction:

$$Cd_iS_i + X^q \rightarrow (X@Cd_iS_i)^q; \qquad q = 0, \pm 1$$

A negative value of $\triangle G_{enc}$ indicates that the endohedral nanoclus-

ter is thermodynamically more stable than the separated fragments. Additionally, we have calculated the deformation energy of the cluster, $\triangle E_{def}$, as the energy required to deform the neutral cluster from its bare structure to the geometry in the endohedral complex:

$$\triangle E_{def} = E_{deform} - E_{opt} \tag{4.1}$$

where $\triangle$E$_{deform}$ is the energy of the bare cluster with the final geometry upon the encapsulation and E$_{opt}$ is the energy of the cluster with its optimized bare geometry.

In Figure 4.2 the characterized X@Cd$_i$S$_i$ endohedral nanoclusters are shown. For the sake of clarity, K and halogen (Cl, Br) endohedral nanoclusters will be discussed separately.

Figure 4.2: Structures of X@Cd$_9$S$_9$, X@Cd$_{12}$S$_{12}$, X@Cd$_{15}$S$_{15}$ and X@Cd$_{16}$S$_{16}$ X= K, Cl, Br. S atoms are drawn in yellow, while Cd atoms are drawn in cyan.

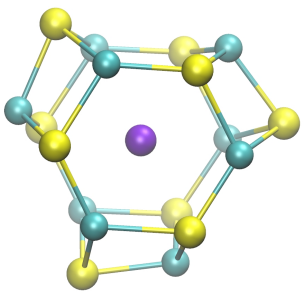

X@Cd$_9$S$_9$

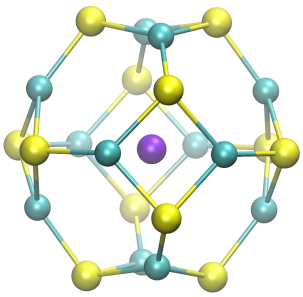

X@Cd$_{12}$S$_{12}$

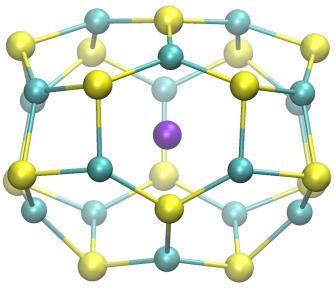

X@Cd$_{15}$S$_{15}$

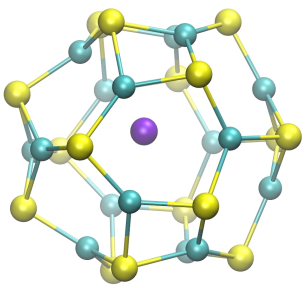

X@Cd$_{16}$S$_{16}$

4.3.2.1 K@Cd_iS_i Endohedral Nanoclusters

In Table 4.2 the geometric, electronic and energetic properties of the characterized local minima of K@Cd_iS_i endohedral nanoclusters are given. In addition, the R^{dyn}_{range} and R^{dyn}_{av} geometrical parameters, representative of the dynamic movement of the trapped potassium atom inside the nanocluster, are given. R^{dyn}_{range} denotes the range of the distance between the trapped atom and the center of the nanocluster, while R^{dyn}_{av} is the average distance of the trapped atom with respect to the center of the nanocluster along the simulation time.

Minima structures are found for both neutral and cationic endohedral structures for i=9, 12, 15, 16. Observe that in all structures K is positively charged, but a bit more for cationic compounds than in neutral ones. In the former case, the Coulombic repulsion between the trapped K atom and the Cd atoms is larger than in the latter, which dramatically affect the calculated encapsulation free energies, ΔG_{enc}. Observe that they are negative for neutral compounds and positive for the cationic endohedral nanoclusters. Hence, cationic compounds are predicted to be thermodynamically unstable with respect to their corresponding separated compounds. Nonetheless, the height of the barrier for the evaporation of potassium atoms might render these complexes with long enough lifetimes as to be amenable to experimental detection. In general, in both neutral and cationic compounds, free energy indicates that the compounds are thermodynamically more stable as the size of the nanoclusters increases. This is due to a combination of two factors, namely, the better size fit of the K atom inside the cavity and the smaller Coulombic repulsion between K and Cd atoms. Recall that S atoms are located at longer distance from the center, and therefore locally the K-Cd interaction prevails. These arguments also account for the fact that when the size of the cluster increases, the cavity radii is less affected and consequently remains almost constant. Notice that the largest increase of cavity compared to the bare case occurs for K@Cd_9S_9, while the smallest increase occurs for K@$Cd_{16}S_{16}$. In these nanoclusters K atom lies at the center of the structure except in neutral and cationic K@$Cd_{16}S_{16}$ structures which are too big to keep guest atom in the center of the cluster.

Looking at the calculated deformation energies in Table 4.2, it is interesting to note that these values are larger in the case of neutral

Table 4.2: Cavity within the Cluster (r_{cavity}), the distance of the guest atom with respect to the center of the cluster (R^{LM} for the stationary local minima; R^{dyn}_{range} and R^{dyn}_{av} : the range and average position in the dynamic simulation) in Å. The free energy of encapsulation, $\triangle G_{enc}$, and the deformation energy, $\triangle E_{def}$, in kcal/mol, the Charge of the endohedral Atom, q_x, and the Ionization Energies, in eV.

	r_{cavity}	R^{LM}	R^{dyn}_{range}	R^{dyn}_{av}	$\triangle G_{enc}$	$\triangle E_{def}$	q_x	IE
$K@Cd_9S_9$	2.41	0.00	0.00-0.62	0.23 (0.11)	-4.78	27.57	0.21	5.74
$K@Cd_{12}S_{12}$	2.83	0.00	0.00-0.67	0.30 (0.13)	-12.40	13.27	0.29	5.50
$K@Cd_{15}S_{15}$	3.29	0.00	0.00-1.39	0.66 (0.32)	-16.45	18.07	0.25	5.24
$K@Cd_{16}S_{16}$	3.40	1.77	0.05-1.17	0.70 (0.25)	-14.26	36.83	0.40	5.50
$(K@Cd_9S_9)^+$	2.35	0.00	0.00-0.44	0.19 (0.07)	23.80	21.23	0.38	
$(K@Cd_{12}S_{12})^+$	2.79	0.00	0.00-0.55	0.27 (0.12)	10.79	8.26	0.51	
$(K@Cd_{15}S_{15})^+$	3.26	0.00	0.00-1.15	0.52 (0.25)	0.60	18.16	0.52	
$(K@Cd_{16}S_{16})^+$	3.37	1.50	0.09-1.52	0.62 (0.28)	8.85	9.30	0.51	

compounds than in the cationic ones. These deformation energies are calculated with respect to the optimized bare neutral clusters, which have a closed-shell electronic structure. In the endohedrally doped neutral nanoclusters, however, there is a charge donation from the potassium to the cage, changing the electronic structure of the cluster, and increasing in this way the deformation energies. Meanwhile, in the cationic nanoclusters, the positive charge is mainly located at the dopant atom, so the deformation experienced by the clusters is smaller. In addition to this, endohedral K doping of the Cd_iS_i nanoclusters lowers the ionization energy from $\sim$ 7.8 eV to a value between 5.24 and 5.74 eV, which is similar to that of potassium atom and $K@Zn_iS_i$ nanoclusters.

The ab-initio Quantum Dynamics simulations of these compounds reveal that the trapped atom moves around the center of the nanocluster, as shown by the values of R^{dyn}_{range} and R^{dyn}_{av} given in Table 4.2. Since the dynamics of all compounds are similar, for discussion we focus on $K@Cd_{12}S_{12}$, and the information about the remaining compounds are given in the appendix (see 10). In Figure 4.3, it is observed that the total energy oscillates around the same value during the simulation time, and that the K atom moves around the center of the nanocluster all along the simulation. Therefore, these nanoclusters are predicted to be thermally stable enough to survive long enough time at room temperature as to allow for their experimental detection.

4.3.2.2 Cl@Cd_iS_i and Br@Cd_iS_i Endohedral Nanoclusters

Table 4.3 the geometric, electronic and energetic properties of the characterized local minima of the endohedral neutral and anionic $Cl@Cd_iS_i$ and $Br@Cd_iS_i$ endohedral nanoclusters are given. In addition, the R^{dyn}_{range} and R^{dyn}_{av} parameters, as representatives of the dynamics of the trapped atoms inside the nanocluster, are also shown.

Cl and Br can be trapped by Cd_iS_i (i=9, 12, 15, 16) nanoclusters, to yield neutral and anionic species. Observe that in all structures Cl and Br are negatively charged. Notice that q_x is predicted to be more negative for the anionic endohedral compounds. In the latter, the Coulombic attraction between the trapped halogen atom and the

Table 4.3: Cavity within the Cluster (r_{cavity}), the distance of the guest atom with respect to the center of the cluster R^{LM} for the stationary local minima; R^{dyn}_{range} and R^{dyn}_{av} : the range and average position in the dynamic simulation in Å. The free energy of encapsulation, ΔG_{enc}, and the deformation energy, $\triangle E_{def}$, in kcal/mol, the Charge of the endohedral Atom, q_x, and the Ionization Energies, in eV.

	r_{cavity}	R^{LM}	R^{dyn}_{range}	R^{dyn}_{av}	ΔG_{enc}	$\triangle E_{def}$	q_x	EA
$Cl@Cd_9S_9$	2.12	0.10	0.02-0.31	0.12 (0.05)	-31.53	14.35	-0.69	4.66
$Cl@Cd_{12}S_{12}$	2.57	0.33	0.03-0.66	0.30 (0.12)	-44.08	13.26	-0.60	5.11
$Cl@Cd_{15}S_{15}$	3.05	0.81	0.15-1.50	0.69 (0.30)	-47.33	18.51	-0.60	5.15
$Cl@Cd_{16}S_{16}$	3.18	1.11	0.59-1.59	1.08 (0.21)	-48.87	18.76	-0.61	4.96
$(Cl@Cd_9S_9)^-$	2.11	0.00	0.00-0.33	0.12 (0.05)	-53.20	5.12	-0.79	
$(Cl@Cd_{12}S_{12})^-$	2.56	0.00	0.00-39	0.20 (0.08)	-76.13	5.66	-0.75	
$(Cl@Cd_{15}S_{15})^-$	3.03	0.14	0.03-1.40	0.73 (0.28)	-80.14	10.10	-0.72	
$(Cl@Cd_{16}S_{16})^-$	3.17	1.02	0.52-1.48	1.05 (0.19)	-77.29	8.05	-0.70	
$Br@Cd_9S_9$	2.16	0.09	0.02-0.29	0.14 (0.06)	-7.42	14.43	-0.67	4.68
$Br@Cd_{12}S_{12}$	2.59	0.21	0.02-0.53	0.26 (0.10)	-31.64	11.84	-0.61	5.13
$Br@Cd_{15}S_{15}$	3.04	0.09	0.03-0.97	0.56 (0.21)	-33.76	21.30	-0.51	5.31
$Br@Cd_{16}S_{16}$	3.18	0.83	0.21-1.31	0.76 (0.21)	-39.17	18.11	-0.62	5.10
$(Br@Cd_9S_9)^-$	2.14	0.00	0.00-0.31	0.14 (0.06)	-32.45	6.46	-0.78	
$(Br@Cd_{12}S_{12})^-$	2.57	0.00	0.00-0.29	0.18 (0.06)	-67.13	4.87	-0.77	
$(Br@Cd_{15}S_{15})^-$	3.04	0.00	0.00-0.87	0.54 (0.20)	-73.36	8.22	-0.73	
$(Br@Cd_{16}S_{16})^-$	3.17	0.51	0.07-1.38	0.69 (0.22)	-73.80	6.23	-0.71	

Cd atoms increases. This affects noticeably the calculated encapsulation free energies, ΔG_{enc}, which are found to be negative in all cases, due to the attractive interactions, but are more negative for the anionic species, due to the larger Coulombic interaction. These compounds are predicted to be thermodynamically stable with respect to their corresponding separated compounds. Moreover, in both neutral and anionic compounds, free energy indicates the compounds are thermodynamically more stable as the size of the nanoclusters increases. This is due to a combination of two factors, namely, the better size fit of the halogen atoms inside the cavity and the larger Coulombic attraction between these and Cd atoms. These same arguments explain also why the cavity radii are contracted upon halogen encapsulation, and why this contraction is larger for large clusters. For these nanoclusters the halogen atoms lie at the center or near the center of the nanocluster, except for some of the Cl@Cd_iS_i nanoclusters and for Br@$Cd_{16}S_{16}$, which are too big nanoclusters as to keep guest atom at the center of their cavity. The charge of trapped atom decreases as the size of the nanocluster increases. For these elements, the anionic structures are more stable than neutral ones. In case of Cl and Br, the stability increases as the size of the cluster increases. Additionally, the calculated deformation energies have been found to be larger for the neutral compounds. In these nanoclusters, there is a charge transfer from the cage to the halogen, modifying the electronic closed-shell structure of the optimized bare neutral clusters. This fact entails big deformation energies, despite the nanoclusters retain their structural motif and do not break.

The ab-initio Quantum Dynamics simulations of these compounds reveal that the trapped atom moves around the center of the nanocluster, as observed by the inspection of the values of R^{dyn}_{range} and R^{dyn}_{av} given in Table 4.3. We focus on Cl@$Cd_{12}S_{12}$ as a representative of the halogen-trapped endohedral compounds. It can be observed in Figure 4.4, that the total energy oscillates slightly around the average value during the whole simulation time. A fact which is very supportive of the thermal stability of the endohedral nanostructures. As seen earlier for the potassium, the Cl atom moves around the center of the cluster. Consequently, these compounds are predicted to be stable enough as to survive long enough time for their experimental detection.

The calculated electron affinities of the halogen endohedral clus-

ters are substantially larger than those of the corresponding guest atoms; EA(Cl)= 3.62 eV; EA(Br)= 3.36 eV. Hence, these endohedral nanoclusters may be seen as superhalogens (53,54), similarly to those of ZnS nanoclusters. It has been observed for electron affinities that EA (Cd_iS_i) < EA (X) < EA (X@Cd_iS_i) and for ionization energies that IE (K) $\sim$ IE(K@Cd_iS_i) < IE (Cd_iS_i). The isolated Cd_iS_i nanoclusters have a closed shell electronic structure. When an alkali is trapped inside the cage, an electron is transferred to the lowest unoccupied molecular orbital (LUMO). This electron can more easily be removed than one from the highest occupied molecular orbital (HOMO) of the isolated cluster, decreasing the ionization potential. Similarly, when a halogen atom is trapped, it takes an electron from the surface, and now the HOMO orbital is singly occupied, therefore increasing the electron affinity with respect to the isolated cluster.

4.4 Conclusions

The geometrical structures, electronic and dynamic properties of the endohedral $(X@Cd_iS_i)^{0,\pm}_{i=9,12,15,16}$ nanoclusters, with X standing either for the Na, and K alkali elements or for the Cl and Br halogens, have been characterized by density functional theory and quantum molecular simulation calculations.

The stability of the resulting structures has been rationalized in terms of three parameters. The first is the appropriate matching between the size of the nanocluster, r_{cavity}, and the size of the trapped atom. The second is the shape of the nanocluster: the spherical nanoclusters are more prone to incarcerate atoms than the irregular ones. The third is the charge of the trapped atom: negatively charged guest atoms are found to be the thermodynamically most stable ones. Due to the larger cavity size inside Cd_iS_i nanoclusters, in comparison to Zn_iS_i nanoclusters, Na is too small to lead to stable X@Cd_iS_i compounds. This fact has been demonstrated by quantum dynamics calculations.

Encapsulation of halogen atoms results in endohedral nanoclusters with enhanced electron affinity relative to the guest halogen atom. These nanoclusters ought, therefore, to be considered as superhalogens in the same vein as the X@Zn_iS_i and the Al@Al_{12} nanoclusters [22], where recent research has confirmed its predicted high electron affinity of EA=3.20 eV as well as its ability to form salts with electropositive elements like potassium.[135] The Cl and Br endohedral

nanoclusters studied in this work have electron affinities substantially larger than Al@Al_{12}, namely, EA > 4.5 eV. Hence, they are expected to have a stronger superhalogen character which makes them suitable to form ionic cluster-assembled materials. Furthermore, the electron affinities of the halogen endohedral nanoclusters and the ionization energies of the alkali endohedral nanoclusters of Cd_iS_i are rather similar. This is an interesting property, since large IE/EA differences would yield substantial heat release during assembling that might destroy the assembled material as it is formed. Interestingly, X@Zn_iS_i compounds were seen to have similar properties, and recently have been shown to be able to build stable cluster-assembled materials [250].

Figure 4.3: Dynamics simulation of K@$Cd_{12}S_{12}$. Top: Dynamical trajectories of the K atom inside the nanocluster. This plot was prepared as follows. For each saved structure along the dynamics, the center of mass of the spheroid was set on the origin, and the coordinates of all atoms in the system referred to this center of mass. Then, the average position for each of the atoms of the spheroid along the dynamics was calculated and the corresponding average spheroid structure is the one shown in the figure. Finally, the blue line corresponds to the positions of the inner atom (K) with respect to the center of mass of the spheroid for each saved structure. Below, the variation of the energy, in eV (left) and the variation of the distance, R, in Å (right), of the trapped K atom from the center of mass of the nanocluster as a function of time. S atoms are drawn in yellow, while Cd atoms are drawn in gray.

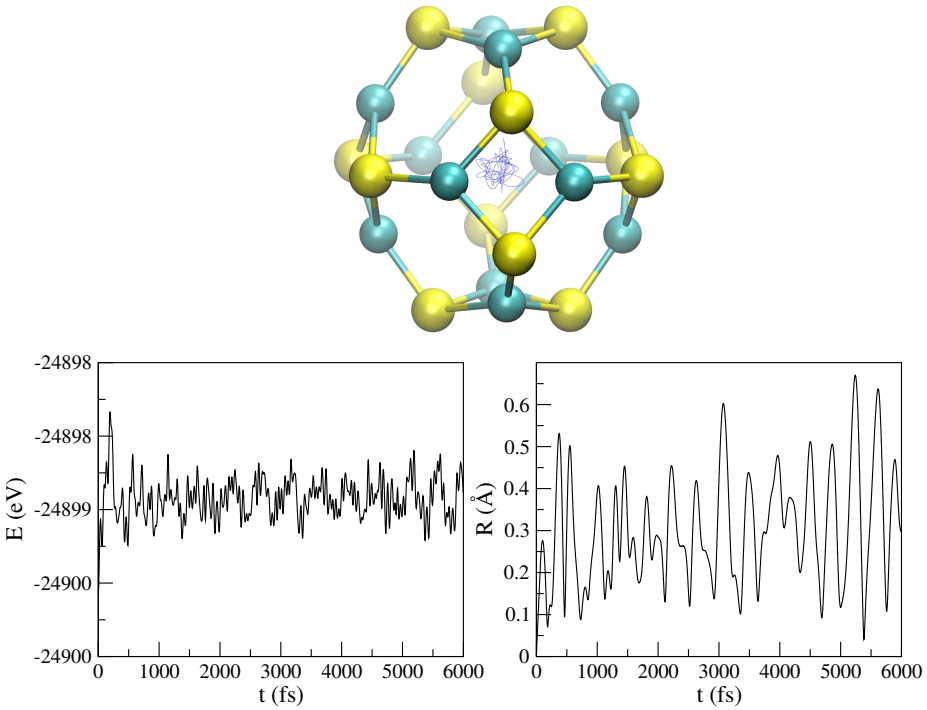

Figure 4.4: Dynamics simulation of $Cl@Cd_{12}S_{12}$. Top: Dynamical trajectories of the Cl atom inside the nanocluster. This plot was prepared as the $K@Cd_{12}S_{12}$ one. Below, the variation of the energy, in eV (left) and the variation of the distance, R, in Å (right), of the trapped Cl atom from the center of mass of the nanocluster as a function of time. S atoms are drawn in yellow, while Cd atoms are drawn in cyan.

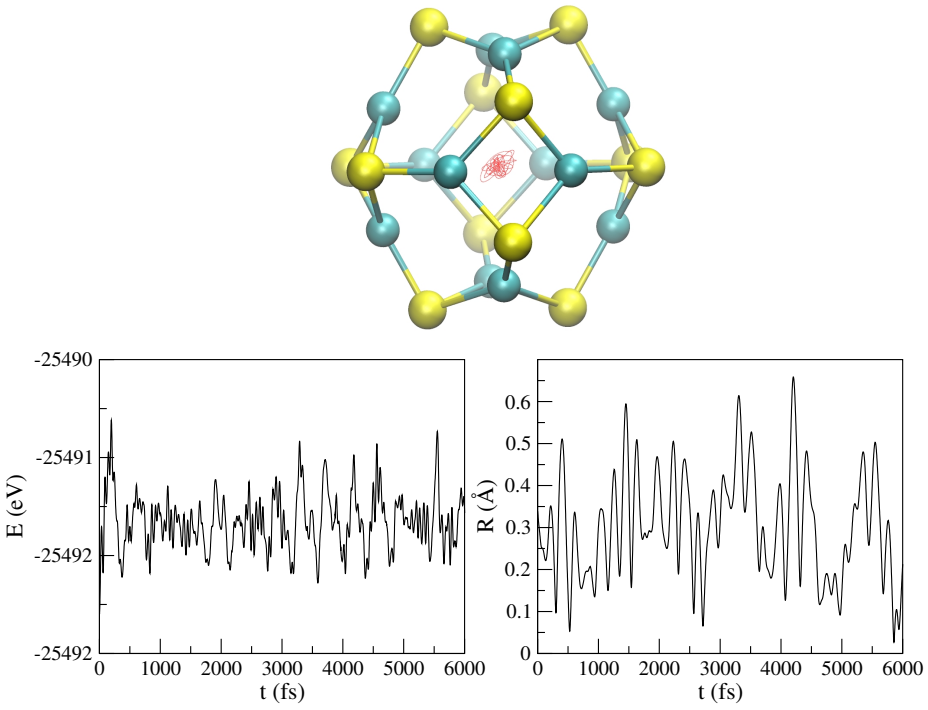

Chapter 5

CdS Nanoclusters Doped with Divalent Atoms

ZnS and CdS small nanoclusters have been predicted to trap alkali metals and halogen atoms. However would this kind of nanocompounds be able to encapsulate dianions and dications? This would be very interesting from an experimental point of view, since it would allow the isolation of such divalent ions. Moreover, the resulting endohedral complexes would serve as building blocks for new cluster-assembled materials, with enhanced stability arising from the electrostatic interaction between the incarcerated ions. In this work we have studied the structure and stability of $(X@(CdS)_i)^{\pm 2}$ with X= Be, Mg, Ca, O, S, Se and i= 9, 12, 15, 16 on the basis of Density Functional Theory and Quantum Molecular Dynamics simulations. Most of the nanoclusters are found to trap both chalcogen and alkaline earth atoms. Furthermore, the chalcogen doped clusters are calculated to be both thermodynamically and thermally stable. However, only a few of alkaline earth metal doped structures are predicted to be thermally stable. Therefore, the charge of the dopant atom appears to be crucial in the endohedral doping. Additionally, the absorption spectra of the title compounds have been simulated by means of TDDFT calculations. The calculated optical features show a blueshift with respect to the bulk CdS wurtzite. Furthermore, doping modifies notably the optical spectra of nanoclusters, as the absorption spectra shift to lower energies upon encapsulation.

5.1 Introduction

Since the discovery of carbon fullerene [4], C_{60}, almost 30 years ago, a large number of nanometric materials have been explored. Nanomaterials have gained fundamental and technological importance due to their novel structural, chemical, and physical properties, which usually differ from those of their bulk counterparts. The large surface-to-volume ratio inherent in nanostructures and the quantum confinement effects are responsible for the particular characteristics of nanosized materials. Additionally, it has been observed that the properties of nanocompounds can be tailored mainly by two parameters: size and doping. Size control is crucial to monitor and stabilize the desired property and much effort has been dedicated to this challenge [30]. On the other hand, spherical hollow nanoclusters provide the opportunity for the endohedral doping, namely, the placement of the dopant inside the cage. Thus, nanoclusters act as hosts encapsulating the dopant atoms.

The first endohedrally doped nanocluster synthesized was La@C_{60} [100]. Thereafter many other endohedral carbon fullerenes were obtained [251, 252, 253], the oxidation state of the endo atoms rationalized [254] and their electronic structure understood [255, 256, 257]. Furthermore, different endohedral metallofullerenes based on lanthanides and their derivatives have found applications in photovoltaic devices that feature greater efficiency than devices fabricated with empty fullerenes [258].

In addition to the carbon fullerenes, nanoclusters made of other elements have also been studied, along with their endohedrally doped counterparts. Si nanoclusters, which are isoelectronic with carbon fullerenes, were found to be unstable because of sp^2-like bonding [259]. Nevertheless, they can be stabilized by the endohedral doping [260, 261]. Other examples of endohedrally doped nanoclusters that have been widely studied are those of aluminum [262], gold [232], tin [122], lead [124] and germanium [263]. Furthermore, nanoclusters made of III-V elements have been doped endohedrally, giving rise to a modification of their properties. It has been shown, for instance, that doping nanoclusters with transition-metals confers them magnetic properties [264].

Regarding hollow binary nanoclusters of II-VI semiconductor elements, few studies on endohedral compounds have been reported.

Interesting examples are $(ZnS)_{i=4-16}$ and $(CdS)_{i=9,12,15,16}$ endohedrally doped with alkali metals and halogen atoms [134, 265]. These clusters were chosen because of their hollow spheroidal shape and most of the doped compounds were predicted to be metastable. It was observed that alkali metals transferred an electron to the cage, while halogen atoms took an electron from the cage leading to charged ions inside the clusters. Interestingly, encapsulation of halogen atoms resulted in endohedral nanoclusters with enhanced electron affinity relative to the guest halogen atom (4.5 eV compared to 3.5 eV). These nanoclusters ought, therefore, to be considered as "superhalogens" [266] in the same vein as the $Al@Al_{12}$ cluster [22].

Furthermore, these ZnS and CdS doped nanoclusters were used as building blocks for the formation of hypothetical cluster-assembled polymorphs [250, 267]. For comparison, solids built up with bare nanoclusters were also characterized and it was hypothesized that the doped solids were more stable. This stabilization is due to the electrostatic interaction between alkali and halogen atoms, along with the formation of inter-cluster covalent Zn-S and Cd-S bonds. The previous characterization and synthesis of these bare ZnS and CdS nanoclusters suggests that these theoretically characterized cluster-like compounds could be within experimental research in near future [85, 57, 83, 58].

However would this kind of nanoclusters be able to incarcerate dianions and dications? This would be very powerful from an experimental point of view, since it would allow the isolation of such divalent ions. Moreover, these endohedral nanoclusters would serve as building blocks for new cluster-assembled materials, with enhanced stability arising from the increased electrostatic interaction between encapsulated ions. Thus, the aim of this work is to check the capability of small CdS clusters to trap dianions and dications. Specifically, we have studied the structure and stability of $(X@(CdS)_i)^{\pm 2}$ with X= Be, Mg, Ca, O, S, Se and i= 9, 12, 15, 16 on the basis of Density Functional Theory and Quantum Molecular Dynamics simulations. Based on the latter, other competitive local minima conformations have also been checked for selected cases, with the dopant atoms placed in the surface of the clusters, i.e. exohedral structure. Additionally, we have simulated the absorption spectra of the title compounds by means of Time Dependent Density Functional Theory calculations. The calculated optical features show a blueshift with respect to the bulk CdS

wurtzite. Furthermore, it is worth mentioning that doping modifies notably the optical spectra of nanoclusters themselves, as the absorption spectra shift to lower energies upon encapsulation. Finally, the calculated optical properties of the endohedral compounds differ significantly from those of the exohedral isomers studied, and therefore they could serve experimentalists as fingerprints of such compounds for their detection.

From our results, the stability of the title endohedral compounds can be rationalized on the basis of three main parameters, as was found in other related studies [134, 265]. First, the appropriate matching between the nanocluster cavity (r_{cavity}), as defined in [134], and the size of the dopant atom have been calculated to favor the formation of the endohedral complex. Second, spherical clusters have been found to better accommodate the trapped atom at the center of the cage than irregular ones. Third, the charge of the encapsulated atom plays an important role on stabilizing the doped complexes. Negatively charged dopant atoms strongly interact with the Cd of the cluster, which lie closer to the center of the cage than the S atoms. Consistently, endohedral complexes with chalcogenide dianions are reported to be more stable than those doped with alkaline earth metal cations.

5.2 Methods

Recent validation studies have demonstrated that Density Functional Theory (DFT) is very reliable for the prediction of the geometrical, electronic and associated optical properties of II-VI nanoclusters [268].

Thus, in the present investigation all geometries, for both endohedrally and exohedrally doped nanoclusters, have been fully optimized using the gradient corrected hybrid B3LYP [243, 218, 219] functional within the Kohn-Sham framework [209] of Density Functional Theory [208] as implemented in the Gaussian09 software package [269]. Harmonic vibrational frequencies have been determined by analytical differentiation of gradients, in order to determine whether the stable structures found are true minima or not. Calculations are carried out at 298 K and 1 atmosphere. Finally, the optical properties of these compounds have been calculated by means of Time Dependent Density Functional Theory (TDDFT), at the same level of theory used for the ground state.

The relativistic compact effective core potentials and shared-exponent basis set [244] of Stevens *et al.* have been used for Cd and S, as in the study of the isolated clusters [83], and the all-electron 6-311+G(d) basis set was used for the trapped atom. The 4d electrons of Cd were included in the valence. In order to perform the geometry optimizations and harmonic frequency calculations an extra d function was added on Cd and S, due to its importance for the proper description of the high coordination of the atoms in the three-dimensional cluster structures. Note that pure angular momentum functions were used throughout this study. All the atomic charges are calculated from the trace of the atomic polar tensor.

To characterize the interaction between the CdS nanoclusters and the divalent ions, we have taken advantage of the energy decomposition analysis developed by Ziegler and Rauk [270, 271, 272] and implemented in the ADF software package [273]. Under this scheme, the instantaneous interaction energy $\triangle E_{int}$ comprises three terms, namely the Pauli repulsion $\triangle E_{Pauli}$, the electrostatic interaction $\triangle V_{elst}$, and the orbital interaction $\triangle E_{oi}$. $\triangle E_{Pauli}$ accounts for the destabilizing interaction between the occupied orbitals. $\triangle V_{elst}$ corresponds to the classical electrostatic interaction, and gives an idea of the ionicity of the bond. $\triangle E_{oi}$ includes the electron pair bonding, charge transfer, and polarization effects, and is related to the covalency of the interaction. For consistency with the rest of the calculations, bond decomposition analyses have been carried out by means of the B3LYP functional, in conjunction with DZ and TZP STO basis sets for cluster and dopant atoms, respectively.

In addition, and to shed light on the charge distribution of the endohedrally doped complexes, their radial electron density distributions have been calculated, following the procedure proposed by Sarasola *et al.* [274]. To do so, the origin of the coordinate system has been placed on position of the incarcerated atom's nucleus.

To further explore the thermal stability of the endohedral compounds, we also undertook ab-initio thermal Molecular Dynamics simulations at 300 K on the calculated local minima structures, controlled by means of the Nose thermostat as implemented in the SIESTA code [221] within DFT approach. Exchange and correlation effects were described by the revised Perdew-Burke-Ernzerhof (rPBE) [245, 246, 247] approximate generalized gradient (GGA) functional. Core electrons were replaced by Troullier-Martins norm-conserving pseudopotentials

[248] in the Kleinman-Bylander factorized form [249]. In the framework of SIESTA, the use of pseudopotentials imposes basis orbitals adapted to them. Furthermore, it employs a localized basis set to represent the Kohn-Sham orbitals for valence electrons. Accordingly, the basis set of atomic orbitals is constructed from numerical solutions of the atomic pseudopotential, and are constrained to be zero beyond a cutoff radius. We used a basis set of double-ζ plus polarization quality (DZP). A single parameter, orbital energy shift (ΔE_{PAO}), defines the confinement radii of different orbitals. With this basis set, SIESTA calculates the self-consistent potential on a grid in real space. The fineness of this grid is determined in terms of an energy cutoff (E_{Cutoff}) in analogy to the energy cutoff when the basis set involves plane waves. Taking into account previous experience [265], these two parameters were set to ΔE_{PAO}= 50 meV and E_{Cutoff}= 300 Ry. All these simulations were carried out for 6 ps with a chosen time step of 1 fs.

5.3 Results

We have considered all possible $(X@(CdS)_i)^{\pm 2}$ endohedral compounds with X= Be, Mg, Ca, O, S, Se and i= 9, 12, 15, 16. The lowest-lying isomers of bare $(CdS)_i$ nanoclusters (i= 9, 12, 15, 16) are known to be cage-like structures [83]. So, as starting point for the optimization, the guest atom (X= Be, Mg, Ca, O, S, Se) is placed at the center of the cavity. The thermodynamic stability of the minima will be assessed by the encapsulation free energy, $\triangle G_{enc}$, corresponding to the following reaction:

$$(CdS)_i + X^{\pm 2} \longrightarrow (X@(CdS)_i)^{\pm 2} \tag{5.1}$$

Accordingly, the more negative the encapsulation free energy, the more stable the endohedral complex. Additionally, we have calculated the deformation energy of the cluster, $\triangle E_{def}$, as the energy required to deform the cluster from its bare structure to the geometry in the endohedral complex:

$$\triangle E_{def} = E_{deform} - E_{opt} \tag{5.2}$$

where E_{deform} is the energy of the bare cluster with the final geometry upon the encapsulation and E_{opt} is the energy of the cluster with its

optimized bare geometry. Then, the thermal stability of these species has been checked by quantum molecular dynamics simulations. For some selected cases, the stability of the endohedral compounds compared to other isomers have also been studied.

In subsection 5.3.1 geometric and energetic features of $(X@(CdS)_i)^{-2}$ dianions (X= O, S and Se) will be shown. In subsection 5.3.2 the $(X@(CdS)_i)^{+2}$ dications (X= Be, Mg and Ca) will be discussed. Finally, in subsection 5.3.4 the optical properties of both dianion and dication structures will be analyzed.

5.3.1 Encapsulated Dianions

The resulting endohedral structures of chalcogen doped clusters are shown in Figure 5.1. Observe that most of them are highly symmetric and that the nanoclusters retain their structural motif after the encapsulation of the dopant atoms.

The geometrical and energetic features of these compounds are given in Table 5.1. All the characterized endohedral structures have negative encapsulation energies, namely, they are predicted to be thermodynamically stable towards the dissociation into X^{-2} and $(CdS)_i$. These encapsulation energies would decrease significantly from gas phase to solution. Indeed, for O trapped compounds, these encapsulation energies are lowered around 200 kcal/mol in solution. For instance, exploratory calculations reveal that for $(O@(CdS)_9)^{-2}$, the encapsulation energy decreases from -298 to -45 kcal/mol when implicit water is introduced by means of the PCM model [275]. Nevertheless, this difference does not alter qualitatively our conclusions, neither for O trapped compounds nor for the other cases. The deformation energies give an indication about how much the nanoclusters have been deformed upon the encapsulation. These energies reach maximum values for $(O@(CdS)_{15})^{-2}$ and $(O@(CdS)_{16})^{-2}$ because oxygen is the most electronegative atom so, it is the one that attracts most the surrounding cadmium atoms.

Regarding the cavity radii of the endohedral compounds, observe that all the nanoclusters are contracted after the chalcogen is trapped

Table 5.1: The symmetry of the molecule, encapsulation free energy, $\triangle G_{enc}$, and deformation energy, $\triangle E_{def}$, are given in kcal/mol. q_x stands for the charge of the dopant atom, and r_{cavity} the cavity within the cluster with the percentage of change with respect to the corresponding cavity radius of bare nanocluster in parenthesis (Å). The distance of the guest atom for the stationary local minima, R^{LM} , and the range position in the dynamics simulation, R^{dyn}_{range}.

	sym	$\triangle G_{enc}$	$\triangle E_{def}$	q_x	$r_{cavity}(\%\triangle)$	$r_{X^{-2}}$	R^{LM}	R^{dyn}_{range}
$(O@Cd_9S_9)^{-2}$	C_{3h}	-299.26	44.59	-1.16	1.87 (-13.0)	1.26	0.00	0.0-0.57
$(O@Cd_{12}S_{12})^{-2}$	C_1	-298.70	46.19	-1.03	2.55 (-3.8)	1.26	1.38	0.90-1.55
$(O@Cd_{15}S_{15})^{-2}$	C_s	-310.06	85.10	-1.04	2.86 (-8.9)	1.26	0.00	0.0-0.76
$(O@Cd_{16}S_{16})^{-2}$	C_1	-282.44	154.52	-1.08	2.96 (-9.5)	1.26	1.14	1.14-2.70
$(S@Cd_9S_9)^{-2}$	C_{3h}	-189.63	24.58	-1.16	2.00 (-6.8)	1.70	0.00	0.0-0.33
$(S@Cd_{12}S_{12})^{-2}$	C_1	-217.09	28.84	-1.26	2.44 (-7.9)	1.70	0.30	0.01-0.65
$(S@Cd_{15}S_{15})^{-2}$	C_s	-228.01	50.80	-1.06	3.05 (-2.9)	1.70	0.00	0.0-1.06
$(S@Cd_{16}S_{16})^{-2}$	C_{2v}	-215.21	39.25	-1.14	3.09 (-5.5)	1.70	1.28	0.77-1.56
$(Se@Cd_{12}S_{12})^{-2}$	T_h	-198.48	25.64	-1.28	2.45 (-7.9)	1.84	0.30	0.0-0.46
$(Se@Cd_{15}S_{15})^{-2}$	C_{3h}	-210.17	43.10	-1.07	2.93 (-6.7)	1.84	0.00	0.0-0.81
$(Se@Cd_{16}S_{16})^{-2}$	C_1	-201.52	36.52	-1.12	3.09 (-5.5)	1.84	1.09	0.56-1.31

Figure 5.1: Optimized structures of the chalcogen doped CdS nanoclusters. In red O atom, in orange Se atom, in yellow S atoms and cyan Cd atoms are depicted.

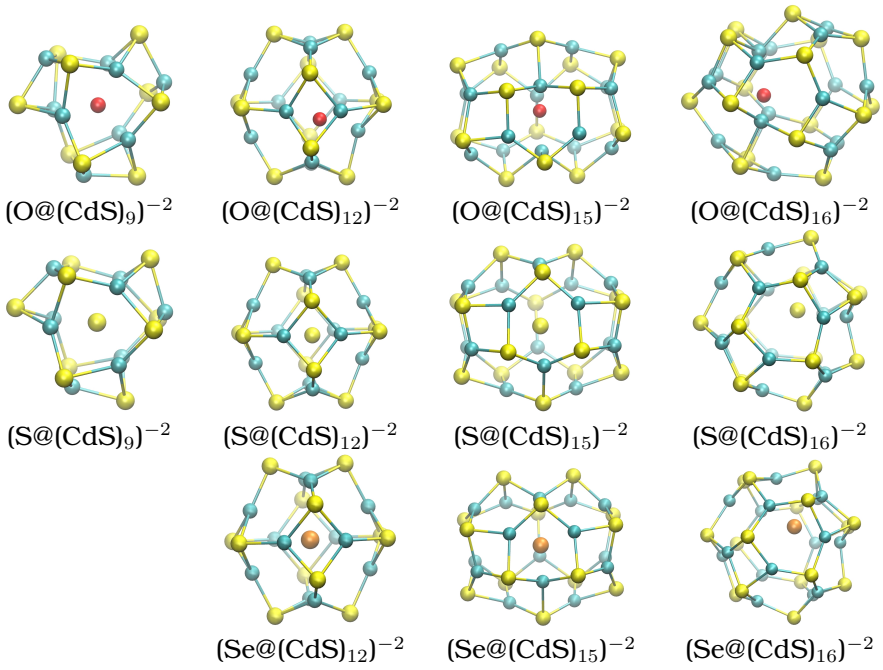

inside the nanocluster, due to the electrostatic interaction between X and Cd atoms. Indeed, this contraction is in general the largest when oxygen is encapsulated and the smallest when the trapped atom is selenium. Nevertheless, in all the compounds the nanoclusters retain their structural motif upon the encapsulation. Additionally, inspection of R^{LM}, the distance of the caged atom with respect to the center of the cavity in the stationary local minimum, reveals that in (X@(CdS)$_9$)$^{-2}$ and (X@(CdS)$_{15}$)$^{-2}$ structures the atoms lie at the center of the nanocluster. In the smallest nanocluster, (X@(CdS)$_9$)$^{-2}$, the reason is that the guest atoms do not have much mobility because of the small size of the structure. (X@(CdS)$_{15}$)$^{-2}$ however, is a very interesting case. Because of its "rugby ball" shape, the chalcogen has a bigger electrostatic interaction with the three closest cadmium atoms. As a consequence, it squeezes towards one end of the cluster. In fact, (X@(CdS)$_{15}$)$^{-2}$ are the most stable structures, with the largest encapsulation energies (in absolute values). This electrostatic attraction is particularly large in (O@(CdS)$_{15}$)$^{-2}$, where the three cadmium atoms approach significantly

to the oxygen.

In addition to this, R_{range}^{dyn} values shown in Table 5.1 are the maximum and minimum distances of the guest atoms from the center of the nanocluster during the molecular dynamics simulation. As expected, this range decreases with the size of the dopant atom, as it has less mobility, i. e, less space to move inside the cluster. The calculated atomic charges of the dopant atoms reveal that most of the negative charge is located at the chalcogen atoms, but part of the charge has moved to the cluster.

In order to unveil the charge distribution of the endohedral compounds, we have evaluated the radial electron density distribution D(r),

$$\mathrm{D(r)} = \sum_{i=1}^{N} \int d\Omega_r \psi_i^*(\mathbf{r})\psi_i(\mathbf{r}) \tag{5.3}$$

were $d\Omega_r$ denotes for the solid angle subtended by the position vector **r**, and $\{\psi_i\}_{i=1}^{N}$ are the Kohn-Sham orbitals. The radial electron density distribution functions for the $(O@(CdS)_i)^{-2}$ i=9, 12, 15, 16 clusters are shown in Figure 5.2. Observe that for all the cases considered the electron density distribution displays a minimum separating the electronic density of the guest atom and the host cluster. Moreover, the incarcerated O atoms display two spherical shells (see inset in Figure 5.2), as the free-standing atom does. These findings suggest the guest atoms retain their identity upon encapsulation. Furthermore, some conclusions can be drawn from the electron density distribution associated to the cluster. For $(O@(CdS)_9)^{2-}$, where the O atom stands in the center of the cluster, we observe two well-resolved maxima, arising the first and the second from the inner Cd atoms and outer S atoms, respectively. For $(O@(CdS)_{12})^{2-}$, the incarcerated atom moves apart from the center. As a consequence, the electron density distribution displays two bands, associated the first one to the cluster atoms close to the O and the second one to the Cd and S atoms far from O. For $(O@(CdS)_{15})^{2-}$, due to the elongated shape of the native cluster, the first peak is related to the closest Cd atoms whereas the second results from the cluster atoms far apart the O atom. Finally, the situation for $(O@(CdS)_{16})^{2-}$ is similar to that observed for $(O@(CdS)_{12})^{2-}$.

We must emphasize that we were able to characterize $(Se@(CdS)_9)^{-2}$ endohedrally doped nanocluster. However, after performing quantum

Figure 5.2: Electron density distribution, D(r), of the $(O@(CdS)_i)^{-2}$ (i = 9, 12, 15, 16) compounds, as a function of the radial distance, r, from guest atom's nucleus position. The inset at the upper left corner shows the detail of the region close to the origin.

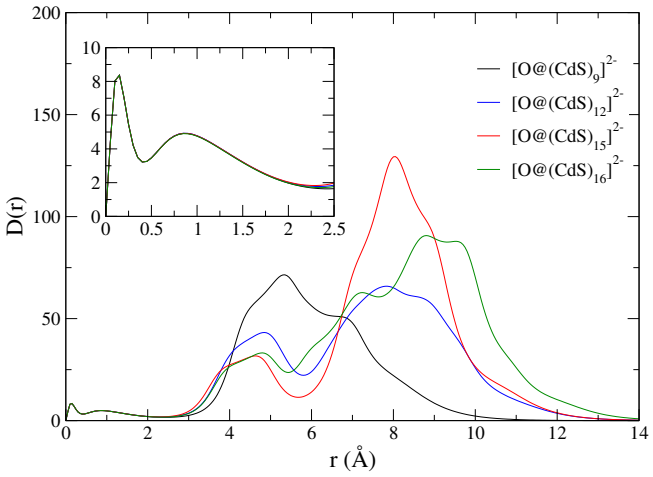

molecular dynamics simulations, it was found that selenium atom moves towards the surface of the nanocluster and finally the cluster breaks apart. So, this compounds is thermally unstable. Conversely, the remaining endohedral compounds were predicted to be thermally stable.

In Figure 5.3, two different cases are confronted. On the left the thermally unstable $(Se@(CdS)_9)^{-2}$ nanocluster and on the right the thermally stable $(O@(CdS)_9)^{-2}$ compound. Note that, in $(Se@(CdS)_9)^{-2}$ system, selenium atom goes from the center of the cage to its surface, giving rise to the break up of the nanocluster. This fact is reflected in the distance of the Se atom with respect to the center of the cavity plot, where it is shown that at about 3.45 ps this distance increases, leading to a more stable structure as it can be concluded from the energy picture, as at the same time the energy drops. This is due to the big size of Se^{-2} (the biggest chalcogen atom considered in this work) relative to the size of the $(CdS)_9$ cavity. In contrast, the picture of the trajectory of the oxygen in $(O@(CdS)_9)^{-2}$ compound, clearly shows that the guest atom moves near the center of the cavity, while the energy oscillates around the same value during all the simulation. $(O@(CdS)_9)^{-2}$ is cho-

sen as representative, since the rest of the endohedrally doped nanoclusters show a similar behavior. Therefore, CdS nanoclusters are able to trap dianions, keeping their identity at the same time. Moreover, these structures are predicted to be stable enough as to survive at room temperature and to allow for their experimental detection.

The electron detachment energies of the dianionic endohedral nanoclusters have been calculated, using the outer valence green function (OVGF) methodology. The calculated electron detachment energies give an indication about the stability of the dianions. All the calculated EDE_{OVGF} are around 2 eV, suggesting that these species are very stable towards electron detachment. Moreover, the large values, close to one, of the pole strengths obtained in the OVGF calculations suggest that the electron dissociation channels are one-electron processes.

5.3.2 Encapsulated Dications

Opposite to chalcogen doped nanoclusters only four alkaline earth metal endohedrally doped nanoclusters were predicted to be stable. Although more endohedral minima were obtained, only $(Be@(CdS)_{12})^{+2}$, $(Mg@(CdS)_{15})^{+2}$, $(Ca@(CdS)_{15})^{+2}$ and $(Ca@(CdS)_{16})^{+2}$ were found to be thermally stable as revealed by quantum molecular dynamics simulations. Anyhow, we must highlight that these structures were predicted to be the most stable ones in terms of encapsulation energies. However, solvent effects significantly lower these values, as occurred for encapsulated dianions. The resulting structures for the four stable endohedrally doped nanoclusters are shown in Figure 5.4. All the structures are highly symmetric and, as it is the case of chalcogen doped compounds, the nanoclusters maintain their structure. It is interesting to note that for the biggest nanocluster, $(CdS)_{16}$, only the biggest alkaline earth metal is encapsulated, while for the smallest metal, Be, only one of the smallest nanocluster is able to trap it, emphasizing size matching as one key factor in the stability of endohedral nanoclusters.

In Figure 5.5, the results of the molecular dynamics simulations are depicted for two selected cases: the first one is the thermally unstable $(Be@(CdS)_{16})^{+2}$ (left) and the second one the thermally stable $(Ca@(CdS)_{16})^{+2}$ (right) endohedral compound. In the former it is ob-

Figure 5.3: Quantum molecular dynamics simulations of $(Se@(CdS)_9)^{-2}$ (left column) and $(O@(CdS)_9)^{-2}$ (right column) nanoclusters. Top panels display the trajectory of the trapped atom; middle panels the distance of the dopant atom with respect to the center of the nanocluster along the dynamics; and bottom panels the energy of the system during the simulation time. In the E vs t plots, the zero of the energy scale has been set to the energy of the most stable structure along the dynamics.

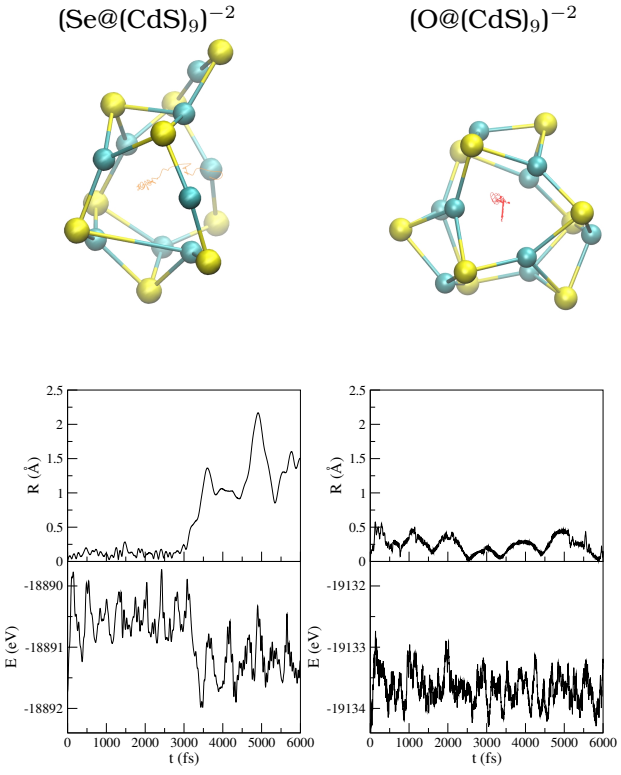

served that, although beryllium is located at the center of the cavity at the beginning of the simulation, it goes towards the surface at 1.0 ps approximately, breaking its structure, which coincides with the energy drop, since it leads to a more stable isomer. $(Ca@(CdS)_{16})^{+2}$, however, shows a radically different behavior: during all the simulation calcium atom moves around the center of the structure, while the energy of the system oscillates around the same value. This is indicative of its thermal stability.

In Table 5.2 the geometric and energetic features of the characterized $(X@(CdS)_i)^{+2}$ dications (X= Be, Mg and Ca) are shown. The small number of stable alkaline earth metal doped nanoclusters clearly sug-

gests that the charge of the dopant atom is a critical factor for the endohedral doping. Indeed, the encapsulation energies reveal that the larger the charge of the dopant atom, the less stable the endohedral structure is.

Figure 5.4: Optimized structures of the alkaline earth metal doped CdS nanoclusters. In light purple Be atom, in blue Mg atom, in deep purple Ca atom, in yellow S atoms and cyan Cd atoms are depicted.

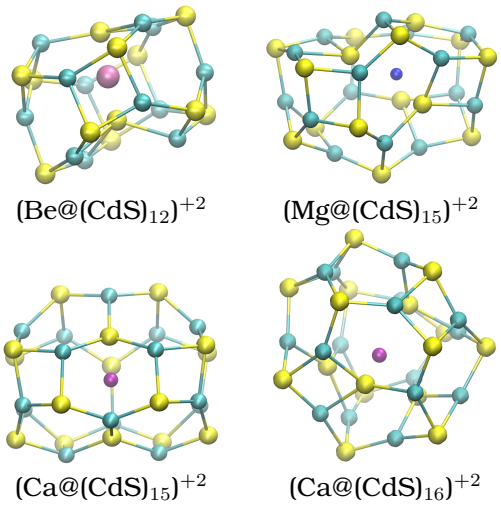

Being the alkaline earth metals positively charged, the cavity radii are increased due to the electrostatic repulsion with the cadmium atoms. However, this increase is slightly smaller than the decrease of the cavity radii shown in dianionic nanoclusters. At the same time, the deformation energies now are bigger. To rationalize this fact, we have to take into account that cadmium atoms are closer to the center of the cluster than sulfur atoms. Thus, in the dianionic structures, Cd atoms approach to the chalcogen atoms while, in the dicationic compounds, besides cadmium atoms move away from the center, sulfur atoms approach to it. This fact entails big deformation energies, despite the nanoclusters retain their structural motif and do not break.

Looking at R^{LM} and R^{dyn}_{range} values shown in Table 5.2, we can conclude, as in the case of dianions, that this range decreases with the

Table 5.2: The symmetry of the molecule, encapsulation free energy, $\triangle G_{enc}$, and deformation energy, $\triangle E_{def}$, are given in kcal/mol. q_x stands for the charge of the dopant atom, and r_{cavity} the cavity within the cluster with the percentage of change with respect to the corresponding cavity radius of bare nanocluster in parenthesis (Å). The distance of the guest atom for the stationary local minima, R^{LM}, and the range position in the dynamics simulation, R^{dyn}_{range}.

	Sym	$\triangle G_{enc}$	$\triangle E_{def}$	q_x	$r_{cavity}(\%\triangle)$	R^{LM}	R^{dyn}_{range}
$(Be@(CdS)_{12})^{+2}$	C_1	-340.11	75.20	0.47	2.78 (+4.9)	0.68	0.68-2.20
$(Mg@(CdS)_{15})^{+2}$	C_1	-245.26	71.07	0.71	3.20 (+3.2)	0.96	0.0-1.34
$(Ca@(CdS)_{15})^{+2}$	C_s	-138.10	46.00	0.93	3.30 (+5.1)	0.00	0.0-1.24
$(Ca@(CdS)_{16})^{+2}$	C_s	-194.56	107.79	0.84	3.29 (+0.6)	0.47	0.23-0.90

size of the dopant atom, as it has less mobility. Finally, we have seen with the radial electron density, that the alkaline earth metals preserve their identity, with a marked minimum between its electronic density and the density of the nanoparticle atoms.

Figure 5.5: Quantum molecular dynamics simulations of $(Be@(CdS)_{16})^{+2}$ (left column) and $(Ca@(CdS)_{16})^{+2}$ (right column) nanoclusters. Top panels display the trajectory of the trapped atom; middle panels the distance of the dopant atom with respect to the center of the nanocluster along the dynamics; and bottom panels the energy of the system during the simulation time. In the E vs t plots, the zero of the energy scale has been set to the energy of the most stable structure along the dynamics.

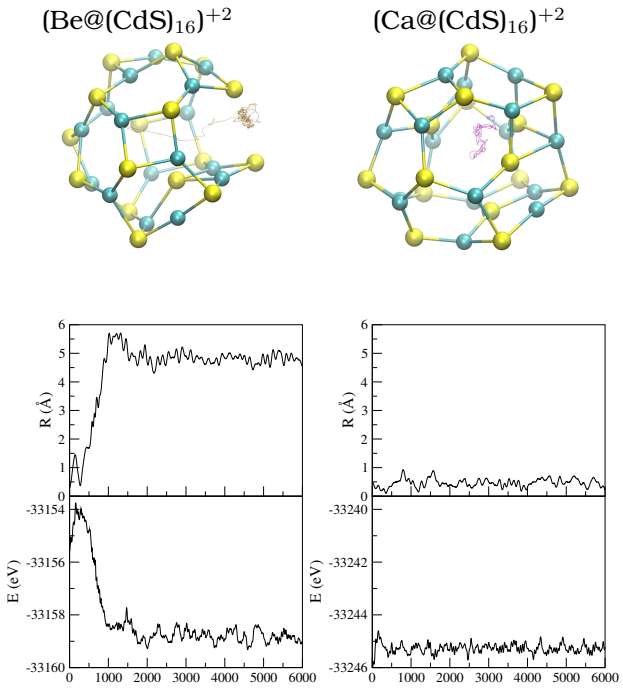

5.3.3 Dianions vs Dications

For completeness, further analysis has been carried out for two selected cases that are taken as representative: $(S@(CdS)_{12})^{-2}$ and $(Be@(CdS)_{12})^{+2}$. On the one hand, we have compared the stability of endohedral compounds towards other isomers. For $(S@(CdS)_{12})^{-2}$, S was placed at different positions in the surface of the cluster, and

outside the cluster. All attempts to locate different minina eventually ended either on the encapsulated structure, or on two other structures with the S located at the surface (exohedral isomers), which were energetically unfavored by 23.89 (see Fig. 5.6) and 60.49 kcal/mol, respectively. These results suggest the higher stabilization of S^{-2} dianion at the center of the cage structure, which, on the other hand, can be expected due to the fact that positively charged Cd atoms are located in the inner part of the surface. For the case of $(Be@(CdS)_{12})^{+2}$, conversely, different isomers calculated for $(Be@(CdS)_{12})^{+2}$ structures show that the exohedral Be-$(CdS)_{12}$ compound is thermodynamically favored by 37.25 kcal/mol, see Figure 5.6. Note that this could be expected, since to achieve the more favorable Be-S interaction instead of Be-Cd (recall that cadmium atoms are in the inner part of the cluster), the cage is highly deformed, destabilizing the system. Therefore, although thermally stable, these cationic endohedral compounds should be considered as labile metastable structures.

Figure 5.6: Optimized structures of the exohedral $(S(CdS)_{12})^{-2}$ and $(Be(CdS)_{12})^{2}$ nanoclusters. In light purple Be atom, in yellow S atoms and cyan Cd atoms are depicted.

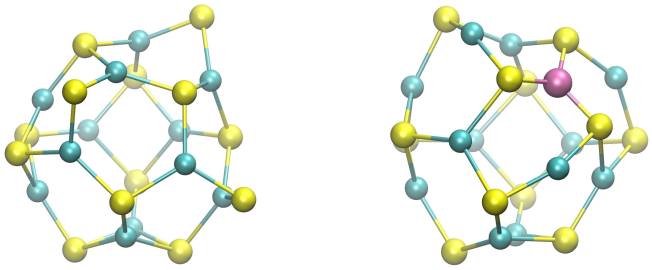

$(S(CdS)_{12})^{-2}$ $(Be(CdS)_{12})^{+2}$

On the other hand, to deepen in the interaction between the CdS nanoclusters and the encapsulated ions, energy decomposition analyses have been performed. Calculations show that for $(S@(CdS)_{12})^{-2}$, the interaction is electrostatically driven, with the electrostatic contribution, $\triangle V_{elst}$, comprising the 75% of the attractive interaction. In fact, as one may notice from Figure 5.1, the S atom is placed close to the center of the $(CdS)_{12}$ and no directional bonds are formed with the Cd atoms in the cage. In the most stable of the exohedral compounds, the interaction is still electrostatic, but to a lesser extent, $\triangle V_{elst}$ cov-

ering the 54% of the attraction. Consistently, the S atom donates as much as 1.36 *e* to the $(CdS)_{12}$ cluster, *vs* 0.84 *e* in the endohedral compound, meaning that charge transfer and polarization effects are more important in the exohedral isomer. Regarding $(Be@(CdS)_{12})^{+2}$, the bond seems to be mainly covalent, with the orbital term, $\triangle E_{oi}$, covering the 79% of the attraction. Indeed, the Be atom forms directional bonds with two S atoms on the $(CdS)_{12}$ surface, see Figure 5.4, and accepts 1.59 *e* from the cage. As found for the endohedral isomer, the orbital terms dominate the interaction between the $(CdS)_{12}$ and the Be atom in the exohedral structure, $\triangle E_{oi}$ comprising the 76% of the interaction. Accordingly, the cation is predicted to accept 1.55 *e* from the cage.

5.3.4 Optical Properties

Due to their singular optical properties of II-VI nanomaterials, UV-Vis spectroscopy is often used to characterize them. The absorption signatures are determined by the size, the shape, and the particular atomic arrangements adopted by the nanostructure. Accordingly, the optical spectrum usually serves as its unique fingerprint. Furthermore, doping is known to modify the electronic levels of the nanocluster, and to introduce new states that could contribute to the absorption bands. The optical properties of bare and ligated II-VI nanoclusters have attracted a great deal of theoretical research over the last years. However, the works regarding the role of doping are scarcer. Aimed at filling this gap, we have simulated the absorption spectra of the title compounds by means of TDDFT calculations.

Figure 5.7 shows the calculated UV-Vis spectra of the bare clusters, obtained by a Gaussian convolution of the 20 lowest singlet electronic transitions. $(CdS)_9$ appears to be the cluster with the lowest optical gap (the lowest electronic excitation with non-zero oscillator strength), with a calculated value of 2.78 eV. For $(CdS)_{12}$, $(CdS)_{15}$, and $(CdS)_{16}$ the absorption onsets locate at 3.24, 3.03, and 3.21 eV respectively. Our numbers reveal an oscillatory pattern of the lowest-lying electronic excitations with the increasing size of the cluster. Although the absorption onsets do not match with the maxima of the TDDFT spectra, the same oscillatory pattern is observed in both cases, and

Figure 5.7: TDDFT absorption spectra of the bare $(CdS)_i$ (i = 9, 12, 15, 16) clusters, drawn by a Gaussian convolution of the lowest 20 singlet excited states with FWHM 3000 cm^{-1}.

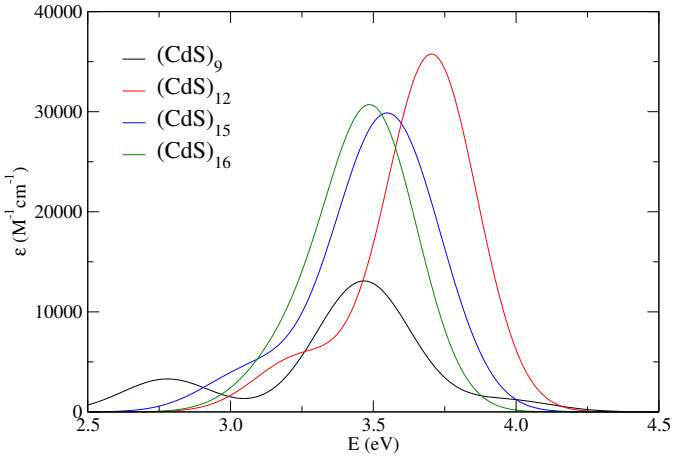

it has already been reported experimentally for II-VI molecular clusters [276, 277, 278]. From quantum confinement considerations, one might expect a blueshift of the absorption features with the decreasing size of the model. In the ultrasmall size regime considered here, however, the properties change discontinuously with cluster dimensions.

Figure 5.8 displays the Density of States (DOS) of the bare $(CdS)_i$ (i = 9, 12, 15, 16) clusters. Their calculated band-gaps values are between 3.33 and 3.63 eV, whereas the band-gap of the bulk CdS wurtzite is 2.42 eV [279], thus showing the expected blueshift. Regarding the composition of the band edges, the higher-lying occupied states arise from the S 3p orbitals, whereas the lowest-lying unoccupied states are comprised primarily of Cd 5s orbitals. The LUMO of the bare clusters, despite having the same nature of the higher lying orbitals, is quite separated in energy from the rest of the conduction band states [280, 281, 282]. The LUMO+1 has been calculated to locate ca. 0.9 eV higher than the LUMO, irrespective of the model. On the contrary, the highest occupied orbitals are densely packed at the edge of the valence band for $(CdS)_{12}$, $(CdS)_{15}$, and $(CdS)_{16}$, as it is evident from the curvature of the DOS. Accordingly, the electronic excitations computed imply transitions from these states to the LUMO,

Figure 5.8: Density of states (DOS) of the bare $(CdS)_i$ (i = 9, 12, 15, 16) clusters, drawn by a Gaussian convolution of FWHM 0.5 eV of the individual Kohn-Sham orbitals (vertical bars).

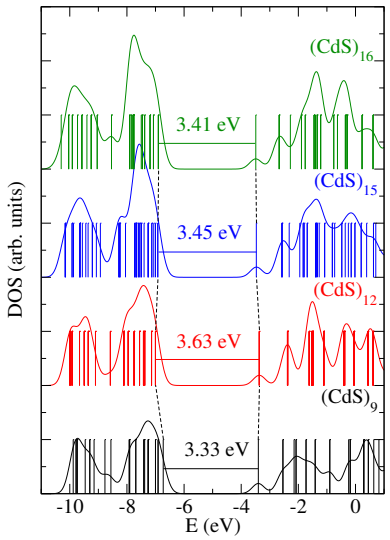

with small contribution from higher lying unoccupied orbitals (see 11). Since photogenerated holes are known to cool rapidly towards the edge of the valence band [283], $(CdS)_{12}$,$(CdS)_{15}$, and $(CdS)_{16}$ are predicted to exhibit narrow emission bands, associated to the LUMO→HOMO transition. The picture is slightly different in $(CdS)_9$, for which a less dense valence band edge is found. As a consequence, the orbitals above the LUMO are predicted to contribute to the lowest-lying electronic excitations. This fact is due to the stronger molecular nature of the smallest cluster.

Doping modifies notably the optical spectra of nanoclusters (see 11). Except for the endohedrally doped $(CdS)_9$ models, the absorption spectra shift to lower energies upon encapsulation. Besides, the intensity of the optical features decreases. To explain the origin of these spectral changes, the electronic structure of the O-doped clusters have been chosen as a case of study and have been examined in detail, see Figure 5.9. Note that the incarceration of the oxygen atom destabilizes both the valence and conduction band edges by ca. 0.6 eV relative to the bare clusters. Recently, surface ligands have been predicted to produce a similar effect [282]. The shift of the band

Figure 5.9: Density of States (DOS, in black) of the O-doped $[O@(CdS)_i]^{-2}$ (i = 9, 12, 15, 16) clusters, drawn by a Gaussian convolution of FWHM 0.5 eV of the individual Kohn-Sham orbitals (grey vertical bars). The contribution of the O orbitals to the DOS and the Kohn-Sham orbitals is highlighted in red. The DOS projected into the O orbitals has been enlarged 5 times to make it visible on the scale of the total DOS.

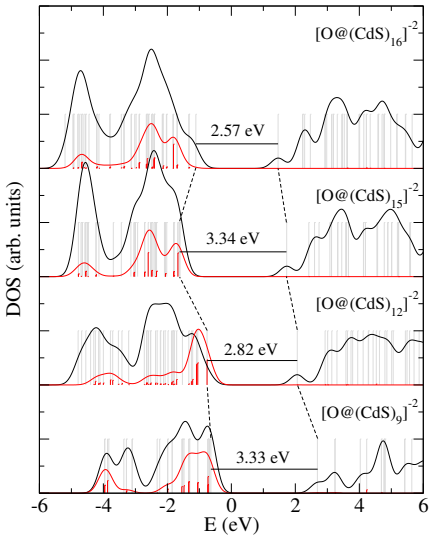

edges leaves the band-gap of $(CdS)_9$ almost unchanged. On the contrary, for $(CdS)_{12}$,$(CdS)_{15}$, and $(CdS)_{16}$ the HOMO-LUMO gap shrinks notably. As observed for the bare species, the occupied states appear densely packed at the top of the occupied band, whereas the LUMO lies separated from the unoccupied orbitals. To unveil the origin of the band edge states, their projection into the O orbitals has been calculated. As it is evident from Figure 5.9, the O 2p orbitals intrude in the dense manifold of the S 3p orbitals. The resulting states are hybridized in nature, i.e. no pure dopant states have been observed close the band-gap. The HOMO of the $[O@(CdS)_{12}]^{-2}$ complex is the orbital most localized on the dopant, with a contribution of 46.2% from the encapsulated O. On the other hand, the role of the dopant to the unoccupied states is marginal. As found for the bare clusters, the TDDFT excitations comprise transitions from the HOMOs mainly to the LUMO. Dopant atom contributes to the occupied orbitals involved in the lowest-lying excitations. Due to their delocalized character, these states overlap notably with the LUMO and the electronic transitions among them are optically allowed.

In order to compare the effect of the exohedral and endohedral doping, the DOS of both endohedral and exohedral isomers of sulfur and beryllium $(S@(CdS)_{12})^{-2}$ and $(Be@(CdS)_{12})^{+2}$ doped clusters have been analyzed (see Fig. 5.10). Interestingly, the position of the dopant seems to determine the electronic structure of the complex. For the exohedral $[S(CdS)_{12}]^{-2}$ compound, for example, the dopant states are spread between -6 and 0 eV, with no contribution greater than 20%. For the endohedral isomer, instead, the dopant concentrates on the highest-lying HOMO, HOMO-1, and HOMO-2 orbitals, with contributions of ca. 50%. Relative to the O-doped compound, the dopant states in the endohedral $[S@(CdS)_{12}]^{-2}$ complex lie closer to the band-gap, in line with the lower ionization potential of S as compared to O. The endohedral and exohedral isomers of $[Be(CdS)_{12}]^{+2}$ have also been considered. Irrespective of the isomer, and opposed to dianions, the encapsulation of dications stabilizes the valence and the conduction band edges. Moreover, dications mainly contributes to the unoccupied states. As found for $[S@(CdS)_{12}]^{-2}$, the dopant states lie closer to the band-gap in the endohedral isomer than in the exohedral compound. These results can be explained in terms of guest-host interaction. Indeed, this interaction is much stronger in the exohedral compounds, since the dopant atom is directly linked with the cage. In the endohe-

Figure 5.10: Density of States (DOS, in black) of the endohedral and exohedral isomers of S- and Be-doped $(CdS)_{12}$ clusters, drawn by a Gaussian convolution of FWHM 0.5 eV of the individual Kohn-Sham orbitals (grey vertical bars). The contribution of the O orbitals to the DOS and the Kohn-Sham orbitals is highlighted in red. The DOS projected into the O orbitals has been enlarged 5 times to make it visible on the scale of the total DOS.

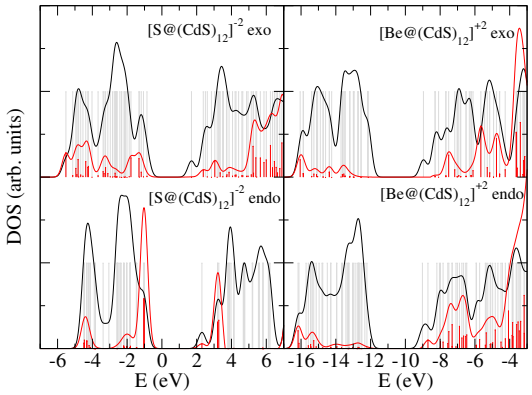

dral structures, conversely, the caged atom interacts weakly with the cluster. As a consequence, the dopant states of the endohedral isomers preserve their atomic-like nature, while in the exohedral isomers they appear mixed with the cluster states due to the strong interactions on the surface.

5.4 Conclusions

We have studied the structure and stability of $(X@(CdS)_i)^{\pm 2}$ with X= Be, Mg, Ca, O, S, Se and i= 9, 12, 15, 16 on the basis of DFT and Quantum Molecular Dynamics simulations. Most of the nanoclusters are found to trap both chalcogen and alkaline earth atoms. Moreover, the chalcogen doped clusters are found to be both, thermodynamically and thermally stable. However, only a few of alkaline earth metals doped structures are predicted to be thermally stable. The fact that all the studied chalcogen doped nanoclusters (except $(Se@(CdS)_9)^{-2}$) are stable and just a few alkaline earth doped ones they are, clearly suggests that the charge of the dopant atom is a fundamental factor for the endohedral doping. It should be remarked that while the endohe-

dral dianionic compounds appear to be the global minima structures, dicationic compounds should be considered as metastable structures. The size of the caged atom related with the size of the nanocluster is an important parameter too. Nevertheless, for the predicted stable compounds, it is confirmed that the dopant atoms keep their identity.

Additionally, we have simulated the absorption spectra of the title compounds by means of Time Dependent Density Functional Theory calculations. The calculated band-gaps show a blueshift with respect to the bulk CdS wurtzite. Furthermore, doping modifies notably the optical spectra of nanoclusters, as the absorption spectra shift to lower energies upon encapsulation. The experimental synthesis of these species are beyond the scope of this work. However, the fact that some of the endohedral compounds are more stable than their surface doped counterparts suggests that synthesizing such structures in the gas phase might be feasible. The calculated optical properties of the endohedral compounds differ significantly from those of the exohedral isomers studied, and therefore they could serve experimentalists as fingerprints of such compounds for their detection.

Chapter 6

Self-assembling Endohedrally Doped CdS Nanoclusters: New Porous Solid Phases of CdS

Hollow CdS nanoclusters were predicted to trap alkali metals and halogen atoms inside their cavity. Furthermore, the electron affinities (EA) of endohedrally halogen doped clusters and the potential ionizations (IE) of the endohedrally alkali doped clusters were predicted to be very similar. This makes them suitable to build cluster-assembled materials, in the same vein as do related ZnO, ZnS and MgO nanoclusters, which yield porous solid materials. With this aim in mind, we have focused on the assembling of bare Cd_iS_i and endohedral $K@Cd_iS_i$-$X@Cd_iS_i$ (i=12, 16, X= Cl, Br) clusters in order to obtain solids with tailored semiconducting and structural properties. Since these hollow nanoclusters posses square and hexagonal faces, three different orientations have to be considered. Namely, edge-to-edge (E-E) square-to-square (S-S) and hexagon-to-hexagon (H-H). These three orientations lead to distinct zeolite-like nanoporous bulk CdS solid phases denoted as SOD, LTA and FAU. These solids are low-density crystalline nanoporous materials that might be useful in a wide range of applications ranging from molecular sieves for heterogeneous catalysis to gas storage templates.

6.1 Introduction

Novel classes of solid materials with nanoclusters as building blocks [284] can be nowadays synthesized due to recent experimental advances that allow the production of nanoclusters of a given size and composition [152]. This fact has developed a new research concept that consists in the fabrication of nanocluster-assembled materials. The success of this assembling depends on the capability of the nanoclusters to retain their structure in the assembled material. In this vein, it is notable that the less prone to collapse nanoclusters are those with closed electronic shells. Fullerite crystals [285, 286], made of hollow spherical C_{60} structures, are a good example.

Consequently, hollow (pseudo) spherical nanoclusters are receiving much attention, not only because their resemblance to C_{60}, but also because they can trap atoms and molecules inside their cavity and thus offer a new way of controlling the properties of the resulting nanocluster by endohedral doping. The first such endohedrally doped cluster was La@C_{60}, which was discovered by Heath *et al.* in 1985 [100]; since then many other carbon fullerene endohedral clusters have been characterized [229, 231]. Endohedral hollow clusters of elemental metals, such as M@Au_n cages [287, 288, 289, 232], endohedrally doped plumbaspherene TM@Pb_{12} cages [290], and endohedrally doped stannaspherene TM@Sn_{12}^{-} cages, which have been seen to exist in gas phase for a large number of transition-metals (TMs) [121], have also been synthesized. Additionally, neutral Mn@Sn_{12} endohedral compound has been predicted to be stable enough as to allow the formation of its corresponding dimer, which yields an antiferromagnetic coupling of the two Mn^{+2} quintet endohedral cations [122].

Binary hollow nanoclusters of semiconductor elements, such as Group II–VI elements, have also been investigated [291, 85, 81, 78, 292, 98, 82, 99, 83, 57, 58]. Likewise, the assembly of this kind of clusters has been studied in the last years. For instance, Carrasco *et al.* predicted new low-density solid phases via assembling $(MO)_{12}$ clusters (M= Mg, Zn) [168]. These structures resemble that of LTA, FAU and SOD zeolite, following the framework notation of the corresponding silicate topologies [169]. Furthermore, Woodley *et al.* constructed cubic nano- and microporous ZnO frameworks from octahedral bubble clusters. The frameworks were constructed by arranging the clusters by corner sharing and, in some cases, with ordered vacancies

[293]. They also considered more dense frameworks by of edge and face sharing the octahedral clusters. Additionally, Wang found using first-principles calculations a metastable solid-phase sodalite structure via coalescence of $(ZnO)_{12}$ cages [172]. Zwijnenburg *et al.* showed that for MX compounds (AgI, ZnO, ZnS, CdS, GaN, GaP and SiC) exists a dense spectrum of as yet undiscovered polymorphs, the majority of which lie only moderately higher in energy than the experimentally observed phases [294]. Moreover, they explored the chemical and structural analogy between nanoporous zeolites and co-substituted binary MX materials (primarily on ZnO derived compounds), finding a numerous low-energy structures [295]. In addition to this, a theoretical study of the assembling of $M_{12}N_{12}$ (M= Al, Ga) nanoclusters by either square or hexagonal faces, giving rise to cubic or rhombohedral nanoporous phases was reported by Yong *et al.*. They found both phases to be wide-gap semiconductors, being the rhombohedral one energetically more favorable [167]. In a later work, they investigated $Zn_{12}O_{12}$-assembled material by attaching $Zn_{12}O_{12}$ cage on hexagonal face, which brings about a new three dimensional ZnO phase with a rhombohedral lattice framework [171]. Finally, the 1-D condensed clusters $(Cd_nS_n)_m$, where n= 1-4 and m= 1-9 were modeled and it was observed that $(Cd_3S_3)_m$ frameworks are energetically more stable as compared with other-sized condensed clusters.

In this vein, the use of endohedral compounds made of these hollow semiconducting nanoclusters as building blocks broaden the horizon of possibilities of obtaining new solids with the desired properties. In previous works we hypothesized the existence of endohedrally doped, both neutral and charged, $X@Zn_iS_i$ compounds (i=4–16; X=Cl, Br, Na, K) [134], and that concretely the $X@Zn_{12}S_{12}$ compounds could form metastable fcc-like cluster-assembled solids [250]. These structures resemble that of LTA zeolite, where the clusters were linked together by their squares. The so formed nanoporous solids were metastable, having band-gaps decreased with respect to their corresponding most stable bulk solid phases by the effect of doping.

In this work we have dealt with the assembling of previously characterized $X@Cd_iS_i$, i=12,16 nanoclusters, (see chapter 4) [265]. These clusters were chosen due to their high stability and high symmetry, which ensures that (i) the stability of the cluster structures themselves are not compromised by the endohedral doping and (ii) a larger variety of properties can be tailored by such doping. Consequently, one could

think of using these bare and doped nanoclusters as building blocks to synthesize stable solids, in the same vein as the other related solids mentioned previously. Specifically, we have considered CdS nanoclusters doped with alkali metals and halogens: K@Cd_iS_i-X@Cd_iS_i (i=12, 16, X= Cl, Br). It should be pointed out the fact that the electron affinities of halogen doped clusters and the potential ionization of the alkali doped clusters are very similar, and even higher than the EA and IP of the corresponding halogen and alkali atoms [265]. Indeed, the encapsulated potassium atom donates an electron to the cage, while the encapsulated halogen atom removes an electron from the cage, which leads to clusters with ions inside the cage. This makes them suitable to form ionic-cluster-assembled materials, in a similar way to the X@$Zn_{12}S_{12}$-Y@$Zn_{12}S_{12}$ (X= Na, K; Y= Cl, Br) case, studied earlier by Matxain *et al.* [250].

The assembling modes considered in this work are the ones resembling the three zeolites mentioned above, FAU, SOD and LTA. The structure of the nanoclusters make it possible, since they are composed of squares and hexagons, three different orientations forming the three zeolite like nanoporous bulk CdS phases: hexagon to hexagon (H-H), square to square (S-S) and edge to edge (E-E), which are related to the FAU, LTA and SOD structures, respectively. First, the dimers formed in such ways have been studied, and then these dimer structures are taken as unit cells for the calculations of the proposed solids.

6.2 Methods

To calculate the interaction energies for the cluster dimers, bare cluster monomer geometries [83] and doped monomer geometries [265] were used. These geometries were fully optimized by the gradient-corrected hybrid B3LYP [243, 296, 219] functional within the Kohn-Sham implementation [209] of density functional theory [208]. Harmonic vibrational frequencies were calculated by analytical differentiation of gradients to determine whether the structures found are true minima and to extract zero-point and thermal corrections for the energies. The relativistic compact effective core potentials and shared-exponent basis set of Stevens *et al.* (SKBJ) [244] were used for Zn and S as described in the study of the isolated clusters [83], and the all-electron 6-311+G(d) basis set for the trapped atoms. Notice that pure

angular momentum functions were used throughout this study. All geometry optimizations and frequency calculations were carried out by using the Gaussian 09 package [269]. All the atomic charges are calculated from the trace of the atomic polar tensor.

Molecular solids composed of both bare and endohedrally doped $Cd_{12}S_{12}$ and $Cd_{16}S_{16}$ clusters were explored by DFT calculations performed by using the SIESTA computer code [221]. Exchange and correlation effects were described by using the generalized gradient approximation (GGA), within the revised Perdew-Burke-Ernzerhof (rPBE) functional [245, 247]. Core electrons were replaced by Troullier-Martins norm-conserving pseudopotentials [248] in the Kleinman-Bylander factorized form [249]. The use of pseudopotentials, as implemented in SIESTA, imposes basis set orbitals adapted to them. Furthermore, SIESTA employs a localized basis set to represent the Kohn–Sham orbitals for valence electrons. Accordingly, the basis set of atomic orbitals is constructed from numerical solutions of the atomic pseudopotential, and are constrained to be zero beyond a cutoff radius. We chose a basis set of double-ζ plus polarization (DZP) quality. The single parameter (orbital energy shift) that defines the confinement radii of different orbitals was $\triangle E_{PAO}$=50 meV, which gives a rather good precision within the accuracy of the GGA functional used. With this basis set, SIESTA calculates the self-consistent potential on a grid in real space. The fineness of this grid is determined in terms of an energy cutoff, in analogy to the energy cutoff when the basis set involves plane waves. In our calculations, we used an equivalent plane wave cutoff energy of 300 Ry. In all cases, the geometry was relaxed until the maximum forces were smaller than 0.04 eVÅ^{-1}. For the solid-state calculations, we have used 18 K points. Both the intra- and intercell parameters have been optimized. The combination of these two methodologies, one for dimers and another one for solids, has been previously proven to be reliable [297, 250].

Finally, in order to check the thermal stability of the characterized solids, ab-initio molecular dynamics simulations were performed at 300 K on the calculated local minima structures, controlled by means of the Nose thermostat as implemented in the SIESTA code [221]. Furthermore, for few selected cases, molecular dynamics simulations were done at 350 and 400 K. All these simulations were carried out for 10 ps with a chosen time step of 1 fs.

6.3 Results

The unit cells of the characterized solids are chosen to be the dimers of the nanoclusters, to ensure the formation of the favorable Cd-S interactions between nanoclusters, in opposition to less favorable Cd-Cd or S-S interactions. Thus, first of all we have characterized the dimers: Cd_iS_i and K@Cd_iS_i-X@Cd_iS_i (i=12, 16, X= Cl, Br). Then, the solids have been constructed by using the optimum dimer structures as starting geometries for the unit cells.

In the subsection 6.3.1 the optimized structures, calculated interaction energies, charges and HOMO-LUMO gaps of both bare and endohedrally doped dimers are discussed. Next, in the subsection 6.3.2, we will focus on the properties of the characterized solids, including band gaps and cohesive energies.

6.3.1 Dimers

The lowest-energy minima for the isolated $Cd_{12}S_{12}$ cluster was found to be composed of eight hexagons and six squares, having T_h symmetry [83, 57]. On the other hand, the lowest-energy minima for $Cd_{16}S_{16}$ is composed of twelve hexagons and six squares and its point group is T_d [83, 57]. This structural pattern and symmetry is not altered after endohedral doping [265]. Therefore, these structures have been chosen as the basis to build up the dimers under study. As these clusters are composed of hexagons and squares, they can be linked together in three different ways: (i) by bonding monomers via hexagonal faces (ii) square-square interfacial bonding (iii) via edge to edge interactions. The resulting dimers are shown in Figure 6.1 for K@Cd_iS_i-Br@Cd_iS_i. The symmetry group corresponding to each case is given in Table 6.1. All bare dimers are highly symmetrical. However, in several of the doped dimers the symmetry is broken due to the fact that the electrostatic interactions force the caged ions to move out the center of the nanoclusters. Nevertheless, the main structural patterns of the monomers are unaffected by dimerization, proving the high stability of $Cd_{12}S_{12}$ and $Cd_{16}S_{16}$ nanoclusters which, henceforth, makes them suitable candidates for assembling into solids.

Figure 6.1: Above $K@Cd_{12}S_{12}$-$Br@Cd_{12}S_{12}$ linked together by their edges, squares and hexagons respectively are shown. Below $K@Cd_{16}S_{16}$-$Br@Cd_{16}S_{16}$ linked together by their edges, squares and hexagons respectively are shown. In blue K atom, in red Br atom, in yellow S atoms and cyan Cd atoms, are depicted.

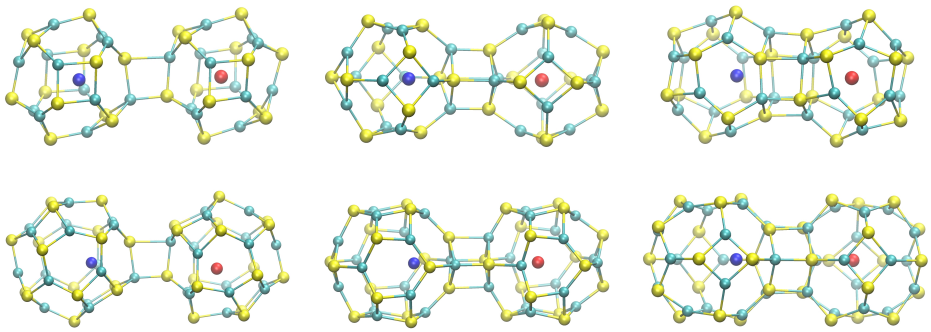

In Table 6.1 the charges of potassium and halogen atoms, the dimerization energies and the HOMO-LUMO energy gaps are shown. The distance between the encapsulated potassium and halogen atoms, R, has been measured to characterize the optimum geometry of the dimers and is also given in Table 6.1. In the case of bare dimers, R is the distance between the centers of mass of the two monomers. Observe that, in bare dimers, as the number of covalent bonds between the monomers decreases from H-H dimers to E-E ones, R increases, as expected. Additionally, after doping, R decreases even more due to the long range electrostatic interaction between the encapsulated K and halogen atoms. This fact is reflected in the charges of guest atoms. To explain it, we have to take into account that the potential ionizations of potassium doped nanoclusters and the electron affinities of halogen doped ones are very similar [265]. Consequently, this leads to a formal charge transfer from the potassium to the halogen, resulting in a cation and an anion trapped in two hollow neutral Cd_iS_i clusters. Notice that this decrease of R after doping is larger in the H-H and S-S cases ($\sim$ 1Å) than in the E-E case ($\sim$ 0.5Å). H-H and S-S dimers form an "empty" zone in the line connecting the trapped atoms, while the E-E dimers have intra-cluster covalent bonds, just on this line, which repel the trapped atoms and prevent them to move closer.

The dimerization energies were calculated with respect to the isolated neutral components of each dimer, in both bare and doped cases.

All the dimers have negative dimerization energies. This means that all of them are predicted to be thermodynamically stable. In all bare and doped dimers, there is a trend in the stability: the stability decreases from dimers linked by hexagons to dimers linked by edges. Namely, the stability decreases when the number of bonds between monomers decreases too. Comparing the dimerization energies of $Cd_{12}S_{12}$ and $Cd_{16}S_{16}$ reveals that they are very similar. So, we can conclude that the size is not a determinant factor for the thermodynamic stability. Finally, it must be highlighted that the overall stability increases after doping.

When analyzing the HOMO-LUMO gaps, we have kept in mind that DFT tends to underestimate these values. However, inspection of the HOMO-LUMO gaps shown in Table 6.1 clearly shows that the endohedral doping significantly reduces the gap. The largest decrease takes place for the E-E dimers (1-1.5 eV), while the lowest decrease occurs for the H-H dimers ($\sim$0.6 eV). The dopant effect is also larger for the $Cd_{12}S_{12}$ compounds. This effect is very similar for different halogen dopants; Cl and Br have similar effects.

6.3.2 Solids

In this subsection the properties of the characterized bare Cd_iS_i-Cd_iS_i and doped K@Cd_iS_i-X@Cd_iS_i (i=12, 16, X= Cl, Br) solids are discussed. These solids have been characterized by using the optimum dimer structures as starting geometries for the unit cells. As these clusters are composed of hexagons and squares, they can be assembled in different ways, H-H, S-S and E-E. Thus, we have constructed three new crystalline phases of CdS to form zeolite like nanoporous bulk phases which are depicted in Figure 6.2: (i) FAU-CdS (based on H-H dimers) (ii) LTA-CdS (based on S-S dimers) and (iii) SOD-CdS (based on E-E dimers).

Table 6.1: Different bare and doped $Cd_{12}S_{12}$ and $Cd_{16}S_{16}$ built dimers. R is the distance between the center of mass of both monomers, in the case of bare dimers, and between the encapsulated potassium atom and the corresponding halogen atom, in the case of doped dimers, and are given in Å. q_K and q_X are the charges of potassium and halogen atoms respectively and Symm stands for the symmetry group of each structure. Finally, E_{dim} is the dimerization energy, and $\triangle\varepsilon_{HL}$ is the HOMO-LUMO energy gap, both given in eV.

Dimer	R	q_K	q_X	Symm	E_{dim}	$\triangle\varepsilon_{HL}$
$Cd_{12}S_{12}$ (H-H)	8.77	-	-	S_6	-1.66	3.32
$Cd_{12}S_{12}$ (S-S)	9.82	-	-	C_{2V}	-1.26	3.43
$Cd_{12}S_{12}$ (E-E)	10.26	-	-	C_S	-0.92	3.45
K@$Cd_{12}S_{12}$-Cl@$Cd_{12}S_{12}$ (H-H)	7.75	0.49	-0.76	C_3	-4.44	2.74
K@$Cd_{12}S_{12}$-Br@$Cd_{12}S_{12}$(H-H)	7.67	0.49	-0.78	C_3	-4.49	2.76
K@$Cd_{12}S_{12}$-Cl@$Cd_{12}S_{12}$(S-S)	8.78	0.51	-0.79	C_1	-3.69	2.44
K@$Cd_{12}S_{12}$-Br@$Cd_{12}S_{12}$(S-S)	8.86	0.51	-0.81	C_1	-3.71	2.42
K@$Cd_{12}S_{12}$-Cl@$Cd_{12}S_{12}$(E-E)	9.65	0.52	-0.80	C_1	-2.94	2.00
K@$Cd_{12}S_{12}$-Br@$Cd_{12}S_{12}$(E-E)	9.58	0.52	-0.82	C_1	-2.97	1.98
$Cd_{16}S_{16}$ (H-H)	10.34	-	-	C_{2H}	-1.65	3.25
$Cd_{16}S_{16}$(S-S)	11.16	-	-	D_{2D}	-1.51	3.33
$Cd_{16}S_{16}$(E-E)	11.48	-	-	C_{2H}	-0.76	3.31
K@$Cd_{16}S_{16}$-Cl@$Cd_{16}S_{16}$(H-H)	8.14	0.51	-0.72	C_1	-4.69	2.65
K@$Cd_{16}S_{16}$-Br@$Cd_{16}S_{16}$(H-H)	8.28	0.51	-0.73	C_S	-4.64	2.63
K@$Cd_{16}S_{16}$-Cl@$Cd_{16}S_{16}$(S-S)	9.17	0.54	-0.73	C_S	-3.97	2.23
K@$Cd_{16}S_{16}$-Br@$Cd_{16}S_{16}$(S-S)	9.19	0.54	-0.75	C_S	-3.95	2.26
K@$Cd_{16}S_{16}$-Cl@$Cd_{16}S_{16}$(E-E)	9.44	0.51	-0.78	C_1	-3.09	2.29
K@$Cd_{16}S_{16}$-Br@$Cd_{16}S_{16}$(E-E)	9.60	0.52	-0.78	C_1	-3.06	2.12

Figure 6.2: Above, assembled SOD, LTA and FAU structures using $K@Cd_{12}S_{12}$-$Br@Cd_{12}S_{12}$ dimers as unit cells, and below SOD, LTA and FAU structures using $K@Cd_{16}S_{16}$-$Br@Cd_{16}S_{16}$ as unit cells are shown. In blue K atom, in red Br atom, in yellow S atoms and cyan Cd atoms, are depicted.

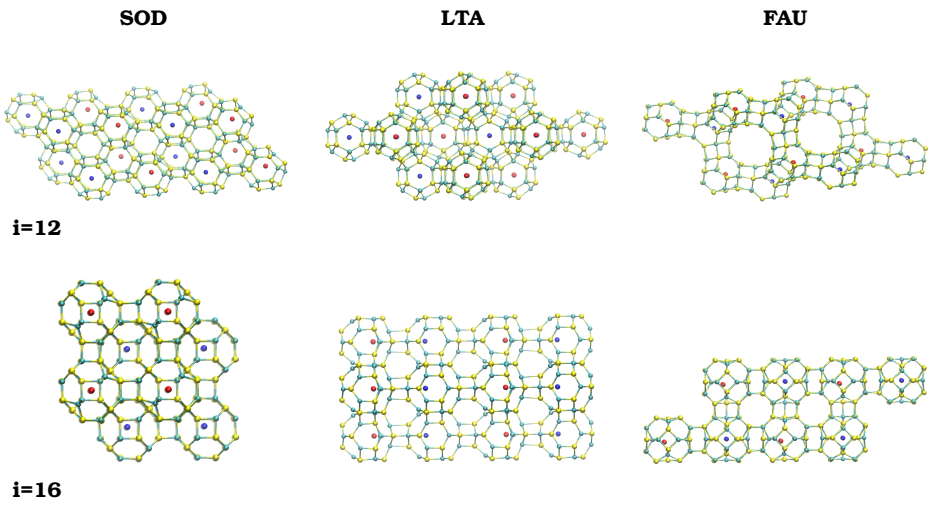

In Table 6.2 the lattice parameters (a, b and c), the distance between the encapsulated atoms (R) and the volume of the unit cell [V (Å^3)] are given along with the cohesive energies [E_{coh}(eV)] and the band gaps calculated at Γ points [$\triangle_\Gamma$ (eV)] of the characterized solids. For the calculation of the cohesive energy, the following thermodynamic cycle has been used:

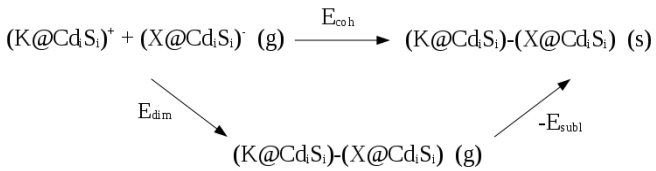

Thus, the cohesive energy is calculated as the sum of the dimerization energy minus the sublimation energy. Notice that in calculating wurtzite cohesive energy, 4 Cd-S bonds are broken per atom, while in all SOD, LTA and FAU structures, 24 Cd-S bonds are broken to yield isolated nanoclusters. Therefore, the ratio is 1/6. So, in order to be comparable the cohesive energies of our structures with the cohesive energy corresponding to bulk CdS wurtzite, the obtained values must be divided by six.

Looking at the cohesive energies given in Table 6.2, it can be observed that, after doping, all solids become thermodynamically more stable, increasing their cohesive energies with respect to their corresponding bare structures. This stabilization due to the doping is also observed in the dimers. However, in the latter the less stable structure (dimers linked by edges) becomes in solid phase the most stable and vice-versa. To rationalize this fact, the reader has to take into consideration an important factor present in the solid structure and not in the dimer: the compactness. The unit cell volume provides an illustration. In the case of solids made of $Cd_{12}S_{12}$, FAU phase is the less compact structure (the largest volume), while SOD is the most compact one (smaller volume). In the case of $Cd_{16}S_{16}$, the order is slightly different: LTA phase is the less compact structure (the largest volume), and SOD is the most compact one (smaller volume). Note that, opposite to $Cd_{12}S_{12}$ solid phases, in all the $Cd_{16}S_{16}$ solid phases there are square-square contacts due to the symmetry of the monomer. In conclusion, in all cases the SOD phase has the largest cohesive energy, being the thermodynamically most stable solid. In fact, the cohesive energy of CdS in the zincblende structure is -2.44 eV [298]; similar to that are SOD doped phases. In addition, it should be noted that SOD structure has the smallest porous, which is directly linked to the cell volume.

Lattice parameters for all calculated solids are shown in Table 6.2. Note that the more compact the structure is, the smaller these parameters are, as expected, and that doping does not affect them significantly. These cell parameters corresponds to bond lengths of around 2.7 Å between cells, which indicates covalent CdS bonds between cells. In the case of LTA and FAU $Cd_{12}S_{12}$ solids, each potassium atom is surrounded by halogens and vice-versa. This yields more spherical cluster moieties in the solids than in the dimers, due to the neighbor effects (in all directions in the solid and in only one in the dimer). Concomitantly, in these solids the dopant ions sit at the center of their corresponding clusters, hence R values for the solids match with the distances between the centers of mass of two adjacent clusters, in opposite to the dimers. However, in the case of SOD $Cd_{12}S_{12}$ phase, each cation is surrounded by anions in 2 directions while in the third direction has cations too on each side and vice-versa. The same happens in the FAU $Cd_{16}S_{16}$ structure. Finally, in SOD and LTA $Cd_{16}S_{16}$ phases,

Table 6.2: Different solids from bare and doped $Cd_{12}S_{12}$ and $Cd_{16}S_{16}$ dimers. R is the distance between the center of mass of each monomer in the case of bare solids, and encapsulated potassium atom and the corresponding halogen atom (Å) for doped solids. V is the volume of the unit cell in $Å^3$. a, b and c are the lattice constants in Å, E_{coh} is the cohesive energy in eV, and the band gaps calculated at Γ point ($\triangle_\Gamma$ in eV).

Unit Cell	R	V	a	b	c	E_{coh}	$\triangle_\Gamma$
FAU-$Cd_{12}S_{12}$	9.26	2324.90	15.04			-1.13	1.67
LTA-$Cd_{12}S_{12}$	9.98	2028.18	14.38			-1.55	1.66
SOD-$Cd_{12}S_{12}$	10.80	1662.51	10.78	21.58		-1.63	1.31
FAU-K@$Cd_{12}S_{12}$-Cl@$Cd_{12}S_{12}$	8.95	2272.52	15.23			-1.65	1.63
FAU-K@$Cd_{12}S_{12}$-Br@$Cd_{12}S_{12}$	9.12	2325.56	15.18			-1.64	1.65
LTA-K@$Cd_{12}S_{12}$-Cl@$Cd_{12}S_{12}$	10.05	2031.61	14.41			-2.00	1.22
LTA-K@$Cd_{12}S_{12}$-Br@$Cd_{12}S_{12}$	10.04	2030.51	14.41			-2.02	1.33
SOD-K@$Cd_{12}S_{12}$-Cl@$Cd_{12}S_{12}$	10.62	1664.62	10.81	21.71		-2.42	1.22
SOD-K@$Cd_{12}S_{12}$-Br@$Cd_{12}S_{12}$	10.90	1661.02	10.77	21.57		-2.43	1.28
FAU-$Cd_{16}S_{16}$	10.86	2588.88	21.76	11.35	15.17	-1.48	1.56
LTA-$Cd_{16}S_{16}$	11.34	2912.21	11.32	22.71		-1.19	1.76
SOD-$Cd_{16}S_{16}$	12.23	2261.21	10.92	18.95		-1.69	1.21
FAU-K@$Cd_{16}S_{16}$-Cl@$Cd_{16}S_{16}$	11.12	2605.10	21.90	11.27	15.29	-2.01	1.52
FAU-K@$Cd_{16}S_{16}$-Br@$Cd_{16}S_{16}$	10.68	2605.73	21.89	11.27	15.34	-2.02	1.52
LTA-K@$Cd_{16}S_{16}$-Cl@$Cd_{16}S_{16}$	11.51	2944.10	11.31	23.01		-1.59	1.32
LTA-K@$Cd_{16}S_{16}$-Br@$Cd_{16}S_{16}$	11.46	2958.16	11.35	22.96		-1.64	1.43
SOD-K@$Cd_{16}S_{16}$-Cl@$Cd_{16}S_{16}$	12.21	2250.04	10.90	18.95		-1.98	0.05
SOD-K@$Cd_{16}S_{16}$-Br@$Cd_{16}S_{16}$	12.23	2270.40	10.96	18.89		-2.15	1.06

cations are surrounded by anions only in one direction, having other cations in the other two. Consequently, the guest atoms are not in the centers of the nanoclusters, but close to them. For these cases, R values shown in Table 6.2 are calculated as the average of all the distances between each potassium to the closest halogens.

The analysis of the band gaps at the Γ point shows that our calculations predict all the solids to be semiconductors. Moreover, the band-gaps highly decrease when doping the solids. This can be understood looking at Figure 6.3, where bare, KCl and KBr LTA-$Cd_{12}S_{12}$ phases are plotted respectively. Observe that some of the dopants occupy bands which are located between the valence and the conduction bands. In all cases, SOD structure is the phase with the smallest band-gap because it has the most compact crystalline structure. This fact is specially marked for SOD-K@$Cd_{16}S_{16}$-Cl@$Cd_{16}S_{16}$, which band-gap is almost zero. As found earlier [83, 250], the valence band of the bare solid is made mainly by the 3p atomic orbitals of the sulfur atoms and the largest contribution to the conduction band comes from the 5s orbitals of the cadmium atoms. Moreover, the bandwidths of the conduction bands of the doped solids (0.6 eV) are similar to that of the bare solid and they also come from the 5s atomic orbitals of the Cd atoms. However, the valence band of the doped solid arises from the valence atomic orbitals of the encapsulated halogen atoms, which nearly interact with the 5s orbitals of the cadmium atoms. This results in substantially decreased bandwidths for the doped solids and a concomitant reduction in the band gap.

Figure 6.3: Band structures of the calculated LTA $Cd_{12}S_{12}$, K@$Cd_{12}S_{12}$-Cl@$Cd_{12}S_{12}$ and K@$Cd_{12}S_{12}$-Br@$Cd_{12}S_{12}$ solids. The occupied bands are depicted with continuous lines and the unoccupied bands with dotted lines.

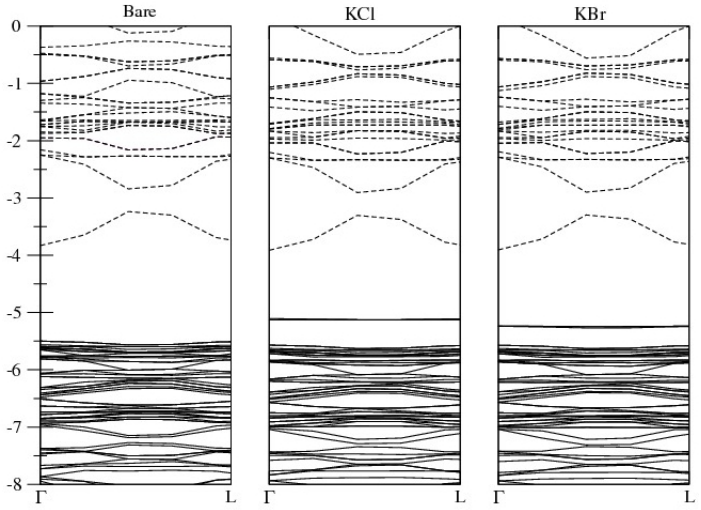

Finally, it should be pointed out that the characterized structures in this work are not the most stable phases of CdS. These structures are much less dense than the more stable structures found in nature, namely wurtzite and zincblende, in fact, these new phases reported here can be regarded as metastable phases of CdS. This can be seen looking at Figure 6.4, where the cohesive energies of the characterized solids are depicted as a function of cell volume. Note that in these structures we have set the same number of atoms in the unit cell for each plot, so the calculations with wurtzite have been carried out on an extended unit cell. For the sake of brevity, we have plotted only bare structures.

For $Cd_{12}S_{12}$, SOD phase is predicted to be almost as stable as wurtzite, but at larger unit cell volume, or, equivalently, at smaller pressure conditions. It is very interesting to relate once again the compactness (volume) of these phases with their thermodynamical stability. As seen in Table 6.2, the most compact phase is the most stable one. In this vein, wurtzite is the most compact solid, followed by SOD, LTA and FAU phases for $Cd_{12}S_{12}$ compounds. Nonetheless it is worth

mentioning that the energy difference between wurtzite and SOD is only 0.66 eV, while the difference between wurtzite and FAU is 4.74 eV.

In the case of $Cd_{16}S_{16}$, we found that the new phases characterized in this work are predicted to be metastable too. Likewise, the order in the stability is now slightly different, being LTA the least stable phase. Nonetheless, it is clear from Figure 6.4 that the energy differences are much larger with respect to wurtzite (wurtzite - SOD = 6.35 eV; wurtzite - LTA = 9.43 eV). One reason for this may be the symmetry of the monomer: as mentioned before, differently to $Cd_{12}S_{12}$-build phases, in all the $Cd_{16}S_{16}$-build solids there are square-square contacts which turns out to decrease the cohesive energies with respect to the wurtzite structures.

It is also remarkable the fact that, while there is a clear energy barrier for the transition between wurtzite and SOD phase occur, it seems that there is not any energetic barrier between LTA and FAU phases. Consequently, FAU-$Cd_{12}S_{12}$ phase would spontaneously transform into LTA-$Cd_{12}S_{12}$ and LTA-$Cd_{16}S_{16}$ into FAU-$Cd_{16}S_{16}$.

Figure 6.4: Total energy as a function of cell volume for SOD, LTA and FAU phases of $Cd_{12}S_{12}$ (left) and $Cd_{16}S_{16}$ (right), comparing with wurtzite structure.

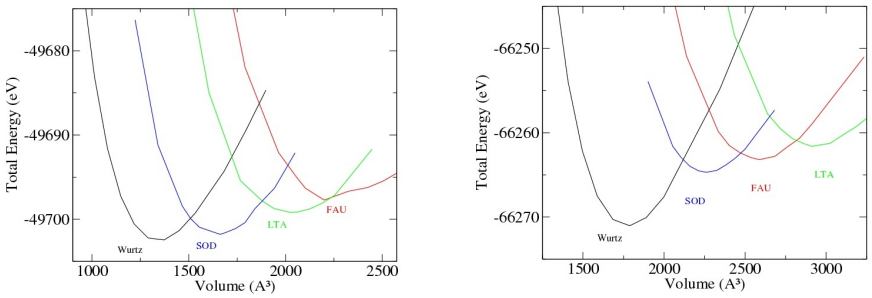

Finally, in order to check the thermal stability of these solids, ab-initio molecular dynamics simulations have been performed at 300 K, with a simulation time of 10 ps. After confirming that all the solids keep stable during all the simulation, we have carried out additional molecular dynamics simulations at 350 and 400 K for three

selected cases, namely, FAU-K@$Cd_{12}S_{12}$-Cl@$Cd_{12}S_{12}$, LTA-K@$Cd_{12}S_{12}$-Cl@$Cd_{12}S_{12}$ and SOD-K@$Cd_{12}S_{12}$-Cl@$Cd_{12}S_{12}$. In all the cases the solids remain stable during all the simulation. In Fig. 6.5, the dynamical behavior of SOD-K@$Cd_{12}S_{12}$-Cl@$Cd_{12}S_{12}$ phase is shown at 400 K. Notice that all the K-Cl distances, the distances between each of the trapped K and Cl atoms with respect to the center of mass of the corresponding cluster, and the distance between the centers of mass of the two neighboring clusters oscillates around the same value. Likewise, the distance between the centers of mass of two adjacent $(CdS)_{12}$ clusters is similar to the distance between their trapped K^+ and Cl^- ions. This reflects the highly symmetrical location of the ions at the centers of their corresponding clusters during the simulation time. The other cases studied showed the same thermal behavior.

Figure 6.5: Dynamic simulation of SOD-K@$(CdS)_{12}$-Cl@$(CdS)_{12}$. The simulation time was set to 10 ps with a time step of 1 fs. Top: Variation in the distance between the centers of mass of each monomer (CM1-CM2), between the center of mass of the monomer containing K and the K atom (CM1-K), between the center of mass of the monomer containing Cl and the Cl atom (CM2-Cl), and between the trapped atoms (K-Cl), for SOD-K@$(CdS)_{12}$-Cl@$(CdS)_{12}$. Bottom: Trajectories of K and Cl atoms inside their respective nanoclusters. Green = Cd, yellow = S, blue = K, and red = Br atoms.

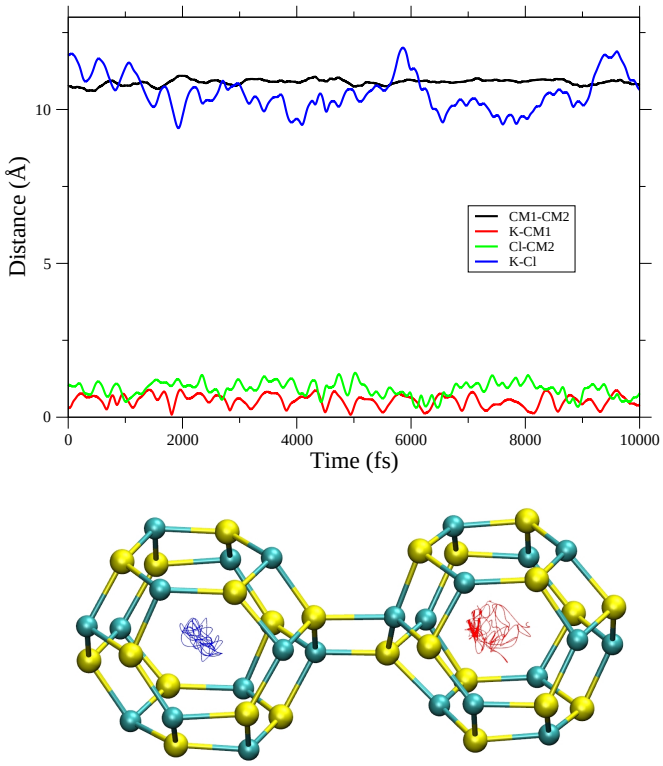

6.4 Conclusions

We have shown that the Cd_iS_i nanoclusters, for i=12, 16, form stable bare and endohedrally doped nanocluster dimers doped with K and halogens such as Cl and Br. As the potential ionization of K doped monomers and the electron affinities of halogen doped ones are very similar, there is a charge transfer from the potassium to the halogen, that can be seen as a cation and an anion trapped in two hollow neutral clusters. These dimers can be different according to

the contact zone: hexagons to hexagons (H-H), squares to squares (S-S) and edges to edges (E-E), where the monomers are linked together by covalent bonds between Zn and S. In all the dimers the electronic and structural integrity of bare nanoclusters are completely retained. We have observed that their stability decreases when the number of bonds between monomers decreases too (being H-H the most stable dimer) and that the size of the cluster does not affect the stability. It must be highlighted that the stability increases and the HOMO-LUMO gaps are reduce after doping.

Additionally, the characterized dimers were further used as starting geometries of the unit cells in solid-state calculations. Hence, we have constructed three new crystalline phases of CdS to form zeolite like nanoporous bulk phases: (i) FAU-CdS (based on H-H dimers) (ii) LTA-CdS (based on S-S dimers) and (iii) SOD-CdS (based on E-E dimers). The analysis of the band gaps at the Γ point shows that all the solids are predicted to be semiconductors. Moreover, endohedral doping decreases the band gaps by 0.4 eV, that is, from 2.2 eV in the bare solid to 1.8 eV in the doped solids. Therefore, these solids may be seen as narrow-gap semiconducting materials. Besides, all the solids have been found to be thermodynamically stable with cohesive energies similar to many soft solids. Furthermore, the endohedral doping increases their stability. However, the characterized structures in this work are not the most stable phases of CdS. These structures are much less dense than the more stable structures found in nature, namely wurtzite and zincblende, in fact, these new phases can be regarded as metastable phases of CdS. As a matter of fact, SOD phase is the most stable solid between all the characterized ones, due to its high compactness.

Thus, we conclude that it should be possible to stabilize new nanoporous polymorphic solid phases of CdS, with much larger unit cells as comparing with the solid phases found in nature. Indeed, the solids characterized in this work are less compact than wurtzite and zincblende. This fact has two important consequences: it makes these new materials thermodynamically metastable. Conversely, they might have many applications, due to their large pores, in heterogeneous catalysis and as storage materials.

Part III

Endohedrally Doped ZnS Nanoclusters

Chapter 7

Thermal Stability of Endohedral First-row Transition-Metal $TM@Zn_iS_i$ Structures, i=12, 16

The thermal stability of the first-row TM doped $TM@Zn_iS_i$ nanoclusters, in which TM stands for the first-row transition-metals from Sc to Zn and i=12,16, has been analyzed for the two lowest-lying spin-states of each metal. These structures were previously characterized by Matxain *et al.* [239]. We have seen that the metal atom can move towards the surface of the nanocluster forming the so-called surface-doped structure. Hence, we have calculated the relative energies between these two isomers. Additionally, we have also characterized the transition states connecting both isomers and the energy barriers needed to move from one to another in order to predict the thermal stability of the endohedral compounds. These values are further used to predict the lifetimes of the endohedrally doped nanoclusters. Most of the lifetimes are predicted to be very small, although most of them are large enough for experimental detection. Conversely, the lifetimes of $Zn@Zn_{12}S_{12}$ and $Zn@Zn_{16}S_{16}$ have proved to be very large.

7.1 Introduction

Interest in nanoclusters made of II-VI compound semiconductors has grown spectacularly in recent years for their paramount technological potential owing to their special semiconductor properties, that make these compounds suitable for applications such as photovoltaic solar cells, optical sensitizers, photocatalysts, quantum devices or nanobiomedicine [299]. Moreover, nanoclusters made of these materials can be doped in order to modified their properties at will. In this context, spherical hollow nanoclusters provide the chance for endohedral doping, namely, the dopant is placed inside the cavity of the hollow nanoparticle. For instance, doping these nanoclusters endohedrally with transition-metals leads to nanoclusters that would combine the appropriate optical and magnetic properties as to be used in nanomedicine, not only for improving of diagnosis applications, but also in the development of tailored nanomaterials with therapeutic properties to treat, for example, the hyperthermic tumoral regression [300].

In this work we focus on first-row transition-metal-doped TM@Zn_iS_i nanoclusters, where TM stands for the first-row transition-metals (Sc-Zn) and i=12,16. Of particular relevance to the present research is the previous characterization of the endohedral first-row transition-metal-doped TM@Zn_iS_i nanoclusters, in which TM stands for the first-row transition-metals from Sc to Zn and i=12 and 16 [239]. $Zn_{12}S_{12}$ and $Zn_{16}S_{16}$ were chosen because of their high stability, on account of their high symmetry and highly spheroidal shape, that allow for favored endohedral structures as compared to other nanoclusters [85]. In this previous work by Matxain and *et al.* [239], they observed that the encapsulation free energies are negative, suggesting that these compounds are thermodynamically stable. They also undertook quantum molecular dynamics calculations for two selected cases, Zn(^{1}S)@$Zn_{12}S_{12}$ and Ti(^{5}S)@$Zn_{12}S_{12}$, as representative of the endohedral nanoclusters with the trapped atom at the center and off-center, respectively. These calculations confirmed the thermal stability of these two compounds. In addition, it was observed that there is negligible charge transfer between the dopant transition-metals and their hollow cluster hosts and that, after encapsulation, the spin densities remain localized on the transition-metal atoms. This points to an atomic-like behavior of the trapped transition-metal atom, which gives rise to atomic-like mag-

netic properties in a protected environment. Consequently, endohedral transition-metal compounds are interesting also due to their magnetic properties, which should yield dimers with (anti)ferromagnetic coupling [122].

In this work we have further studied the thermal stability of these previously characterized endohedral clusters [239], by carrying out quantum molecular dynamics calculations for several $TM@Zn_iS_i$ (i=12,16). It has been observed that some of these endohedrally doped nanoclusters are not thermally stable for the dopant atom moves from the inner part of the cluster to the surface. These latter structures will be called surface-doped structures here-after. In order to complement the quantum molecular dynamics simulations, we have additionally characterized the surface-doped structures for all compounds, along with the TS's connecting both isomers. In this manner we have estimated the lifetime of each endohedral nanocluster using the calculated energy barriers for the endohedral-doped to surface-doped transformations.

Nevertheless, we would like to emphasize that both techniques are approximate. On the one hand, one single MD simulation is not representative, i.e., we are replacing a full sampling on the appropriate statistical ensemble by a single trajectory. On the other, lifetimes are calculated from the reaction rate constants. These reaction rate constants are very sensitive with respect to the activation energies. Consequently, the data obtained with both methodologies should not to be taken quantitatively, but qualitatively.

7.2 Methods

All geometries have been fully optimized using the gradient corrected hybrid B3LYP [243, 296, 219] functional within the Kohn-Sham implementation [209] of density functional theory [208]. Harmonic vibrational frequencies are determined by analytical differentiation of gradients, in order to determine whether the structures found are true minima or transition states, and to extract zero-point energies and enthalpy and entropy contributions to Gibbs free energy, G, which is reported at room temperature. The relativistic compact effective core potentials and shared-exponent basis set [244] of Stevens et. al. (SKBJ) have been used for Zn and S, as described in the study of the isolated clusters [81], and the fully relativistic multielectron fit pseu-

dopotentials, with 10 electrons in the core, developed by Dolg et. al., were used for the trapped atoms [301, 302]. Note that pure angular momentum functions were used throughout this study. All the geometry optimizations and frequency calculations were carried out with the GAUSSIAN03 package [303]. The transition states between the characterized endohedral nanoclusters and their corresponding surface-doped structures have been calculated using the STQN method for locating transition structures [304, 223].Intrinsic reaction coordinate (IRC) calculations [305, 306][GS89, GS190] are further performed to assess that the calculated transition states connect the appropriate reactants and products. All the atomic charges are calculated from the Mulliken population analysis.

To further explore the thermal stability of these compounds, we undertook ab-initio thermal MD simulations at 298 K on some selected cases, controlled by means of the Nose thermostat as implemented in the SIESTA code [221], within the DFT approach. Exchange and correlation effects were described using the generalized gradient approximation (GGA), within the revised Perdew-Burke-Ernzerhof (rPBE) functional [245, 246, 247]. Core electrons were replaced by Troullier-Martins norm-conserving pseudopotentials [248] in the Kleinman-Bylander factorized form [249]. Within the context of SIESTA, the use of pseudopotentials imposes basis orbitals adapted to them. Furthermore, SIESTA employs a localized basis set to represent the Kohn-Sham orbitals for valence electrons. Accordingly, the basis set of atomic orbitals is constructed from numerical solutions of the atomic pseudopotential, and are constrained to be zero beyond a cutoff radius. We used one basis set of double-z plus polarization quality (DZP). The single parameter (orbital energy shift) that defines the confinement radii of different orbitals was DEPAO=150 meV, which gives typical precision within the accuracy of the used GGA functional. With this basis set, SIESTA calculates the self-consistent potential on a grid in real space. The fineness of this grid is determined in terms of an energy cutoff in analogy to the energy cutoff when the basis set involves plane waves. In our calculations, we used an equivalent plane wave cutoff energy of 200 Ry. These simulations were carried out for 5 ps with a chosen time step of 1 fs.

7.3 Results

First of all, in subsection 7.3.1 we present the results for the ab-initio molecular dynamics simulations on two selected cases, namely, Mn(^{4}D)@$Zn_{12}S_{12}$ and Ni(^{1}D)@$Zn_{16}S_{16}$. Then, in subsections 7.3.2 and 7.3.3 the surface-doped and TS structures are characterized.

7.3.1 Quantum Molecular Dynamics

In ref. [239], Matxain et. al. carried out quantum molecular dynamics for two selected cases, Zn(^{1}S)@$Zn_{12}S_{12}$ and Ti(^{5}S)@$Zn_{12}S_{12}$. These calculations confirmed the thermal stability of these two compounds, since in both cases the dopant atom was kept inside the cage. Here we present two new selected cases, Mn(^{4}D)@$Zn_{12}S_{12}$ and Ni(^{1}D)@$Zn_{16}S_{16}$, where the guest transition-metal does not remain confined into the cavity but it moves to the surface of the nanocluster. We have set a simulation time of 5 ps, with a time step of 1 fs, and the trajectories have been calculated at a constant average temperature of 298 K.

Figure 7.1 shows how the energies vary during the simulation. It can be observed in both cases that, at a given time, the energy decreases dramatically. This happens when the transition-metal goes toward the surface of the nanocluster, which leads to a more stable structure. Together with the total energy pictures, the representations of the distance of the Mn and Ni respectively from the center of mass of the nanoclusters during the simulation time, confirm that the guest atom moves away from the center. Likewise, the final structures of these two clusters are depicted: in the resulting structures the metals interact covalently with the Zn and S atoms that are around them.

Therefore, quantum dynamics calculations of these selected cases predict that they are not thermally stable and the TM would move towards the surface of the cage through a transition state. In the next subsections we have characterized these surface-doped and transition state structures, in order to rationalize the behavior and stability of these compounds.

Figure 7.1: Above the resulting structures for Mn(^{4}D)@$Zn_{12}S_{12}$ and Ni(^{1}D)@$Zn_{16}S_{16}$ respectively. In brown Mn atom, in green Ni atom, in yellow S atoms and gray Zn atoms are depicted. Below, the variation of the energy, in eV, and the distance of the TM from the center of mass of the nanocluster, in Å, as a function of time, in fs.

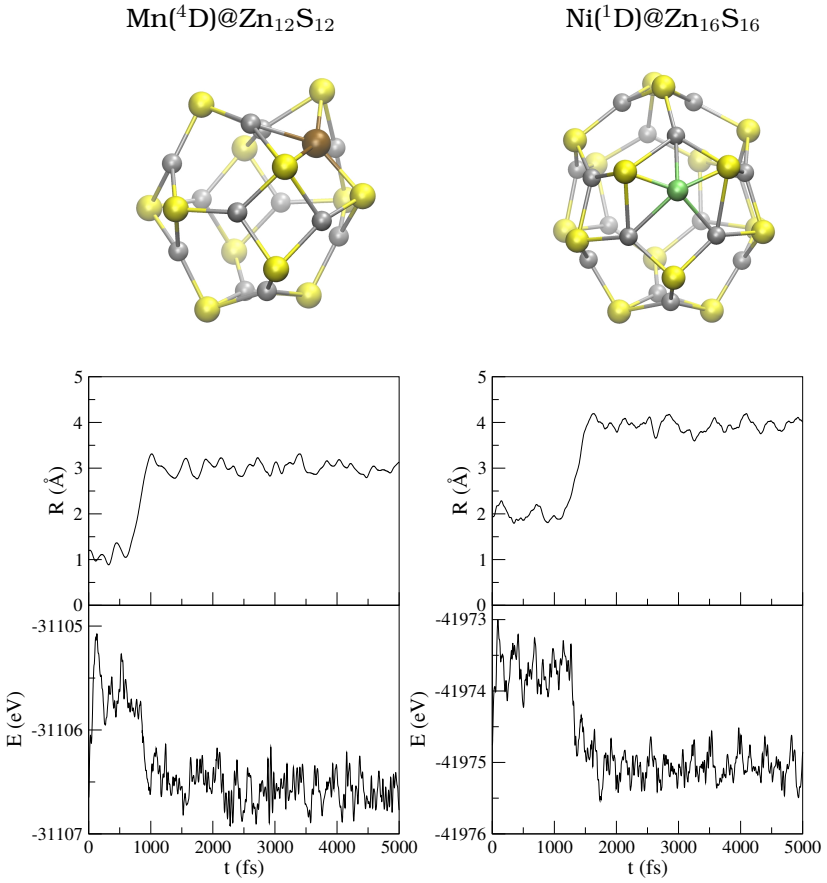

7.3.2 Surface Structures

In this subsection the nanoclusters with the corresponding transition-metal at the surface will be analyzed and their properties will be discussed. For each TM, the two lowest-lying spin states have been considered, like in the endohedrally doped ones [239]. In Table 7.1 the geometrical, electronic and energetic properties of the characterized local minima are given. The spin densities of each metal and the maximum spin density of zinc and sulfur atoms in the surface-doped and

endohedral compounds are shown in Table 7.2. The spin densities of the transition-metals in the endohedral nanoclusters are taken from the work of Matxain *et al.* [239] Hereinafter, a comparison between endohedral nanoclusters and surface-doped structures will be made.

The surface-doped compounds do not resemble the square-hexagon structure of bare spheroids in the neighborhood of the TM. The TM breaks some of the Zn-S bonds and forms new polarized covalent bonds with a number of Zn and S atoms. Depending on the TM, the number of bonds, i.e., the coordination number, changes, as can be seen in Table 7.1. To determine the coordination number, we have considered a bond when the bond length between two atoms is smaller than the sum of their van der Waals radii. Different local minima have been characterized for each TM, with different coordination numbers. For the sake of clarity the properties presented here are those corresponding to the most stable isomer of surface-doped structure.

For Ti(^{5}F), Mn(^{4}D), Co(^{2}F), Co(^{4}F), and Zn(^{1}S) the coordination number is the same in both $Zn_{12}S_{12}$ and $Zn_{16}S_{16}$ compounds. There are mainly two facts that must be pointed out regarding the coordination number of the metals in these surface-doped structures. On one hand, in most of the nanoclusters, the coordination number is higher or the same in TM-$Zn_{12}S_{12}$ compared to TM-$Zn_{16}S_{16}$ compounds. On the other hand, in most cases low-spin compounds are higher coordinated than high-spin ones. Combining these two facts, we observe that the highest coordinated compound is Ni(^{1}S)-$Zn_{12}S_{12}$. There are few exceptions. For instance, the high-spin compounds are higher-coordinated than the low-spin ones for V-$Zn_{12}S_{12}$, Sc-$Zn_{16}S_{16}$ and Ti-$Zn_{16}S_{16}$.

Looking at the energy difference between the surface-doped and endohedral nanoclusters, $\triangle G_{surf-end}$, which is defined as G_{surf}- G_{end}, it is clear that the surface-doped compounds are thermodynamically more stable than the corresponding endohedral ones, except for Zn(^{1}S)@$Zn_{16}S_{16}$ and Cr(^{7}S)@$Zn_{16}S_{16}$ (the latter one is remarkable for its large spin momentum). However, kinetically the endohedral compounds could be metastable. Large enough barriers would prevent the TM to move towards the surface. The kinetics of these reactions will be analyzed in subsection 7.3.3.

The relative energies between the high-spin and low-spin state of

Table 7.1: The charge of transition-metal atom and the coordination number. ΔE is the relative energy between the low-spin state and the high-spin state, and $\Delta G_{end-surf}$ is the energy difference between the endohedral and the surface-doped structures, both in Kcal/mol. The ground spin-state of each metal is in bold.

		X-$Zn_{12}S_{12}$				X-$Zn_{16}S_{16}$			
	2S+1	q_x	C.N.	ΔE	$\Delta G_{surf-end}$	q_x	C.N.	$\triangle E$	$\Delta G_{surf-end}$
Sc	2	0.69	5	0.00	-	0.70	3	0.00	-50.23
Sc	**4**	0.60	3	2.16	-	0.58	4	9.86	-
Ti	3	0.29	5	0.00	-	0.39	3	0.00	-40.77
Ti	**5**	0.28	4	18.32	-17.42	0.51	4	21.51	-10.45
V	4	0.43	2	0.00	-26.22	0.71	3	0.00	-52.35
V	**6**	0.05	5	5.10	-13.88	0.26	2	25.39	-6.36
Cr	**5**	0.16	4	0.00	-29.65	0.39	3	0.00	-27.84
Cr	7	0.29	4	12.54	-2.29	0.33	2	12.78	0.73
Mn	**4**	0.61	4	13.22	-33.81	0.43	4	15.43	-30.29
Mn	6	0.36	2	0.00	-22.62	0.77	3	0.00	-15.67
Fe	**3**	0.21	4	5.39	-20.60	0.20	3	14.37	-14.82
Fe	5	0.25	2	0.00	-19.55	0.57	3	0.00	-22.44
Co	**2**	0.15	4	0.00	-21.52	0.11	4	5.66	-11.53
Co	4	0.21	2	0.99	-11.98	0.25	2	0.00	-21.04
Ni	**1**	-0.22	6	0.00	-	-0.26	5	0.00	-20.00
Ni	3	0.23	5	7.31	-15.58	0.32	4	5.25	-14.31
Cu	2	0.23	5	-	-9.97	0.16	2	-	-8.10
Zn	1	0.29	2	-	-4.73	0.32	2	-	1.45

each compound are shown in Table 7.1. These values reveal that transition-metal surface-doped structures favor the low-spin states, with the exception of the middle transition-metals, unlike the endohedral nanoclusters, where high-spin were, in general, more stable than the low-spin compounds.

Table 7.2: The spin densities of the transition-metals in both endohedral ($X@Zn_{12}S_{12}$ and $X@Zn_{16}S_{16}$) and surface-doped ($XZn_{12}S_{12}$ and $XZn_{16}S_{16}$) compounds.

		X-$Zn_{12}S_{12}$		X-$Zn_{16}S_{16}$	
		Surface	Endohedral	Surface	Endohedral
	2S+1	$\rho_{S_{TM}}$	$\rho_{S_{TM}}$	$\rho_{S_{TM}}$	$\rho_{S_{TM}}$
Sc	2	0.74	-	0.99	0.87
Sc	4	1.45	-	1.26	-
Ti	3	2.00	-	2.06	1.86
Ti	5	3.00	3.17	2.89	3.49
V	4	3.27	2.91	3.18	2.86
V	6	4.15	4.46	4.42	4.61
Cr	5	4.45	3.94	4.35	3.94
Cr	7	5.11	5.53	5.37	5.61
Mn	4	4.27	3.16	4.14	3.35
Mn	6	5.04	4.65	4.86	4.80
Fe	3	2.84	2.23	2.52	2.27
Fe	5	3.82	3.60	3.65	3.85
Co	2	1.66	1.25	1.69	2.69
Co	4	2.69	2.70	2.69	2.90
Ni	3	1.36	1.64	1.47	1.71
Cu	2	0.22	0.66	0.41	0.70

In general the charges of the transition-metals, given in Table 7.1 are larger in the surface-doped structures than in the endohedral ones. In the endohedral cases, most of the atomic charges reported by Matxain *et al.* [239] were lower than 0.2. Therefore the TM trapped inside maintains its atomic-like properties, being the interaction with the cage weak. In surface-doped structures, on the other hand, the TM now interacts strongly with the cage, in fact, is part of the cage and is covalently bonded to other atoms. Therefore, the charge of the TM is larger in this case. The spin densities given in Table 7.2 also support this idea: in the endohedral compounds are closer to the values corresponding to their multiplicities than in the case of surface-doped

nanoclusters. So, the interaction between the guest and the host is bigger in the latter.

7.3.3 Transition States

The endohedral and surface-doped structures are connected by a transition state (TS), a maximum in a reaction coordinate, as was observed in the quantum dynamics simulations. In this subsection we have characterized these transition states in order to analyze the kinetic and thermal stability of the endohedral compounds. Although surface-doped structures are thermodynamically more stable, large enough barriers would prevent endohedral compounds to rearrange into the surface-doped structures. In Table 7.3 the energy barriers between the endohedral structures and the TS, $\triangle G^{\ddagger}$, the reaction rate constants (k) and the lifetimes of the endohedral compounds are given. The calculated energy barriers, $\triangle G^{\ddagger}$, are calculated as $\triangle G^{\ddagger} = G_{TS} - G_{end}$. These values are further used to calculate the reaction rate constants (k), at room temperature, using the Eyring equation:

$$k = \frac{k_B T}{h} e^{-\frac{\triangle G^{\ddagger}}{RT}}$$

where k is the reaction rate constant, T is the absolute temperature, $\triangle$G‡ is the energy barrier as defined above, k$_B$ the Boltzmann constant, h is the Planck's constant and R is the constant of ideal gas. The lifetime of each endohedral nanocluster is then calculated as the inverse of the reaction rate constant.

It is important to note that the reaction rate constants calculated using the Eyring equation are approximate, because they are very sensitive with respect to the calculated activation energies being an exponential dependence between them. So, our aim is to have qualitative information about the stability of the endohedral nanoclusters and to point out potential stable structures.

At first glance, it is worth noticing that most of the calculated lifetimes are very small, although most of them are predicted to be large enough for experimental detection. We must emphasize that the lifetimes of Zn(^{1}S)@Zn$_{12}$S$_{12}$ and Zn(^{1}S)@Zn$_{16}$S$_{16}$ are the largest ones, being 2.86 days and 836 years, respectively.

Table 7.3: Characterized transition states between endohedral compounds and their respective surface-doped compounds, for TM@$Zn_{12}S_{12}$ and TM@$Zn_{16}S_{16}$. $\triangle G^{\ddagger}$ (kcal/mol) is the energy difference between the transition states and the endohedral structures, i.e., the activation energy. k is the calculated reaction rate constant (s^{-1}) and τ is the lifetime (s). The ground spin-state of each metal is in bold.

		$Zn_{12}S_{12}$			$Zn_{16}S_{16}$		
	2S+1	$\triangle G^{\ddagger}$	k (s^{-1})	τ (s)	$\triangle G^{\ddagger}$	k (s^{-1})	τ (s)
Sc	2	-	-	-	-	-	-
Sc	**4**	-	-	-	-	-	-
Ti	3	-	-	-	-	-	-
Ti	**5**	4.77	$1.98{\cdot}10^{9}$	$5.05{\cdot}10^{-10}$	-	-	-
V	4	2.62	$7.46{\cdot}10^{10}$	$1.34{\cdot}10^{-11}$	-	-	-
V	**6**	5.54	$5.39{\cdot}10^{8}$	$1.85{\cdot}10^{-9}$	6.26	$1.60{\cdot}10^{8}$	$6.25{\cdot}10^{-9}$
Cr	**5**	8.54	$3.41{\cdot}10^{6}$	$2.93{\cdot}10^{-7}$	-19.8	-	-
Cr	7	12.45	$4.64{\cdot}10^{3}$	$2.15{\cdot}10^{-4}$	14.95	6.83·10	$1.46{\cdot}10^{-2}$
Mn	**4**	3.93	$8.17{\cdot}10^{9}$	$1.22{\cdot}10^{-10}$	-	-	-
Mn	6	11.95	$1.08{\cdot}10^{4}$	$9.26{\cdot}10^{-5}$	15.11	5.21·10	$1.92{\cdot}10^{-2}$
Fe	**3**	4.87	$1.67{\cdot}10^{9}$	$5.98{\cdot}10^{-10}$	1.36	$6.25{\cdot}10^{11}$	$1.60{\cdot}10^{-12}$
Fe	5	6.73	$7.24{\cdot}10^{7}$	$1.38{\cdot}10^{-8}$	2.93	$4.42{\cdot}10^{10}$	$2.26{\cdot}10^{-11}$
Co	**2**	1.49	$5.02{\cdot}10^{11}$	$1.99{\cdot}10^{-12}$	5.17	$1.01{\cdot}10^{9}$	$9.92{\cdot}10^{-10}$
Co	4	10.12	$2.37{\cdot}10^{5}$	$4.22{\cdot}10^{-6}$	5.29	$8.23{\cdot}10^{8}$	$1.22{\cdot}10^{-9}$
Ni	**1**	-	-	-	2.13	$1.71{\cdot}10^{11}$	$5.86{\cdot}10^{-12}$
Ni	3	0.80	$1.61{\cdot}10^{12}$	$6.21{\cdot}10^{-13}$	12.18	$7.32{\cdot}10^{3}$	$1.36{\cdot}10^{-4}$
Cu	2	6.50	$1.07{\cdot}10^{8}$	$9.37{\cdot}10^{-9}$	5.02	$1.30{\cdot}10^{9}$	$7.70{\cdot}10^{-10}$
Zn	1	24.81	$4.04{\cdot}10^{-6}$	$2.47{\cdot}10^{5}$	31.66	$3.85{\cdot}10^{-11}$	$2.60{\cdot}10^{10}$

To explain this fact we have to take into account that in the endohedral compounds, the interaction between the guest and the host is very weak, while in the surface-doped structures this interaction is stronger. Moreover, the 3d-orbital shell in the Zn atom is full. Hence, Zn is the least reactive of all the first-row transition-metals. This fact also explains why the endohedral Zn@$Zn_{16}S_{16}$ is thermodynamically more stable than the surface-doped Zn-$Zn_{16}S_{16}$. Additionally, lifetimes reveal that endohedral nanoclusters favor high-spin states which coincide with the most stable endohedrally doped nanoclusters.

In subsection 7.3.1 we described the results of the quantum dynamics simulations of Mn(^{4}D)@$Zn_{12}S_{12}$ and Ni(^{1}S)@$Zn_{16}S_{16}$, and observed that after few ps the endohedral compounds converted into the more stable surface-doped structures. Note that the calculated energy barriers for these compounds are 3.93 kcal/mol and 2.13 kcal/mol respectively. These small barriers explain the obtained dynamical results. Likewise, the energy barriers calculated for Zn(^{1}S)@$Zn_{12}S_{12}$ and Zn(^{1}S)@$Zn_{16}S_{16}$ are the largest ones. The dynamical behavior of the former was analyzed in the previous work by Matxain *et al.*[239]. They carried out a quantum molecular dynamic simulation of 5 ps and they observed that in the endohedral structure the Zn atom remained confined at the center of the nanocluster, in agreement with the large energy barrier.

We have performed a longer simulation of 30 ps for this compound, to further confirm its thermal stability. In Figure 7.2 it is observed that the energy oscillates around the same value during all the simulation time, and that the Zn atom moves around the center of the nanocluster along the simulation up to a maximum radial distance of 0.55 Å. The average radial separation of the caged Zn atom is 0.27$\pm$0.11Å. In addition, the trajectory of the zinc atom along the simulation time is also depicted in Figure 7.2. Therefore, this nanocluster is predicted to be thermally stable enough to survive long time at room temperature as to allow for its experimental detection.

Figure 7.2: Quantum Dynamic simulation of $Zn(^1S)@Zn_{12}S_{12}$. On top, the movement of the trapped Zn atom inside the cage. In yellow S atoms and gray Zn atoms are depicted. Below the variation of the energy, in eV, and the variation of the distance R (Å), of the trapped atom from the center of mass of the nanocluster as a function of time, during the simulation.

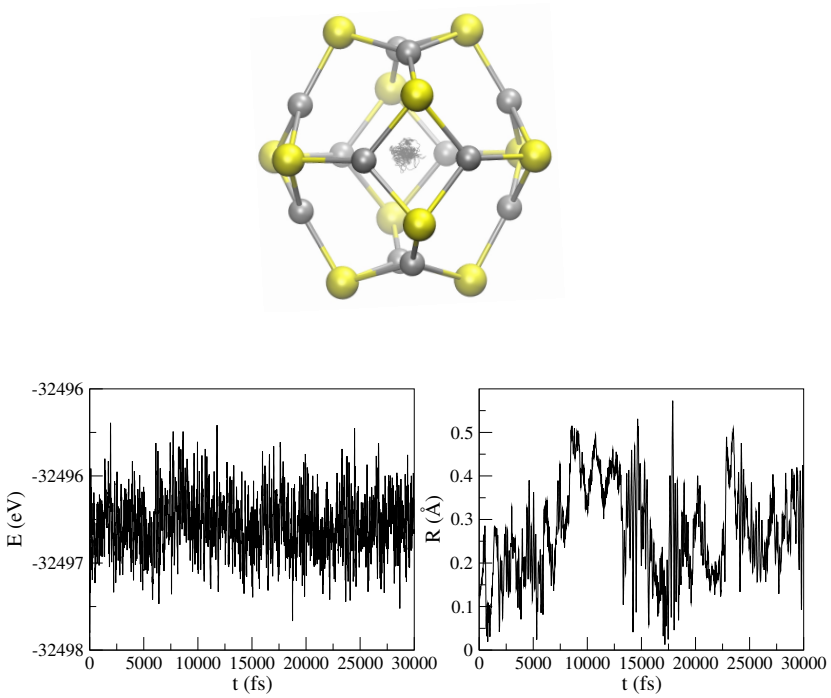

7.4 Conclusions

The thermal stability of the first-row TM doped $TM@Zn_iS_i$ nanoclusters, in which TM stands for the first-row transition-metals from Sc to Zn and i=12,16, has been analyzed by using two different methodologies. The first one is to carry out quantum molecular dynamic simulations, in which atoms and molecules are allowed to interact for a period of time, giving a view of the motion of the particles. This tech-

nique allows us to predict the thermal stability of Zn@$Zn_{12}S_{12}$, while Mn(^{4}D)@$Zn_{12}S_{12}$ and Ni(^{1}S)@$Zn_{16}S_{16}$ are seen to be thermally unstable. In these cases, the TM moves towards the surface, leading to the more stable surface-doped structures. The large number of TM@Zn_iS_i structures along with the high cost of each quantum dynamical simulation made it impossible to carry out these simulations for all structures. Therefore, we have followed another methodology to study the thermal stability of the endohedral compounds. Based on the calculated energy differences between the endohedral compounds and the TS compounds that connect the former with the surface-doped structures, we have estimated the lifetime of each endohedral structure. As mentioned before, these techniques are approximate. Hence, the data obtained have not to be taken quantitatively, but qualitatively. Thus, our aim is to point out potential stable structures. In this vein, both methodologies are in agreement in predicting Zn@Zn12S12 and Zn@Zn16S16 as the most stable structure with a lifetime of around three days and 900 years, respectively. The other endohedral compounds have much smaller lifetimes, although could be large enough for experimental detection.

Chapter 8

Second-row Transition-Metal Doping of $(ZnS)_{i=12,16}$ Nanoclusters: Structural and Magnetic Properties

TM@Zn_iS_i nanoclusters have been characterized by means of the Density Functional Theory, in which Transition-Metal (TM) stands from Y to Cd, and i=12 and 16. These two nanoclusters have been chosen owing to their highly spheroidal shape which allow for favored endohedral structures as compared to other nanoclusters. Doping with TM is chosen due to their magnetic properties. In similar cluster-assembled materials, these magnetic properties are related to the Transition Metal-Transition Metal (TM-TM) distances. At this point, endohedral doping presents a clear advantage over substitutional or exohedral doping, since in the cluster-assembled materials, these TM would occupy the well-fixed center of the cluster, providing in this way a better TM-TM distance control to experimentalists. In addition to endohedral compounds, surface structures and the TS's connecting both isomers have been characterized. In this way the kinetic and thermal stability of endohedral nanoclusters is predicted. We anticipate that silver and cadmium endohedrally doped nanoclusters have the longest life-times.

This is due to the weak interaction of these metals with the cage, in opposite to the remaining cases where the TM covalently bond to a region of the cage. The open-shell electronic structure of Ag provides magnetic properties to $Ag@Zn_iS_i$ clusters. Therefore,we have further characterized $(Ag@Zn_{12}S_{12})_2$ and $(Ag@Zn_{16}S_{16})_2$ dimers both in the ferromagnetic and antiferromagnetic state, in order to calculate the corresponding magnetic exchange coupling constant, J.

8.1 Introduction

The recent explosion of research in nanoclusters has been driven in part by the wide-ranging of applications in nanotechnology, due to their novel properties that usually differ from those of the bulk matter. The size and composition dependent properties, which arise from the quantum confinement effect, promise new materials with novel properties. Likewise, during the last decade interest in II-VI nanocompounds has increased notably, as they have potential applications in photovoltaic solar cells, optical sensitizers or quantum devices [33, 307, 308, 309, 310]. In addition, nanoclusters made of these materials can be doped changing their properties at will. For instance, doping the nanoclusters with transition-metals can confer to them magnetic properties [122, 311, 132, 131]. In this context, spherical hollow clusters provide the chance for endohedral doping, namely, the dopant is placed inside the cavity of the hollow nanoparticle [284, 312, 265, 82, 134]. So far, few II-VI nanoclusters doped with transition-metals have been explored. Yadav *et al.* studied the properties of Cr-doped $(ZnTe)_{12}$ clusters by first principles density functional calculations, concluding that it is energetically most favorable for Cr atoms to substitute at Zn sites [313]. Moreover, a theoretical investigation on $(ZnSe)_n$ (n= 6-13) nanoclusters doped with manganese atoms, revealed that Mn atoms prefer to substitute Zn atoms in the doped compound [314].

$(ZnO)_{12}$ nanoclusters doped with one and two Mn atoms were studied taking into account the substitutional, exohedral and endohedral doping [131]. The calculations suggested that, for the monodoped clusters, the substitutional isomer is energetically favorable, and an exohedral isomer may appear as a low-lying metastable state. The endohedral bi-doped isomer, however, is found to be a stable local minimum. The structural and magnetic properties of $(ZnO)_{12}$ nanoclus-

ters substitutionally doped with 3d transition-metals were also studied theoretically [315]. It was found that doping of TM at the Zn site is energetically more favorable than doping it at O site. Other studies on Cu-doped $(ZnO)_n$ (n= 3, 9, 12) [316], Mn-doped $(ZnS)_{12}$ [317], and Cr-doped $(CdS)_{12}$ determined that, among the substitutional, exohedral and endohedral doping, the substitutional mono- and bi-doped clusters are the most stable ones. Likewise, Chen *et al.* found that substitutional isomer is the most favorable in energy for monodoped clusters, while the exohedral isomers are the most favorable for bidoped clusters [318].

Additionally, $(ZnS)_{12}$ and $(ZnS)_{16}$ nanostructures have been doped endohedrally with first-row transition-metals [239]. Both clusters were chosen due to their high symmetry [99] and highly spheroidal shape, that allow for more favorable endohedral doping as compared to other nanoclusters [85]. Nevertheless, although the theoretically characterized endohedral TM@Zn_iS_i (i=12 and 16) structures were predicted to be thermodynamically stable, a later work [132] showed that most of them may not be thermally stable (see chapter 7). The reason is that the dopant atom tends to move from the inner part of the cluster to the surface, giving rise to the so-called surface-doped structures [132]. However, the exception were Zn-doped endohedral $(ZnS)_{12}$ and $(ZnS)_{16}$ nanoclusters, which were predicted to have a very long lifetimes.

Nevertheless, although substitutional doping is in general more stable than endohedral doping, the latter presents a very important feature in dealing with the magnetic properties of cluster-assembled materials. In fact, the magnetic properties of such materials have been found to be related with the TM - TM distances in related materials [315]. At short distances, the antiferromagnetic coupling is favored, while the enlargement of this distance leads to a near-degeneracy of both AF and F states. The advantage of endohedral doping over substitutional doping is that the TM-TM distances can be easily fixed, since the dopant atoms are localed at the center of the clusters. Therefore, in the assembled materials, the TM-TM distance would be fixed. In substitutional doping, the TM-TM distances would be different in the assembled materials, depending on the location of the TM at the cluster surface. More interestingly, the assembled materials of small clusters would lead to short TM-TM distances with antiferromagnetic properties, while large enough clusters would lead to materials with ferromagnetic properties. Therefore, it appears interesting to find suf-

ficiently stable endohedrally doped materials, in order to design materials with well fixed magnetic properties. Unfortunately, no experimental works have been carried out on such structures yet.

In this work, we focus on endohedrally doped second-row transition-metals TM@Zn_iS_i nanoclusters (i= 12, 16), where TM stands for the second-row transition-metals (Y-Cd), with the aim of unveiling whether some of these endohedral compounds may be stable and, thus, experimentally detectable. Bearing in mind the previous experience, we have not only characterized the endohedral TM@Zn_iS_i structures, but we have also analyzed their thermal stability. With this purpose, we have additionally characterized the surface-doped structures for all compounds, along with the TS's connecting both isomers. In this manner we have estimated the lifetime of each endohedral nanocluster by estimating the energy barriers for the endohedral-doped to surface-doped transitions. Specifically, the Eyring model has been used,

$$k = \frac{k_B T}{h} e^{-\frac{\triangle G^{\ddagger}}{RT}} \qquad (1)$$

where k is the reaction rate constant, T is the absolute temperature, $\triangle G^{\ddagger}$ is the free energy barrier, k_B the Boltzmann constant, h is the Planck's constant and R is the constant of the ideal gas. The lifetime of each endohedral nanocluster is then calculated as the inverse of the reaction rate constant. We must emphasize that the reaction rate constants are very sensitive with respect to the activation energies. Consequently, the data obtained with this methodology should not to be taken quantitatively, but qualitatively. Nevertheless, we must emphasize that the obtained results are very conclusive. Thus, we anticipate that silver and cadmium-doped endohedral nanoclusters are the only ones that have very long lifetimes. Since Cd does not have magnetic properties because it is a closed-shell transition-metal, we have focused on silver doped nanoclusters, i. e., Ag@$Zn_{12}S_{12}$ and Ag@$Zn_{16}S_{16}$. Silver atoms have a doublet electronic ground state and, therefore, two silver atoms may couple in a ferromagnetic way, with parallel spins, or in an antiferromagnetic manner, with antiparallel spins. Accordingly, we have further characterized (Ag@$Zn_{12}S_{12}$)$_2$ and (Ag@$Zn_{16}S_{16}$)$_2$ magnetic dimers and calculate their exchange coupling constant, J. In this respect, it is noteworthy that the antiferromagnetically coupled systems require a multideterminantal treatment, such as the complete space self consistent field (CASSCF) method. However, these kind of methods are not amenable for so big systems. Thus, we have used

the spin-unrestricted approximation and the broken-symmetry solution (BS) within the DFT framework, that showed to provide a good description of weakly bonded metal-metal interactions [122, 319].

To interpret the magnetic properties, we have used the Heisenberg-Dirac-van Vleck spin-Hamiltonian:

$H = -2JS_1\hat{A}\cdot S_2$ (2)

where S_1 is the local spin of Ag_1 and S_2 is the local spin of Ag_2. The exchange coupling constant,J, in (2) quantifies the strength of the interaction between magnetic centers. When J is positive the coupling is ferromagnetic. Conversely, a negative value of J represents an antiferromagnetic coupling. Then, in order to estimate the magnetic exchange coupling constant, we have used the formulation proposed by Yamaguchi *et al.* [320, 321]:

$J = -\frac{E_{HS}-E_{BS}}{<\hat{S}^2>_{HS}-<\hat{S}^2>_{BS}}$ (3)

where E_{HS} stands for the energy of the high-spin state, namely the ferromagnetic state, and E_{BS} for the energy of the broken symmetry state, i. e., antiferromagnetic state.

8.2 Methods

All geometries have been fully optimized using the gradient corrected hybrid B3LYP [243, 296, 219] functional within the Kohn-Sham formulation [209] of density functional theory [208]. Harmonic vibrational frequencies are determined by analytical differentiation of gradients, in order to determine whether the structures found are true minima or transition states, and to extract enthalpy and entropy contributions to Gibbs free energy, G, at room temperature. The relativistic compact effective core potentials and shared-exponent basis set [244] of Stevens et. al. (SKBJ) have been used for Zn and S, as described in the study of the isolated clusters [81], and the fully relativistic multielectron fit pseudopotentials, with 10 electrons in the core, developed by Dolg *et. al.*, were used for the trapped atoms [301, 302]. The reliability of this method was checked in a previous work, (see chapter 7) [132]. Note that pure angular momentum functions were used throughout this study. All the geometry optimizations and frequency calculations were carried out with the GAUSSIAN03 package [303]. The transition states between the characterized endohedral nanoclusters and their corresponding surface-doped structures have been calculated using the STQN method for locating

transition structures [223]. Intrinsic reaction coordinate (IRC) calculations [305, 306][GS89, GS190] are further performed to assess that the calculated transition states connect the appropriate reactants and products. All the atomic charges are calculated from the trace of the atomic polar tensor. The spin densities shown in the text are the Mulliken atomic spin densities, as calculated in Gaussian 03 [303], which are defined as the difference of the Mulliken charges of spin-up and spin-down electrons. The sum over the Mulliken spin densities equals the total spin of the system [322].

In order to calculate the magnetic exchange coupling in silver-doped dimers, we have performed single-point DFT calculations using the ORCA package developed by Neese and co-workers [323]. Ahlrichs' valence triple-ξ basis set [324] with two sets of polarization functions, TZV(pp), were used for all the atoms. All calculations were carried out with an integration grid of 4.0 and employed the gradient corrected hybrid B3LYP [243, 296, 219] functional.

8.3 Results

First of all, in subsection 8.3.1 we present the characterized endohedrally doped structures, along with their electronic and geometrical features. In subsection 8.3.1.1 we focus on the surface-doped structures. In subsection 8.3.1.2, thee characterized transition states between the endohedral and surface-doped structures are shown and their properties discussed. In subsection 8.3.1.2 the estimated lifetimes of each endohedral transition-metal-doped nanocluster are given and discussed too. Finally, in subsection 8.3.1.3 we focus on the magnetic properties of $(Ag@Zn_iS_i)_2$ dimers.

8.3.1 Endohedral TM@Zn_iS_i Nanoclusters

In this subsection the characterized TM@Zn_iS_i nanoclusters, in which TM stands for the second-row transition-metals from Y to Cd and i=12 and 16, are shown and their properties discussed. For each transition-metal the two lowest-lying spin states have been considered. In Figure 8.1 TM@$Zn_{12}S_{12}$ and TM@$Zn_{16}S_{16}$ endohedral nanoclusters are shown. Observe that the transition-metal is located close to the center of each nanocluster. In Table 1 the geometrical properties (the distance of the TM with respect to the geometrical center of the nan-

Figure 8.1: TM@$Zn_{12}S_{12}$ and TM@$Zn_{16}S_{16}$ endohedral nanoclusters. S atoms are drawn in yellow, Zn atoms in gray and TM in green.

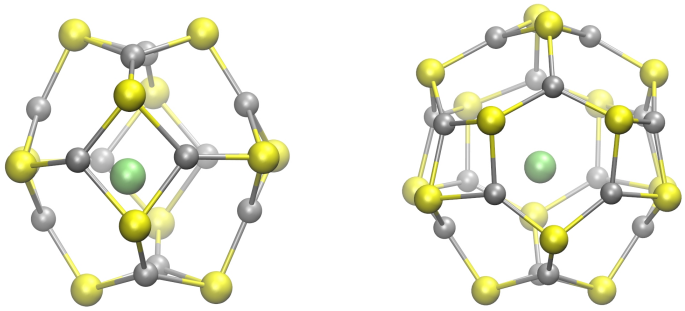

ocluster, R, and the cavity radius of the cluster, r_{cavity}) and electronic properties (the charge, q, and spin densities of the TM, ρ_s) are shown for TM@$Zn_{12}S_{12}$ and TM@$Zn_{16}S_{16}$ respectively. The encapsulation energies, $\triangle G_{enc}$, in kcal/mol are given too. The cavity radii together with their standard deviations are calculated as in ref. [134, 265].

The cavity radii of bare $Zn_{12}S_{12}$ and $Zn_{16}S_{16}$ are 2.53Å and 3.10 Å respectively, with standard deviations of 0.00 and 0.03 (see ref. [134]). This indicates that these two clusters are spherical.

Comparing the r_{cavity} and the standard deviations of the calculated endohedrally doped compounds with respect to the isolated nanoclusters, it is observed that the nanoclusters do not get distorted appreciably upon encapsulation. However, if we compare these data with the data of first-row transition-metal endohedrally doped nanoclusters (see chapter 7) [132], we can notice that here the standard deviations are slightly larger. In addition, the spin densities are localized on the TM and the charges of these guest atoms are small indicating that the charge and spin transfer from the TM to the nanocluster are negligible. In order to unveil how strong the interaction between the TM and the cluster is, we have performed a Natural Bond Orbital analysis [325] for two selected cases. The first one is Y(^{4}F)@Zn_iS_i, where yttrium moves 0.97 Å from the center in the $Zn_{12}S_{12}$ cluster and 1.54 Å when it is encapsulated within the $Zn_{16}S_{16}$ cluster. In these two compounds the transition-metal was found to be bounded to two adjacent Zn atoms of the $Zn_{12}S_{12}$ cage and to four Zn atoms of the $Zn_{16}S_{16}$ cage, through

Table 8.1: R stands for the distance of the TM with respect to the center of the clusters and r_{cavity} is the cavity radius of the cluster (standard deviation in parentheses), in Å. The charge (q_x) and the spin density (ρ_S) is the transition-metals are given along with the encapsulation free energy, $\triangle G_{enc}$(kcal/mol).

		$Zn_{12}S_{12}$						$Zn_{16}S_{16}$					
	2S+1	R	r_{cavity}	Sym	q	ρ_S	$\triangle G_{enc}$	R	r_{cavity}	Sym	q	ρ_S	$\triangle G_{enc}$
Y	^2D	-	-	-	-	-	-	0.00	3.15 (0.03)	S_4	0.49	0.88	-4.31
Y	^4F	0.97	2.56 (0.20)	C_1	0.19	1.67	-25.75	1.54	3.09 (0.22)	C_1	0.24	1.82	-32.11
Zr	^3F	-	-	-	-	-	-	-	-	-	-	-	-
Zr	^5F	0.81	2.55 (0.13)	C_1	0.18	3.18	-26.05	1.49	3.09 (0.15)	C_1	-0.08	3.20	-33.16
Nb	^4F	0.97	2.56 (0.17)	C_1	0.04	2.86	-35.09	-	-	-	-	-	-
Nb	^6D	0.001	2.53 (0.05)	C_1	0.12	4.33	-24.86	1.04	3.08 (0.06)	C_1	0.13	4.42	-27.22
Mo	^5S	0.80	2.55 (0.14)	C_1	0.04	3.74	-19.15	0.88	3.14 (0.08)	C_1	0.08	3.92	-13.91
Mo	^7S	0.02	2.53 (0.01)	C_1	0.46	5.18	-9.17	0.25	3.14 (0.02)	C_{2v}	0.26	5.64	-11.15
Tc	^4D	1.01	2.54 (0.09)	C_1	-0.06	2.91	-36.97	1.56	3.09 (0.16)	C_1	-0.02	3.00	-33.43
Tc	^6S	0.77	2.53 (0.09)	C_2	0.26	4.45	-15.01	1.38	3.09 (0.07)	C_1	0.12	4.62	-17.80
Ru	^3F	1.03	2.53 (0.07)	C_1	-0.03	1.87	-45.82	1.67	3.10 (0.11)	C_1	-0.05	1.90	-43.66
Ru	^5F	0.94	2.52 (0.08)	C_1	0.21	3.49	-20.78	-	-	-	-	-	-
Rh	^2F	0.98	2.53 (0.10)	C_1	-0.01	0.85	-40.49	1.69	3.10 (0.09)	C_1	-0.08	0.87	-39.64
Rh	^4F	0.98	2.52 (0.08)	C_1	0.13	2.40	-17.96	1.56	3.09 (0.06)	C_1	0.06	2.54	-18.68
Pd	^1S	0.51	2.51 (0.03)	C_1	0.09	-	-31.51	1.46	3.09 (0.07)	C_1	0.01	-	-27.22
Pd	^3F	0.77	2.51 (0.07)	C_1	0.15	1.32	-21.29	1.59	3.08 (0.10)	C_1	-0.07	1.33	-23.07
Ag	^2S	0.08	2.52 (0.01)	C_1	0.36	0.78	3.47	0.65	3.14 (0.03)	C_1	0.20	0.86	2.94
Cd	^1S	0.005	2.55 (0.00)	C_1	0.34	-	23.41	0.00	3.13 (0.02)	D_{2d}	0.16	-	11.27

the d orbitals of the metal and the p orbitals of the Zn atoms. However, in the case of Ag@$Zn_{12}S_{12}$ (R= 0.08 Å) and Ag@$Zn_{16}S_{16}$ (R= 0.65 Å) we found that silver does not make any bond. Indeed, NBO analysis shows that there are only second order interactions between the most diffuse lone-pairs of silver and empty orbitals belonging to Zn atoms, which are oriented toward the center of the cage. Therefore, the interaction between the host and the caged atom depends on the distance of the TM from the center of the nanocluster. As a consequence, one may conclude that most of the second-row transition-metals interact strongly with the host nanocluster, with the exception of ^{6}Nb, ^{7}Mo, ^{2}Ag and ^{1}Cd.

Observing the distances with respect to the center of mass of the nanoclusters, R, it is worth noticing that in the TM@$Zn_{16}S_{16}$, the distance is larger than in TM@$Zn_{12}S_{12}$ clusters, because the matching between the size of $Zn_{12}S_{12}$ cluster and the trapped atom is more appropriate and the mobility of the TM inside this nanocluster decreases. Observe that again the ^{6}Nb, ^{7}Mo, ^{2}Ag and ^{1}Cd TM show the smallest R.

Let us consider now the encapsulation energies, $\triangle G_{enc}$. It must be emphasized that all of these endohedrally doped compounds are thermodynamically stable ($\triangle G_{enc}$ are negative) with two exceptions: Ag@Zn_iS_i and Cd@Zn_iS_i. Besides, the $\triangle G_{enc}$ indicate that the most stable clusters are those where the corresponding TM are in low-spin state, except for Y metal.

8.3.1.1 Surface-doped Structures

An alternative way for doping the Zn_iS_i nanoclusters is to place the TM on the surface of the clusters. As a consequence, these compounds do not resemble the square-hexagon structure of spheroids any more. Indeed, the insertion of the transition-metal in the surface of these nanoclusters breaks their original structure, due to the formation of the new covalent bonds between the TM and the S and Zn atoms adjacent to them. Such structures are called surface-doped structures. In this subsection the surface-doped nanoclusters will be analyzed and their properties will be discussed. For each TM, the two lowest-lying spin states have been considered, as for the endohedrally doped ones. In Table 2 the geometrical, electronic and energetic properties of the characterized local minima are given. The coordination number of the metal, given in Table 2, is calculated considering that the TM bonds to

Figure 8.2: 4-coordinated TM-$Zn_{12}S_{12}$ is depicted on the left and 2-coordinated TM-$Zn_{16}S_{16}$ surface-doped structure is shown on the right. S atoms are drawn in yellow, Zn atoms in gray and TM in green.

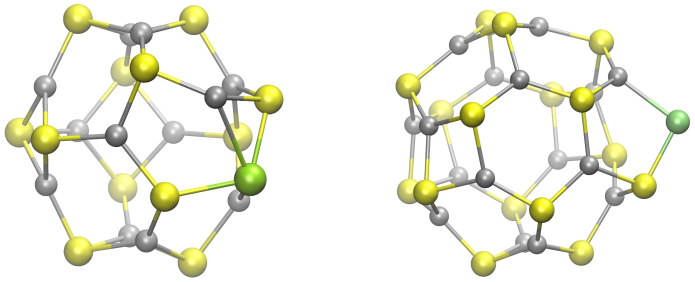

a neighbor atoms when the distance between them is smaller than the sum of the van der Waals radii of both atoms.

Different local minima have been characterized for each TM, from 2-coordinated to 6-coordinated structures. Two representative cases are depicted in Figure 8.2. For the sake of clarity the properties presented here are those corresponding to the most stable isomers. For Tc(^{4}D), Rh(^{2}F), Ag(^{2}S) and Cd(^{1}S) the coordination number is the same in both $Zn_{12}S_{12}$ and $Zn_{16}S_{16}$ compounds. However, in the rest of the nanoclusters, the coordination number is bigger in TM-$Zn_{12}S_{12}$.

Comparing the data of the endohedral nanoclusters given in Table 1 and the properties of surface structures shown in Table 2, it is observed that, in general, the spin densities and charges of TM's are larger and smaller, respectively, in the endohedral structures. This is due to the much larger interaction between TM and the remaining atoms in the surface-doped structures. Hence, in these compounds the interaction between the host and the guest atoms is larger.

The $\triangle$G's are negative for all structures except for the compounds formed by Ag and Cd, which are predicted to be thermodynamically unstable. The values of $\triangle$G indicate that the low spin states are more stable than high spin states, as it happens in the endohedral structures.

The $\triangle G_{surf-end}$= G_{surf} - G_{end} reveal that the surface-doped structures are thermodynamically more stable than the corresponding endohedral compounds. For this reason, we have searched a transition state connecting these two isomers, in order to analyze the thermal

stability of the endohedral nanoclusters. The obtained results are shown and discussed in the next subsection.

8.3.1.2 Transition States

The endohedral and surface-doped structures are connected by a transition state (TS), as it was observed in the chapter 7 [132]. In this subsection we have characterized these transition states in order to analyze the kinetic and thermal stability of the endohedral compounds. Although surface-doped structures are thermodynamically more stable, large enough barriers would prevent endohedral compounds to rearrange into the surface-doped structures. In Table 3 the energy barriers between the endohedral structures and the TS, $\triangle G^{\ddagger}$, the reaction rate constants (k) and the lifetimes of the endohedral compounds are given. The calculated energy barriers, $\triangle G^{\ddagger}$, are calculated as $\triangle G^{\ddagger} = G_{TS} - G_{end}$. These values are further used to estimate the reaction rate constants (k), at room temperature, using the Eyring equation (see subsection 8.1). The lifetime of each endohedral nanocluster is then calculated as the inverse of the reaction rate constant.

At first glance, it is worth noting that most of the calculated lifetimes are small, although most of them are predicted to be large enough as to enable experimental detection. Zr(^{5}F)@$Zn_{12}S_{12}$, Nb(^{4}F)@$Zn_{12}S_{12}$ and Rh(^{2}F)@$Zn_{12}S_{12}$ are not kinetically stable at all, as there is not any energetic barrier protecting these endohedral structures. Conversely, we must emphasize that the lifetimes of Ag(^{2}S)@Zn_iS_i and Cd(^{1}S)@Zn_iS_i are extremely large, despite their $\triangle G_{enc}$ are positive (see subsection 8.3.1). Thus, these compounds are predicted to be metastable. Note that in these two cases, along with (also in^{6}Nb and ^{7}Mo), the TM is located near the center of the nanocluster. Therefore, calculated life-times are related with the distance the trapped atom is from the center of the cage. In fact, in those cases NBO analysis showed that there is a weak interaction between the cage and the host atom. Note that the 4s3d shells are (almost) half-filled or filled in these cases, and therefore, the guest is stabilized without forming covalent bonds

Table 8.2: Surface structures and properties. q_x stands for the atomic charge, $\rho_{S_{TM}}$ for the spin density and C.N. for the coordination number of the TM. $\triangle$G is the formation free energy and $\Delta G_{surf-end}$ the energy difference between the surface and endohedral isomers (kcal/mol).

		$Zn_{12}S_{12}$					$Zn_{16}S_{16}$				
	2S+1	q_x	$\rho_{S_{TM}}$	C.N.	$\triangle$G	$\Delta G_{surf-end}$	q_x	$\rho_{S_{TM}}$	C.N.	$\triangle$G	$\Delta G_{surf-end}$
Y	2	0.72	0.05	4	-60.88	-	0.72	0.94	3	-59.72	-55.42
Y	4	0.57	0.84	8	-73.18	-47.45	0.51	1.52	5	-54.20	-22.11
Zr	3	0.50	1.33	6	-77.89	-	0.33	1.48	4	-68.69	
Zr	5	0.24	2.68	5	-50.97	-24.92	0.32	2.71	4	-44.79	-11.62
Nb	4	0.33	2.80	6	-77.45	-42.35	0.64	3.05	3	-73.53	-
Nb	6	0.01	4.05	6	-38.35	-13.49	0.08	4.01	5	-32.24	-5.05
Mo	5	0.16	4.05	4	-51.59	-32.42	0.38	4.02	3	-49.05	-35.13
Mo	7	0.32	4.89	4	-8.48	0.682	0.40	5.23	2	-8.51	2.62
Tc	4	0.09	3.10	4	-63.08	-26.082	0.19	3.11	4	-62.61	-29.15
Tc	6	0.39	4.45	3	-29.63	-14.65	0.44	4.67	2	-31.86	-14.04
Ru	3	-0.05	1.92	5	-60.13	-14.30	0.11	1.86	4	-57.15	-13.50
Ru	5	0.26	3.07	4	-26.81	-6.00	0.39	3.42	2	-25.96	
Rh	2	-0.07	0.89	4	-50.46	-9.96	-0.05	0.85	4	-45.04	-5.41
Rh	4	0.27	2.03	4	-19.78	-1.81	0.31	2.31	2	-17.80	0.87
Pd	1	-0.13	-	4	-29.94	1.60	-0.05	-	2	-25.14	2.06
Pd	3	0.25	0.93	4	-26.49	-5.21	0.23	1.10	2	-27.34	-4.24
Ag	2	0.26	0.42	2	2.72	-0.778	0.28	0.40	2	2.13	-0.81
Cd	1	0.30	-	2	15.95	-7.47	0.35	-	2	14.60	3.32

Table 8.3: Characterized transition states between endohedral compounds and surface compounds for TM@$Zn_{12}S_{12}$ and TM@$Zn_{16}S_{16}$. $\triangle G^{\ddagger}$ (kcal/mol) is the energy difference between the TS and the endohedral structure, k (s^{-1}) stands for the calculated reaction rate constant and and τ (s) are the calculated lifetimes of the endohedral isomers.

		TM@$Zn_{12}S_{12}$			TM@$Zn_{16}S_{16}$		
	2S+1	$\triangle G^{\ddagger}$	k	τ	$\triangle G^{\ddagger}$	k	τ
Y	2	-	-	-	-	-	-
Y	4	-	-	-	-	-	-
Zr	3	-	-	-	-	-	-
Zr	5	-0.66	-	-	9.19	1.14×10^{6}	8.78×10^{-7}
Nb	4	-0.59	-	-	-	-	-
Nb	6	9.74	4.50×10^{5}	2.22Â·$\times10^{-6}$	13.20	1.31×10^{3}	7.64×10^{-4}
Mo	5	7.51	1.94×10^{7}	5.15×10^{-8}	-	-	-
Mo	7	14.65	1.13×10^{2}	8.83×10^{-3}	17.12	1.75	0.57
Tc	4	6.53	1.01×10^{8}	9.85×10^{-9}	0.96	1.23×10^{12}	8.14×10^{-13}
Tc	6	5.30	8.09×10^{8}	1.24×10^{-9}	6.30	1.50×10^{8}	6.68×10^{-9}
Ru	3	8.63	2.93×10^{6}	3.41×10^{-7}	5.03	1.28×10^{9}	7.84×10^{-10}
Ru	5	7.22	3.17×10^{7}	3.15Â·$\times10^{-8}$	-	-	-
Rh	2	-0.84	-	-	3.30	2.37×10^{10}	4.22×10^{-11}
Rh	4	14.00	3.39×10^{2}	2.95Â·$\times10^{-3}$	9.11	1.30×10^{6}	7.67×10^{-7}
Pd	1	13.93	3.82×10^{2}	2.62×10^{-3}	10.63	1.00×10^{5}	9.98×10^{-6}
Pd	3	5.69	4.19×10^{8}	2.39Â·$\times10^{-9}$	2.72	6.30×10^{10}	1.59×10^{-11}
Ag	2	21.26	1.62×10^{-3}	6.18×10^{2}	24.44	7.55×10^{-6}	1.32×10^{5}
Cd	1	27.07	8.91×10^{-8}	1.12×10^{7}	39.70	4.92×10^{-17}	2.03Â·$\times10^{16}$

with the host, like the remaining cases. Nevertheless, note that lifetimes of atoms with semi-filled shells are much smaller, since they are able to form more stable surface-structures than Ag and Cd.

Finally, it should be pointed out that, in general, second-row transition-metal doped nanoclusters are thermodynamically more stable, so they have longer lifetimes, than first-row ones.

8.3.1.3 Silver-doped Dimers

Transition-metal compounds are interesting, among other features, due to their magnetic properties. Therefore, endohedral nanoclusters with large enough lifetimes would lead to materials with combined magnetic and semiconducting properties. In this vein, the only magnetic endohedral structures with large enough lifetimes are those of silver, since Ag atoms have one unpaired electron. We have studied both the ferromagnetic and antiferromagnetic coupling on $(Ag@Zn_{12}S_{12})_2$ and $(Ag@Zn_{16}S_{16})_2$ dimers and calculated the exchange-magnetic coupling, J.

Both $Zn_{12}S_{12}$ and $Zn_{16}S_{16}$ nanoclusters can be linked together in different ways as they are made up of squares and hexagons. In a previous work with similar compounds (see chapter 6) [267], it was observed that the most stable dimers are those which are bonded via hexagon-to-hexagon. Accordingly, we have made the dimers linking the monomers through their hexagons. In this manner we have considered the magnetic exchange coupling of the two Ag centers. First, we have calculated the ferromagnetic state, where the two unpaired electrons of the silver atoms (one unpaired electron on each Ag atom) are spin parallel (triplet state), and the antiferromagnetic state, where the unpaired electron of one Ag atom is spin up and the other unpaired electron of the second Ag is spin down (singlet state).

In Table 8.4 the data corresponding to the characterized dimers are given. For both cases the dimerization energies are negative, specially for $(Ag@Zn_{16}S_{16})_2$, meaning that the formation of these dimers is thermodynamically allowed.

The exchange coupling constant, J, for $(Ag@Zn_{12}S_{12})_2$ reveals that the antiferromagnetic interaction is clearly favored. However, in the case of $(Ag@Zn_{16}S_{16})_2$, the value of J is very small indicating that there is a competition between ferromagnetic and antiferromagnetic

Table 8.4: Symmetry of the dimers and the distance between the two Ag atoms, R_{Ag-Ag}, in Å. The dimerization energies, $\triangle G_{dim}$, are given in kcal/mol. J is the exchange coupling constant (cm^{-1}) and $< S^2 >_{HS}$ and $< S^2 >_{BS}$ are the spin expectation values of high spin and broken symmetry states respectively.

Dimer	Symm	R_{Ag-Ag}	$\triangle G_{dim}$	J	$< S^2 >_{HS}$	$< S^2 >_{BS}$
$(Ag@Zn_{12}S_{12})_2$	C_i	6.65	-5.81	-133.93	2.0029	0.9670
$(Ag@Zn_{16}S_{16})_2$	C_{2h}	8.69	-13.92	0.63	2.0028	1.0027

states. Indeed, the distance between the two magnetic centers is much smaller in $(Ag@Zn_{12}S_{12})_2$ than in $(Ag@Zn_{16}S_{16})_2$ (6.65 and 8.69 Å respectively) due to the size of the clusters. Thus, we can conclude that silver atoms tend to couple between them antiferromagnetically in short distances, but the AF and F coupling are near-degenerate when increasing the distance, in agreement with previous calculations in related systems [315]. Hence, control of the TM-TM distance would lead to different magnetic properties. Regarding the assembly in 2D or 3D, the endohedral doping facilitates the control of the distance between guest metals, since the position of the TM at the center of the cage is well defined. Therefore, assemblies of small clusters would lead to AF materials, while assemblies of large clusters would lead to F materials, being the AF coupling close in energy. Moreover, considering the Ag-Ag distances in these dimers, along with related studies on other encapsulated X@ZnS and X@CdS assemblies [250, 267], we suggest that the Ag-Ag distances would remain quite similar in the solid compared to the dimers.

In Figure 8.3 the spin density of the most stable states are depicted, i. e., the ferromagnetic $(Ag@Zn_{12}S_{12})_2$ and the antiferromagnetic $(Ag@Zn_{16}S_{16})_2$. Observe that in the former electron of Ag_1 is spin up and electron of Ag_2 is spin down, while in $(Ag@Zn_{16}S_{16})_2$ dimer, the unpaired electron of each Ag atom have the same sign. Finally, the spin expectation values show that, although there is spin contamination, it is small.

Figure 8.3: The spin density of the the antiferromagnetic $(Ag@Zn_{12}S_{12})_2$ and the ferromagnetic $(Ag@Zn_{16}S_{16})_2$ structures.

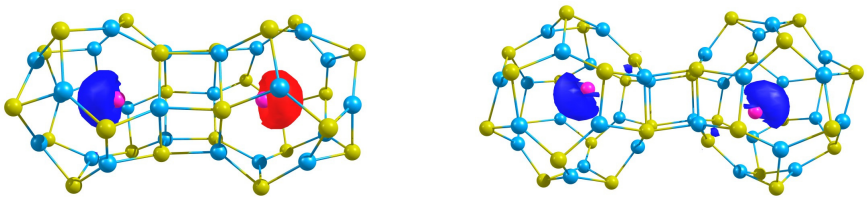

8.4 Conclusions

The thermal stability of the second-row transition-metal-doped $TM@Zn_iS_i$ nanoclusters (i=12, 16) has been analyzed. On the basis of the calculated energy differences between the endohedral compounds and the TS compounds that connect the former with the surface-doped structures, we have estimated the lifetime of each endohedral structure. Although surface-doped structures are thermodynamically more stable than endohedral ones, large enough barriers would prevent endohedral compounds to rearrange into the surface-doped structures. As mentioned before, these techniques are approximate. Hence, the data obtained have not to be taken quantitatively, but qualitatively. In spite of that, the data obtained are very enlightening, as all the calculated lifetimes are very small, indicating that most of the endohedrally doped nanoclusters are not thermally stable. However there are two exceptions: the lifetimes of $Ag(^2S)@Zn_iS_i$ and $Cd(^1S)@Zn_iS_i$ are extremely large. These compounds are predicted to be metastable. This metastability is associated to the electronic structure of Ag and Cd, where the 3d and 4s shells are almost or completely filled. As mentioned in the Introduction, no experiments have been carried out regarding endohedral II-VI compounds. Nevertheless, hollow bare II-VI structures have been characterized experimentally by Belbruno and coworkers [57, 58]. They generated these structures by means of direct laser ablation, and then the generated compounds were analyzed in a time-of-flight mass spectrometer. We believe that this technique could also be used for the detection of endohedral compounds.

Since Cd does not have magnetic properties because it is a closed-shell transition-metal, we have focused on silver doped nanoclusters, i. e., $Ag@Zn_{12}S_{12}$ and $Ag@Zn_{16}S_{16}$. We have characterized $(Ag@Zn_{12}S_{12})_2$

and $(Ag@Zn_{16}S_{16})_2$ magnetic dimers and calculate their exchange coupling constant, J. In the case of $(Ag@Zn_{12}S_{12})_2$, J reveals that the antiferromagnetic interaction is clearly favored. Conversely, in the case of $(Ag@Zn_{16}S_{16})_2$, the value of J is small but positive indicating a weak ferromagnetic coupling between the two encapsulated silver atoms. This difference is ascribed to the Ag-Ag distance. Short Ag-Ag distances lead to antiferromagnetic coupling, while long distances stabilize the ferromagnetic coupling. These results are in agreement with those obtained for related II-VI compounds.

Part IV

Summary and Final Remarks

Chapter 9

Summary and Final Remarks

Nanotechnology offers the possibility of creating materials with novel properties, due to the unique nature of nanoscaled compounds. Control of the composition and structure of nanomaterials allows the tuning and optimization of their properties. Hollow binary nanoclusters of II-VI semiconductor elements have been widely studied in the literature, both theoretically and experimentally. However, studies of the properties of endohedral compounds made of II-VI hollow nanoclusters are scarce. It is worth noting that the advantage of endohedral doping compared to other ways of doping is the better control of dopant-dopant distance in the assembled materials. The aim of this thesis has been to shed light on this field, studying the stability of endohedrally doped CdS and ZnS nanoclusters, in order to predict the feasibility of their further synthesis, along with their physico-chemical properties. We propose that using endohedrally doped selected $(ZnS)_i$ and $(CdS)_i$ hollow clusters represents a wiser choice to achieve materials new traits, because (i) the stability of the cluster structures themselves are not compromised by the endohedral doping and (ii) a larger variety of properties can be tailored by such doping. Additionally, the possibility of using such tailored nanoclusters as building blocks for cluster assembled dimers and solids has been considered.

The clusters studied in this thesis, $(CdS)_i$ and $(ZnS)_i$ (i= 9, 12, 15, 16), are made of squares and hexagons, where Cd (Zn) atoms are located in the inner part of the cluster and S atoms in the outer part of it. They are chosen because their high symmetry, which favors the clus-

ters to retain their structural identity upon doping. We have analyzed the structure and stability of these compounds on the basis of density functional theory and quantum molecular dynamics simulations.

Endohedrally Doped CdS Nanoclusters First, we have considered all possible $(X@(CdS)_i)^q$ endohedral compounds, with i= 4, 9, 12, 15, 16; q= 0, ± 1, ± 2 and X= Na, K, Be, Mg, Ca, Cl, Br, O, S, Se. It has been observed that in these compounds the charge is mainly located on the dopant atoms and, importantly, in most of the cases the nanoclusters do retain their structure upon the doping.

The negatively charged compounds are more stable than the positively charged ones. Since cadmium atoms are in the inner part of the clusters, dopant atoms interact directly with them, being this interaction attractive in the case of (di)anions and repulsive in the (di)cationic compounds. Indeed, when halogens and chalcogens are trapped inside the cage, the cluster gets squeezed (specially in the case of dianions) and when metals are incarcerated inside the clusters, they get enlarged (specially in the case of alkali earth metals). These Coulombic interactions are also responsible of the lower stability of (di)cationic compounds compared to (di)anionic ones. This fact is reflected in the large number of stable (di)anionic systems, while only few of the (di)cationic clusters are stable. Moreover, (di)cationic compounds, even those with negative encapsulation energies, are predicted to be metastable. This fact clearly suggests that the charge of the dopant atom is a critical factor for the endohedral doping.

In addition, the encapsulation and deformation energies of dicationic and dianionic compounds are larger than those of the monocationic and monoanionic compounds. It should be highlighted that there is an important difference between alkaline and earth alkaline metals-doped clusters: in the former, potassium repeals Cd atoms. In the case of dications, however, they not only repeal cadmium atoms but they are also able to attract sulfur atoms. This fact entails big deformation energies, despite the nanoclusters retain their structural motif and do not break.

Another important component affecting the endohedral doping is the appropriate matching between the size of the guest atom and the size of the cage. For instance, $(Se@(CdS)_9)^{-2}$ is predicted to be thermally unstable due to the big size of Se^{-2} (the biggest chalcogen atom considered in this work) relative to the size of the $(CdS)_9$ cavity. Like-

wise, for the biggest nanocluster, $(CdS)_{16}$, only the biggest alkaline earth metal is encapsulated (Ca), while for the smallest earth alkaline metal (Be), only one of the smallest nanocluster, $(CdS)_{12}$ is able to trap it, emphasizing size matching as one key factor in the stability of endohedral nanoclusters.

Thus, overall, the stability of the resulting structures can be rationalized in terms of three parameters. The first one is the appropriate matching between the size of the nanocluster, and the size of the trapped atom. The second one is the charge of the trapped atom: negatively charged guest atoms are found to be the thermodynamically most stable ones. The third one is the shape of the nanocluster: the spherical nanoclusters are more prone to incarcerate atoms than the irregular ones, as it was previously demonstrated by Matxain *et al.* [134].

Regarding the properties of the endohedrally doped nanoclusters, it has been found that their optoelectronic properties are changed upon the doping. On the one hand, endohedral K doping of the $(CdS)_i$ nanoclusters lowers the ionization energy from $\sim$ 7.8 eV to a value between 5.24 and 5.74 eV, which is similar to that of potassium atom. Likewise, the calculated electron affinities of the halogen endohedral clusters are substantially larger than those of the corresponding guest atoms. Hence, these endohedral nanoclusters may be seen as superhalogens. The reason is that the isolated Cd_iS_i nanoclusters have a closed shell electronic structure. However, when an alkali is trapped inside the cage, an electron is transferred to the lowest unoccupied molecular orbital (LUMO) of the bare nanocluster. This electron can more easily be removed than one from the highest occupied molecular orbital (HOMO) of the isolated cluster, decreasing the ionization potential. Similarly, when a halogen atom is trapped, it takes an electron from the surface, and now the HOMO orbital is singly occupied, therefore increasing the electron affinity with respect to the isolated cluster.

On the other hand, our calculations reveal an oscillatory pattern of the lowest-lying electronic excitations with the increasing size of the cluster. So, in the ultrasmall size regime considered here the properties change discontinuously with cluster dimensions. Their calculated band-gaps decreased as compared to the band-gap of the bulk CdS wurtzite, thus showing the expected blueshift. The higher-lying occupied states arise from the S 3p orbitals, whereas the lowest-lying unoc-

cupied states are comprised primarily of Cd 5s orbitals. Furthermore, we have shown that doping these clusters with chalcogens and earth alkali metals also modifies notably the optical spectra of nanoclusters, as the absorption spectra shift to lower energies upon encapsulation. The calculated optical properties of the endohedral compounds differ significantly from those of the exohedral isomers studied, and therefore they could serve experimentalists as fingerprints of such compounds for their detection.

Self-assembling of Endohedrally Doped CdS Nanoclusters One of the significant developments in the field of nanoclusters is the possibility of building materials where individual stable clusters serve as the elementary building blocks. The first step towards this goal is to identify designer clusters that are interesting and stable enough as to maintain their identity and individual features upon assembly. The discovery of fullerenes and the eventual synthesis of fullerides is just one example of such a possibility. Extending the fullerene experience to semiconductor systems is therefore an important task. Thus, we have considered the assembly of bare and potassium and halogen doped $(CdS)_{12}$ and $(CdS)_{16}$ nanoclusters into solids. As these clusters are composed of hexagons and squares, we have considered three different ways of linking them together, namely, by their hexagons, squares and edges. First of all, dimers have been characterized, in order to use them as starting point for the unit cell of the solids. Interestingly, the main structural patterns of the monomers are unaffected by dimerization, proving the high stability of $(CdS)_{12}$ and $(CdS)_{16}$ nanoclusters.

Since the potential ionizations of potassium doped nanoclusters and the electron affinities of halogen doped ones are very similar, it leads to a formal charge transfer from the potassium to the halogen, resulting in a cation and an anion trapped in two hollow neutral $(CdS)_i$ clusters. All the dimers are predicted to be thermodynamically stable. In all bare and doped dimers the stability decreases when the number of bonds between monomers decreases too. Comparing the dimerization energies of $(CdS)_{12}$ and $(CdS)_{16}$ reveals that they are very similar. So, we can conclude that the size is not a determinant factor for the thermodynamic stability of dimers. HOMO-LUMO gaps shows that the endohedral doping significantly reduces the gap. Cl and Br have similar effects.

Finally, six different CdS phases have been designed, where the building blocks are linked by covalent Cd-S bonds. The endohedrally doped solids are more stable than their corresponding counterparts, due to the electrostatic interaction between potassium and halogens. This stabilization due to the doping is also observed in the dimers. However, the least stable dimers (those linked by edges) lead to the most stable solids, and vice-versa. To rationalize this fact, the compactness of the solids has to be taken into consideration. Hence, in all cases the SOD phase has the largest cohesive energy, being the thermodynamically most stable solid and the most compact CdS phase studied in this work.

The analysis of the band gaps at the Γ point shows that all the solids are predicted to be semiconductors. Moreover, the band-gaps highly decrease when doping these solids because some of the dopants's states occupy bands which are located between the valence and the conduction bands. The valence band of the bare solids is made mainly by the 3p atomic orbitals of the sulfur atoms and the largest contribution to the conduction band comes from the 5s orbitals of the cadmium atoms. Finally, quantum molecular dynamics simulations carried out at 350 and 400 K are representative of the thermal stability of the characterized solids.

Thus, we conclude that it should be possible to stabilize new nanoporous solid phases of CdS. The solids characterized in this work are less compact than wurtzite and zincblende. This fact has two important consequences: it makes these new materials thermodynamically metastable. Conversely, they might have many applications, due to their large pores, in heterogeneous catalysis and as storage materials.

Endohedrally Doped ZnS Nanoclusters Regarding the endohedrally doped nanoclusters with transition-metals, substitutional doped compounds are in general more stable than endohedrally doped systems, according to literature. However, the latter presents a very important feature in dealing with the magnetic properties of 2D or 3D cluster-assembled materials, as the TM-TM distance would be fixed. In fact, the magnetic properties of such materials have been found to be connected with the TM - TM distances in related materials [315]. At short distances, the antiferromagnetic coupling is favored, while the enlargement of this distance leads to a near-degeneracy of both AF and F states. Therefore, it appears interesting to find sufficiently

stable endohedrally doped materials, in order to design materials with well fixed magnetic properties.

With this aim, we have examined all possible TM@$(ZnS)_i$ endohedral compounds, with i= 12 and 16 and TM= first- and second-row transition-metals, considering the two lowest-lying spin-states of each metal. The the first-row transition-metal-doped nanoclusters were previously characterized and suggested to be thermodynamically stable by Matxain *et al.* [239]. But we have seen that the metal atom can move towards the surface of the nanocluster, breaking it and forming the so-called surface-doped structure.

Regarding endohedrally doped nanoclusters, it is notable that the nanoclusters do not get distorted appreciably upon encapsulation. On the contrary, the surface-doped compounds do not resemble the square-hexagon structure of bare spheroids in the neighborhood of the TM. The TM breaks some of the Zn-S bonds and forms new polarized covalent bonds with a number of Zn and S atoms. Different local minima have been characterized for each TM, with different coordination numbers. In general spin densities and charges of TM's are smaller and larger, respectively, in the surface-doped structures comparing to the endohedral ones. This is due to the much larger interaction between TM and the remaining atoms in the surface-doped structures. Hence, in these compounds the interaction between the host and the guest atoms is larger. Oppositely, in the endohedral structures the TM trapped inside maintains its atomic-like properties, being the interaction with the cage weak.

In order to determine the thermal stability of these endohedral structures, we have carried out quantum molecular dynamics simulations for several endohedrally doped first-row TM nanoclusters. Some of the clusters have been found to break apart during the simulation, because the TM goes to the surface. These simulations are computationally expensive and they may not be determining. In order to complement the quantum molecular dynamics simulations, we have additionally characterized the surface-doped structures for each first- and second-row TM-doped compounds, along with the TS's connecting both isomers. In this manner we have estimated the lifetime of each endohedral nanocluster using the calculated energy barriers for the endohedral-doped to surface-doped transformations. Thus, our aim is to point out potential stable structures.

We must point out that both techniques are approximate. On the

one hand, one single MD simulation is not representative, i.e., we are replacing a full sampling on the appropriate statistical ensemble by a single trajectory. On the other, lifetimes are calculated from the reaction rate constants. These reaction rate constants are very sensitive with respect to the activation energies. Consequently, the data obtained with both methodologies should not to be taken quantitatively, but qualitatively. Nevertheless, the obtained data are very enlightening. Indeed, most of the endohedrally doped transition-metal nanoclusters are not the global minima, but local minima, with very short life-times, although could be large enough for experimental detection. However, there are three exceptions: Zn, Cd and Ag endohedrally doped systems. These compounds, although metastable, are predicted to have very long life-times. This metastability is associated to the electronic structure of these transition-metals, where the d and s shells are almost or completely filled. Unfortunately, Zn and Cd do not have magnetic properties because they have closed-shell electronic structures. Fortunately, silver doped nanoclusters does, since Ag atoms have one unpaired electron. Hence, we have studied both the ferromagnetic and antiferromagnetic coupling on $(Ag@Zn_{12}S_{12})_2$ and $(Ag@Zn_{16}S_{16})_2$ dimers, bonded via hexagon-to-hexagon. For both cases the dimerization energies are negative, meaning that the formation of these dimers is thermodynamically allowed. The exchange coupling constant, J, for $(Ag@Zn_{12}S_{12})_2$ reveals that the antiferromagnetic interaction is clearly favored. However, in the case of $(Ag@Zn_{16}S_{16})_2$, the value of J is very small indicating that there is a competition between ferromagnetic and antiferromagnetic states. Indeed, the distance between the two magnetic centers is much smaller in $(Ag@Zn_{12}S_{12})_2$ than in $(Ag@Zn_{16}S_{16})_2$ due to the size of the clusters. Thus, we can conclude that silver atoms tend to couple between them antiferromagnetically in short distances, but the AF and F coupling are near-degenerate when increasing the distance.

It is evident that the intrinsic versatility of the transition-metals, due to their d orbitals, do not favor the endohedral structures. In $(X@(CdS)_i)^q$ compounds, however, the electrostatic interaction plays a major role: both the Coulombic repulsion and the Coulombic attraction makes the guest atom to be trapped inside the cage. Furthermore, the electrostatic attraction between the dopant and the cadmium atoms seems to be a guarantee of stability. In addition, all the dopant atoms change the physico-chemical properties of the CdS and

ZnS nanoclusters. So, the work done in this thesis shows the wide range of possibilities that the endohedral doping offers to tailor the traits of clusters. Finally, it is clear that the theoretical prediction is a powerful tool, also to dismiss compounds that are not feasible.

The potential technological applications of these newly designed II-VI nanoclusters in a large variety of fields, like solar cells, heterogeneous catalysis, molecular transport, optical sensors, atomic or molecular sieves, and so on, makes the searching of new stable nanoclusters for such materials worthwhile. Within this context, the theoretical investigations reported herein could help, or guide, experimentalists towards such a goal.

Bibliography

[1] G. Binning, H. Rohrer, Ch. Gerber, and E. Welbel, *Phys. Rev. Lett.*, **1982**, *49*, 57.

[2] G. Binning, F. Quate, and Ch. Gerber, *Phys. Rev. Lett.*, **1986**, *56*, 930.

[3] W. D. Knight, K. Clemenger, W. A. de Heer, W. A. Saunders, M. Y. Chou, and M. L. Cohen, *Phys. Rev. Lett.*, **1984**, *52*, 2141.

[4] H. W. Kroto, H. R. Heath, S. C. O'Brien, R. F. Curl, and R. E. Smalley, *Nature*, **1985**, *318*, 162.

[5] A. W. Castleman Jr. and P. Jena, *PNAS*, **2006**, *103*, 10554.

[6] A. P. Alivisatos, *J. Phys. Chem. C*, **1996**, *100*, 13226.

[7] C. N. R. Rao, G. U. Kulkarni, P. J. Thomas, and P. P. Edwards, *Chem. Soc. Rev.*, **2000**, *29*, 27.

[8] T. Pellegrino, S. Kudera, T. Liedl, A. M. Javier, L. Manna, and W. J. Parak, *Small*, **2005**, *1*, 48.

[9] Y. Zhu, R. Jin, and Y. Sun, *Catalysts*, **2011**, *1*, 3.

[10] E. Osawa, *Kagaku*, **1970**, *25*, 854.

[11] L. D. Marks, *Rep. Prog. Phys.*, **1994**, *57*, 603.

[12] B. K. Teo, *J. Clust. Sci.*, **2014**, *25*, 5.

[13] T. P. Martin, T. Bergmann, H. Gohlich, and T. Lange, *Chem. Phys. Lett.*, **1990**, *172*, 209.

[14] H. W. Kroto, *Nature*, **1987**, *329*, 529.

[15] M. Terrones, *Annu. Rev. Mater. Res.*, **2003**, *33*, 419.

[16] A. K. Geim, *Science*, **2009**, *324*, 1530.

[17] A. D. Zdetsis, *Phys. Rev. B*, **2007**, *76*, 075402.

[18] A. D. Zdetsis, *Phys. Rev. B*, **2009**, *80*, 195417.

[19] D. Palagin and K. Reuter, *Phys. Rev. B*, **2012**, *86*, 045416.

[20] T. Lange, H. Gohlich, T. Bergmann, and T. P. Martin, *Z. Phys. D*, **1991**, *19*, 113.

[21] A. N. Alexandrova and A. I. Boldyrev, *J. Chem. Theory Comput.*, **2005**, *1*, 566.

[22] J. E. Fowler and J. M. Ugalde, *Phys. Rev. A*, **1998**, *58*, 383.

[23] X. Li, H. Wu, X. Wang, and L. Wang, *Phys. Rev. Lett.*, **1998**, *81*, 1909.

[24] R. Ahlrichs and S. D. Elliott, *Phys. Chem. Chem. Phys*, **1999**, *1*, 13.

[25] L. Wang and L. Wang, *Nanoscale*, **2012**, *4*, 4038.

[26] K. Yabana and G. F. Bertsch, *Phys. Rev. A*, **1999**, *60*, 3809.

[27] S. Bulusu, X. Li, L.S. Wang, and X. C. Zeng, *Proc.Natl. Acad. Sci.*, **2006**, *103*, 8326.

[28] K. Koga, T. Ikeshoji, and K. Sugawara, *Phys. Rev. Lett.*, **2004**, *92*, 115507.

[29] R. Rousseau, G. Dietrich, S. Kruckeberg, K. Lutzenkirchen, D. Marx, L. Schweikhard, and C. Walther, *Chem. Phys. Lett.*, **1998**, *295*, 41.

[30] Jean-Philippe Sylvestre, Andrei V. Kabashin, Edward Sacher, Michel Meunier, and John H. T. Luong, *J. Am. Chem. Soc.*, **2004**, *126*(23), 7176–7177.

[31] L. Wang and L. Wang, *Nanoscale*, **2012**, *4*, 4038.

[32] W. Ekardt, *Phys. Rev. B*, **1984**, *29*, 1558.

[33] K. Chuchev and J. BelBruno, *J. Phys. Chem. A.*, **2005**, *109*, 1564.

[34] S. S. Alexandre, H. Chacham, and R. W. Nunes, *Phys. Rev. B*, **2001**, *63*, 045402.

[35] F. Jensen and H. Toftlund, *Chem. Phys. Lett.*, **1993**, *201*, 89.

[36] G. Seifert, P. W. Fowler, D. Mitchell, D. Porezag, and Th. Frauenheim, *Chem. Phys. Lett.*, **1997**, *268*, 352.

[37] T. Oku, T. Hirano, M. Kuno, T. Kusunose, K. Niihara, and K. Suganuma, *Mat. Sci. Eng.*, **2000**, *B74*, 206.

[38] T. Oku, M. Kuno, H. Kitahara, and I. Narita, *Int. J. Inorg. Mat.*, **2001**, *3*, 597.

[39] T. Oku, A. Nishiwaki, and I. Narita, *Sci. Tech. Adv. Mat.*, **2004**, *5*, 635.

[40] S. S. Alexandre, M. S. C. Mazzoni, and H. Chacham, *Appl. Phys. Lett.*, **1999**, *75*, 61.

[41] D. L. Strout, *J. Phys. Chem. A*, **2000**, *104*, 3364.

[42] T. Oku, A. Nishiwaki, and I. Narita, *Physica B*, **2004**, *531*, 184.

[43] J. Beheshtian, M. Kamfiroozi, Z. Bagheru, and A. Ahmadi, *Comp. Mat. Sci.*, **2012**, *54*, 115.

[44] H. Wu, F. Zhang, X. Xu, C. Zhang, and H. Jiao, *J. Phys. Chem. A*, **2003**, *107*, 204.

[45] V. Tozzini, F. Buda, and A. Fasolino, *Phys. Rev. Lett.*, **2000**, *85*, 4554.

[46] G. L. Gutsev, R. H. O'Neal Jr., B. C. Saha, M. D. Mochena, E. Johnson, and C. W. Bauschlicher Jr., *J. Phys. Chem. A*, **2008**, *112*, 10728.

[47] B. Brena and L. Ojamae, *J. Phys. Chem. C*, **2008**, *112*, 13516.

[48] J. Beheshtian, Z. Bagheri, M. Kamfiroozi, and A. Ahmadi, *J. Mol. Model.*, **2012**, *18*, 2653.

[49] S. A. Shevlin, Z. X. Guo, H. J. J. van Dam, P. Sherwood, C: R: A. Catlow, A. A. Sokol, and S. M. Woodley, *Phys. Chem. Chem. Phys.*, **2008**, *10*, 1944.

[50] C. Harris and P. V. Kamat, *ACS Nano*, **2009**, *3*, 682.

[51] D. Jimenez de Aberasturi, J. Montenegro, I. Ruiz de Larramendi, T. Rojo, T. A. Klar, R. Alvarez-Puebla, L. M. Liz-Marzan, and W. J. Parak, *Chem. Mater.*, **2012**, *24*, 738.

[52] P. V. Kamat, *J. Phys. Chem. C*, **2008**, *112*, 18737.

[53] T. Nann and W. M. Skinner, *ACS Nano*, **2011**, *5*, 5291.

[54] I. L. Medintz, H. T. Uyeda, E. R. Goldman, and H. Mattoussi, *Nat. Mater.*, **2005**, *4*, 435.

[55] K. Koyasu, K. Komatsu, and F. Misaizu, *J. Chem. Phys.*, **2013**, *139*, 164308.

[56] A. Burnin and J. J. BelBruno, *Chem. Phys. Lett.*, **2002**, *362*, 341.

[57] A. Burnin, E. Sanville, and J. J. BelBruno, *J. Phys. Chem. A*, **2005**, *109*, 5026.

[58] E. Sanville, A. Burnin, and J. J. BelBruno, *J. Phys. Chem. A*, **2006**, *110*, 2378.

[59] L. M. Kukreja, A. Rohlfing, P. Misra, F. Hillenkamp, and K. Dreisewerd, *Appl. Phys. A*, **2004**, *78*, 641.

[60] A. Dmytruk, I. Dmitruk, and A. Kasuya, *Mat.-wiss. u. Werstofftech*, **2009**, *40*, 265.

[61] A. Dmytruk, I. Dmitruk, I. Blonskyy, R. Belosludov, Y. Kawazoe, and A. Kasuya, *Microelectr. J.*, **2009**, *40*, 218.

[62] S. M. Harrel, J. R. McBride, and S. J. Rosenthal, *Chem. Mater.*, **2013**, *25*, 1199.

[63] J. R. McBride, A. D. Dukes III, M. A. Schreuder, and S. J. Rosenthal, *Chem. Phys. Lett.*, **2010**, *498*, 1.

[64] J. C. Newton, K. Ramasamy, M. Mandal, G. K. Joshi, A. Kumbhar, and R. Sardar, *J. Phys. Chem. C*, **2012**, *116*, 4380.

[65] C. M. Evans, A. M. Love, and E. A. Weiss, *J. Am. Chem. Soc.*, **2012**, *134*, 17298.

[66] H. Chen and R. V. Kumar, *RSC Adv.*, **2012**, *2*, 11586.

[67] Y. Park, A. Dmytruk, I. Dmitruk, A. Kasuya, Y. Okamoto, N. Kaji, M. Tokeshi, and Y. Baba, *J. Phys. Chem. C*, **2010**, *114*, 18834.

[68] A. Kasuya, R. Sivamohan, Y. A. Barnakov, I. M. Dmitruk, T. Nirasawa, V. R. Romanyuk, V. Kumar, S. V. Mamykin, K. Tohji, B. Jeyadevan, K. Shinoda, T. Kudo, O. Terasaki, Z. Liu, R. V. Belosludov, V. Sundararajan, and T. Kavazoe, *Nat. Mat.*, **2004**, *3*, 99.

[69] A. Kasuya, Y. Noda, I. Dmitruk, V. Romanyuk, Y. Barnakov, K. Tohji, V. Kumar, R. Belosludov, Y. Kawazoe, and N. Ohuchi, *Eur. Phys. J. D*, **2005**, *34*, 39.

[70] J. Alvarez-Ruiz, M. Lopez-Arias, R. de Nalda, and M. Martin, *Appl. Phys. A*, **2008**, *92*, 831.

[71] J. Alvarez-Ruiz, M. Lopez-Arias, R. de Nalda, M. Martin, A. Arregui, and L. Bañares, *Appl. Phys. A*, **2009**, *95*, 681.

[72] Y. Wang, Y. Liu, Y. Zhang, F. Wang, P. J. Kowalski, H. W. Rohrs, R. A. Loomis, M. L. Gross, and W. E. Buhro, *Angew. Chem. Int. Ed.*, **2012**, *51*, 6154.

[73] Jon M Azpiroz, Jon M Matxain, Ivan Infante, Xabier Lopez, and Jesus M Ugalde, *Phys. Chem. Chem. Phys.*, **2013**, *15*, 10996–11005.

[74] K. A. Nguyen, P. N. Day, and R. Pachter, *J. Phys. Chem. C*, **2010**, *114*, 16197.

[75] W. Sangthong, J. Limtrakul, F. Illas, and S. T. Bromley, *Nanoscale*, **2010**, *2*, 72.

[76] S. M. Woodley, A. A. Sokol, and C. R. A. Catlow, *Z. Anorg. Allog. Chem.*, **2004**, *630*, 2343.

[77] J. M. Matxain, J. M. Mercero, J. E. Fowler, and J. M. Ugalde, *J. Phys. Chem. A*, **2003**, *107*, 9981.

[78] J. M. Matxain, J. E. Fowler, and J. M. Ugalde, *Phys. Rev. A*, **2000**, *62*, 53201.

[79] A. Al-Sunaidi, A. A. Sokol, C. R. A. Catlow, and S. M. Woodley, *J. Phys. Chem. C*, **2008**, *112*, 18860.

[80] B. Wang, S. Nagase, J. Zhao, and G. Wang, *J. Phys. Chem. C.*, **2007**, *111*, 4956.

[81] J. M. Matxain, J. E. Fowler, and J. M. Ugalde, *Phys. Rev. A*, **2000**, *61*, 53201.

[82] J. M. Matxain, J. M. Mercero, J. E. Fowler, and J. M. Ugalde, *Phys. Rev. A*, **2001**, *64*, 53201.

[83] J. M. Matxain, J. M. Mercero, J. E. Fowler, and J. M. Ugalde, *J. Phys. Chem. A*, **2004**, *108*, 10502.

[84] S. Hamad, S. M. Woodley, and C. R. A. Catlow, *Mol. Sim.*, **2009**, *35*, 1015.

[85] S. Hamad, C. R. A. Catlow, E. Spano, J. M. Matxain, and J. M. Ugalde, *J. Phys. Chem. B*, **2005**, *109*, 2703.

[86] E. Spanó, S. Hamad, and C. R. A. Catlow, *Chem. Comm.*, **2004**, page 864.

[87] S. Hamad and C. R. A. Catlow, *J. Cryst. Growth*, **2006**, *294*, 2.

[88] D. C. Sayle, B. C. Mangili, J. Klinowski, and T. X. T. Sayle, *J. Am. Chem. Soc.*, **2006**, *128*, 15283.

[89] B. J. Morgan, *Phys. Rev. B*, **2008**, *78*, 024110.

[90] J. Joswig, S. Roy, P. Sarkar, and M. Springborg, *Chem. Phys. Lett.*, **2002**, *365*, 75.

[91] J. Joswig, M. Springborg, and G. Seifert, *J. Phys. Chem. B*, **2000**, *104*, 2617.

[92] C. E. Junkermeier, J. P. Lewis, and G. W. Bryant, *Phys. Rev. B*, **2009**, *79*, 125323.

[93] M. Li, J. Ouyang, C. I. Ratcliffe, L. Pietri, X. Wu, D. M. Leek, I. Moudrakovski, Q. Li, B. Yang, and K. Yu, *ACS Nano*, **2009**, *3*, 3832.

[94] F. S. Riehle, R. Bienert, R. Thomann, G. A. Urban, and M. Kruger, *Nano Lett.*, **2009**, *9*, 514.

[95] H. Zeng, R. R. Vanga, D. S. Marynick, and Z. A. Schelly, *J. Phys. Chem. B*, **2008**, *112*, 14422.

[96] A. Aparisi, V. Fornes, F. Marquez, R. Moreno, C. Lopez, and F. Meseguer, *Soli-State Electr.*, **1996**, *40*, 641.

[97] E. Kuçur, J. Ziegler, and T. Nann, *Small*, **2008**, *4*, 883.

[98] J. M. Matxain, A. Irigoras, J. E. Fowler, and J. M. Ugalde, *Phys. Rev. A*, **2001**, *64*, 13201.

[99] J. M. Matxain, J. M. Mercero, J. E. Fowler, and J. M. Ugalde, *J. Am. Chem. Soc.*, **2003**, *125*, 9494.

[100] J. R. Heath, S. C. O'Brien, Q. Zheng, Y. Liu, R. F. Curl, H. W. Kroto, F. K. Tittel, and R. E. Smalley, *J. Am. Chem. Soc.*, **1985**, *107*, 7779.

[101] K. Komatsu, M. Murata, and Y. Murata, *Science*, **2005**, *307*, 238.

[102] J. Hernadez-Rojas, V. Monteseguro, J. Breton, and J. M. Gomez Llorente, *Chem. Phys.*, **2012**, *399*, 240.

[103] P. Ravinder and V. Subramanian, *Comput. Theor. Chem.*, **2012**, *998*, 106.

[104] S. Guha and K. Nakamoto, *Coord. Chem. Rev.*, **2005**, *249*, 1111.

[105] C. Wang, T. Kai, T. Tomiyama, T. Yoshida, Y. Kobayashi, E. Nishibori, M. Takata, M. Sakata, and H. Shinohara, *Nature*, **2000**, *408*, 426.

[106] S. Stevenson, G. Rice, T. Glass, K. Harich, F. Cromer, M. R. Jordan, J. Craft, E. Hadju, R. Bible, M. M. Olmstead, K. Maitra, A. J. Fisher, A. L. Balch, and H. C. Dorn, *Nature*, **1999**, *401*, 55.

[107] S. Stevenson, P. W. Fowler, T. Heine, J. C. Duchamp, G. Rice, T. Glass, K. Harich, E. Hajdull, R. Bible, and H. C. Dorn, *Nature*, **2000**, *408*, 427.

[108] T. Akasaka and S. Nagase, Ed., *Endofullerenes: A new family of carbon clusters;* Springer, Berlin, 2002.

[109] W. Zhao, B. Xu, and Y. Wang, *Comput. Mat. Sci.*, **2011**, *50*, 2167.

[110] W. Zheng, J. M. Nilles, D. Radisic, and K. H. Bowen Jr., *J. Chem. Phys.*, **2005**, *122*, 071101.

[111] A. Willand, M. Gramzow, S. A. Ghasemi, L. Genovese, T. Deutsch, K. Reuter, and S. Goedecker, *Phys. Rev. B*, **2010**, *81*, 201405.

[112] V. Kumar, A. K. Singh, and Y. Kawazoe, *Phys. Rev. B*, **2006**, *74*, 125411.

[113] F. Avaltroni, S. N. Steinmann, and C. Corminboeuf, *Phys. Chem. Chem. Phys.*, **2012**, *14*, 14842.

[114] S. Yoo, J. Zhao, J. Wang, and X. Zeng, *Journal of the American Chemical Society*, **2004**, *126*, 13845–13849.

[115] M. Harada, S. Osawa, E. Osawa, and E. D. Jemmis, *Chemistry Letters*, **1994**, *23*, 1037–1041.

[116] M. N. Huda and A. K. Raya, *The European Physical Journal D*, **2004**, *31*, 63–68.

[117] Q. Sun, Q. Wang, P. Jena, B. K. Rao, and Y. Kawazoe, *Physical Review Letters*, **2003**, *90*, 135503(1–4).

[118] X. Li, B. Kiran, J. Li, H. Zhai, and L. Wang, *Angew. Chem. Int. Ed.*, **2002**, *41*, 4786.

[119] T. K. Ganthy, A. Banerjee, and A. Chakrabarti, *J. Phys. Chem. C*, **2010**, *114*, 20.

[120] B. D. Yadav and V. Kumar, *Appl. Phys. Lett.*, **2010**, *97*, 133701.

[121] L. Cui, X. Huang, L. Wang, J. Li, and L. Wang, *Ang. Chem. Int. Ed.*, **2007**, *46*, 742.

[122] J. M. Matxain, M. Piris, E. Formoso, J. M. Mercero, X. Lopez, and J. M. Ugalde, *ChemPhysChem*, **2007**, *8*, 2096.

[123] E. N. Esenturk, J. Fettinger, and B. Eichhorn, *Chem. Commun.*., **2005**, page 247.

[124] E. N. Esenturk, J. Fettinger, and B. Eichhorn, *J. Am. Chem. Soc.*, **2006**, *128*, 9178.

[125] B. Molina, J. R. Soto, and J. J. Castro, *J. Phys. Chem. C*, **2012**, *116*, 9290.

[126] F. Y. Naumkin and D. J. Wales, *Chem. Phys. Lett.*, **2012**, *545*, 44.

[127] Binbin Zhou, Mark S. Denning, Deborah L. Kays, and Jose M. Goicoechea, *J. Am. Chem. Soc.*, **2009**, *131*, 2802–2803.

[128] Nikolaus Korber, *Angew. Chem., Int. Ed.*, **2009**, *48*(18), 3216–3217.

[129] A. Nishiwaki, T. Oku, and K. Suganuma, *Phys. B*, **2004**, *349*, 254.

[130] J. Wang, L. Ma, J. Zhao, G. Wang, X. Chen, and R. B. King, *J. Chem. Phys.*, **2008**, *129*, 044908.

[131] H. Liu, S. Wang, G. Zhou, J. Wu, and W. Duan, *J. Chem. Phys.*, **2006**, *124*, 174705.

[132] E. Jimenez-Izal, J. M. Matxain, M. Piris, and J. M. Ugalde, *J. Phys. Chem. C*, **2011**, *115*, 7829.

[133] N. Ganguli, I. Dasgupta, and B. Sanyal, *Appl. Phys. Lett.*, **2009**, *94*, 192503.

[134] J. M. Matxain, L. A. Eriksson, E. Formoso, M. Piris, and J. M. Ugalde, *J. Phys. Chem. C*, **2007**, *111*, 3560.

[135] W.-J. Zheng, O. C. Thomas, T. P. Lippa, S.-J. Xu, and Jr K. H. Bowen, *J. Chem. Phys.*, **2006**, *124*, 144304.

[136] O. Zhou, J. E. Fischer, N. Coustel, S. Kycia, Q. Zhu, A. R. McGhie, W. J. Romanow, J. P. McCauley Jr., A. B. Smith III, and D. E. Cox, *Nature*, **1991**, *351*, 462.

[137] I. Turek and J. Hafner, *Phys. Rev. B*, **1993**, *48*, 14925.

[138] M. Yao, T. Wagberg, and B. Sundqvist, *Phys. Rev. B*, **2009**, *80*, 115405.

[139] R. Poloni, G. Aquilanti, P. Toulemonde, S. Pascarelli, S. Le Floch, D. Machon, D. Martinez-Blanco, G. Morard, and A. San-Miguel, *Phys. Rev. B*, **2008**, *77*, 205433.

[140] Julio A. Alonso, Eds., *Structure and Properties of Atomic Nanoclusters;* Imperial College Press, London, 2005.

[141] P. Jena, S. N. Khanna, and B. K. Rao, *Mat. Sci. Forum*, **1996**, *232*, 1.

[142] G. Hodes and D. Cahen, *Acc. Chem. Research*, **2012**, *45*, 705.

[143] U. F. Keyser, B. N. Koeleman, S. van Dorp, D. Krapf, R: M. M. Smeets, S. G. Lemay, N. H. DEkker, and C. Dekker, *Nature Phys.*, **2006**, *2*, 473.

[144] D. Fologea, M. Gershow, B. Ledden, D. S. McNabb, J. A. Golovchenco, and J. Li, *Nano Lett.*, **2005**, *5*, 1905.

[145] M. L. Pinto, L. Mafra, J. M. Guil, J. Pires, and J. Rocha, *Chem. Mater.*, **2012**, *23*, 1387.

[146] T. X. Nguyen, H. Jobic, and S. K. Bhatia, *Phys. Rev. Lett.*, **2010**, *105*, 085901.

[147] D. Cohen-Tanugi and J. C. Grossman, *Nano Lett.*, **2012**, *12*, 3602.

[148] Z. Zhang, Y. Wang, and X. Wang, *Nanoscale*, **2011**, *3*, 1663.

[149] S. Tang, S. Vongehr, Z. Zheng, H. Ren, and X. Meng, *Nanotech.*, **2012**, *23*, 255606.

[150] J. M. Thomas, J. C. Hernandez-Garrido, R. Raja, and R. G. Bell, *Phys. Chem. Chem. Phys.*, **2009**, *11*, 2799.

[151] G. Q. Lu and X. S. Zhao, Ed., *Nanoporous Materials, Science and Technology;* Imperial College Press, London, 2004.

[152] P. Jena and A. W. Castleman, *PNAS*, **2006**, *103*, 10560.

[153] J. A. Alonso, M. J. Lopez, L. M. Molina, F. Duque, and A. Ma nanes, *Nanotech.*, **2002**, *13*, 253.

[154] V. V. Belavin, L. G. Bulusheva, A. V. Okotrub, and D. Tomanek, *J. Phys. Chem. Sol.*, **2000**, *61*, 1901.

[155] E. Burgos, E. Halac, R. Weht, H. Bonadeo, E. Artacho, and P. Ordejon, *Phys. Rev. Lett.*, **2000**, *85*, 2328.

[156] M. Menon and E. Richter, *Phys. Rev. B*, **1999**, *60*, 13322.

[157] G. Seifert, A. N. Enyashin, and T. Heine, *Phys. Rev. B*, **2005**, *72*, 012102.

[158] M. B. Torres, E. M. Fernández, and L. C. Balbás, *Int. J. Quant. Chem.*, **2011**, *111*, 444.

[159] J. M. Pacheco, G. K. Gueorguiev, and J. L. Martins, *Phys. Rev. B*, **2002**, *66*, 033401.

[160] C. L. Reis and J. M. Pacheco, *J. Phys.: Condens. Matter*, **2010**, *22*, 035501.

[161] C. Ashman, S. N. Khanna, F. Liu, P. Jena, T. Kaplan, and M. Mostoller, *Phys. Rev. B*, **1997**, *55*, 15868.

[162] F. Duque, A. Ma nanes, L. M. Molina, M. J. Lopez, and J. A. Alonso, *Int. J. Quantum Chem.*, **2002**, *86*, 226.

[163] K. Kirihara and K. Kimura, *Sci. Technol. Adv. Mater.*, **2000**, *1*, 227.

[164] S. Mandal, A. C. reber, M. Qian, P. S. Weiss, S. N. Khanna, and Y. Sen, *Acc. Chem. Res.*, **2013**.

[165] S. S. Batsanov, G. E. Blohina, and A. A. Deribas, *Zh. Strukt. Khim.*, **1965**, *6*, 227.

[166] A. V. Pokropivny, *Diamond and Related Mat.*, **2006**, *15*, 1492.

[167] Y. Yong, B. Song, and P. He, *Phys. Chem. Chem. Phys.*, **2011**, *13*, 16182.

[168] J. Carrasco, F. Illas, and S. T. Bromley, *Phys. Rev. Lett.*, **2007**, *99*, 235502.

[169] S. M. Auerbach, K. A. Carrado, and P. K. Dutta, Ed., *Handbook of Zeolite Science and Technology;* Marcel Dekker, New York, 2003.

[170] D. Stradi, F. Illas, and S. T.-Bromley, *Phys. Rev. Lett.*, **2010**, *105*, 045901.

[171] Y. Yong, B. Song, and P. He, *J. Phys. Chem. C*, **2011**, *115*, 6455.

[172] B. Wang, X. Wang, and J. Zhao, *J. Phys. Chem. C*, **2010**, *114*, 5741.

[173] S. Karthikeyan, E. Deepika, and P. Murugan, *J. Phys. Chem. C*, **2012**, *116*, 5981.

[174] W. Kratschmer, L. D. Lamb, K. Fostiropoulos, and D. R. Huffman, *Nature*, **1990**, *347*, 354.

[175] E. Schrödinger, *Ann. Phys.*, **1926**, *80*, 437.

[176] W. Heisenberg, *Z. Physik*, **1925**, *33*, 879.

[177] P.A.M. Dirac, *R. Soc. Lond. A*, **1926**, *112*, 661–677.

[178] M. Born and J. R. Oppenheimer, *Ann. Physik*, **1927**, *44*, 455.

[179] N. I. Levine, *Quantum Chemistry;* Prentince-Hall Inc., 1991.

[180] A. Szabo and N. S. Ostlund, *Modern Quantum Chemistry;* McGraw-Hill, 1992.

[181] Robert G. Parr and Weitao Yang, *Density-Functional Theory of Atoms and Molecules;* International Series of Monographs on Chemistry 16. Oxford University Press, New York, 1989.

[182] E. S. Kryachko and Eduardo V. Ludeña, *Energy Density Functional Theory of Many-Electron Systems;* Understanding Chemical Reactivity. Kluwer Academic Publishers, London, 1990.

[183] W. M. C. Foulkes, L. Mitas, R. J. Needs, and G. Rajagopal, *Rev. Mod. Phys.*, **2001**, *73*, 33.

[184] W. Heitler and F. London, *Z. Phys.*, **1927**, *44*, 455.

[185] F. Hund, *Z. Physik*, **1931**, *73*, 1.

[186] R. S. Mulliken, *Phys. Rev.*, **1932**, *40*, 55.

[187] D.R. Hartree, *Math. Proc. Cambridge Philos. Soc.*, **1928**, *24*(1), 89–110.

[188] V. Fock, *Z. Physik*, **1930**, *61*, 126.

[189] C. Möller and M. S. Plesset, *Phys. Rev.*, **1934**, *46*, 618–622.

[190] Isaiah Shavitt, *Mol. Phys.*, **1998**, *94*(1), 3–17.

[191] C. David Sherrill and Henry F. Schaefer III, *Adv. Quantum Chem.*, **1999**, *34*, 143–269.

[192] J. A. Pople, R. Krishnan, H. B. Schlegel, and J. S. Binkley, *Int. J. Quant. Chem.*, **1978**, *14*(5), 545–560.

[193] R. J. Bartlett and G. D. Purvis, *Int. J. Quant. Chem.*, **1978**, *14*, 516.

[194] R. J. Bartlett; 1995; Vol. 2 of *Advanced Series in Physical Chemistry;* chapter Coupled-Cluster Theory: An Overview of Recent Developments.

[195] K. Andersson, Per-Åke Malmqvist, Björn O. Roos, Andrzej J. Sadlej, and Krzysztof Wolinski, *J. Phys. Chem.*, **1990**, *94*, 5483–5488.

[196] K. Andersson, Per-Åke Malmqvist, and Björn O. Roos, *J. Chem. Phys.*, **1992**, *96*(2), 1218–1226.

[197] J. C. Grossman and L. Mitas, *Phys. Rev. Lett.*, **1995**, *74*, 1323.

[198] J. C. Grossman and L. Mitas, *Phys. Rev. Lett.*, **1997**, *79*, 4353.

[199] J. C. Grossman, L. Mitas, and K. Raghavachari, *Phys. Rev. Lett*, **1995**, *75*, 3870.

[200] W. M. C. Foulkes, R. Q. Hood, and R. J. Needs, *Phys. Rev. B*, **1999**, *60*, 4558.

[201] A. R. Porter, M. D. Towler, and R. J. Needs, *Phys. Rev. B*, **2001**, *64*, 35320.

[202] A. Luchow and J. B. Anderson, *Annu. Rev. Phys. Chem*, **2000**, *51*, 501.

[203] M. Piris; Wiley: New York, 2007; Vol. 134 of *Advances in Chemical Physics;* chapter 14, pages 387–428.

[204] V. N. Staroverov and G. E. Scuseria, *J. Chem. Phys.*, **2002**, *117*, 2489.

[205] Gabor Csanyi, Stefan Goedecker, and T. A. Arias, *Phys. Rev. A*, **2002**, *65*, 32510.

[206] Jerzy Cioslowski, Katarzyna Pernal, and Paul Ziesche, *J. Chem. Phys.*, **2002**, *117*, 9560.

[207] J. M. Herbert and J. E. Harriman, *J. Chem. Phys.*, **2003**, *118*, 10835.

[208] P. Hohenberg and W. Kohn, *Phys. Rev.*, **1964**, *136*, B864.

[209] W. Kohn and L. J. Sham, *Phys. Rev.*, **1965**, *140*, A1133.

[210] R. Stowasser and R. Hoffmann, *J. Am. Chem. Soc.*, **1999**, *121*, 3414.

[211] O. Gunnarsson, B. I. Lundqvist, and J. W. Wilkens, *Phys. Rev. Lett.*, **1974**, *10*, 1319–1327.

[212] T. Kar, J. G: Angyan, and A. B. Shannigrahi, *J. Phys. Chem. A*, **2000**, *104*, 9953.

[213] S. H. Vosko, L. Wilk, and M. Nusair, *Can. J. Phys.*, **1980**, *58*, 1200.

[214] J. C. Slater, *Quantum Theory of Molecules and Solids. Vol. 4. The Self-Consistent Field for Molecules and Solids;* McGraw-Hill, New York, 1974.

[215] J. Labanowski and J. Andelzelm; Springer-Verlag, New York, 1991.

[216] V. Tschinke and T. Ziegler, *Theor. Chim. Acta*, **1991**, *81*, 651.

[217] B. G. Johnson, P. M. W. Gill, and J. A. Pople, *J. Chem. Phys.*, **1993**, *98*, 5612.

[218] A. D. Becke, *J. Chem. Phys.*, **1993**, *98*, 5648–5652.

[219] C. Lee, W. Yang, and R. G. Parr, *Phys. Rev. B*, **1988**, *37*, 785.

[220] P. R. T. Schipper, O. V. Gritsenko, and E. J. Baerends, *Phys. Rev. A*, **1998**, *57*, 1729.

[221] J. M. Soler, E. Artacho, J. D. Gale, A. Garcia, J. Junquera, P. Ordejon, and D. Sanchez-Portal, *J. Phys.: Condens. Matter*, **2002**, *14*, 2745.

[222] C. Peng and H. B. Schlegel, *Israel J. Chem.*, **1993**, *33*, 449.

[223] C. Peng, P. Y. Ayala, H. B. Schlegel, and M. J. Frisch, *J. Comp. Chem.*, **1996**, *17*, 49.

[224] S. A. Arrhenius, *Z. Physik. Chem.*, **1989**, *4*, 96.

[225] H. Eyring, *J. Chem. Phys.*, **1935**, *3*, 107.

[226] Edward Sacher, Michel Meunier, John H. T. Luong, Andrel V. Kabashin, and Jean-Philippe Sylvestre, *J. Am. Chem. Soc.*, **2004**, *126*, 7176.

[227] J. Cioslowski and E.D. Fleischmann, *J. Chem. Phys.*, **1991**, *94*(5).

[228] T. Nakane, *Fullerene Sci. Tech.*, **1997**, *5*, 829–838.

[229] M. S. Dresselhaus, G. Dresselhaus, and P. C. Eklund; Academic Press, San Diego, 1996.

[230] L. Forro and L. Mihaly, *Rep. Prog. Phys.*, **2001**, *64*, 649.

[231] C. M. Cardona, B. Elliott, and L. Echegoyen, *J. Am. Chem. Soc.*, **2006**, *128*, 6480.

[232] L. M. Wang, S. Bulusu, H. J. Zhai, X. C. Zeng, and L. S. Wang, *Angew. Chem. Int. Ed.*, **2007**, *46*, 2915.

[233] S. Scharfe, T. F. Fässler, S. Stegmaier, S. D. Hoffmann, and K. Ruhland, *Chem. Eur. J.*, **2008**, *14*, 4479.

[234] E. N. Esenturk, J. Fettinger, and B. W. Eichhorn, *Chem. Commun.*, **2005**, page 247.

[235] E. N. Esenturk, J. Fettinger, and B. W. Eichhorn, *J. Am. Chem. Soc.*, **2006**, *128*, 9178.

[236] Binbin Zhou, Mark S. Denning, Deborah L. Kays, and Jose M. Goicoechea, *J. Am. Chem. Soc.*, **2009**.

[237] Jian-Qiang Wang, Saskia Stegmaier, and Thomas F. Fässler, *Angew. Chem. Int. Ed.*, **2009**, *48*, 1998–2002.

[238] Nikolaus Korber, *Angew. Chem. Int. Ed.*, **2009**, *48*, 3216–3217.

[239] J. M. Matxain, E. Formoso, J. M. Mercero, M. Piris, X. Lopez, and J. M. Ugalde, *Chem. Eur. J.*, **2008**, *14*, 8547.

[240] J. M. Matxain, M. Piris, X. Lopez, and J. M. Ugalde, *Chem. Eur. J.*, **2009**, *15*, 5138.

[241] A. Kasuya, Y. Noda1, I. Dmitruk, V. Romanyuk, Y. Barnakov, K. Tohji, V. Kumar, R. Belosludov, Y. Kawazoe, and N. Ohuchi, *Eur. Phys. J. D.*, **2005**, *34*, 39.

[242] F. S. Riehle, R. Bienert, R. Thomann, G. A. Urban, and M. Krüger, *Nano Letters*, **2009**, *9*, 514.

[243] A. D. Becke, *Phys. Rev. A*, **1988**, *38*, 3098.

[244] W. J. Stevens, M. Krauss, H. Basch, and P. G. Jasien, *Can. J. Chem.*, **1992**, *70*, 612.

[245] J.P. Perdew, K. Burke, and M. Ernzerhof, *Phys. Rev. Lett.*, **1996**, *77*, 3865.

[246] Y. Zhang and W. Yang, *Phys. Rev. Lett.*, **1998**, *80*, 890.

[247] B. Hammer, L. B. Hansen, and J. K. Norskov, *Phys. Rev. B*, **1999**, *59*, 7413.

[248] N. Troullier and J. L. Martins, *Phys. Rev. B*, **1991**, *43*, 1993.

[249] L. Kleinman and D. M. Bylander, *Phys. Rev. Lett.*, **1982**, *48*, 1425.

[250] J. M. Matxain, M. Piris, X. Lopez, and J. M. Ugalde, *Chem. Eur. J*, **2009**, *15*, 5138.

[251] M. M. Olmstead, A. de Bettencourt-Dias, S. Stevenson, H. C. Dorn, and A. L. Balch, *J. Am. Chem. Soc.*, **2002**, *124*, 4172.

[252] H. Yang, M. Yu, H. Jin, Z. Liu, M. Yao, B. Liu, M. M. Olmstead, and A. L. Balch, *J. Am. Chem. Soc.*, **2012**, *134*, 5331.

[253] Alexey A. Popov, Shangfeng Yang, and Lothar Dunsch, *Chem. Rev.*, **2013**, *113*, 5989–6113.

[254] C. Sarasola, J. M. Elorza, and J. M. Ugalde, *Chem. Phys. Lett.*, **1998**, *285*, 226–229.

[255] Jerzy Cioslowski, *J. Am. Chem. Soc.*, **1991**, *113*, 4139–4141.

[256] R. Klingeler, G. Kann, I. Wirth, S. Eisebitt, P. S. Bechthold, M. Neeb, and W. Eberhart, *J. Chem. Phys.*, **2001**, *115*, 7215.

[257] A. V. Krisilov and B. A. Zon, *Russ. J. Phys. Chem. A*, **2011**, *85*, 1778–1782.

[258] Marc Rudolf, Silke Wolfrum, Dirk M. Guldi, Lai Feng, Takahiro Tsuchiya, Takeshi Akasaka, and Luis Echegoyen, *Chem. Eur. J.*, **2012**, *18*, 5136–5148.

[259] Sonia M. Aguilera-Segura and Jorge M. Seminario, *J. Phys. Chem. C*, **2014**, *118*, 1397–1406.

[260] H. Hiura, T. Miyazaki, and T. Kanayama, *Phys. Rev. Lett.*, **2001**, *86*, 1733.

[261] Vu Thi Ngan, Kristine Pierloot, and Minh Tho Nguyen, *Phys. Chem. Chem. Phys.*, **2013**, *15*, 5493.

[262] O. P. Charkin, D. O. Charkin, N. M. Klimenko, and A. M. Mebel, *Faraday Discuss.*, **2003**, *124*, 215.

[263] T. B. Tai and M. T. Nguyen, *Chem. Phys. Lett.*, **2010**, *492*, 290.

[264] J. Wang, L. Ma, J. Zhao, B. Wang, and G. Wang, *J. Chem. Phys.*, **2008**, *128*, 084306.

[265] E. Jimenez-Izal, J. M. Matxain, M. Piris, and J. M. Ugalde, *J. Phys. Chem. C*, **2010**, *114*, 2476.

[266] Puru Jena, *J. Phys. Chem. Lett.*, **2013**, *4*, 1432–1442.

[267] E. Jimenez-Izal, J. M. Matxain, M. Piris, and J. M. Ugalde, *Phys. Chem. Chem. Phys.*, **2012**, *14*, 9676.

[268] J. M. Azpiroz, J. M. Ugalde, and I. Infante, *J. Chem. Theor. Comp.*, **2014**, *10*, 76–89.

[269] M. J. Frisch, G. W. Trucks, H. B. Schlegel, G. E. Scuseria, M. A. Robb, J. R. Cheeseman, G. Scalmani, V. Barone, B. Mennucci, G. A. Petersson, H. Nakatsuji, M. Caricato, X. Li, H. P. Hratchian, A. F. Izmaylov, J. Bloino, G. Zheng, J. L. Sonnenberg, M. Hada, M. Ehara, K. Toyota, R. Fukuda, J. Hasegawa, M. Ishida, T. Nakajima, Y. Honda, O. Kitao, H. Nakai, T. Vreven, J. A. Montgomery, Jr., J. E. Peralta, F. Ogliaro, M. Bearpark, J. J. Heyd, E. Brothers, K. N. Kudin, V. N. Staroverov, R. Kobayashi, J. Normand, K. Raghavachari, A. Rendell, J. C. Burant, S. S. Iyengar, J. Tomasi, M. Cossi, N. Rega, J. M. Millam, M. Klene, J. E. Knox, J. B. Cross, V. Bakken, C. Adamo, J. Jaramillo, R. Gomperts, R. E. Stratmann, O. Yazyev, A. J. Austin, R. Cammi, C. Pomelli, J. W. Ochterski, R. L. Martin, K. Morokuma, V. G. Zakrzewski, G. A. Voth, P. Salvador, J. J. Dannenberg, S. Dapprich, A. D. Daniels, O. Farkas, J. B. Foresman, J. V. Ortiz, J. Cioslowski, and D. J. Fox, **2009;** Gaussian Inc. Wallingford CT 2009.

[270] T. Ziegler and A. Rauk, *Inorg. Chem.*, **1979**, *18*, 1558–1565.

[271] T. Ziegler and A. Rauk, *Inorg. Chem.*, **1979**, *18*, 1755.

[272] T. Ziegler and A. Rauk, *Theor. Chim. Acta*, **1977**, *46*, 1–10.

[273] G. te Velde, F. M. Bickelhaupt, E. J. Baerends, C. Fonseca Guerra, S. J. A. van Gisbergen, J. G. Snijders, and T. Ziegler, *Journal of Computational Chemistry*, **2001**, *22*, 931–967.

[274] C. Sarasola, J. M. Elorza, and J. M. Ugalde, *J. Math. Chem.*, **1998**, *23*, 405.

[275] M. Cossi, G. Scalmani, N. Rega, and V. Barone, *J. Chem. Phys.*, **2002**, *117*, 43.

[276] S Wu, N Yuan, H Xu, X Wang, and Z A Schelly, *Nanotech.*, **2006**, *17*, 4713–4718.

[277] Xinshou Wang, Hongtao Xu, Hongzeng Liu, Zoltan A. Schelly, and Sixin Wu, *Nanotech.*, **2007**, *18*, 155604(1–5).

[278] S Wu, H Liu, Z Wu, Z Du, and Z A Schelly, *Nanotech.*, **2007**, *18*, 485607–485612.

[279] A. E. Rakhshami, B. Pradeep, and H. A. Ramazaniyan, *Electrochem. Proc.*, **2003**, *32*, 49.

[280] Jon M Azpiroz, Edoardo Mosconi, and Filippo De Angelis, *J. Phys. Chem. C*, **2011**, *115*, 25219–25226.

[281] Jon M. Azpiroz, Ivan Infante, Xabier Lopez, Jesus M. Ugalde, and Filippo De Angelis, *J. Mater. Chem.*, **2012**, *22*, 21453–21465.

[282] Jon M Azpiroz, Jon M Matxain, Ivan Infante, Xabier Lopez, and Jesus M Ugalde, *Phys. Chem. Chem. Phys.*, **2013**, *15*, 10996–11005.

[283] V. I. Klimov and M. Dekker, *Semiconductor and Metal Nanocystals: Synthesis and Electronic and Optical Properties;* CRC Press, 2003.

[284] S. N. Khanna, B. K. Rao, and P. Jena, *Phys. Rev. Lett.*, **2002**, *89*, 16803.

[285] M. R. Pederson and A. A. Quong, *Phys. Rev. Lett.*, **1995**, *74*, 2319.

[286] B. L. Zhang, C. Z. Wang, K. M. Ho, and C. T. Chan, *Europhys. Lett.*, **1994**, *28*, 219.

[287] P. Pyykko and N. Runeberg, *Angew. Chem. Int. Ed.*, **2002**, *41*, 2174.

[288] X. Li, B. Kiran, J. Li, H. J. Zhai, and L. S. Wang, *Angew. Chem. Int. Ed.*, **2002**, *41*, 4786.

[289] H. J. Zhai, J. Li, and L. S. Wang, *J. Chem. Phys.*, **2004**, *121*, 8369.

[290] Xuan Chen, Kaiming Deng, Yuzhen Liu, Chunmei Tang, Yongbo Yuan, Fenglan Hu, Haiping Wu, Decai Huang, Weishi Tan, and Xin Wang, *Chem. Phys. Lett.*, **2008**, *462*, 275.

[291] S. Hamad, S. Cristol, and C. R. A. Catlow, *J. Am. Chem. Soc.*, **2005**, *127*, 9479.

[292] J. M. Matxain, A. Irigoras, J. E. Fowler, and J. M. Ugalde, *Phys. Rev. A*, **2001**, *63*, 13202.

[293] S. M. Woodley, M. B. Watkins, A. A. Sokol, S. A. Shevlin, and C. R. A. Catlow, *Phys. Chem. Chem. Phys.*, **2009**, *11*, 3176.

[294] M. A. Zwijnenburg, F. Illas, and S. T. Bromley, *Phys. Rev. Lett.*, **2010**, *104*, 175503.

[295] M. A. Zwijnenburg and S. T. Bromley, *J. Mater. Chem.*, **2011**, *21*, 15255.

[296] A. D. Becke, *J. Chem. Phys.*, **1993**, *98*, 1372.

[297] J. M. Matxain, L. A. Eriksson, J. M. Mercero, X. Lopez, M. Piris, J. M. Ugalde, J. Poater, E. Matito, and M. Sola, *J. Phys. Chem. C*, **2007**, *111*, 13354.

[298] F. Benkabou, H. Aourag, and M. Certier, *Mat. Chem. Phys.*, **2000**, *66*, 10.

[299] M. A. Stroscio and M. Dutta, Ed.; Kluwer, New York, 2004.

[300] C. L. Dennis, A. J. Jackson, J. A. Borchers, P. J. Hoopes, R. Strawbridge, A. R. Foreman, J. van Lierop, C. Grüttner, and R Ivkov, *Nanotech.*, **2009**, *20*, 395103.

[301] M. Dolg, U. Wedig, H. Stoll, and H. Preuss, *J. Chem. Phys.*, **1987**, *86*, 866.

[302] J. M. L. Martin and A. Sundermann, *J. Chem. Phys.*, **2001**, *114*, 3408.

[303] M. J. Frisch, G. W. Trucks, H. B. Schlegel, G. E. Scuseria, M. A. Robb, J. R. Cheeseman, J. A. Montgomery, Jr., T. Vreven, K. N. Kudin, J. C. Burant, J. M. Millam, S. S. Iyengar, J. Tomasi, V. Barone, B. Mennucci, M. Cossi, G. Scalmani, N. Rega, G. A. Petersson, H. Nakatsuji, M. Hada, M. Ehara, K. Toyota, R. Fukuda, J. Hasegawa, M. Ishida, T. Nakajima, Y. Honda, O. Kitao, H. Nakai, M. Klene, X. Li, J. E. Knox, H. P. Hratchian, J. B. Cross, V. Bakken, C. Adamo, J. Jaramillo, R. Gomperts, R. E. Stratmann, O. Yazyev, A. J. Austin, R. Cammi, C. Pomelli, J. W. Ochterski, P. Y. Ayala, K. Morokuma, G. A. Voth, P. Salvador, J. J. Dannenberg, V. G. Zakrzewski, S. Dapprich, A. D. Daniels, M. C. Strain, O. Farkas, D. K. Malick, A. D. Rabuck, K. Raghavachari, J. B. Foresman, J. V. Ortiz, Q. Cui, A. G. Baboul, S. Clifford, J. Cioslowski, B. B. Stefanov, G. Liu, A. Liashenko, P. Piskorz, I. Komaromi, R. L. Martin, D. J. Fox, T. Keith, M. A. Al-Laham, C. Y. Peng, A. Nanayakkara, M. Challacombe, P. M. W. Gill, B. Johnson, W. Chen, M. W. Wong, C. Gonzalez, and J. A. Pople; Gaussian 03, Revision C.02; Gaussian, Inc., Wallingford, CT, 2004.

[304] C. Peng and H. B. Schlegel, *Isr. J. Chem.*, **1993**, *33*, 449.

[305] C. Gonzalez and H. B. Schlegel, *J. Chem. Phys.*, **1989**, *90*, 2154.

[306] C. Gonzalez and H. B. Schlegel, *J. Phys. Chem.*, **1990**, *94*, 5523.

[307] S. Datta, M. Kabir, T. Saha-Dasgupta, and D. D. Sarma, *J. Phys. Chem. C*, **2008**, *112*, 8206.

[308] D. Mocatta, G. Cohen, J. Schattner, O. Millo, E. Rabani, and U. Banin, *Science*, **2011**, *332*, 77.

[309] S. Wei and S. B. Zhang, *Phys. Rev. B*, **2002**, *66*, 155211.

[310] T. Z. Markus, S. Itzhakov, Y. I. Alkotzer, D. Cahen, G. Hodes, D. Oron, and R. Naaman, *J. Phys. Chem. C*, **2011**, *115*, 13236.

[311] P. I. Archer, S. A. Santangelo, and D. R. Gamelin, *JACS*, **2007**, *129*, 9808.

[312] S. N. Khanna, B. K. Rao, and P. Jena, *Phys. Rev. B*, **2002**, *65*, 125105.

[313] M. K. Yadav, B. Sanyal, and A. Mookerjee, *J. Magn. Magn. Mater.*, **2009**, *321*, 235.

[314] D. Zhang, L. Chen, J. Zhang, and X. Miao, *J. Am. Ceram. Soc.*, **2011**, *94*, 759.

[315] N. Ganguli, I. Dasgupta, and B. Sanyal, *J. Appl. Phys.*, **2010**, *108*, 123911.

[316] Y. Yong, Z. Wang, K. Liu, B. Song, and P. He, *Comput. Theor. Chem.*, **2012**, *989*, 90.

[317] H. Chen, D. Shi, J. Qi, and B. Wang, *Phys. E*, **2010**, *43*, 117.

[318] H. Chen, D. Shi, J. Qi, and B. Wang, *Phys. Lett. A*, **2010**, *374*, 4133.

[319] G. H. Timmer and J. F. Berry, *C. R. Chemie*, **2011**.

[320] V. H. Smith Jr.and H. F. Schaefer and K. Morokuma, Ed., *Applied Quantum Chemistry;* D. Reidel, Holland, 1986.

[321] T. Soda, Y: Kitagawa, T. Onishi, Y. Takano, Y. Shigeta, H. Nagao, Y. Yoshioka, and K. Yamaguchi, *Chem. Phys. Lett.*, **2000**, *319*, 223.

[322] K. I. Ramachandran, G. Deepa, and K. Namboori, Ed., *Computational chemistry and molecular modelling: principles and applications;* Springer, Berlin, 2008.

[323] F. ORCA-an ab inito DFT "Neese and version 2.8.0" Semi-empirical Electronic Structure Package, **2010;** University of Bonn Germany.

[324] A. Schafer, H. Horn, and E. Ahlrichs, *J. Chem. Phys.*, **1992**, *97*, 2571.

[325] A. E. Reed, L. A. Curtiss, and F. Weinhold, *Chem. Rev.*, **1988**, *88*, 899–926.

Part V

Appendix

Chapter 10

Supporting Information of Chapter 1

10.1 1. Influence of ΔE_{PAO} and E_{Cutoff} in X@(CdS)$_{12}$ Dynamics Simulations

Figure 10.1: (Na@(CdS)$_{12}$)$^{+}$, using different ΔE_{PAO} and E_{Cuttof}.

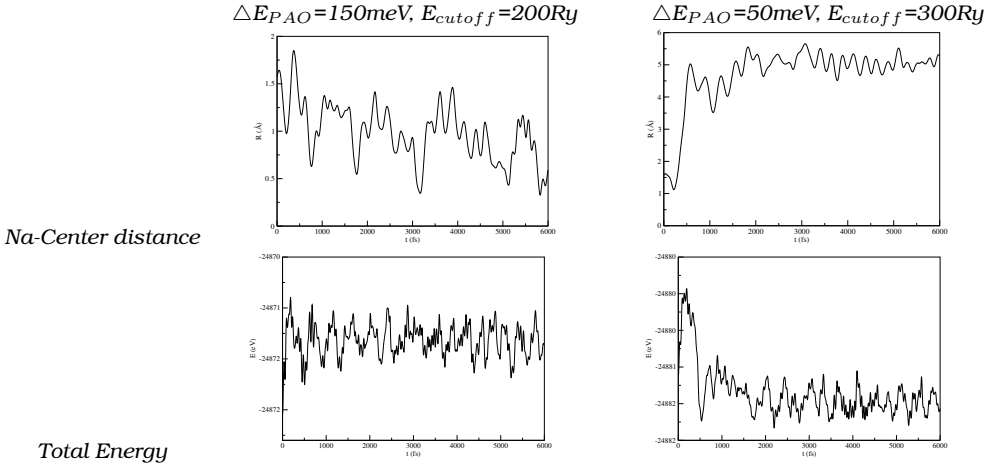

Figure 10.2: $(K@(CdS)_{12})^{+}$, using different ΔE_{PAO} and E_{Cuttof}.

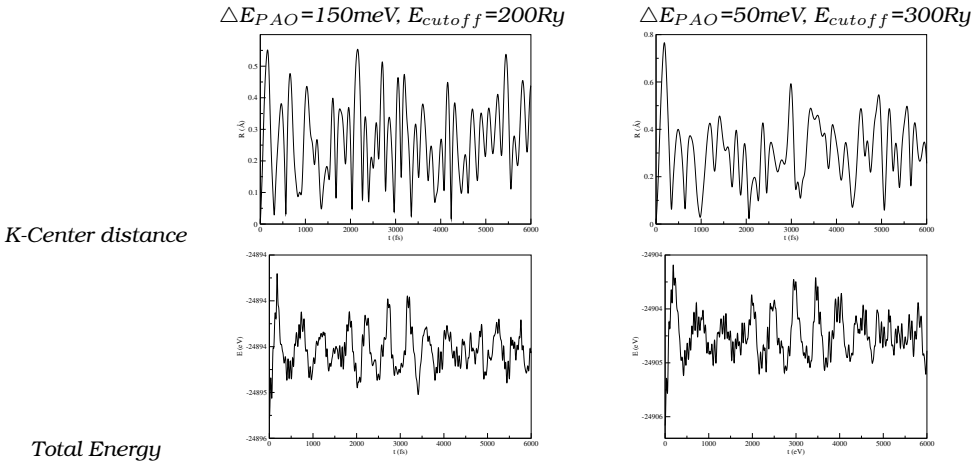

Figure 10.3: $K@(CdS)_{12}$, using different ΔE_{PAO} and E_{Cuttof}.

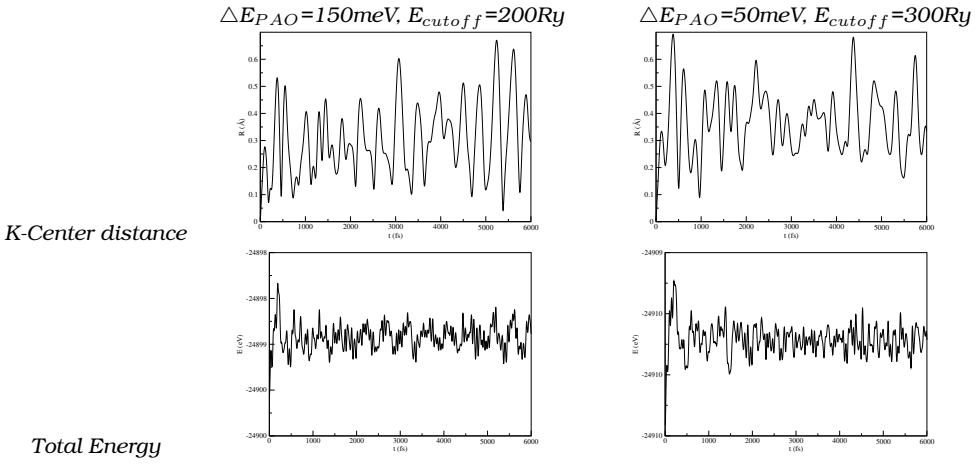

Figure 10.4: $(Cl@(CdS)_{12})^{-}$, using different ΔE_{PAO} and E_{Cuttof}.

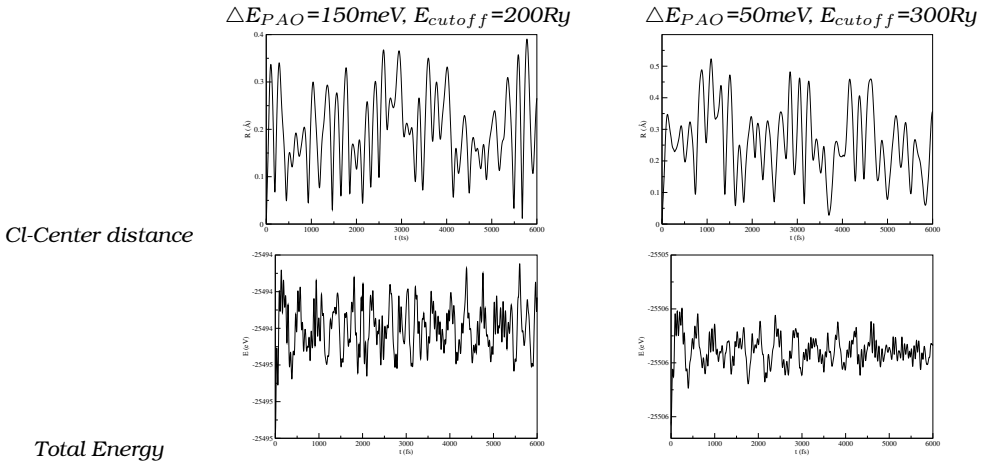

Figure 10.5: $Cl@(CdS)_{12}$, using different ΔE_{PAO} and E_{Cuttof}.

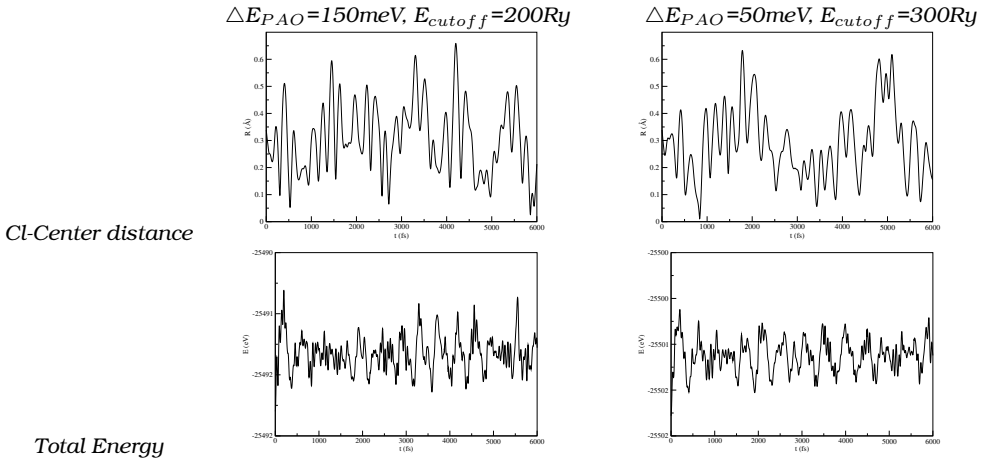

Figure 10.6: (Br@(CdS)$_{12}$)$^{-}$, using different ΔE_{PAO} and E_{Cuttof}.

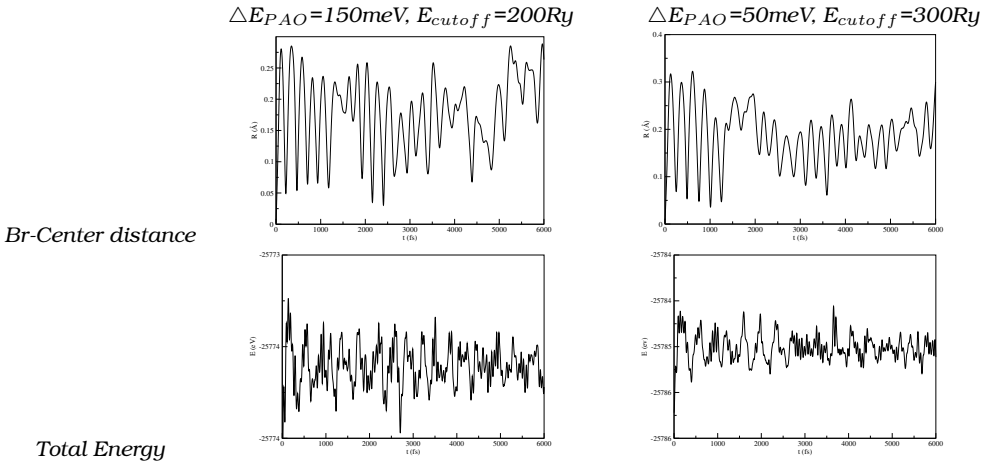

Figure 10.7: Br@(CdS)$_{12}$, using different ΔE_{PAO} and E_{Cuttof}.

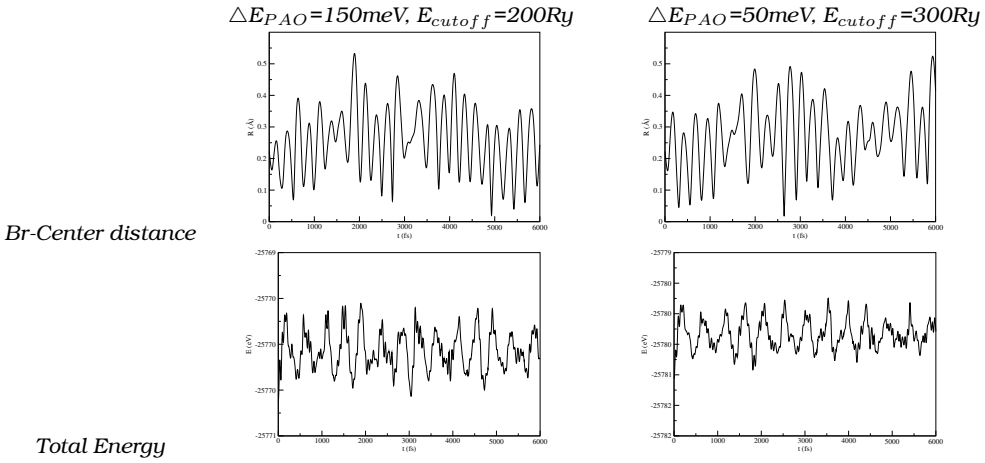

10.2 Properties of Characterized (Na@(CdS)$_{i=9,12,15,16}$)$^{0,+}$ Local Minima

Table 10.1: Cavity within the Cluster, the distance of the guest atom with respect to th center of the cluster (R^{LM}), r_{cavity} (Å), the free energy of encapsulation, $\triangle G_{enc}$, in Kcal/mol, the Charge of the endohedral Atom, q_x, and the Ionization Energies, in eV.

	r_{cavity}	R^{LM}	$\triangle G_{enc}$	q_x	IE
$Na@(CdS)_9$	-	-	-	-	-
$Na@(CdS)_{12}$	2.66	0.00	-2.25	0.34	5.26
$Na@(CdS)_{15}$	3.14	0.00	-7.94	0.23	4.98
$Na@(CdS)_{16}$	3.26	0.00	-8.36	0.18	5.25
$(Na@(CdS)_9)^+$	2.35	0.45	-5.48	0.47	
$(Na@(CdS)_{12})^+$	2.78	1.55	-5.96	0.44	
$(Na@(CdS)_{15})^+$	3.24	0.00	-18.09	0.46	
$(Na@(CdS)_{16})^+$	3.36	2.14	-12.26	0.44	

10.3 Dynamics of the Characterized $(X@(CdS)_{i=9,12,15,16})^{0,\pm1}$ Clusters, X=K,Cl,Br

Figure 10.8: $K@(CdS)_9$. Top: Dynamical trajectories of the K atom inside the nanocluster. This plot was prepared as the $K@(CdS)_{12}$ one. Below, the variation of the energy, in eV (left) and the variation of the distance, R, in Å (right), of the trapped K atom from the center of mass of the nanocluster as a function of time.

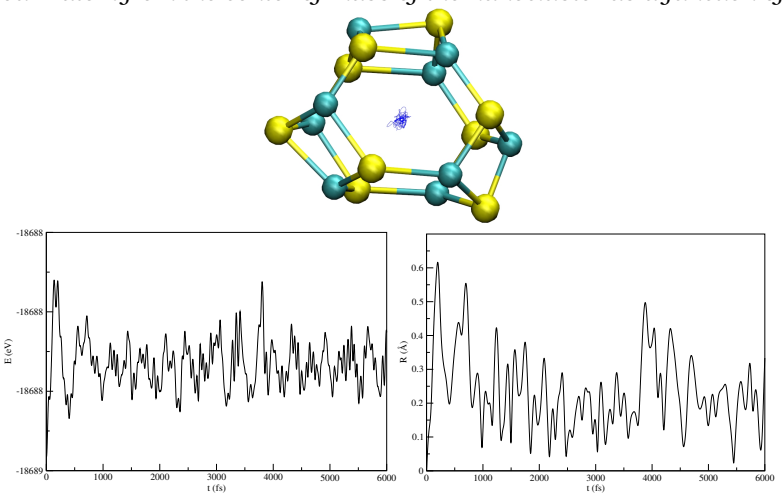

Figure 10.9: K@(CdS)$_{15}$. Top: Dynamical trajectories of the K atom inside the nanocluster. This plot was prepared as theK@(CdS)$_{12}$ one. Below, the variation of the energy, in eV (left) and the variation of the distance, R, in Å (right), of the trapped K atom from the center of mass of the nanocluster as a function of time.

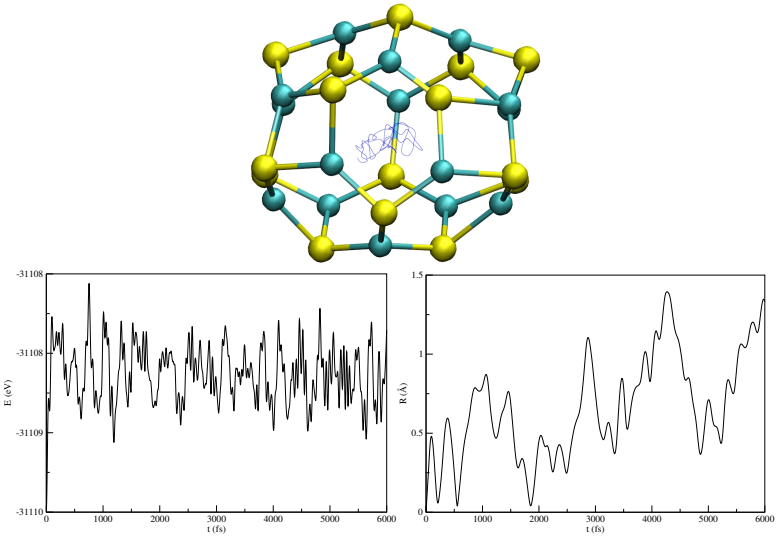

Figure 10.10: K@(CdS)$_{16}$. Top: Dynamical trajectories of the K atom inside the nanocluster. This plot was prepared as the K@(CdS)$_{12}$ one. Below, the variation of the energy, in eV (left) and the variation of the distance, R, in Å (right), of the trapped K atom from the center of mass of the nanocluster as a function of time.

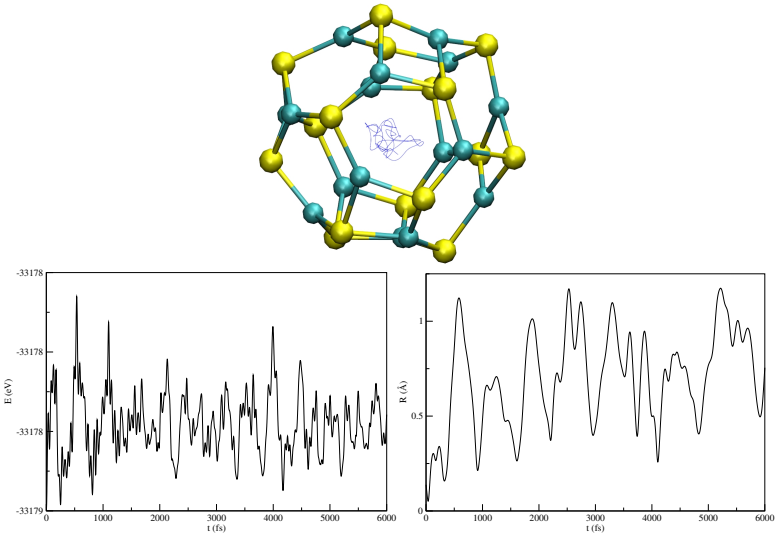

Figure 10.11: $(K@(CdS)_9)^+$. Top: Dynamical trajectories of the K atom inside the nanocluster. This plot was prepared as the $K@(CdS)_{12}$ one. Below, the variation of the energy, in eV (left) and the variation of the distance, R, in Å (right), of the trapped K atom from the center of mass of the nanocluster as a function of time.

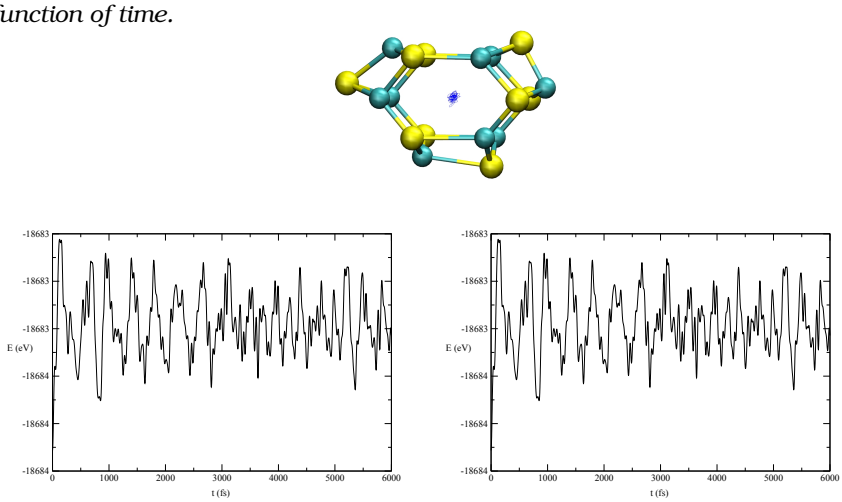

Figure 10.12: $(K@(CdS)_{12})^+$. Top: Dynamical trajectories of the K atom inside the nanocluster. This plot was prepared as the $K@(CdS)_{12}$ one. Below, the variation of the energy, in eV (left) and the variation of the distance, R, in Å (right), of the trapped K atom from the center of mass of the nanocluster as a function of time.

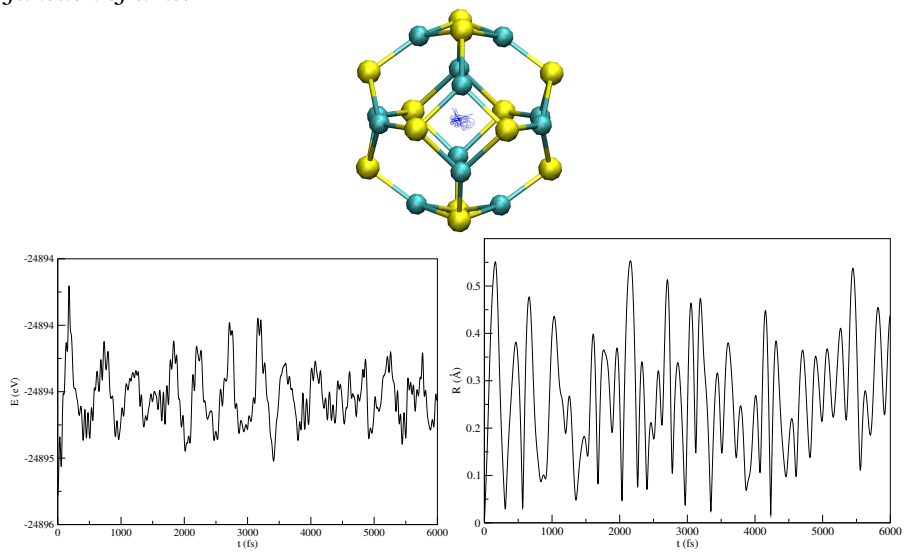

Figure 10.13: $(K@(CdS)_{15})^{+}$. Top: Dynamical trajectories of the K atom inside the nanocluster. This plot was prepared as the$K@(CdS)_{12}$ one. Below, the variation of the energy, in eV (left) and the variation of the distance, R, in Å (right), of the trapped K atom from the center of mass of the nanocluster as a function of time.

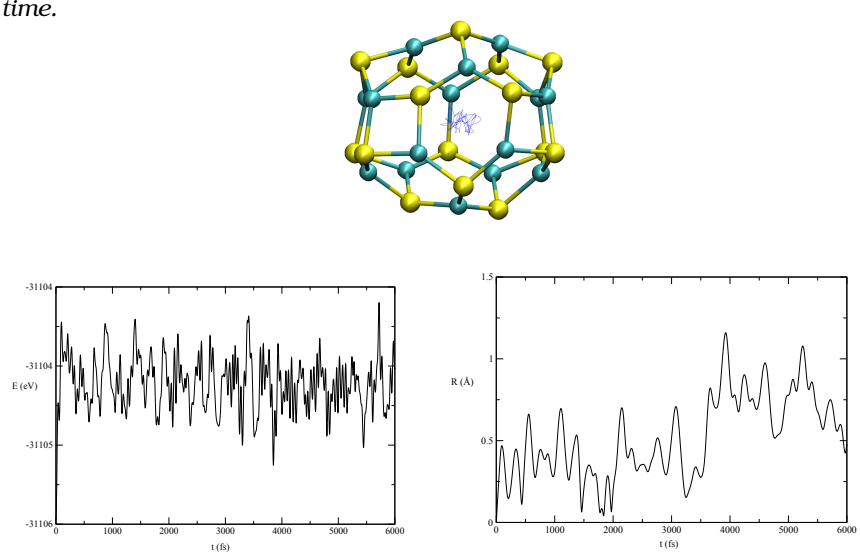

Figure 10.14: $(K@(CdS)_{16})^+$. Top: Dynamical trajectories of the K atom inside the nanocluster. This plot was prepared as the $K@(CdS)_{12}$ one. Below, the variation of the energy, in eV (left) and the variation of the distance, R, in Å (right), of the trapped K atom from the center of mass of the nanocluster as a function of time.

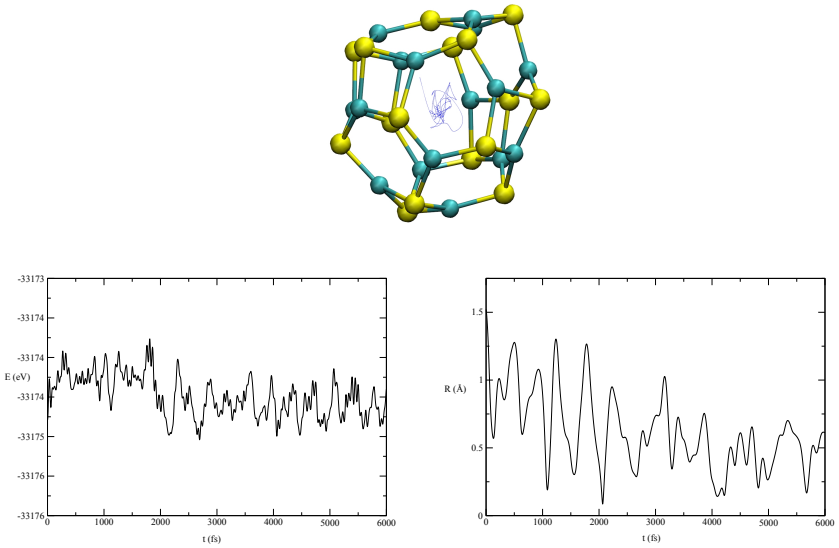

Figure 10.15: $Cl@(CdS)_9$. Top: Dynamical trajectories of the K atom inside the nanocluster. This plot was prepared as the $K@(CdS)_{12}$ one. Below, the variation of the energy, in eV (left) and the variation of the distance, R, in Å (right), of the trapped Cl atom from the center of mass of the nanocluster as a function of time.

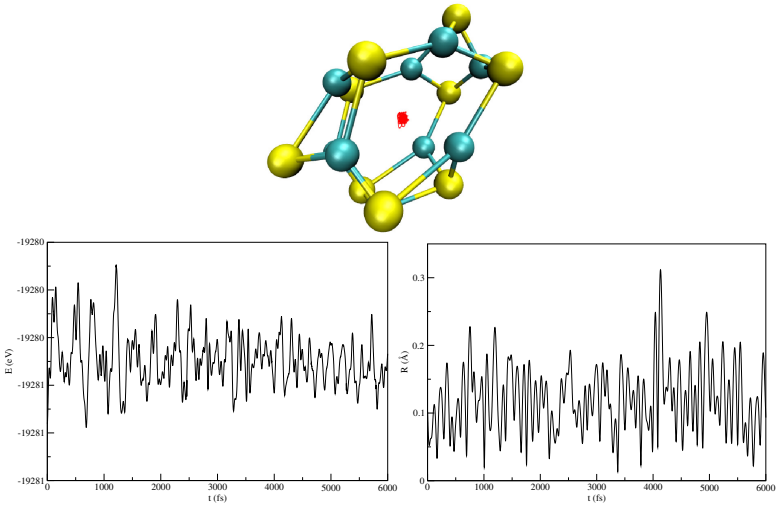

Figure 10.16: $Cl@(CdS)_{15}$. Top: Dynamical trajectories of the K atom inside the nanocluster. This plot was prepared as the $K@(CdS)_{12}$ one. Below, the variation of the energy, in eV (left) and the variation of the distance, R, in Å (right), of the trapped Cl atom from the center of mass of the nanocluster as a function of time.

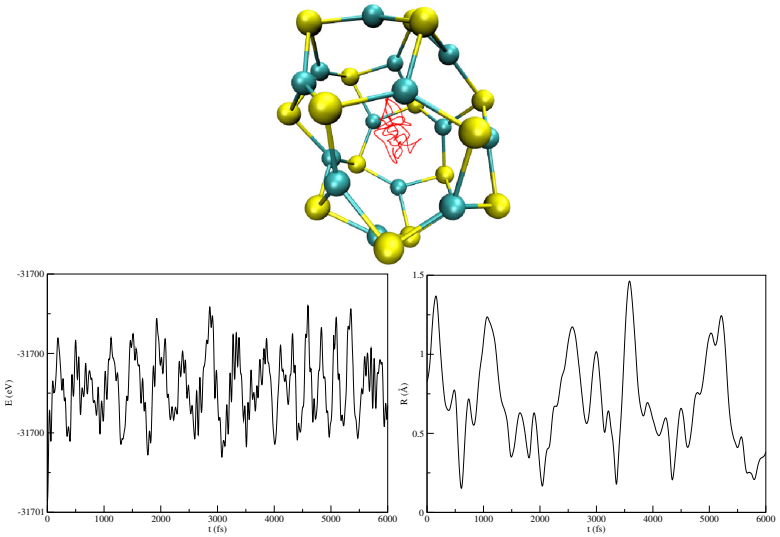

Figure 10.17: $Cl@(CdS)_{16}$. Top: Dynamical trajectories of the K atom inside the nanocluster. This plot was prepared as the $K@(CdS)_{12}$ one. Below, the variation of the energy, in eV (left) and the variation of the distance, R, in Å (right), of the trapped Cl atom from the center of mass of the nanocluster as a function of time.

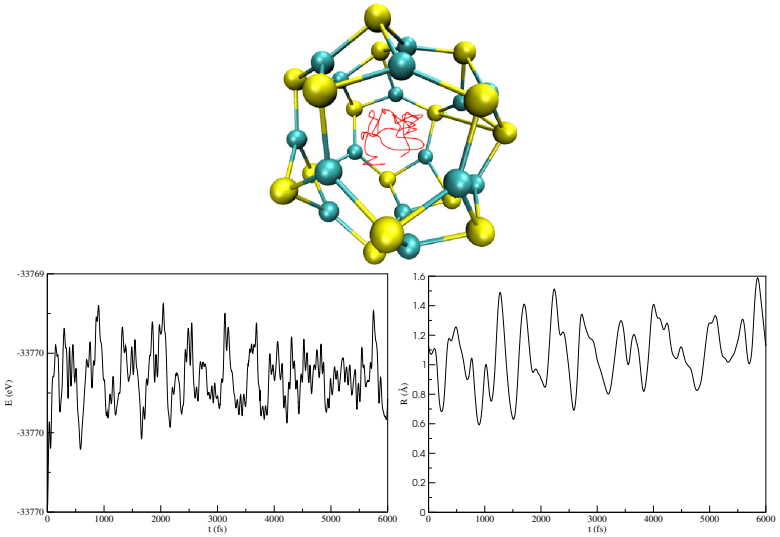

Figure 10.18: $(Cl@(CdS)_9)^-$. Top: Dynamical trajectories of the K atom inside the nanocluster. This plot was prepared as the $K@(CdS)_{12}$ one. Below, the variation of the energy, in eV (left) and the variation of the distance, R, in Å (right), of the trapped Cl atom from the center of mass of the nanocluster as a function of time.

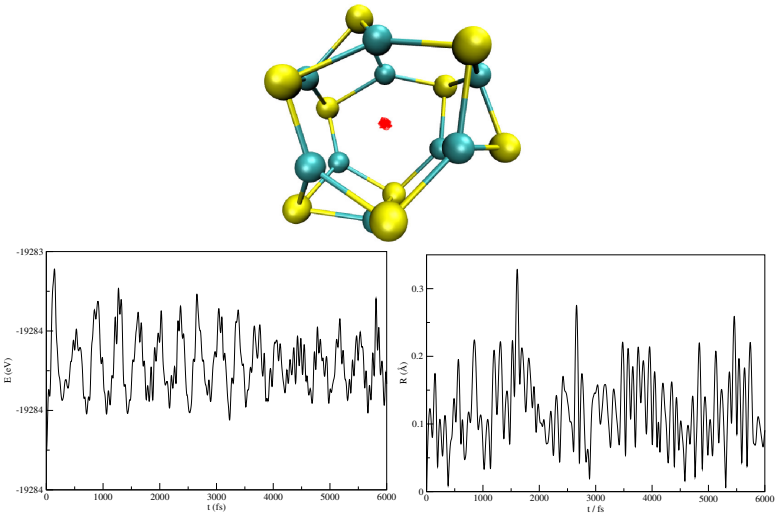

Figure 10.19: $(Cl@(CdS)_{15})^-$. Top: Dynamical trajectories of the K atom inside the nanocluster. This plot was prepared as the $K@(CdS)_{12}$ one. Below, the variation of the energy, in eV (left) and the variation of the distance, R, in Å (right), of the trapped Cl atom from the center of mass of the nanocluster as a function of time.

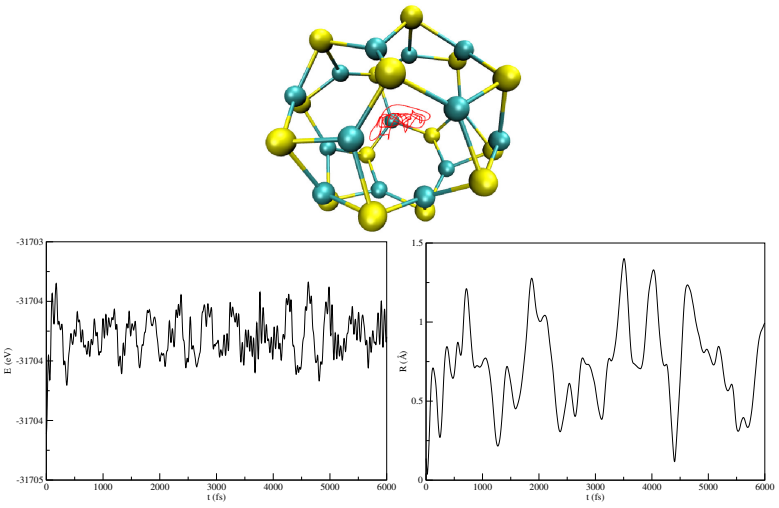

Figure 10.20: $(Cl@(CdS)_{16})^{-}$. Top: Dynamical trajectories of the K atom inside the nanocluster. This plot was prepared as the $K@(CdS)_{12}$ one. Below, the variation of the energy, in eV (left) and the variation of the distance, R, in Å (right), of the trapped Cl atom from the center of mass of the nanocluster as a function of time.

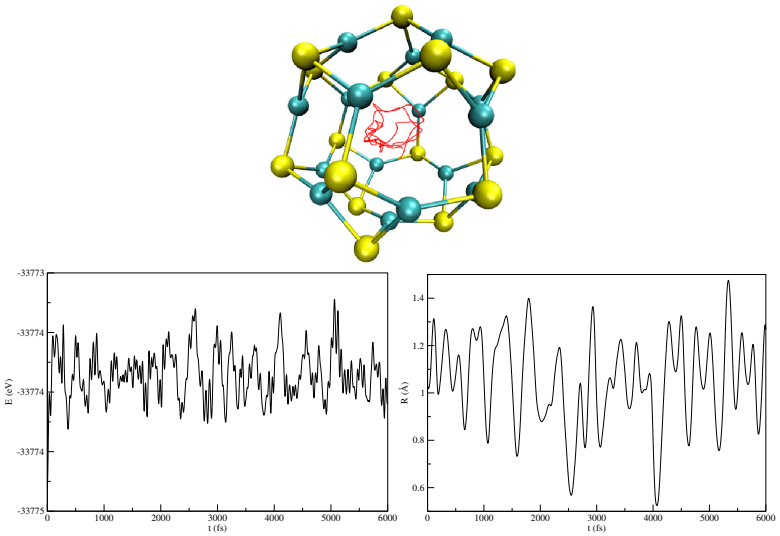

Figure 10.21: $Br@(CdS)_9$. Top: Dynamical trajectories of the K atom inside the nanocluster. This plot was prepared as the $K@(CdS)_{12}$ one. Below, the variation of the energy, in eV (left) and the variation of the distance, R, in Å (right), of the trapped Br atom from the center of mass of the nanocluster as a function of time.

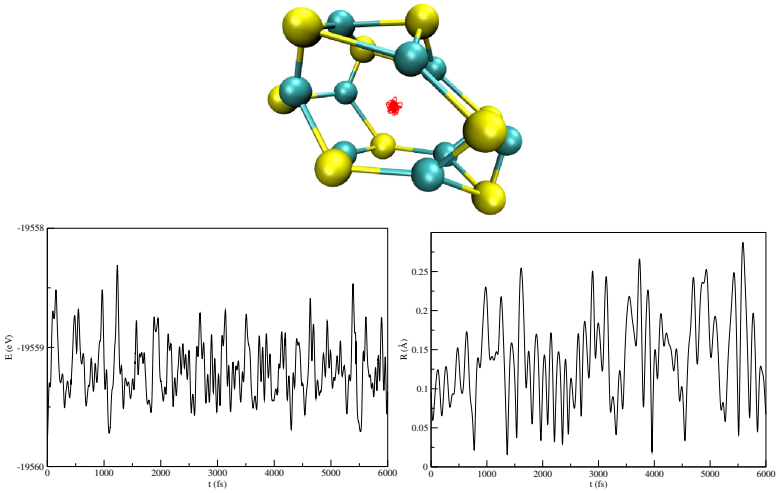

Figure 10.22: Br@(CdS)$_{12}$. Top: Dynamical trajectories of the K atom inside the nanocluster. This plot was prepared as the K@(CdS)$_{12}$ one. Below, the variation of the energy, in eV (left) and the variation of the distance, R, in Å (right), of the trapped Br atom from the center of mass of the nanocluster as a function of time.

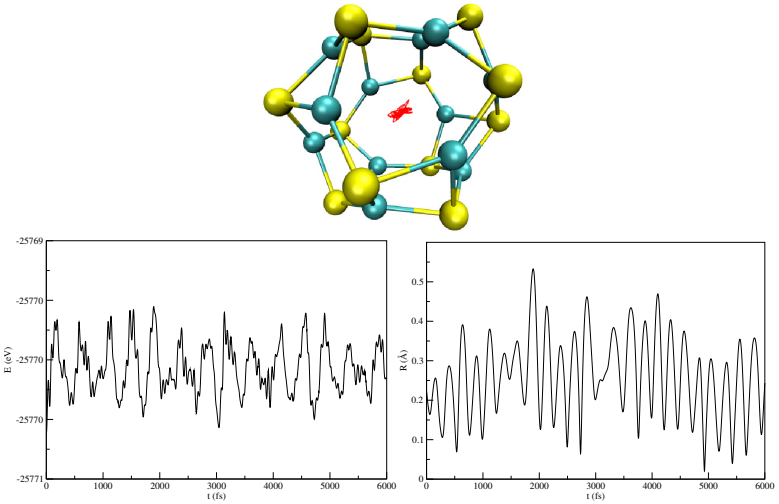

Figure 10.23: Br@(CdS)$_{15}$. Top: Dynamical trajectories of the K atom inside the nanocluster. This plot was prepared as the K@(CdS)$_{12}$ one. Below, the variation of the energy, in eV (left) and the variation of the distance, R, in Å (right), of the trapped Br atom from the center of mass of the nanocluster as a function of time.

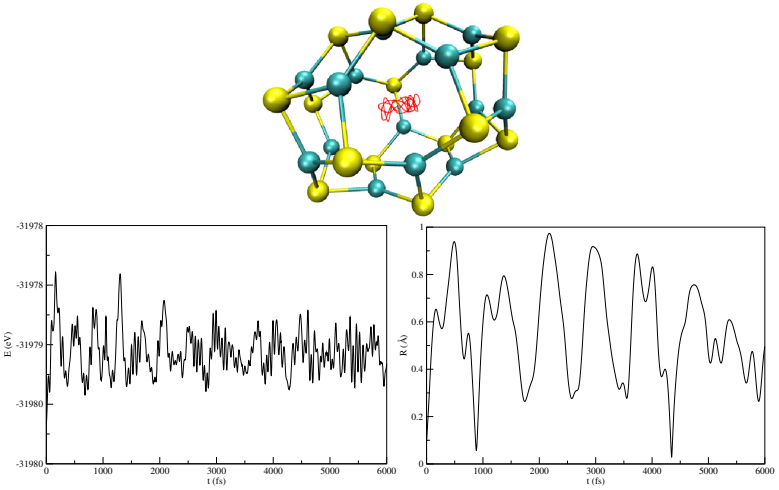

Figure 10.24: Br@(CdS)$_{16}$. Top: Dynamical trajectories of the K atom inside the nanocluster. This plot was prepared as the K@(CdS)$_{12}$ one. Below, the variation of the energy, in eV (left) and the variation of the distance, R, in Å (right), of the trapped Br atom from the center of mass of the nanocluster as a function of time.

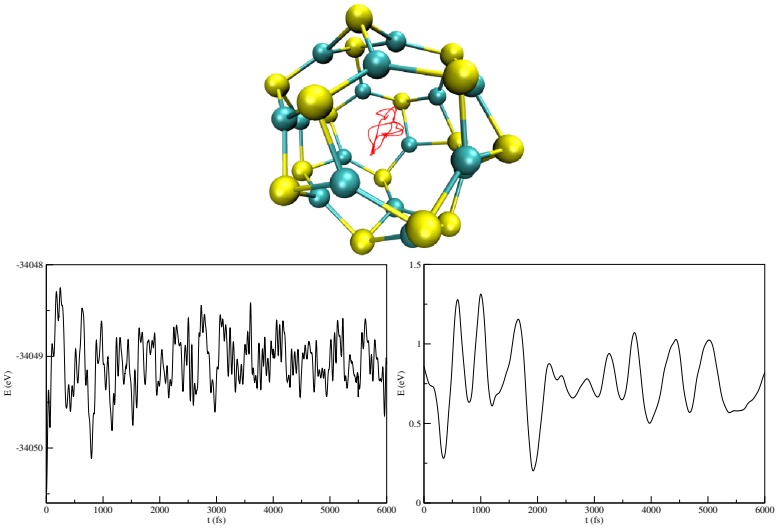

Figure 10.25: (Br@(CdS)$_9$)$^-$. Top: Dynamical trajectories of the K atom inside the nanocluster. This plot was prepared as the K@(CdS)$_{12}$ one. Below, the variation of the energy, in eV (left) and the variation of the distance, R, in Å (right), of the trapped Br atom from the center of mass of the nanocluster as a function of time.

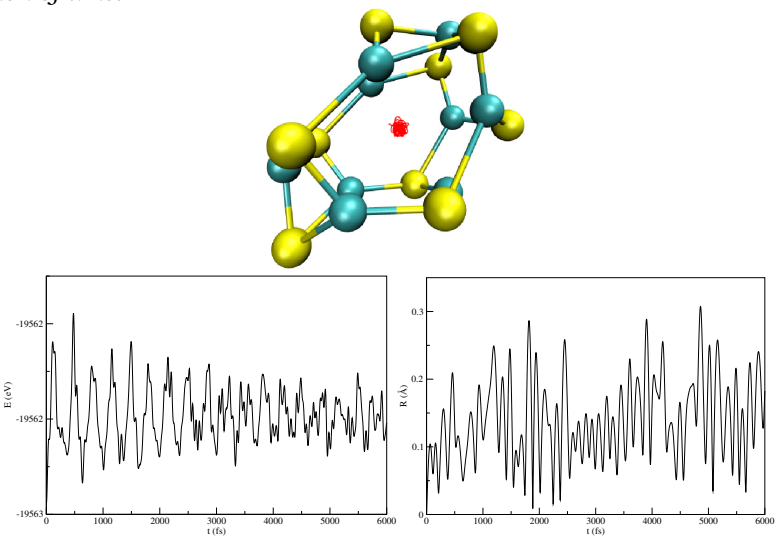

Figure 10.26: $(Br@(CdS)_{12})^-$. Top: Dynamical trajectories of the K atom inside the nanocluster. This plot was prepared as the $K@(CdS)_{12}$ one. Below, the variation of the energy, in eV (left) and the variation of the distance, R, in Å (right), of the trapped Br atom from the center of mass of the nanocluster as a function of time.

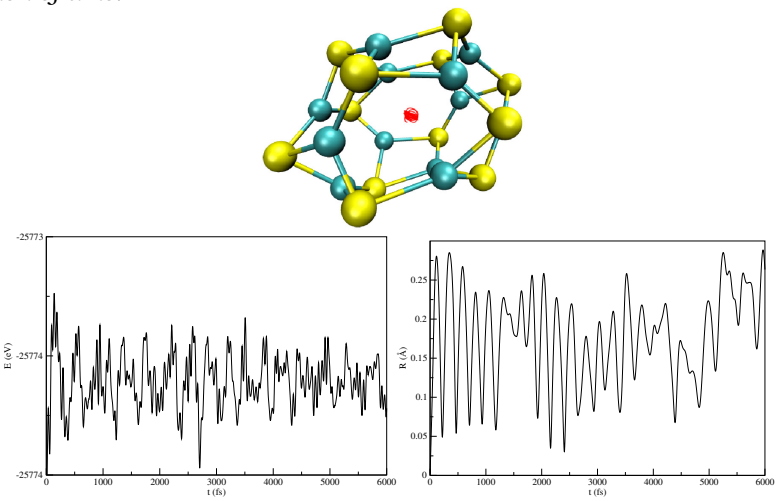

Figure 10.27: $(Br@(CdS)_{15})^-$. Top: Dynamical trajectories of the K atom inside the nanocluster. This plot was prepared as the $K@(CdS)_{12}$ one. Below, the variation of the energy, in eV (left) and the variation of the distance, R, in Å (right), of the trapped Br atom from the center of mass of the nanocluster as a function of time.

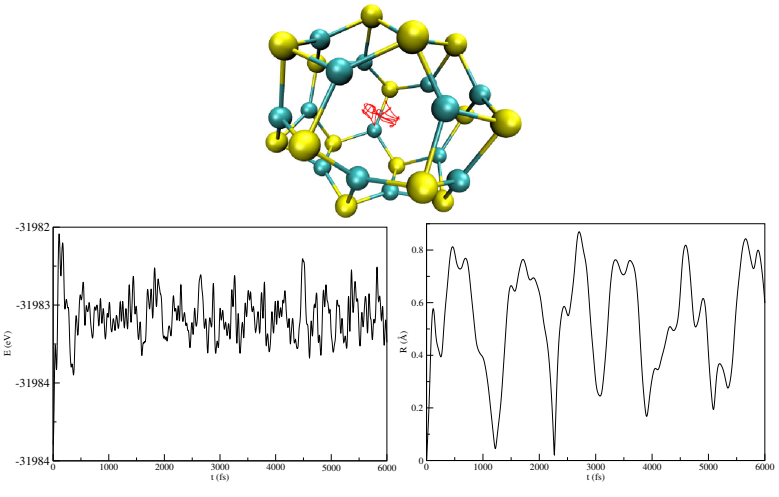

Figure 10.28: (Br@(CdS)$_{16}$)$^{-}$. Top: Dynamical trajectories of the K atom inside the nanocluster. This plot was prepared as the K@(CdS)$_{12}$ one. Below, the variation of the energy, in eV (left) and the variation of the distance, R, in Å (right), of the trapped Br atom from the center of mass of the nanocluster as a function of time.

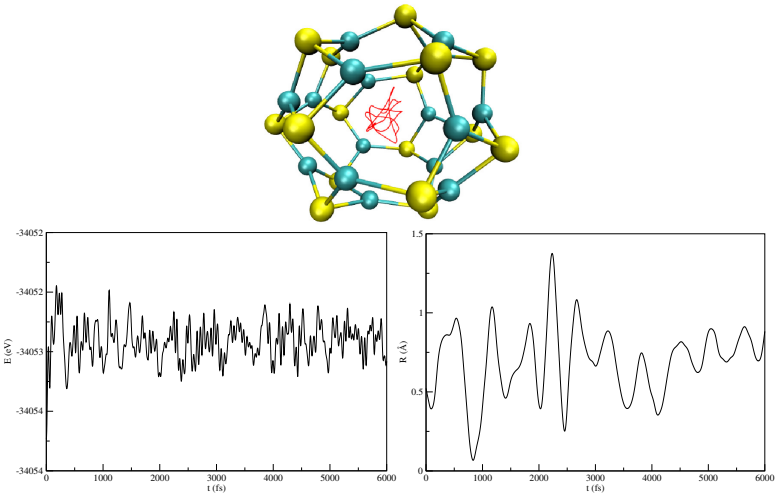

Chapter 11

Supporting Information of Chapter 2

Figure 11.1: TDDFT absorption spectra of the endohedrally doped $(X@(CdS)_i)^{\pm 2}$ (X = Be, Mg, Ca, O, S, Se and i = 9, 12, 15, 16) clusters, drawn by a Gaussian convolution of the lowest 20 singlet excited states with FWHM 3000 cm^{-1}. Excitation energies are depicted as vertical bars with heights equal to their oscillator strengths. For comparison, the spectra of the bare clusters, in black, are also shown.

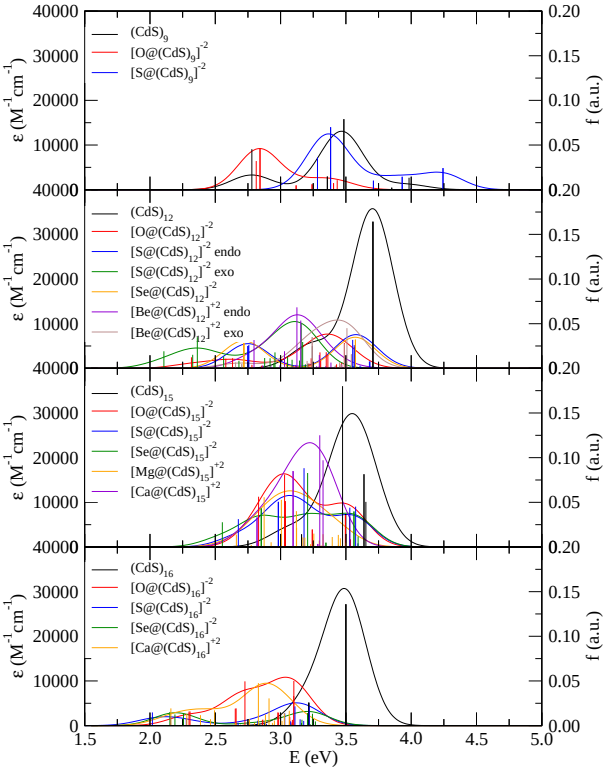

Table 11.1: Valence excitation spectra of the bare $(CdS)_i$ (i = 9, 12, 15, 16) clusters. Vertical excitation energy (in eV) and the corresponding oscillator strength (f, in a.u.) are reported, along with the composition of the excited state. Among the lowest-lying excitations, the first and those with f > 0.01 are shown. Only transitions with contribution > 20% are shown.

Cluster	#Trans.	E (eV)	f (a.u.)	Composition				Cluster	#Trans.	E (eV)	f (a.u.)	Composition			
$(CdS)_9$	1	2.53	0.0000	99%	H	→	L	$(CdS)_{12}$	1	3.98	0.0000	75%	H	→	L
	3	2.78	0.0454	99%	H-2	→	L					21%	H-1	→	L
	8	3.36	0.0148	59%	H	→	L+1		4	3.24	0.0248	95%	H-4	→	L
				37%	H-7	→	L		5	3.24	0.0248	53%	H-5	→	L
	9	3.36	0.0148	59%	H-1	→	L+1					42%	H-3	→	L
				37%	H-8	→	L		6	3.24	0.0248	54%	H-3	→	L
	11	3.48	0.0790	59%	H-7	→	L					43%	H-5	→	L
				32%	H	→	L+1		12	3.71	0.1642	58%	H-13	→	L
	12	3.48	0.0790	59%	H-8	→	L					25%	H-12	→	L
				32%	H-1	→	L+1			3.71	0.1642	59%	H-12	→	L
	19	3.98	0.0134	42%	H	→	L+2					32%	H-11	→	L
				42%	H-1	→	L+3			3.71	0.1642	52%	H-11	→	L
												32%	H-13		L

Cluster	#Trans.	E (eV)	f (a.u.)	Composition				Cluster	#Trans.	E (eV)	f (a.u.)	Composition			
$(CdS)_{15}$	1	2.91	0.0000	53%	H-1	→	L	$(CdS)_{16}$	1	2.89	0.0000	95%	H	→	L
				44%	H	→	L		7	3.22	0.0258	96%	H-6	→	L
	3	3.04	0.0357	97%	H-2	→	L		8	3.22	0.0258	96%	H-7	→	L
	5	3.16	0.0142	51%	H-4	→	L		9	3.22	0.0258	96%	H-8	→	L
				45%	H-5	→	L		13	3.50	0.1354	95%	H-11	→	L
	6	3.16	0.0142	51%	H-5	→	L		14	3.50	0.1354	95%	H-12	→	L
				45%	H-4	→	L		15	3.50	0.1354	95%	H-13	→	L
	10	3.47	0.1797	94%	H-9	→	L								
	11	3.50	0.0369	60%	H-11	→	L								
				24%	H-10	→	L								
	12	3.50	0.0369	60%	H-10	→	L								
				24%	H-11	→	L								
	15	3.64	0.0816	52%	H-15	→	L								
				32%	H-14	→	L								
	16	3.64	0.0816	52%	H-14	→	L								
				32%	H-15	→	L								
	17	3.65	0.0503	89%	H-18	→	L								

Table 11.2: Valence excitation spectra of the O-doped $[O@(CdS)_i]^{-2}$ (i = 9, 12, 15, 16) clusters. Vertical excitation energy (in eV) and the corresponding oscillator strength (f, in a.u.) are reported, along with the composition of the excited state. Among the lowest-lying excitations, the first and those with f > 0.01 are shown. Only transitions with contribution > 20% are shown.

Cluster	#Trans.	E (eV)	f (a.u.)	Composition				Cluster	#Trans.	E (eV)	f (a.u.)	Composition			
$[O@(CdS)_9]^{-2}$	1	2.73	0.0000	96%	H	→	L	$[O@(CdS)_{12}]^{-2}$	1	2.32	0.0000	98%	H	→	L
	4	2.81	0.0321	95%	H-3	→	L		2	2.58	0.0108	95%	H-1	→	L
	5	2.84	0.0465	76%	H-4	→	L		3	2.63	0.0113	95%	H-2	→	L
	6	2.84	0.0465	76%	H-5	→	L		10	3.23	0.0112	51%	H-7	→	L
	20	3.43	0.0107	31%	H-4	→	L+1					37%	H	→	L+2
				23%	H-10	→	L		12	3.30	0.0179	53%	H-8	→	L
				21%	H-5	→	L+2		14	3.35	0.0181	38%	H-10	→	L
												21%	H	→	L+3
									15	3.36	0.0151	56%	H-11	→	L
									19	3.49	0.0284	69%	H-12	→	L

Cluster	#Trans.	E (eV)	f (a.u.)	Composition				Cluster	#Trans.	E (eV)	f (a.u.)	Composition			
$[O@(CdS)_{15}]^{-2}$	1	2.79	0.0000	97%	H	→	L	$[O@(CdS)_{16}]^{-2}$	1	2.07	0.0000	97%	H	→	L
	3	2.83	0.0563	96%	H-2	→	L		2	2.30	0.0157	95%	H-1	→	L
	5	3.03	0.081	94%	H-4	→	L		3	2.31	0.0159	95%	H-2	→	L
	6	3.04	0.0513	96%	H-5	→	L		4	2.65	0.0193	95%	H-4	→	L
	7	3.04	0.0513	96%	H-6	→	L		5	2.66	0.0496	96%	H-5	→	L
	9	3.24	0.0196	90%	H-8	→	L		11	2.98	0.0148	94%	H-7	→	L
	10	3.24	0.0195	90%	H-9	→	L		13	2.98	0.0145	93%	H-8	→	L
	13	3.50	0.0358	65%	H-12	→	L		15	3.07	0.0101	23%	H-10	→	L
	14	3.50	0.0358	64%	H-13	→	L					20%	H-2	→	L+1
	15	3.53	0.0343	48%	H-3	→	L+1		19	3.10	0.0332	53%	H-12	→	L
				41%	H-16	→	L					38%	H-9	→	L
									20	3.10	0.0500	55%	H-9	→	L
												34%	H-12	→	L

Table 11.3: Valence excitation spectra of the endohedral and exohedral isomers of S- and Be-doped $(CdS)_{12}$ clusters. Vertical excitation energy (in eV) and the corresponding oscillator strength (f, in a.u.) are reported, along with the composition of the excited state. Among the lowest-lying excitations, the first and those with f > 0.01 are shown. Only transitions with contribution > 20% are shown.

Cluster	#Trans.	E (eV)	f (a.u.)	Composition				Cluster	#Trans.	E (eV)	f (a.u.)	Composition			
$[S@(CdS)_{12}]^{-2}$endo	1	2.75	0.0249	60%	H-1	→	L	$[S(CdS)_{12}]^{-2}$exo	1	2.10	0.0191	94%	H	→	L
				37%	H	→	L		2	2.33	0.0152	90%	H-2	→	L
	2	2.75	0.0252	49%	H-2	→	L		3	2.36	0.0349	82%	H-1	→	L
				26%	H-1	→	L		5	2.56	0.0135	81%	H-3	→	L
				24%	H	→	L		7	2.88	0.0116	47%	H-4	→	L+1
	3	2.76	0.0259	49%	H-2	→	L					25%	H-2	→	L+1
				38%	H	→	L		8	2.92	0.0113	92%	H	→	L+2
	11	3.56	0.0320	75%	H	→	L		10	2.96	0.0179	85%	H-5	→	L
	12	3.57	0.0250	29%	H-10	→	L		12	3.05	0.0129	57%	H-2	→	L+1
				23%	H-9	→	L					26%	H-4	→	L+1
				22%	H-6	→	L		16	3.16	0.0498	40%	H-1	→	L+2
	13	3.57	0.0254	29%	H-9	→	L					35%	H-7	→	L
				24%	H-10	→	L		17	3.17	0.0295	61%	H-1	→	L+3
				21%	H-7	→	L								

Cluster	#Trans.	E (eV)	f (a.u.)	Composition				Cluster	#Trans.	E (eV)	f (a.u.)	Composition			
$[Be@(CdS)_{12}]^{+2}$endo	1	2.64	0.0004	93%	H	→	L	$[Be(CdS)_{12}]^{+2}$endo	1	2.66	0.0067	98%	H	→	L
	2	2.80	0.0317	98%	H-1	→	L		7	3.24	0.0350	67%	H-6	→	L
	7	3.03	0.0192	77%	H-5	→	L					20%	H-5	→	L
	10	3.12	0.0683	78%	H-6	→	L		8	3.24	0.0349	62%	H-7	→	L
	11	3.15	0.0535	33%	H-7	→	L								
				32%	H-8	→	L								
	14	3.30	0.0149	79%	H-9	→	L								

Part VI

List of publications

- **Doped Aluminum Cluster Anions: Size Matters**

  Elisa Jimenez-Izal, Jose Maria Mercero, Jon M. Matxain, Martha Audiffred, Diego Moreno, Gabriel Merino, and Jesus M. Ugalde

  J. Phys. Chem. A **2014**, DOI: 10.1021/jp501496b

- **CdS Nanoclusters Doped with Divalent Atoms**

  Elisa Jimenez-Izal, Jon M. Azpiroz, Riti Gupta, Jon M. Matxain, and Jesus M. Ugalde

  J. Mol. Model. **2014**, 20, 2227.

- **Second-row Transition-Metal Doping of $(ZnS)_i$, i= 12, 16 Nanoclusters: Structural and Magnetic Properties**

  Elisa Jimenez-Izal, Jon M. Matxain, Mario Piris, and Jesus M. Ugalde

  Computation ***2013***, *1*, 31.

- **On the Directionality of Halogen Bonding**

  Stefan M. Huber, Joseph D. Scanlon, Elisa Jimenez-Izal, Jesus M. Ugalde, and Ivan Infante

  Phys. Chem. Chem. Phys. ***2012***, *15*, 10350.

- **Glycine Adsorption at Nonstoichiometric (010) Hydroxyapatite Surfaces: A B3LYP Study**

  Elisa Jimenez-Izal, Fabio Chiatti, Marta Corno, Albert Rimola, and Piero Ugliengo

  J. Phys. Chem. C ***2012***, *116*, 14561.

- **Unexpected Trends in Halogen-Bond Based Noncovalent Adducts**

  Stefan M. Huber, Elisa Jimenez-Izal, Jesus M. Ugalde, and Ivan Infante

  Chem. Comm. ***2012***, *48*, 7708.

- **Self-assembling Endohedrally Doped CdS Nanoclusters: New Porous Solid Phases of CdS**

  Elisa Jimenez-Izal, Jon M. Matxain, Mario Piris, and Jesus M. Ugalde

  Phys. Chem. Chem. Phys. ***2012***, *14*, 9676.

- **Thermal Stability of Endohedral First-Row Transition-Metal TM@Zn_iS_i Structures, i=12, 16**

  Elisa Jimenez-Izal, Jon M. Matxain, Mario Piris, and Jesus M. Ugalde

  J. Phys. Chem. C ***2011***, *115*, 7829.

- **Structure and Stability of the Endohedrally Doped (X@Cd_iS_i)$^{q=0,\pm1}_{i=4,9,12,15,16}$, X=Na,K,Cl,Br Nanoclusters**

  Elisa Jimenez-Izal, Jon M. Matxain, Mario Piris, and Jesus M. Ugalde

  J. Phys. Chem. C ***2010***, *114*, 2476.